Studies of cosmic dust analogues using synchrotron X-ray powder diffraction

Sarah Joanne Day
B.Sc (Hons.)

Doctor of Philosophy in Physics

School of Physical and Geographical Sciences, University of Keele.

June 2014

Abstract

The structural evolution of cosmic dust analogues has been investigated using in situ synchrotron X-ray powder diffraction (SXPD) at the Diamond Light Source. Amorphous Mg/Ca silicates are produced as analogues of cosmic dust using a modified sol-gel method. They are studied under non-ambient temperature and pressure conditions using in situ powder diffraction, complemented by FTIR and Raman spectroscopy. The solid-state mineralisation of amorphous grains is observed by thermal annealing and the results of this allow the environmental conditions leading to the formation of crystalline dust grains in astrophysical environments to be constrained.

The solid-gas carbonation of amorphous Ca-rich silicates is studied using in situ SXPD and analysed using full-profile fitting techniques, while the effect of ex situ carbonation on the short range ordering of amorphous grains is investigated using high energy SXPD and Pair Distribution Function (PDF) analysis. The formation of a metastable calcium carbonate phase (vaterite) is observed and the importance of this in relation to astrophysical environments is discussed.

In situ Raman and SXPD data of CO_2 clathrate hydrates are presented and the importance of the Raman data obtained here with relevance to future remote sensing missions to Solar System bodies is discussed. This work indicates the importance of laboratory work to the field of astrophysics and provides novel experimental approaches to aid our understanding of astrophysical processes.

Acknowledgements

I would like to express my sincere thanks to my supervisor, Professor Nye Evans, for all of his support, encouragement and advice during the course of my PhD. I could not have done this without him.

Equally, to my Diamond supervisor, Dr Stephen Thompson, I would like to express my gratitude for his invaluable guidance and advice over the last three years. I would also like to send special thanks to Dr. Julia Parker, for her help with sample preparation and for teaching me how to use TOPAS, Jonathan Potter, for providing technical support during our beamtime, and the other members of I11; Chiu, Alastair, Claire and Paul, for being so friendly and for making me feel welcome on my regular visits to Diamond.

Furthermore, I would like to thank everyone in the Astrophysics group at Keele for all of the good times, interesting discussions, inspirational words and most of all their friendship.

On a more personal note, I want to thank my partner, Nick, who has been there through all of the ups and downs, providing encouragement and comfort when I needed it most. Finally, I want to say a heartfelt thank you to my family for all of their love and unending support and for always encouraging me to follow my dreams.

Contents

List of Figures

List of Tables

1 Introduction

1.1 Overview

The Earth was originally formed 4.6 billion years ago from the material that was present within the early Solar nebula. This material was in the form of small, solid grains of 'dust' ranging in size from a few microns down to large molecules made up of tens of atoms that originated in the atmospheres of evolved stars (Draine 2003). Grains surviving the initial gravitational collapse which formed the Sun then become incorporated into a dense disc of dust and gas surrounding the newly formed star and collisions between the dust grains within this disc lead to the agglomeration of these materials into larger planetesimal bodies, of which some became planets, such as Earth. Therefore the initial, fundamental composition of the Earth is directly determined by the composition of the material present within the pre-Solar nebula.

There is, therefore, a direct link between present day Earth and the dust produced by dying stars. This compositional information could be incorporated into current models, based on N-body simulations, for understanding the Earth's composition and interior structure that do not currently account for the compositional nature of the planet-forming materials. The relationship between pre-planetary and post-planetary matter is still poorly understood. The formation (including nucleation and grain growth) of dust in the turbulent atmospheres of evolved stars proceeds under chaotic conditions, far from chemical equilibrium, yielding non-crystalline, poorly ordered solids. While a small amount of crystalline silicate material has been observed in such environments (Waters et al. 1996; Sylvester et al. 1999; Molster et al. 2001, 2002) it is associated with a very small fraction of the total silicate dust mass (<10%; Kemper et al. 2001). That being said, no crystalline silicate material has been detected in the interstellar medium (ISM), suggesting that all of the material ejected into the ISM is amorphous in nature or that amorphisation processes are at work within the ISM that break down the crystalline structure of the grains. Crystalline silicates are

however known to have existed within the early solar nebula, as determined by their presence within planetesimals such as meteorites and cometary bodies, indicating that the grains have experienced some form of processing between their residence in the ISM and their incorporation into a newly formed planetary system.

Two dominant mechanisms that have been associated with crystallisation of initially amorphous materials are: annealing through irradiation by high-energy ions and/or electrons, thermal annealing and/or a combination of the two. Observations of protoplanetary discs in the Taurus star cluster confine the crystalline silicate population to a radial distance of less than 10 AU, with amorphous grains present at much further distances. This supports the process of thermal annealing by the central star as an important factor in the crystallisation of dust in early planetary systems; therefore obtaining a clear understanding of the structural and compositional effects of thermal annealing on these dust grains could provide important information relating to the processes that acted upon the materials that eventually became the Earth.

The main technique used for the observation of cosmic materials is spectroscopy. A wealth of observational data, collected at ultraviolet (UV) and mid- and far-infrared (IR) wavelengths, relating to dust grains in planetary, cometary, circumstellar and interstellar environments (Molster & Waters 2003; Sitko et al. 2004; Tielens 2008) has been obtained to date, but it is only through laboratory experiments providing modelled IR spectra of terrestrial materials and/or laboratory analogues that the interpretation and understanding of these spectra has been achieved. Comparison of astronomical spectra with those of laboratory analogues and known terrestrial materials is, however, not without difficulty. Often, spectra cannot be associated with just one material and a number of spectral features can be fit by multiple mineral species, preventing reliable identification in many cases. Therefore, IR spectroscopy alone cannot be used to obtain a complete account of the processing history of dust grains but, with additional structural information, as provided by synchrotron X-ray diffraction, these processes and the effect they have on materials can be better understood, providing an understanding of the underlying crystal structure that will also aid subsequent interpretation of IR spectra.

IR spectroscopy has, however, allowed the identification of a rich variety of minerals (Molster & Waters 2003) within a range of astrophysical environments. These include:

1. Amorphous Mg-rich silicates of olivine ($MgSiO_3$) and pyroxene ($MgSi_2O_4$) composition
2. Amorphous and crystalline silica
3. Crystalline Mg- and Fe-rich olivines and pyroxenes.
4. Ca-rich pyroxenes (such as diopside; $MgCaSi_2O_6$)
5. Carbonate minerals (including calcite ($CaCO_3$) and dolomite ($CaMg(CO_3)_2$)

Of these, the most abundant are the amorphous Mg-rich silicates, being present in all O-rich dust-forming regions (Gail 2003) and responsible for the ubiquitous 10μm feature observed in astronomical spectra. However, also interesting are the carbonate materials, identified in protostellar and protoplanetary environments (Kemper, Jager & Waters 2002; Ceccarelli & Caux 2002; Chiavassa, Ceccarelli & Tielens 2005) by their features in the far-IR (65μm and 90-100μm). Terrestrial carbonates are known to form almost exclusively in the presence of liquid water and therefore the presence of such minerals in non-aqueous circumstellar environments is surprising. Due to the nature of carbonates and their low condensation temperature of $<$800 K it has been determined that carbonate dust would unlikely be formed through vapour-phase condensation in the atmospheres of stars. The high velocity outflows caused by radiation pressure on previously condensed grains significantly dilute the remaining gas to a point where the particle densities are so small that carbonate formation is no longer viable (Ferrarotti & Gail 2005). The mechanisms governing the formation of carbonate materials in non-aqueous circumstellar environments are therefore not well understood. One mechanism of formation, based on the presence of Ca-rich silicates (such as diopside) and SiO_2 in circumstellar environments is the formation through solid-gas interaction of amorphous Ca-rich silicates and hot gaseous CO_2 via the reaction: $CaSiO_3 + CO_2 \longrightarrow CaCO_3 +$

SiO_2 which is consistent with the observed materials. In order to determine the viability of this formation method, laboratory experimentation under simulated astrophysical conditions is essential.

1.2 Research Objectives

The main research objectives for this thesis are, therefore, to improve our understanding of the structural evolution of refractory cosmic dust grains through thermal annealing and to study the formation mechanisms of carbonate formation in astrophysical environments using an experimental approach.

1.3 Thesis Plan

This thesis consists of a total of 11 chapters. This introductory chapter (Chapter 1) is followed by Chapter 2, which provides a comprehensive literature review of the nature of cosmic dust, from its formation, through to detection, and finally to our current understanding of the dominant materials that constitute cosmic dust. Chapter 3 summarises previous laboratory work focused on the study of cosmic materials. The Methodology chapter, Chapter 4, provides the detailed theory of all experimental methods and analytical techniques used during this project, while Chapter 5 provides technical details of the facilities used for data collection, as well as providing an in-depth description of the sample preparation procedure and initial characterisation of the synthesised samples. The next five chapters are results chapters. Chapter 6 presents the results of in situ thermal annealing experiments of cosmic dust analogues of varying composition. Chapters 7 and 8 focus on the in situ and ex situ carbonation of amorphous silicate grains using conventional synchrotron powder diffraction and the Total Scattering method, respectively, while Chapter 9 presents the results of in situ carbonation experiments in which a rare calcium carbonate polymorph is produced. Chapter

10 describes the results of a study into the formation and stability of clathrate hydrate compounds with relevance to Solar System bodies. Finally, Chapter 11 presents the conclusions of this work based on a summary of the results from Chapters 6 to 10 and identifies future work to be carried out as a continuation of this project.

2 Background

2.1 Cosmic dust

Dust is widespread throughout the Universe, present within a wide range of astrophysical environments, from the ISM to dense molecular clouds, circumstellar discs and around the active cores of galaxies (AGN). It has been determined that the mass of dust in the ISM is only 1% of the total mass of the ISM (Whittet 2003). The presence of interstellar dust was first convincingly inferred by Trumpler (1930) through extinction, the absorbance of starlight by what he interpreted as "fine dust particles of varying sizes" in the line of sight towards the measured objects. Since then, interstellar dust has been a topic of great interest, with the study of interstellar extinction curves providing a great deal of information about the properties of dust, such as absorption, scattering and emission, as well as allowing interpretation of the composition of interstellar dust particles and the importance they have in a number of astrophysical processes. Interstellar dust absorbs UV photons from starlight and re-radiates in the infrared (IR). This IR emission of dust accounts for almost 30% of the bolometric luminosity of the Galaxy (Mathis 1990) and provides a wealth of information about the properties and composition of the emitting grains, as well as information about local environmental conditions, temperatures and grain processes.

Dust, being so abundant, plays an important role in a vast majority of complex astrophysical processes, with its study helping to define and improve our understanding of such processes. It is responsible for controlling temperature regimes in a number of environments though photo-electron heating of surrounding gas or cooling within dense molecular clouds by infrared emission, and is a dominant factor in the chemical evolution of molecular clouds and ultimately is a major constituent in the formation of new stars and planetary systems.

The vast number of dust grains, together with their small size, provides a large surface area over which solid-gas chemical reactions can occur, promoting the forma-

tion of more complex molecules within the ISM. Refractory, primitive dust particles are first condensed out of the hot gas within the atmospheres of evolved stars, through the process of vapour-phase condensation and are then ejected into the ISM by energetic stellar winds of pulsating asymptotic giant branch (AGB) stars, or via supernova explosions. This means that the ISM is constantly being enriched with new material, with each new generation of stars. It is important to note that the dust within molecular clouds is that which accumulates through gravitational collapse to eventually form new stars and planetary systems, such as our own. These stars then ultimately evolve to end their lives as a supernovae explosion or planetary nebulae, releasing new dust that will eventually become part of a molecular cloud and go on to form another generation of new stars – the life cycle of dust (see Figure 2.1).

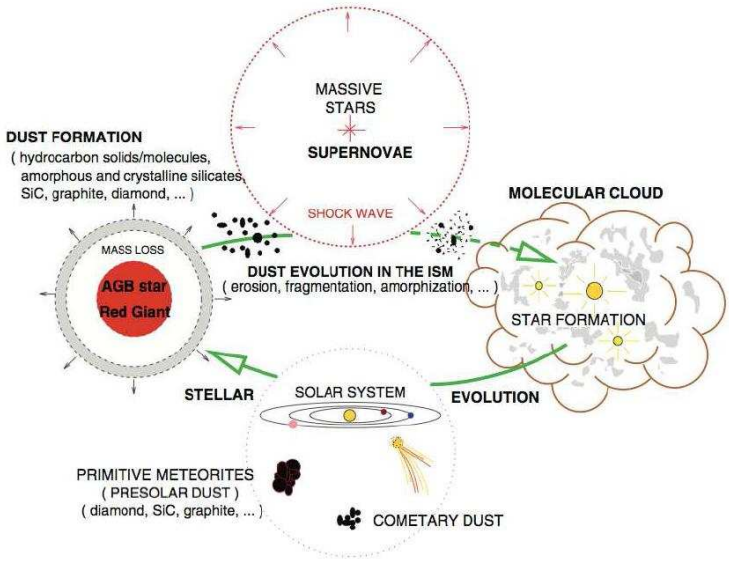

Figure 2.1: Illustrative figure showing the evolutionary cycle of dust grains (Compiegne 2011; Jones 2004)

Throughout this cycle a single dust grain will be exposed to a multitude of processes, over a large number of different environments, experiencing extremes of temperature and radiation, as well as chemical reactions with hot and cold gases, forming

mantles around its original refractory core. These processes throughout the life of dust grains are what lead to the evolution from the original primitive materials produced through condensation within evolved stellar atmospheres to the complex mineral species present within the pre-solar nebula, and ultimately to the complex crystalline minerals that now constitute the basic composition of the Earth. It is this evolution from primordial, disordered dust grains to complex ordered mineral species that this thesis is aiming to study.

2.2 Dust formation

Solid dust particles are initially formed during the later stages of stellar evolution, starting once stars reach the AGB phase, and continuing right through until the formation of planetary nebulae or supernovae. It was found by Gehrz (1989), through comparison of average mass loss rates for different dust-producing stellar phases, that pulsating AGB stars are the dominant source of dust input into the ISM, having a dust return rate, $(\frac{dM}{dt})_{\rm dust}$, of 0.01 – 0.08$\rm M_{\odot}$ $\rm yr^{-1}$, compared to the dust return rate of supernovae, given to be 0.001 – 0.006$\rm M_{\odot}$ $\rm yr^{-1}$ (Ferrarotti & Gail 2006). It is important to note that during supernovae explosions, large shocks are responsible for grain destruction, through sputtering by the hot gases between shocks at a rate of 0.1 – 0.3$\rm M_{\odot}$ $\rm yr^{-1}$ (Gehrz 1989).

In the case of AGB stars it is the pulsation of the star that provides the driving force for the production of dust within the circumstellar envelope. Atmospheric gas from the surface of the star, containing a number of heavy elements brought up from the centre of the star in 'dredge-up' events (Niyogi, Speck & Onaka 2011), gets ejected by the violent pulsations, outflowing radially away from the star. It has been determined by van Loon et al. (2005) that at this stage stars can lose up to 80% of their total mass, at a rate of 10^{-6} – $10^{-4}\rm M_{\odot}$ $\rm yr^{-1}$. As the outflow begins to cool with distance from the star, dust grains begin to condense at temperatures dependent on the chemical composition of the grains. The composition and structure of the dust grains produced

in such an outflow are determined by the initial chemistry of the star itself and the temperature and density of the outflow.

The C/O ratio of the stars will play an important role in determining the chemistry of the condensates. Stars initially have a C/O ~ 0.4, indicating an over abundance of oxygen relative to carbon, however in the case of AGB stars, due to the production of carbon within the helium-burning core and processes bringing this newly formed carbon up to the surface, it is possible for carbon to become abundant over oxygen, producing a ratio of C/O >1. For C-rich outflows the main dust species likely to form are carbonaceous, such as pure C (in multiple forms), TiC and SiC, whereas in an oxygen-rich outflow the dominant dust species would be oxides – Al_2O_3, SiO_2 and MgO (Gail & Sedlmayr 1999).

Presently, there are three main methods of silicate dust formation being considered for circumstellar environments (Niyogi, Speck & Onaka 2011), these are:

1. Thermodynamic equilibrium condensation

2. Formation of chaotic solids in a supersaturated gas

3. Formation of seed nuclei in supersaturated gas, followed by mantle growth

However, there is observational evidence to suggest that methods (1) and (3) occur consecutively within the condensation sequence (Dijkstra et al. 2005).

The first minerals to form out of the hot gas as it cools are refractory oxides, forming at temperatures below 1760 K, including TiO_2 as suggested by Gail & Sedlmayr (1998) and Al_2O_3 which then reacts with gaseous SiO, Mg and Ca at lower temperatures to form melilite ($Ca_2[Al,Mg]_2SiO_7$) and then diopside ($CaMgSi_2O_6$). Below 1440 K silicates begin to form on the refractory grains as mantles. Due to the abundance of Mg and Fe over Ca and Al it is forsterite (Mg_2SiO_4) that forms primarily, being transformed to enstatite ($MgSiO_3$) through gas-grain interactions. Fe is not found to be an abundant component within the silicate end-members but Okada et al. (2009) have shown that in such environments, Fe is greatly depleted from the gas phase

and so it must be in a solid state of some form, possibly as grains of pure metallic iron (Niyogi, Speck & Onaka 2011; McDonald et al. 2010) .

Mattsson (2011) has proposed, from studies of high-redshift galaxies, that the net stellar dust formation rate is insufficient to account for the amount of dust measured for such galaxies and he suggests an alternative method of dust formation to account for this. The formation route he proposed for the high dust mass in galaxies such as SDSS J1148+5251, a quasar host galaxy, is through significant non-stellar dust production. He proposes two non-stellar formation mechanisms that could account for the large dust mass, these are; i) dust growth in the interstellar gas of quasar host galaxies through accretion onto seed particles and ii) nucleation and growth of dust in broad emission line clouds in quasar wind outflows.

2.3 Interstellar extinction

The presence of dust in interstellar space was first conclusively detected in 1930 by Robert J. Trumpler (Trumpler 1930) who compared the distances to 100 open clusters, obtained through two independent methods. The first used the magnitudes and spectral types of the stars within the clusters to determine the "photometric distance" of the cluster, while the second relied on the assumption that clusters of similar age have similar dimensions, using the observed angular diameter of the cluster to determine its distance. When plotted against each other these measurements should follow a straight line if no absorption of light is present; however, Trumpler (1930) found that, with increasing distance, the difference between the measured values became greater. This indicated that the starlight from more distant stars was being attenuated on its way to Earth. He concluded that this effect, now known as extinction, was due to "fine cosmic dust particles of various sizes" causing the absorption and scattering of starlight. He predicted that these grains were made up of calcium, due to prominent absorption lines within the spectra of O and B class stars. Extinction is most accurately measured using the 'pair method', where two stars of the same spectral class are observed and one of

these is known not to be affected by the presence of interstellar dust. The difference in the measured spectra of these stars allows the extinction affecting the second star in that line of sight to be determined, as a function of wavelength, (Draine 2003) using the equation:

$$A_\lambda = 2.5 \log_{10} \frac{F^0_\lambda}{F_\lambda}$$

where F^0_λ is the flux in the absence of extinction and F_λ is the observed flux. This can be applied to a number of objects, not just stars, and extinction is found to be heavily wavelength and position dependent. Extinction becomes greater towards the Galactic plane where the volume density of dust is much greater. Measurements of extinction have been conducted over a wide range of wavelengths, from the near-infrared to the UV and more recently into the X-ray spectrum. The extinction curves produced by such measurements across this wide wavelength range show a number of defining features, as seen in Figure 2.2.

Extinction now plays a large role in the study of interstellar dust, extinction curves and the features seen within them can provide a great deal of information relating to the physical characteristics of the dust, as well as information about the environmental conditions in which the dust grains exist. A number of features are seen within extinction curves at different wavelengths, the most studied one being a broad feature centred at 2175Å in the UV.

2.3.1 The 2175Å feature

This feature is usually referred to as the '2200Å' or '2175Å' feature. The 'bump' in the UV part of the interstellar extinction, peaking at 2175 Å and discovered by Stecher (1965), has been the source of interest for a long time, however, the observed variability of this feature from one sight-line to another has made it very difficult to reliably identify a carrier. Currently the most readily accepted suggestion for the carrier of this feature is a form of graphitic carbon. A wealth of papers have been published

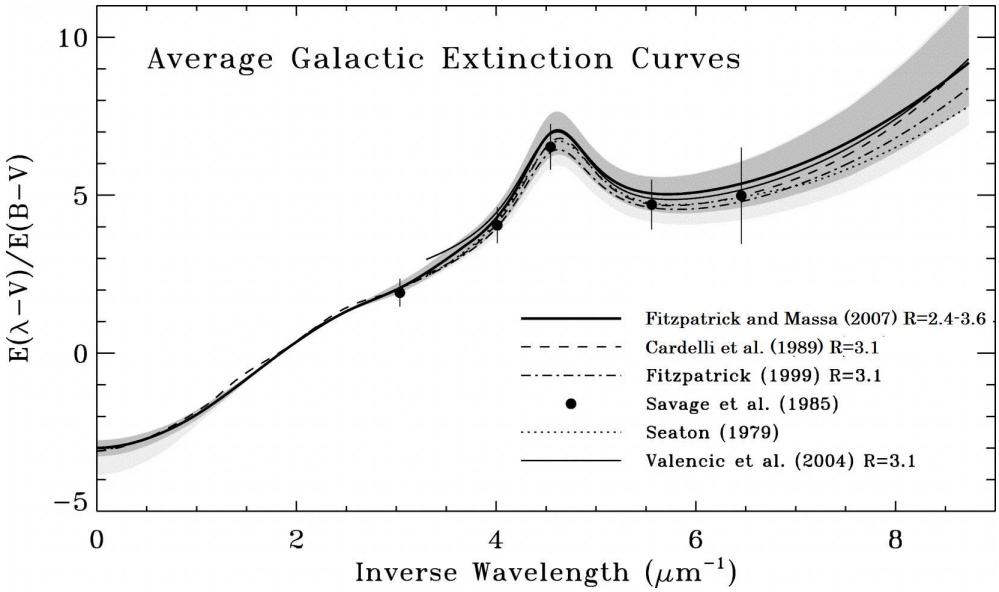

Figure 2.2: Plot showing average extinction curves of the Milky Way, LMC and SMC from stated sources. The 2175Å feature is clearly seen in all of them. Figure adapted from Fitzpatrick & Massa (2007).

suggesting the unique types of carbon compounds that could be responsible for this broad UV feature. Papers to note are those of Hoyle & Wickramasinge (1962); Hecht (1986); Fitzpatrick & Massa (1986); Bradley et al. (2005).

It was found by Fitzpatrick & Massa (1986) that neither the intensity or the observed position of the bump is dependent on the interstellar environment, however the broadness of the bump is in fact sensitive to changes in the surrounding environment. The feature is broader when looking through a dense medium and narrower when looking through a diffuse medium. The original suggestion for the carrier of the 2175Å bump in UV extinction was graphite (Hoyle & Wickramasinge 1962), which also accounts for almost half of the extinction features in the visible wavelength region and the additional turn-up in the UV extinction $> 7\mu\text{m}^{-1}$. However, this leads to the peak position of the bump being linked to the average particle size of the graphite grains. The studies by Fitzpatrick & Massa (1986) indicate that there is very little shift in peak position of the bump, even across a number of different environments,

therefore they suggest that the bump is in fact due to much smaller graphitic particles of < 50Å in size. These smaller particles would still accurately account for the bump and the visible extinction features as graphite did but the peak position would be independent of grain size. Other suggestions for the carrier of the UV feature include one by Hecht (1986) that it is due to graphite grains forming mantles or absorbing impurities, and the theory by Chen et al. (2008) that buckyonions (layered, multishell fullerenes) could be a plausible carrier for the feature, along with amorphous silicates and other carbonaceous species. Bradley et al. (2005), have reported the presence of a 2175Å feature within interplanetary dust particles, suggesting that the carrier of this feature in the interstellar extinction is in fact a composite of carbonaceous material and amorphous silicates, both of which are abundant in interstellar space. He suggests this multi-component approach as a solution of the variation in the bandwidth of the feature.

2.4 Infrared astronomy

IR radiation was discovered by William Herschel in the 19th century but it was not until a few decades later that any attempts were made to observe astronomical objects in the IR. A few attempts were made (Huggins 1869; Ranyard 1878; Hale 1899) but results were often inconclusive and even the authors were reluctant to confirm that a true detection had been made (Rieke 2009). It was not until the 1960s that modern IR astronomy saw its true beginnings, with the IR observations made by Johnson (1962, 1966); Wildey & Murray (1963) annd Low & Johnson (1965).

2.4.1 Infrared absorption

IR radiation is mostly absorbed by the Earth's atmosphere, therefore observations of IR features from ground-based telescopes can be difficult, requiring the removal of background atmospheric noise from observed spectra before they can be properly analysed.

However, with the launch of a number of orbiting IR telescopes such as the Infrared Space Observatory (ISO) (Kessler, Steinz & Anderegg 1996) and Spitzer (Werner et al. 2004) astronomical spectra can now be obtained over a larger range of wavelengths, with increased resolution. The main focus of studies into interstellar extinction curves has been in the UV-visible wavelength range, focusing on features such as the 2175Å 'bump' discussed previously, but there is a large number of important extinction features seen from extinction curves focusing on IR wavelengths between 2.5 – 25μm. These include absorption bands at 3.1μm, due to the O-H stretching feature in water ice, at 3.4μm, due to hydrocarbons and the broad bands at 9.7μm and 18μm due to silicate Si-O stretching and O-Si-O bending modes, respectively. Absorption features within the IR spectral region are due to vibronic transitions within solid-state compounds caused by the interaction of such particles with IR photons (Snow 2004). This means that the intensity and shape of these features can provide information relating to the nature of the observed interstellar grains, including composition, size distribution and shape. More detailed analysis of the absorption features, when accompanied by laboratory data, can also provide information about the thermal history and degree of crystallisation of grains. Thermal processing of grains can transform disordered amorphous grains into more structured, crystalline materials that show different absorption features. Amorphous materials have very broad absorption features (see Figure 2.3a), whereas the features of crystalline materials are much sharper, with well-defined peaks (see Figure 2.3b).

Interstellar silicates are primarily detected through IR emission features at 9.7 and 18μm as they are very efficient at re-radiating in IR wavelengths. However, due to the low temperature of dust within the ISM relative to circumstellar environments, silicates are more prominently seen through extinction in the ISM. The silicate features at 9.7μm and 18μm are conclusively due to amorphous, disordered silicate grains, most accurately represented by laboratory analogues having terrestrial olivine ($Mg_{2x}Fe_{2-2x}SiO_4$) and pyroxene ($Mg_xFe_{1-x}SiO_3$) composition. As can be seen in Figure 2.4, both features are broad, and relatively featureless, a defining characteristic of amorphous grains.

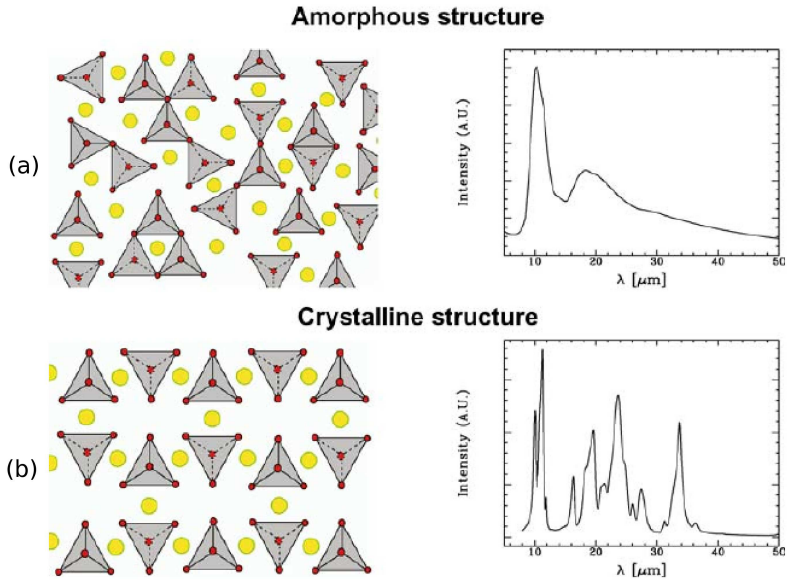

Figure 2.3: Comparison of IR spectra for amorphous (a) and crystalline silicates (b), along with their respective crystal structures. (Molster & Kemper 2005)

Although amorphous silicates are by far the most abundant grains in the ISM, little evidence has been found to date to confirm the presence of crystalline silicates, even though they are now known to be present both around evolved stars and within comets and meteors, representing the dust present in the pre-solar nebula as the Sun and planets were forming. This absence of crystalline silicates within the ISM is evidence that there are disrupting processes occurring within the interstellar environment, causing the silicates to lose their long-range structure (Demyk et al. 2004). This provides questions as to this absence of crystalline silicates within the ISM, how they are destroyed and formed again during planetary formation. Kemper, Vriend & Tielens (2005) have calculated that the percentage of crystalline silicates within the ISM is no more that 3%, whereas the percentage of crystalline silicates in circumstellar environments is calculated at $> 20\%$ (Kemper et al. 2001; Kemper, Markwick & Woods 2011).

However, it has been suggested that current observations of the ISM have not

been thorough enough to find sharp crystalline features and that these features may in fact be drowned out by the strength of the amorphous silicate features. Onaka & Okada (2003) reported the detection of a feature at 65μm in the diffuse emission from two active star-forming regions. They attribute this feature to diopside ($CaMgSi_2O_6$), supported by laboratory measurements of the optical properties of diopside (Chihara, Koike & Tsuchiyama 2001); if correct this is the first identification of crystalline silicates in interstellar diffuse emission. The absence of crystalline silicates within the ISM is currently a mystery, when they have been conclusively detected within the dust shells around evolved stars. It is this dust from the circumstellar envelopes of AGBs and other evolved stars that enriches the ISM with dust, so the injection and subsequent inferred destruction of circumstellar crystalline silicates is a process in need of more detailed study (Woolf 1973; Draine 2003; Snow 2004).

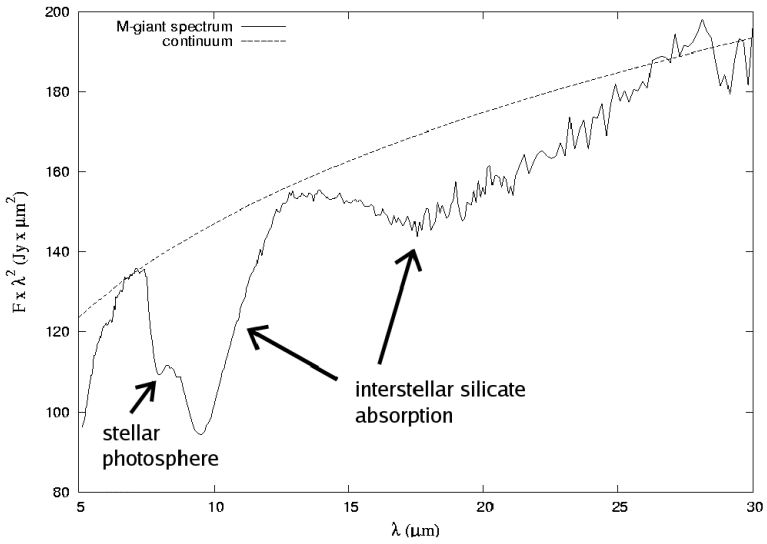

Figure 2.4: Silicate absorption features in the spectrum of a M-class giant star, taken with Spitzer. From van Breemen et al. (2011)

2.4.2 Infrared emission

The other defining feature indicating the presence of dust grains is their emission in the IR. Dust grains, irradiated by UV photons from stars, re-radiate in the IR. Whereas extinction is the most reliable way of studying the properties of grains within the ISM, the study of this IR emission is the predominant method of studying dust grains in stellar environments, for example, within envelopes of evolved stars or within debris discs around young, newly formed protostars.

2.4.2.1 Silicate features

Amorphous silicates also show prominent features at $\sim$10μm and 18μm in emission. As with the absorption features, due to the lack of long-range structure within amorphous materials, the emission features at these wavelengths are also broad and fairly featureless. Even so, these features in emission provide valuable information about the grains in question. The appearance of silicate emission features is shown in Figure 2.5.

The composition of the grains can have an effect on the location of the peak position for each of these features. For example, in pyroxenes (SiO_3) the peak will be at 9.7μm, whereas for olivine (Mg_2SiO_4) the peak can be shifted to a longer wavelength of $\sim$10.25μm (Jager et al. 2003a; Henning 2010). Koike et al. (2010) also find that the grain shape can greatly effect the IR spectra of dust. Their study of forsterite and enstatite grains show that, in comparison to laboratory spectra of irregularly shaped grains of forsterite, the features observed by ISO of dust in discs are shifted to shorter wavelengths. They also note that certain wavelengths are more sensitive to the effect of grain shape on spectra, with features at 11.9μm, 49μm and 69μm remaining relatively unchanged for different grain shapes. It is found that the shift of features to a shorter wavelength is obtained with a near-spherical grain shape, produced in the laboratory by annealing of initially amorphous silicate grains between 873 K and 1423 K (Koike et al. 2010). Crystalline silicates are now known to be present throughout a number of astrophysical environments, typically around evolved stars and in the discs of proto-

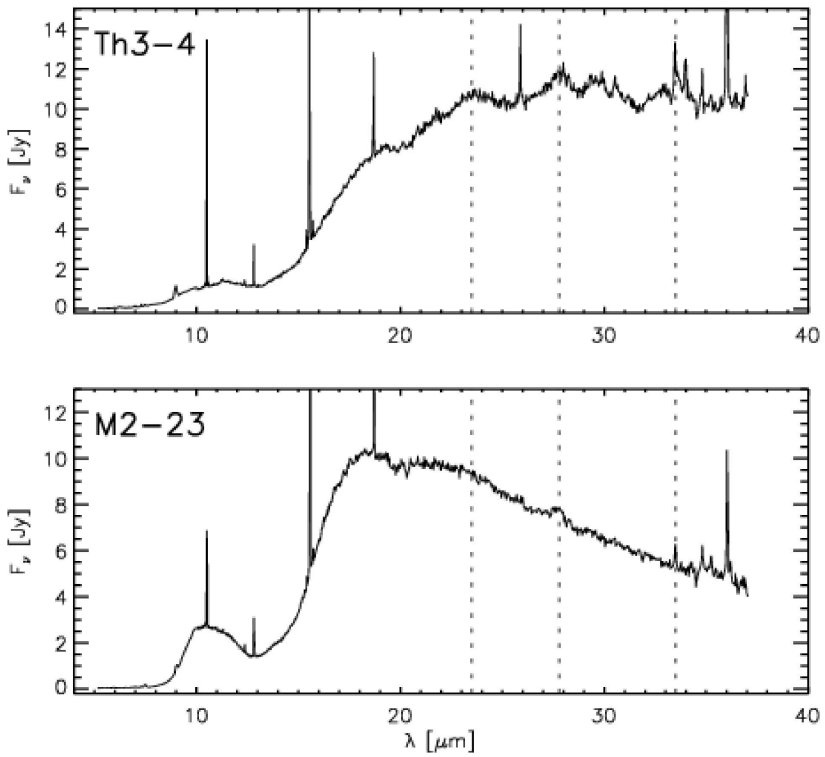

Figure 2.5: Total dust emission spectrum for the Diffuse High Galactic Latitude (DHGL) medium >15° latitude. After Compiegne (2011).

stars. Crystalline silicates show well defined, sharp peaks in the IR due to their ordered lattice structure and inter-tetrahedral bonds. The main features lie at 11, 16, 18, 23.6, 28 and 33.6μm, and are often well matched to laboratory spectra of the olivine group mineral forsterite ($MgSiO_4$).

2.4.2.2 Carbonate features

Infrared features representing carbonate materials in the far IR include bands at $\sim$50μm, 65μm and 92μm. Carbonates also exhibit features in the mid-IR region at $\sim$6μm, 6.8μm and 9μm but, these features are generally very weak and are greatly overshadowed by the large number of near – mid-IR water ice and silicate features that are much stronger. This makes it very difficult to use the mid-IR features to detect or confirm the presence of carbonates, instead relying solely on the distinctive far-IR features. Figure 2.6, shows the IR spectra of the most common astrophysical minerals, including carbonates, that contribute to the NGC6302 emission spectrum (Kemper, Jager & Waters 2002).

The near-IR features of carbonates at $\sim$6μm and $\sim$6.8μm are due to vibrational modes of the carbonate anions, while the feature at $\sim$9μm is indicative of the forbidden symmetric stretching feature of carbonates.

2.4.2.3 Carbonaceous features

A number of features seen within the ISM and certain carbon-rich stellar environments indicate the presence of very fine-grained carbonaceous material. The features attributed to this material are known as the Unidentified Infrared Bands (UIB's) although recently it has been suggested that these features are due to small molecules known as Polycyclic Aromatic Hydrocarbons (PAH) and small graphite particles. The features lie in the Near Infrared (NIR) at 3.3, 6.2, 7.7 8.6 and 11.3μm (Tielens 2008). There is also a PAH complex at 17μm, although this was never studied with ISO and therefore little is known about this.

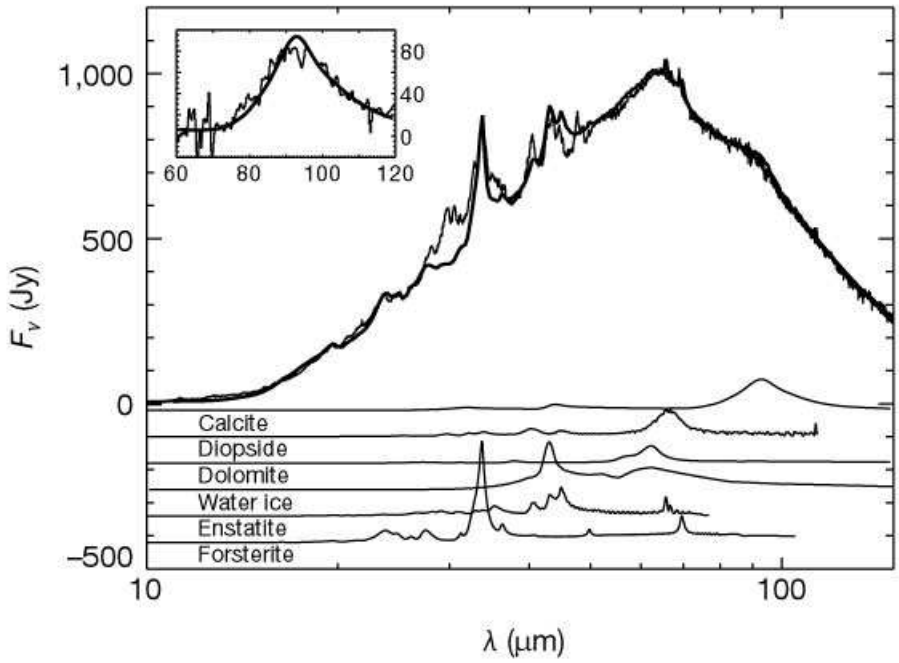

Figure 2.6: Spectra of planetary nebula NGC6302 identifying the main dust components that comprise the NGC6302 emission and showing the main features due to carbonate materials. (Kemper, Jager & Waters 2002).

2.5 Detecting dust

There have been a number of missions developed for the study of astrophysical environments, the most relevant to us are the IR missions, of which there have been three major contributors.

2.5.1 ISO

The Infrared Space Observatory (Kessler, Steinz & Anderegg 1996), launched in November 1995, was the defining mission with regards to the detection of carbonates

in space. It was the first of its kind, an orbiting Infrared Observatory able to operate at wavelengths from 2.5 – 240μm, unhindered by the effects of the atmosphere. This opened up a whole new way of looking at interstellar and circumstellar dust, allowing the discovery of carbonate materials through the detection of far-IR features that could not have been observed using ground-based telescopes. Due to ISO, carbonates have been found in planetary nebulae, including the well-studied NGC 6302 (Kemper, Jager & Waters 2002), star-forming regions, such as the Carina Nebula (Onaka & Okada 2003), and in the environments around protostars, e.g IRAS-4 within the NGC1333 complex (Ceccarelli & Caux 2002), amongst many others.

2.5.2 Spitzer Space Telescope

The Spitzer Space Telescope (Werner et al. 2004) was launched in 2003 and is able to observe in the mid-IR between 5 - 40μm. This is a small range compared to that of ISO, but Spitzer has played a large role in the detection of cosmic carbonates since its launch in 2005. The Deep Impact Mission (A'Hearn et al. 2005), in which the Deep Impact Probe impacted the surface of Comet Tempel-1 and sent a cloud of ejecta out from the surface of the comet, used Spitzer to study the composition of the ejecta and this led to the first conclusive detection of carbonates in comets (Lisse et al. 2006; Woodward et al. 2009).

2.5.3 Herschel

Herschel Space Observatory (Pilbratt et al. 2010) is a European Space Agency (ESA) mission that covered the far IR to the submillimeter wavelength range (55 - 675μm). It was launched in 2009 and ceased operations in April 2013 when its supply of liquid helium coolant was exhausted. Using instruments such as the Photodetector Array Camera and Spectrometer (PACS; Poglitsch et al. 2010) and the Spectral and Photometric Imaging Receiver (SPIRE; Griffin et al. 2010) it covers an IR range never before observed by previous orbiting observatories. Carbonates and crystalline sili-

cates exhibit features at wavelengths between 60 and 100μm and it is expected that the analysis of the data obtained by Herschel will provide more detailed information about the environment and mass of carbonates in astrophysical environments. The analyses of these data have yet to be published.

2.6 Grain materials

2.6.1 Silicates

2.6.1.1 Introduction

Through the study of absorption and emission features within the ISM and related environments it has been determined that the two major components of the total dust mass are silicates and carbon compounds (including graphite, amorphous carbon and PAHs; Draine 2003). Silicates make up a substantial fraction of the total dust mass, being present in a wide variety of environments throughout the cosmos, ranging from the ISM to circumstellar discs and in discs around AGN. Silicates were even present during the formation of our Solar System and became an important component of the Earth's outer layers, forming rocks such as peridotite (the main component of the Earth's mantle), granite and quartzite, and also being found within many other rock types in the form of silicate minerals such as quartz (SiO_2, the most abundant mineral on Earth), olivines ((Mg,Fe,Al)SiO_4, of varying compositions) and clinopyroxenes ((Mg,Fe,Al)SiO_2, of varying composition). The fact that silicate grains could be a dominant species within the ISM was discovered quite early in the study of dust in space as the elements that make up silicates are some of the most abundant in the universe; Si, O, Mg, Fe, Al and Ca (Henning 2010). The first suggestion of silicates being present as components of interstellar grains was by Kamijo (1963). He stated that silica (SiO_2) should be present within the atmospheres of M-type stars through the reaction:

$$SiO_2 \longleftrightarrow SiO + \frac{1}{2}O_2 \tag{2.1}$$

The dissociation energy of this reaction is much greater than the reaction to form CO_2

$$CO_2 \longleftrightarrow CO + \frac{1}{2}O_2 \tag{2.2}$$

and therefore silicates are the dominant grain species within this environment.

2.6.1.2 Chemistry

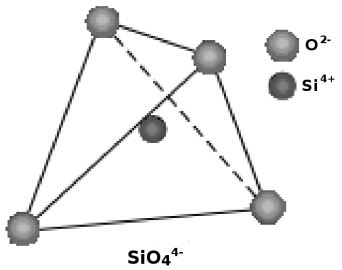

Figure 2.7: $[SiO_4]^{4-}$ tetrahedron

Silicates are defined as any compound made up of SiO_4 tetrahedra, as seen in Figure 2.7. These tetrahedra are formed by a single Si atom in the centre, surrounded by 4 oxygen atoms. The way in which these tetrahedra connect determines the unique structure and therefore optical properties of the silicate. Silicates are extremely diverse in terms of structure and composition as the SiO_4 tetrahedra can link in a number of ways, including in chains, sheets, loops, along with isolated tetrahedra. Due to the vast number of structures the tetrahedra can form, silicates are divided into a number of sub-groups. In the case of astrophysical environments, only two of these need to be considered (Deer, Howie & Zussman 1992):

- Nesosilicates - Isolated $[SiO_4]^{4-}$ tetrahedra that form minerals such as olivine.
- Inosilicates - Single chains of SiO_4 tetrahedra sharing two oxygen atoms, therefore having the chemical composition $[Si_xO_{3x}]^{2-}$. Pyroxenes fall into this group.

Due to the net negative charge on these silicate anions, positive cations must combine with these in order to produce neutrally charged compounds. The most likely cations available to cosmic silicates are Mg^{2+} and Fe^{2+}.

The terms above are all relevant to crystalline silicates that show definite long-range structures and are bounded by a 3D framework; however, as stated previously, the majority of silicates within the ISM are amorphous. Amorphous silicates are still based on the basic SiO_4 tetrahedra but the long-range structure, characteristic of crystalline silicates, has been lost and the Si-O tetrahedra link together randomly, often producing a mixture of structural forms, such as chains and loops, and exhibiting only short and medium-range lattice structure (refer to Figure 2.3). The terms olivine and pyroxene should strictly only be used when describing crystalline silicates, but for ease of description these terms will be used from now on for both crystalline and amorphous samples, in order to differentiate between the different compositions of the grains in focus, rather than the structural characteristics.

2.6.2 Carbonates

2.6.2.1 Introduction

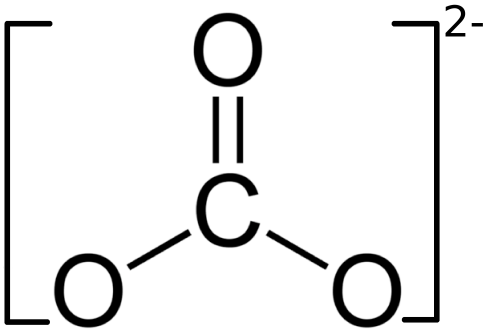

Figure 2.8: CO_3^{2-} structure. A central carbon atom is surrounded by three oxygen atoms.

Carbonates are defined as any molecule which contains the carbonate ion CO_3^{2-} (see Figure 2.8). These form on Earth predominantly as chemical precipitates in marine environments, and are a main constituent of sedimentary rocks. A number of rocks on Earth are made up purely of this carbonate precipitate, limestone and chalk being the most well known. Carbonates form through aqueous alteration of silicate materials by CO_2-rich water, leading to the production of carbonates such as calcite or aragonite ($CaCO_3$), magnesite ($MgCO_3$), siderite ($FeCO_3$) and dolomite ($MgCaCO_3$). However, this is not the only way carbonates are produced on Earth: there are also certain marine animals, such as molluscs and corals whose shells and skeletal structures are made from calcium carbonate.

Due to the obvious link between carbonate formation and the presence of water it has always been thought that the presence of carbonates on an extra-terrestrial body would be a reliable indicator for liquid water and therefore, most likely, life. However, the recent discoveries of carbonates in a wide variety of different astronomical environments including proto-planetary nebulae (Kemper, Jager & Waters 2002), in the atmospheres of evolved stars (Ceccarelli & Caux 2002), and in reflection nebulae (NGC 6208; Chiavassa, Ceccarelli & Tielens 2005), some known definitely not to possess liquid water, has led to the conclusion that there must be other, non-aqueous, routes of formation for carbonates in astronomical environments.

2.6.2.2 Evidence for carbonates in space

Carbonates have been known to exist in meteorites for a long time and are also found within Calcium-Aluminium Rich inclusions (CAIs). However the carbonates found in meteorites were still formed in much the same way as carbonates on Earth are, through aqueous/hydrothermal alteration. On sufficiently large bodies in the Solar System it is possible for liquid water to form on the surface. Although most meteorites we observe now are not large enough for this to occur, they would once have been part of a significantly larger body that got shattered, therefore leaving the meteorites with the minerals formed while still attached to the parent body. There is evidence of

high levels of alteration in the carbonates from meteorites that have been separated from their parent bodies for a long time, indicating that these bodies are subject to large amounts of radiation as they travel around our Solar System, leading to their constituent materials being highly processed. Although meteoritic carbonates are well known it has not always been so easy to detect carbonates elsewhere in space. The main spectral features for carbonate minerals are found within the far-IR region of the spectrum, which unfortunately happens to be the region that is predominantly absorbed by the Earth's atmosphere. It has therefore not been possible to look for these features in other astronomical environments using ground based observatories and it is only since the launch of orbital missions such as ISO and Hershel in recent years that have allowed this far IR region to be studied in great detail. Results from these missions have shown that carbonates are much more abundant in space than previously thought, being found in planetary nebulae (Kemper, Jager & Waters 2002), in the environments of young protostars (Chiavassa, Ceccarelli & Tielens 2005), around AGB stars (Kerschbaum, Posch & Nowotny 2009) and on comets (A'Hearn et al. 2005). The presence of carbonates in such environments is now a matter of great interest, to find out how carbonates could have formed in environments devoid of liquid water and how these fragile carbonate minerals are affected by the intense radiation of such environments.

2.6.2.3 Carbonate abundance

Measurements have been conducted for a number of carbonate containing environments, such as planetary nebulae, protostars, cometary bodies etc. The fraction of carbonates in the dust mass has been calculated and the carbonate abundance in all of the different environments differs by very little. The percentage abundance of carbonates in these environments is also, incredibly, about the same as the carbonate abundance on earth, $\sim$2%. The total range of abundance calculated through all these environments is $\sim$0.1% - 3% of the total dust mass (Lisse et al. 2006).

2.6.2.4 Non-aqueous carbonate formation

There are a number of theories speculating on the formation of carbonates in the astronomical environments described previously, but it is still not known for sure how they do actually form and this is currently an area that is very active in research. Some of the formation routes put forward include:

1. The interaction of silicate grains with CO_2 - H_2O-rich vapour in gaseous environments (Kemper, Jager & Waters 2002).

2. The interaction of silicate grains with their CO_2-rich ice mantles, made possible by X-ray heating of the grains giving the ice mantle increased mobility (Kemper, Jager & Waters 2002; Ceccarelli & Caux 2002).

3. Direct condensation of carbonates at high temperatures from mixed CO_2 - CaO-rich gas (Kemper, Jager & Waters 2002).

4. Carbonate formation through chemical reactions between hot silicate gas and 300-500K H_2O - CO_2 rich gas during far from equilibrium condensation processes (Toppani et al. 2005).

However, Toppani et al. (2005) state that due to the short lifetimes of these environments and the low pressures of the H_2O and CO_2 gases the formation processes proposed by Kemper, Jager & Waters (2002) would be unlikely to yield carbonates. They suggest an alternative solution based on the interaction of hot silicate gas and H_2O, CO_2-rich gas during non-equilibrium condensation, which is believed to be efficient enough in protostellar and planetary nebulae environments to lead to the formation of carbonate minerals. Toppani et al. (2005) propose that carbonates formed by this mechanism around young protostars would form within the region where stellar outflows interact with the inner part of the circumstellar envelope, a H_2O-rich region where hard X-rays cause sputtering of silica grains, producing a Si-rich hot gas. On the other hand, Ferrarotti & Gail (2005) calculate that the condensation of carbonates

from the gas phase in circumstellar dust shells is unlikely and would, at most, contribute less than 1% of the total dust. They therefore claim that this small amount would be undetectable and that the observations by Kemper, Jager & Waters (2002) are unlikely to be due to carbonate materials. There are other papers such as Ceccarelli & Caux (2002), Chiavassa, Ceccarelli & Tielens (2005) and Gillot et al. (2009) that support the methods put forward by Kemper, Jager & Waters (2002).

Mineral Name	Composition	Condensation Temp (K)
Corundum	Al_2O_3	1770
Hibonite	$CaAl_{12}O_{19}$	1720
Perovskite	$CaTiO_3$	1680
Metal Alloys	Fe,Ni,Co	1470
Ca-Pyroxene	$Ca(Mg,Fe,Al,Si)_2O_6$	1450
Olivine	Mg_2SiO_4	1440
Orthopyroxene	$Mg_2Si_2O_6$	1350
Carbonates	$(Ca,Mg,Fe)CO_3$	< 800

Table 2.1: Condensation values of major mineral species known to make up interstellar dust. Values taken from Ebel (2000) and Lodders (2003)

Condensation temperatures of minerals also play an important part in assessing the formation methods of particular minerals phases in astronomical environments. The condensation temperatures for some of the most common mineral phases found within cosmic dust are displayed in Table 2.1. These temperatures are based on a gas of initially solar composition (C/O = 0.42) and a total pressure of $\sim$100 Pa.

These condensation temperatures are, however, greatly dependent on the total pressure. As Ebel (2000) shows in Figure 2.9, increasing pressure leads to increased initial condensation temperatures for most materials. As can been seen from the table, carbonates have a very low condensation temperature in relation to other mineral phases that make up interstellar dust, forming between 800 – 500 K. These low temperatures would only be reached at a significant distance away from the central object, at which point, due to the the rapid acceleration of the stellar outflow caused by radi-

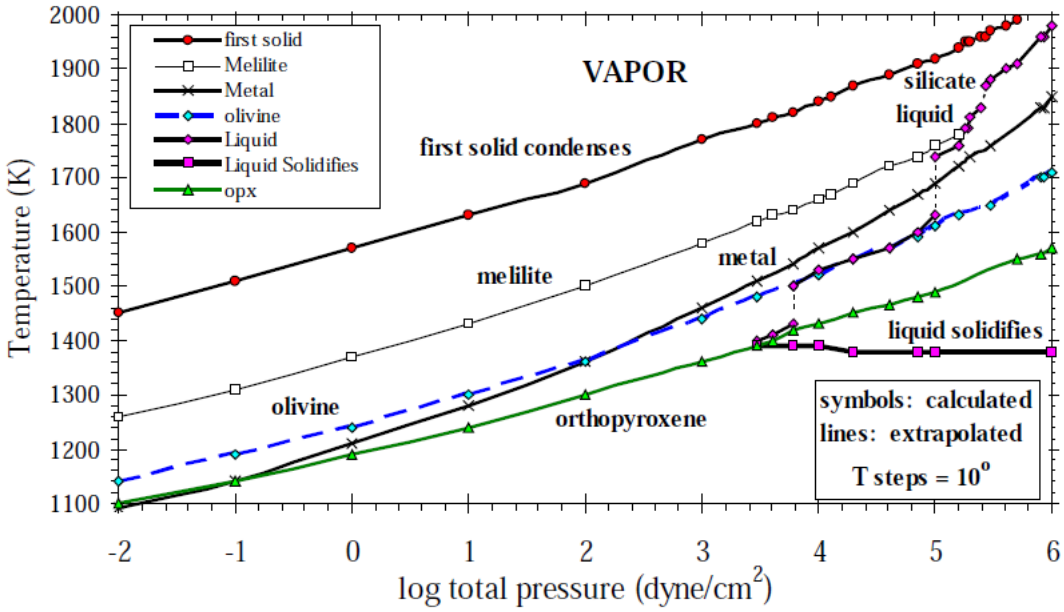

Figure 2.9: Effect of initial condensation temperatures with pressure (Ebel 2000).

ation pressure on the grains condensed at higher temperatures, the gas density would be extremely diluted and therefore would prevent the formation of any carbonate dust species (Ferrarotti & Gail 2005).

2.7 Conclusion

In this chapter we have provided a detailed review of the current literature relating to cosmic dust. The ubiquitous nature of dust is made clear and the importance of dust in a range of astrophysical environments is discussed. The life cycle of dust grains has been examined, identifying how disordered refractory grains, formed in the atmospheres of evolved stars, undergo significant processing throughout their lifetime and evolve into the crystalline mineral components that become incorporated into meteorites and larger planetary bodies, including the Earth. Infrared spectroscopy

is identified as the most reliable method for the identification of dust components, identifying amorphous silicates and carbon compounds (such as graphite, amorphous carbon and PAH's) as the most abundant dust species. The detection of carbonate minerals in circumstellar and proto-stellar environments is noted and the problems surrounding their formation in astrophysical environments are discussed in detail. It is shown that the formation mechanisms governing the formation of carbonate minerals are poorly understood and very little has been done, experimentally, in an attempt to understand these formation processes. We therefore identify a need for laboratory experiments studying the evolution of the structure of dust grains under a range of non-ambient conditions in order to better understand the structural evolution of dust grains throughout their lifetimes and to test, experimentally, the formation mechanisms suggested for the formation of cosmic carbonates.

3 Previous Laboratory Work

3.1 Overview

In order to reliably determine the chemical, physical and structural characteristics of cosmic dust, through astronomical observations of infrared absorption and emission features, it is necessary that the optical properties of minerals present on Earth are well known. The best way to do this is through laboratory studies of the structure, composition and corresponding optical properties of a large variety of materials thought to be analogous to cosmic dust. Fitting laboratory-gained spectra to astronomical observations is the only reliable way of determining the physical properties of the dust producing the unique features seen in astronomical spectra. Obviously terrestrial minerals can not serve as direct analogues of cosmic dust due to the extremely different environmental conditions under which they formed; the formation of materials in a vacuum would lead to a number of physical and perhaps structural differences. It therefore creates limitations on how accurately the astronomical spectra can be interpreted in this way. It is for this reason that cosmic dust analogues have, for a long time, been synthetically produced in laboratories. A number of methods have been developed with the aim of producing the most realistic cosmic dust analogues. It has been possible to test these methods in recent years due to the successful completion of the Stardust mission that succeeded in collecting samples of cometary and interplanetary dust particles and returning them to Earth. This has made it possible to make direct comparisons of real dust particles and their analogues. In this chapter I provide an overview of the research that has been performed in the field of laboratory astrophysics over the last few decades. I start by explaining the various techniques used to produce cosmic dust analogues, and then go on to discuss the main experiments conducted using these analogues to simulate the processing and destruction of cosmic dust.

3.2 Formation of Dust Analogs

3.2.1 The sol-gel Method

In an attempt to replicate the optical properties of silicates present within the matrix material of carbonaceous chondrite meteorites, Day (1976) produced synthetic silicates of Mg-rich composition using a method adapted from that first put forward by Sabatier (1950). This method, known as the sol-gel method (or gel reaction method), uses wet chemical reactions, known as hydrolysis, to form solid aggregates from a combined solution of metal salts dissolved in a liquid. In the case of Day (1976), magnesium silicates were produced via the reaction:

$$Na_2SiO_3 + MgCl_2 \longrightarrow MgSiO_3 + 2NaCl$$

where the metal salts were dissolved in distilled water. These salts can be substituted to produce amorphous materials of different compositions, for example Ca-rich or Fe-rich silicates.

Day (1976) used two modes of formation, fast and slow. The fast mode of formation entailed rapidly combining the solutions, whilst stirring vigorously, before filtering off the precipitate after just a few minutes. Conversely, the slow formation method allowed the solutions to drip simultaneously into a single beaker at a rate of one drop every 20 seconds. Once the solutions had filled the beaker, the solution was left to settle for 1 day prior to filtering off the precipitate. To complete the process the precipitated gels are then dried to produce solid particulates. Using scanning electron microscopy (SEM) and Raman spectroscopy it was determined that the materials formed using the fast mode produced completely amorphous silicates, showing no crystalline features in the Raman spectra and appearing fluffy and irregular in SEM images. On the other hand, the slow-grown products formed small, solid particles that exhibited a number of crystalline features. This method can easily be adapted by substituting the salt component of the reaction. For example, $MgCl_2$ can be substituted for $CaCl_2$ to produce calcium-rich silicates or by ammonium iron(II) sulphate to produce iron-rich silicates.

Amorphous magnesium and calcium-rich silicates have also been produced as cosmic dust analogues using a nitrate-based acid sol-gel method (Bansal 1988; Gillot et al. 2009). This method involves using nitrate salts as the source of magnesium ($Mg(NO_3)_2$) and calcium ($Ca(NO_3)_2$), diluted in solvents (ethanol and water). These solutions are then mixed with tetraethyl orthosilicate (TEOS) in acidic conditions to polymerise a silica network. Once aged, the samples then require thermal annealing to at least 500°C to remove residual by-products, including water and nitrates, resulting in a pure amorphous material.

The sol-gel method is very adaptable and can be used to produce a wide range of materials, including materials that may otherwise present difficulties in other methods of synthesis due to thermodynamic instability. Astrophysical analogues most commonly produced using the sol-gel method include magnesium, calcium and iron-rich silicates, as well as combinations of these. The main advantage of the sol-gel technique is the simplicity, not requiring any specialist experimental set-up, it is easy to produce large quantities of the sample in a short time and can be done at low temperatures. The samples produced by the sol-gel method also exhibit a high degree of purity and homogeneity (Colangeli et al. 2003). The gels can also be dried in a vacuum furnace to produce very 'fluffy', porous samples that closely resemble interplanetary dust grains. The sol-gel method was chosen as the method of sample formation as described in this thesis and our adapted method is described in greater detail in Section 5.2.

3.2.2 Vapour Phase Condensation

The vapour-phase condensation method is used primarily to produce refractory grains analogous to those formed in the atmospheres of evolved stars. The produced material in this case is referred to as a smoke and early studies found that if the growth and nucleation of particles is fast, on the order of microseconds, the produced materials are highly amorphous (Nuth & Ferguson 1993; Nuth 1996). This method is a powerful tool to investigate the complex process of dust formation, including grain growth and nucleation. This process uses a condensation flow apparatus, as described by Nel-

son et al. (1989), in which a gas-phase mixture of the required composition is flowed through a thin alumina-lined furnace at a temperature of 1200 K and a pressure of $\sim$ 0.133 bar, before entering a 10 cm stainless steel collection chamber in which the particles settling out of the gas stream are collected on a copper plate at the base. A number of experiments have been conducted using this method, or similar, on a number of astrophysically relevant materials, including magnesium silicate smokes (Day 1979; Rietmeijer et al. 2002), mixed magnesium-iron smokes (Hallenbeck 1997) and calcium silicate smokes (Rietmeijer et al. 2008). In most cases, smokes of such compositions are condensed out of gas mixtures of silane (SiH_4), O_2 and He, mixed with the required metals. In the case of magnesium and calcium, no volatile precursors are available and so they are placed into the furnace in a graphite boat, while the source of iron (iron-pentacarbonyl), being in liquid form, has an additional flow of He bubbled through it (Hallenbeck 1997).

3.2.3 Alternative Methods

The two methods of formation detailed above are the most commonly used in the synthesis of amorphous cosmic dust analogues, however, as the study of cosmic dust analogues in the laboratory has grown many other methods have been developed to synthetically produce materials that are analogous to cosmic dust. Two additional methods that have been used include the laser ablation technique (e.g. Rotundi et al. 2000; Mennella, Brucato & Colangeli 2001; Brucato et al. 2002) and shock-quenching of silicate melts (Fabian et al. 2000). The laser ablation technique involves vapourising a target sample, often of bulk crystalline silicate, using a high-powered laser beam and subsequently collecting the particles that condense out of this vapour. The target samples used for such experiments are often natural minerals of olivine or pyroxene composition, but these are likely to contain terrestrial impurities and to obtain purer samples oxides, such as MgO, SiO_2 and Fe_2O_3, are often combined in specific ratios to produce materials of equivalent compositions. A substrate is placed a few centimetres away from the target sample on which the particles condensing from the vapour are

collected. Characterisation of the smokes produced via this method is essential prior to further study, as the composition of the material may be altered by the vapourisation process. The use of silicate melts in the production of cosmic dust analogues have been described by Fabian et al. (2000), in which silicate melts were produced from a mixture of magnesium carbonate and silica powder proportionate to the composition of enstatite ($MgSiO_3$). The melt is then shock-quenched at a rate of $\sim$ 1000 K/s by pouring through copper rollers, producing very thin (a few 100μm) glassy sheets. Silicate melts can also be used to produce crystalline silicates (Jäger et al. 1998) in a similar manner, by simply changing the cooling rate of the melts ($\sim$ 0.3 K/s) and allowing nucleation and growth of crystals.

3.3 Experimental Processing of Dust Analogues

Dust formed in the envelopes of evolved stars is transported into the ISM by stellar winds. It is believed that many harsh processes occur within the ISM, including sputtering, ion irradiation, thermal erosion and fragmentation due to grain-grain collisions (Henning, Grun & Jurgen 2009), all leading to chemical and structural changes of the grain materials, which, in turn, has a profound effect on the observed spectral signatures of the grains. In order to determine how each of these processes effects the composition and structure of the grains and how these changes effect the spectra that we observe, these processes can be simulated in laboratories using synthetic dust analogues (Demyk et al. 2001, 2004; Brucato et al. 2004; Henning, Grun & Jurgen 2009; Rietmeijer et al. 2008; Speck, Whittington & Hofmeister 2011). Different grain materials will obviously be affected differently by each process and many groups have carried out studies on a large range of grain materials, but the focus of this study is on the processing of silicate and carbonate materials.

Composition	Production method	E_a/k (K)
Mg_2SiO_4	vapour-phase condensation	45,500[1]
Mg_2SiO_4	laser ablation	39,100[2]
$Mg_{0.95}Fe_{0.05}SiO_3$	glass	38,500[2]
Mg_xSiO_{2+x} (x = 0.7 - 2.4)	sol-gel	26,600-31,700[3]

Table 3.1: Activation energies of crystallisation for magnesium silicate samples produced using different techniques. Activation energies from [1]Hallenbeck, Nuth & Daukantas (1998), [2]Fabian et al. (2000), [3]Jager et al. (2003a). After Henning, Grun & Jurgen (2009).

3.3.1 Thermal Annealing

The predominant source of grain processing across all astrophysical environments is thermal annealing. This happens through basic heating of the grains to high temperature in protoplanetary discs or even around evolved stars and can also occur through collisional heating. Annealing leads to the conversion of disordered, amorphous grains to crystalline minerals exhibiting long-range structural order. The timescale for crystallisation at a specific temperature can be determined using Equation (3.1) (Henning 2010), where $\mathcal{V}_0$ is a constant proportional to the mean vibrational frequency of the silicate lattice ($\mathcal{V}_0 = 2 \times 10^{13}$ s^{-1}), E_a is the activation energy, T is the dust temperature and k is the Boltzmann constant.

$$\tau^{-1} = \mathcal{V}_0 \exp(-E_a/kT) \tag{3.1}$$

Table 3.1 provides experimentally derived activation energies for magnesium silicate samples, produced using different methods. Calculating the activation energy of the materials under investigation then allows the crystallisation timescale to be determined for any temperature, using Equation (3.1), allowing the crystallisation timescales of such materials in different astrophysical environments to be calculated.

The activation energies presented in Table 3.1 demonstrate the difference of each production method. The lower activation energies observed in the glass and sol-gel

synthesised samples is attributed to the homogeneity of the samples as vapour-phase products are often inhomogeneous, having segregated regions of different composition (Colangeli et al. 2003). The range of temperatures given for samples produced using the sol-gel method is due to the presence of OH within the samples, the activation energy is decreased with increasing Si-OH content.

IR spectroscopy has predominantly been used to study the spectral changes caused by thermal annealing of dust analogues as this provides a direct reference to astronomical spectra. Over the last few decades a great deal of work has been done on the collection of spectroscopic data for laboratory analogues of varying compositions across large temperature ranges in order to provide comparison spectra for astronomical observations and allowing the composition and temperatures of cosmic dust in a number of different environments to be constrained (Hallenbeck, Nuth & Daukantas 1998; Brucato et al. 1999, 2004; Fabian et al. 2000; Jager et al. 2003a; Speck, Whittington & Hofmeister 2011).

Studies of the thermal annealing of cosmic dust analogues have been performed by a number of groups, some of the earliest experiments were conducted by Day (1976) using materials produced via the sol-gel method. In these experiments amorphous grains of $MgSiO_3$ and Mg_2SiO_4 composition were heated up to 1273 K and it was noted that the amorphous materials are less stable, easily evolving into crystalline phases of olivine and pyroxene, respectively. X-ray powder diffraction of amorphous silicate analogues is used, alongside IR and Raman spectroscopy, to study in further detail the structural changes that occurring during the thermal annealing of cosmic dust analogues (Thompson, Evans & Jones 1996; Thompson & Tang 2001; Thompson et al. 2002, 2007). Thompson, Evans & Jones (1996) used synchrotron X-ray powder diffraction to probe the structural changes of Fe- and Mg-rich silicates from ambient temperature up to 1173 K, finding that upon crystallisation by thermal annealing, Mg-rich silicates lose all features of their once amorphous state, whereas Fe-rich silicates, even at 1173 K, retain structural indicators of their original amorphous structure, therefore providing an insight into its formation history.

3.3.2 Irradiation

Irradiation of dust grains by energetic ions may play an important role in the processing of silicates from their origin around evolved stars to their residence in the ISM. Crystalline silicates have been detected in a number of circumstellar environments, with masses calculated as $\sim 20\%$ of the total silicate mass in the environments in which they are found (Kemper, Jager & Waters 2002), but crystalline silicates are yet to be discovered in the ISM. Li & Draine (2003) have determined that if crystalline silicates are not detectable in IR spectra then the maximum mass of crystalline silicates in the ISM is $< 5\%$. As the vast majority of dust present in the ISM is supplied by the dusty outflows and stellar winds of evolved stars it could be assumed that there would be a similar mass of silicates in the ISM as is seen in these circumstellar environments, but as this is not the case it is believed that an amorphisation process occurs (e.g. Demyk et al. 2001; Carrez et al. 2002; Brucato et al. 2004; Bringa et al. 2007) causing the crystalline silicates to lose their long-range structure once in the ISM. This occurs through atomic displacements by nuclear interactions and ionisation that lead to the modification of the silicate structure (Leroux 2009). Day (1977) was one of the first to irradiate cosmic analogues to determine the effect this would have on the observed spectra. He used high energy (1.5–2 Mev) H^+ ions to irradiate olivine and enstatite grains; however no change in the IR spectral properties was observed and he concluded that no structural modification had occurred. A few years later, Kraetschmer & Huffman (1979) irradiated olivine grains with 1.5 MeV Ne^+ ions, observing changes in the IR spectra that suggested amorphisation of the mineral. Further experiments studying the effect of irradiation on olivine and pyroxene-type materials, using lower energy (1–20keV) ions, confirmed that the amorphisation of grains is possible through irradiation (Bradley 1994; Dukes, Baragiola & McFadden 1999). Bradley (1994) also observed a depletion of Mg at the surface of the samples after amorphisation, leading to a relative enrichment of oxygen. More recent studies on the irradiation of cosmic dust grains, simulating conditions that would be expected in high-velocity supernovae shock fronts, have shown that the efficient amorphisation of crystalline mineral species with

light ions (e.g. H^+,He^+) is only observed for low energies (below 50keV; Jager et al. 2003b). It is reported by Demyk et al. (2001), using He^+ ions with energies between 4 – 10keV, that the irradiation of crystalline forsterite triggered the amorphisation of the mineral but also caused the chemical structure of the material to change from olivine to pyroxene stoichiometry. They also note a depletion of MgO due to irradiation along with significant changes to the morphology of the grains after irradiation (Demyk et al. 2001; Carrez et al. 2002). The observation of 'bubbles' formed by the implanted ions within the irradiated materials, causing an increase in the porosity, has been reported by several groups (e.g. Jager et al. 2003b; Demyk et al. 2004). In addition to the Mg-rich olivine and pyroxene materials studied by most groups, Demyk et al. (2004) also studied the irradiation of the calcium-rich pyroxene, diopside, and concluded that full amorphisation occurred with He^+ ions at an energy of 20keV. A comparison of the IR spectra obtained from their irradiated materials with ISO observations of the Galactic Centre led the group to conclude that the interstellar spectrum is better reproduced by irradiated enstatite than with irradiated forsterite or diopside. They confirm that the abundance of light ions (H^+ and He^+) in the diffuse ISM, having energies <50keV, would indeed be favourable for the efficient amorphisation of silicate grains.

3.4 Conclusions and continuation of work

Since the discovery that silicates are the predominant interstellar mineral species, their properties have been studied in great detail to determine how they act under astronomical temperature and pressures and how their structure and therefore optical properties change though thermal annealing and/or irradiation. Understanding the behaviour of laboratory analogues is key to better understanding the behaviour of materials in the cosmos. Laboratory studies of such materials allow astronomical spectra to be interpreted, determining the composition and environmental conditions of dusts in many different environments as well as providing a means of understanding the formation and evolutionary history of dust in the universe.

4 Methods

4.1 Introduction

The work discussed in this thesis is almost exclusively based on data obtained through the use of synchrotron radiation produced by the Diamond Light Source (DLS) synchrotron facility in Oxford, UK. A number of techniques have been utilised, taking advantage of the high brightness and flux of such a source, including X-ray Powder Diffraction (XRPD), both conventional and total scattering (TS). This is also complemented by laboratory based spectroscopy such as Fourier Transform Infrared Spectroscopy (FTIR), covering the mid-IR wavelength range (2.5 - 28μm), and Raman. This chapter describes the theory governing each of the techniques used for the work presented in this thesis, as well as a detailed explanation of how the data obtained from each of these techniques is analysed. The theory of X-ray diffraction, including the comparison of Bragg and Laue formulations and the diffraction geometries follow that of Hammond (2009), while the detailed theory and analysis specific to powder diffraction data follows that described by Dinnebier & Billinge (2008).

4.2 Generation of synchrotron radiation

Synchrotron radiation refers to the electromagnetic radiation emitted when charged particles are accelerated to relativistic speeds along a circular trajectory (Elder et al. 1947). In the storage ring of a synchrotron, electrons with an energy of a few GeV (3GeV for the Diamond Light Source) are guided by strong magnetic fields which keep the electrons travelling in a circular motion. The storage ring is made up of a number of straight segments, connected by bending magnets. It is at the position of these bending magnets, when the path of the electron is altered, that synchrotron radiation is produced in a tangential direction to the curved path of the electron.

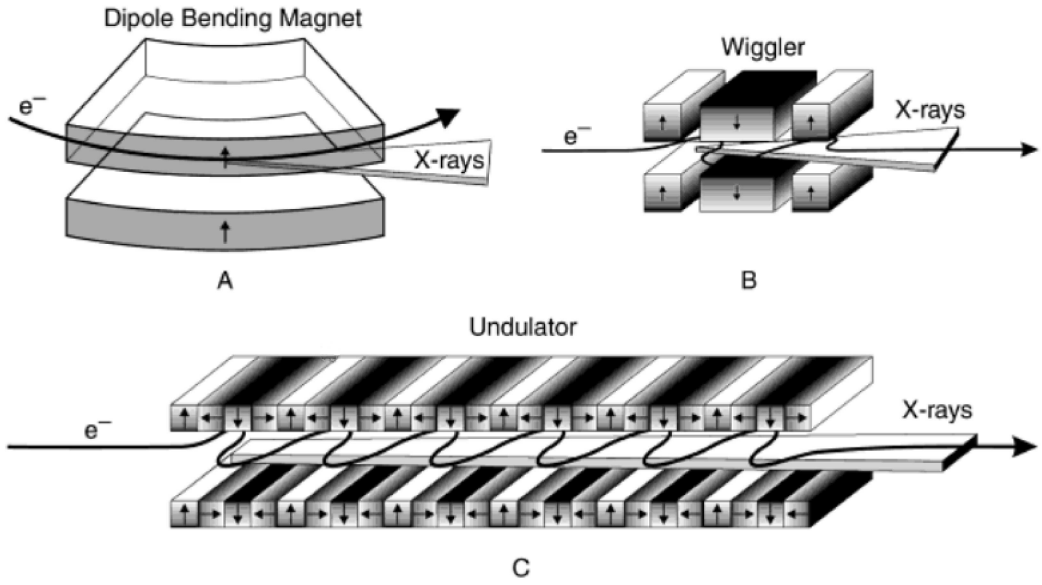

Figure 4.1: Different insertion devices used on synchrotron beamlines and the shape of the synchrotron radiation produced. Dinnebier & Billinge (2008)

In third-generation synchrotron facilities, such as DLS, insertion devices are used in place of bending magnets. These devices produce alternating magnetic fields that cause the path of the electron to oscillate, which in turn produces synchrotron radiation. The number and amplitude of oscillations experienced by the electron determines certain properties of the synchrotron radiation allowing it to be tailored to specific experiments. Figure 4.1 provides examples of the three most common devices for producing synchrotron radiation; a bending magnet (a), wiggler (b) and undulator (c), as well as conveying the shape of the beam produced by each one.

There are many benefits of using synchrotron radiation over standard sources, these are:

- Polarisation: Depending on the insertion device used, synchrotron radiation can be linear or circularly polarised.
- Broad spectrum of electromagnetic (EM) radiation: Synchrotron radiation cov-

ers wavelengths from the Infrared (10^4 Å) to hard X-rays (10^{-1} Å).

- High brightness: Very high photon flux hitting the sample, allowing for very fast data collection times, even for nominally weakly scattering samples.
- High brilliance: the beam can be trimmed to very small sizes (to the order of microns), providing very small divergence and a highly collimated beam.
- Stability: refined experimental setup provides sub-micron stability, a micron sized beam can be focused onto a specified point on a sample with very little variation throughout the experiment.

4.3 The Theory of X-ray diffraction

X-rays are used to investigate the structural properties of materials as they provide a non-destructive method with which to probe deep into a material, the penetration depth being determined by the energy of the X-rays and the electron density of the elements that compose the sample being studied. X-ray photons with energies of a few keV have wavelengths, λ, comparable to the typical atomic spacings in solid materials ($\sim$1Å), therefore under certain conditions crystalline arrays of atoms can act as interference gratings, causing the diffraction of an incident X-ray beam. Other than X-rays, only neutrons and electrons also satisfy this criterion, allowing diffraction from different parts of the atomic structure. X-ray diffraction therefore provides a simple means to directly determine the structure, composition and atomic properties of materials in a non-destructive manner.

4.3.1 Brief History of X-Ray Diffraction

Wilhelm Röntgen first detected X-rays in 1895 but it was not until 1912 that Max von Laue suggested that periodic crystalline structures might be able to diffract waves if their wavelength was of the same order of magnitude as the distance between atoms in

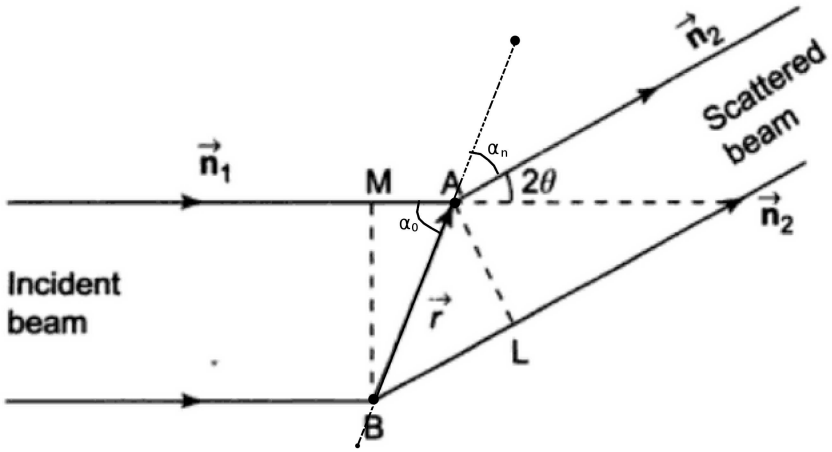

Figure 4.2: Laue scattering of two atoms, A and B, separated by distance r. After Singh (2012).

a crystal lattice and concluded that X-rays were a viable choice. He recorded the first X-ray diffraction pattern from a single crystal of copper sulphate. Subsequently, father and son team William H. and William L. Bragg (1913) devised a theory for obtaining detailed atomic structural information from diffraction spot positions and intensities, this is now known as Bragg's Law which defines when diffraction from a crystal will occur.

4.3.2 Laue Theory

To explain the nature of X-ray diffraction, von Laue viewed the crystal structure as a three-dimensional array, consisting of rows of individual atoms, that act as a three-dimensional diffraction grating. Each atom is regarded as a scattering centre situated at lattice points. Imagine two identical scattering centres, A and B, located at a distance, r, from each other in a crystal, as shown in Figure 4.2.

The incident beam of X-rays is scattered by both scattering centres where the

path difference between the the scattered rays from A and B is given by:

$$\mathrm{AM} - \mathrm{BL} = \mathrm{r}\mathbf{n}_1 - \mathrm{r}\mathbf{n}_2 = \mathrm{r}(\mathbf{n}_1 - \mathbf{n}_2) = \mathrm{r}\mathbf{N} \tag{4.1}$$

where $\mathbf{N}$ = ($\mathbf{n}_1$ - $\mathbf{n}_2$) and $\mathbf{n}_1$ and $\mathbf{n}_2$ are unit vectors in the direction of the incident and scattered beams as shown in Figure 4.2. In a three-dimensional array of atoms, diffraction can occur from rows of atoms along three different axes, x, y and z.

For constructive interference to occur, the path difference (AM–BL) needs to be a whole number, n, of wavelengths e.g.

$$(\mathrm{AM} - \mathrm{BL})_\mathrm{x} = \mathbf{r_x}(\cos\alpha_\mathrm{n} - \cos\alpha_0) = \mathrm{n_x}\lambda \tag{4.2}$$

where r_x is the atom spacing along the x-axis, α_n and α_0 are the angles between the diffracted and incident beams and the x-axis and n_x is an integer relating to the order of diffraction. This can now be repeated for diffraction along the y-axis

$$(\mathrm{AM} - \mathrm{BL})_\mathrm{y} = \mathbf{r_y}(\cos\beta_\mathrm{n} - \cos\beta_0) = \mathrm{n_y}\lambda \tag{4.3}$$

and z-axis

$$(\mathrm{AM} - \mathrm{BL})_\mathrm{z} = \mathbf{r_z}(\cos\gamma_\mathrm{n} - \cos\gamma_0) = \mathrm{n_z}\lambda \tag{4.4}$$

leading to the three Laue equations. For constructive interference to occur from all three axes simultaneously, all three Laue equations must be satisfied.

4.3.3 Bragg Theory

The theory derived by Laue, while correct, has a large disadvantage when it comes to calculating the direction of the diffracted beams as it requires the determination of 12 independent values (six angles, three lattice spacings and three integers as in the equations). W. L. Bragg devised a simpler means in which to explain the theory of diffraction. He viewed crystals as being made up of repeating, parallel planes from which X-rays are reflected. These are known as crystallographic planes and are defined

by the Miller Indices, *hkl*. Parallel planes all share the same indices and are separated by a standard distance, d_{hkl}. Figure 4.3 is a simple diagram showing successive parallel lattice planes in a crystal reflecting an incident beam of X-rays. From this figure, Bragg's law can be derived.

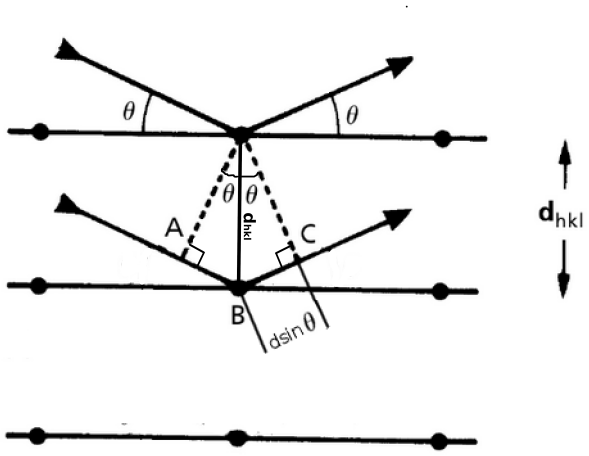

Figure 4.3: Schematic of Bragg diffraction. An X-ray beam incident on a lattice plane at an angle, θ, is partially reflected according to the ordinary laws of reflection, while the transmitted beam is then incident on next lattice plane and is reflected in the same manner. After Hammond (2009).

The path difference between the two reflected beams is:

$$(AB + BC) = (d_{hkl}\sin\theta + d_{hkl}\sin\theta) = 2d_{hkl}\sin\theta \tag{4.5}$$

where d_{hkl} is the interplanar spacing and θ is the angle of reflection. If the path difference between the two beams is equal to a whole number of wavelengths then the reflections will constructively interfere. The constructive interference of the reflected beams from all further parallel planes results in an increased intensity, that would show as a strong feature, known as a Bragg reflection, in the final diffraction pattern. This leads to the well known Bragg's Law:

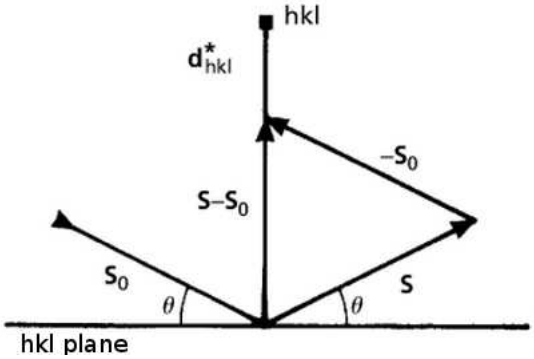

Figure 4.4: Bragg's Law described in vector notation. Hammond (2009)

$$n\lambda = 2d_{hkl}\sin\theta \tag{4.6}$$

This is the simple relationship that describes the condition for constructive interference from successive crystalline planes in a crystal lattice.

Bragg's Law can also be defined in terms of vector notation, but this is not commonly used. However it is a useful concept when linking to Ewald's construction later on in the chapter.

Figure 4.4 illustrates Bragg reflection from a single plane, where $\mathbf{s}_0$ is the incident X-ray beam, $\mathbf{s}$ is the diffracted beam. The vector $\mathbf{(s\text{-}s_0)}$ is in the same direction as $\mathbf{d}^*_{hkl}$ (the reciprocal lattice vector, normal to the plane). Comparing this to the conventional description of Braggs law shows that $|\mathbf{s}\text{-}\mathbf{s}_0| = 2\sin\theta$ and $|\mathbf{d}^*_{hkl}| = 1/\mathrm{d}_{hkl}$.

Therefore, Bragg's Law can be written in vector format as:

$$\frac{(\mathbf{s}-\mathbf{s_0})}{\lambda} = \mathbf{d^*_{hkl}} \tag{4.7}$$

Constructive interference can then be defined to occur when $(\mathbf{s}\text{-}\mathbf{s}_0)/\lambda$ coincides with the reciprocal lattice vector.

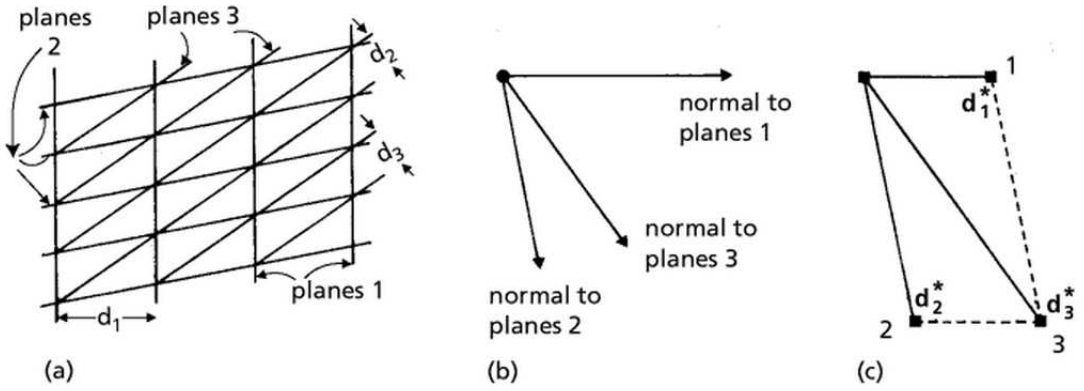

Figure 4.5: The origin of the reciprocal lattice. (a) Identifies three sets (families) of crystallographic planes in the direct lattice. (b) The normals of these planes originating from a common origin. (c) The reciprocal lattice vectors defining the crystal planes and their d-spacing - the lattice points are represented by the filled squares at the end of the vectors. Hammond (2009)

4.3.4 The reciprocal lattice and Ewald's construction

The reciprocal lattice is used to simplify the notation of crystallographic planes by using just one point, at a normal to the plane, to define a family of planes described by their Miller indices, hkl. It forms a regular array of points, each of which represents a family of crystallographic planes and therefore a diffraction opportunity.

Consider the real lattice (otherwise known as the direct lattice) of a crystal exhibiting multiple crystal planes, as shown in Figure 4.5(a). Here, three families of planes are shown, labelled simply as 1, 2 and 3. The normals to these planes are drawn, starting from a shared origin (Figure 4.5(b)) and can subsequently be described as vectors $\mathbf{d}_1^*$, $\mathbf{d}_2^*$ and $\mathbf{d}_3^*$ (reciprocal lattice vectors) where their magnitude is inversely proportional to the d-spacing between the planes (Figure 4.5(c)). Repeating this for all crystal planes leads to the formation of a regular lattice, with the origin at 000 (Figure 4.6).

Just as a unit cell of a direct lattice can be defined using the primitive vectors a, b, c, a unit in the reciprocal cell is defined as a^*, b^*, c^*. Any point in the reciprocal

lattice can then be defined, relative to the origin, as $\mathbf{d}^*_{hkl} = ha^* + kb^* + lc^*$.

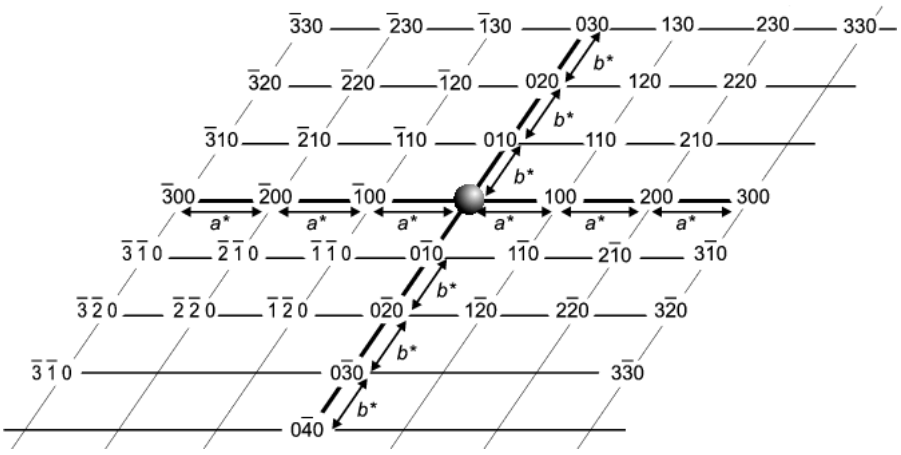

Figure 4.6: A 2D representation of the reciprocal lattice showing lattice points corresponding to all $hk0$ planes. Barnes, Jaques & Vickers (2006)

A geometric expression of Bragg's Law was devised by Ewald (1913). The Ewald sphere, as it is now known, uses the reciprocal lattice of a crystal to demonstrate the relationship between:

- the wavevector of the incident and diffracted beams
- the diffraction angle for a given reflection
- the reciprocal lattice of a crystal

A sphere of radius $1/\lambda$ is drawn on the reciprocal lattice with the incident wave vector, $\mathbf{s}_0$, pointing in the direction of the incident beam, from the centre of the sphere to the edge. The point at which this intercepts the edge of the sphere is the origin of the reciprocal lattice. Any reciprocal lattice point that intercepts the edge of the sphere at this point determines the position of a diffracted ray. As shown in Figure 4.7, the diffracted wave vector, $\mathbf{s}$, is drawn from the centre of the sphere to the position

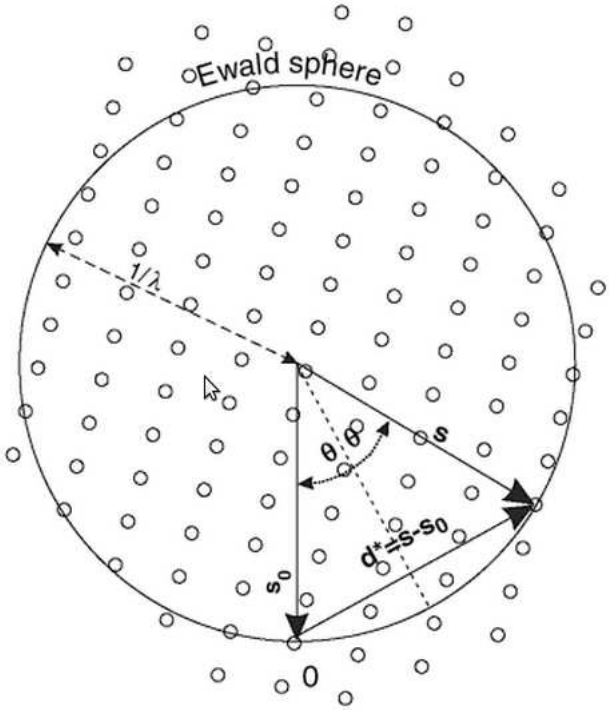

Figure 4.7: Ewald construction on the reciprocal lattice. Where the reciprocal lattice points touch the surface of the sphere, a Bragg peak will occur. Dinnebier & Billinge (2008)

on the edge of the sphere where a reciprocal lattice point is present. The scattering vector, $\mathbf{h} = \mathbf{s}$ - $\mathbf{s}_0$, joins the end positions of the wavevectors $\mathbf{s}$ and $\mathbf{s}_0$ and is equivalent to $\mathbf{d}^*_{hkl} = 1/d_{hkl}$.

4.4 Powder diffraction

Following from the derivation of Bragg's Law it is apparent that for a monochromatic beam of X-rays incident on a single crystal of a particular material, a full diffraction pattern would not be produced. In this case only a single Bragg feature would be

observed as only one family of planes would be in the correct orientation to satisfy the Bragg condition at any one time, this is shown in Figure 4.8(a) where only the planes shown in purple are satisfying the Bragg condition. If the crystal were to be rotated, the set of planes initially shown in pink would eventually become correctly orientated in the beam to exhibit diffraction, as shown in Figure 4.8(b). Rotating again would then also bring the next set of planes (green) into the required orientation. In order to obtain a full diffraction pattern for the material, the crystal would need to be rotated through all possible orientations to ensure that every crystallographic plane would have the opportunity to fulfil Bragg's Law. This method is known as single-crystal diffraction. Single crystal diffraction is very useful for determining the structure, space group etc. of materials, however it is not always viable due to the difficulty of obtaining individual single crystals for certain materials. This is where powder diffraction excels. Nearly all materials can be in the form of powder and, although this loses some crystal symmetry information due to overlapping reflections from multiple crystals in the same orientation, it provides a bulk, average structure of a material and is advantageous due to its ability to perform particle averaging.

On the other hand, a powdered sample consists of millions of individual, small crystallites (usually a few microns in size) that are randomly orientated. Therefore, in presenting a powder to an X-ray beam, statistics would suggest that every possible orientation would be presented to the beam simultaneously. Figure 4.9 shows a representation of this for just two unique planes (red and green), but in reality each crystallographic plane would have an equal probability of satisfying the Bragg condition in this case.

In this case, the reciprocal lattices of all crystal orientations are effectively stacked on top of each other so that each lattice point can be thought of as being 'smeared out' over the surface of a sphere centred on the reciprocal lattice origin. Figure 4.10 is a representation of one of these reciprocal lattice spheres, defined by the reciprocal lattice vectors, $\mathbf{d}^*_{hkl}$, in relation to the Ewald sphere, the points at which these spheres intersect identifies where the greatest diffraction intensity (Bragg reflection) occurs. In three dimensions this leads to the formation of a cone of diffraction intensity, known as

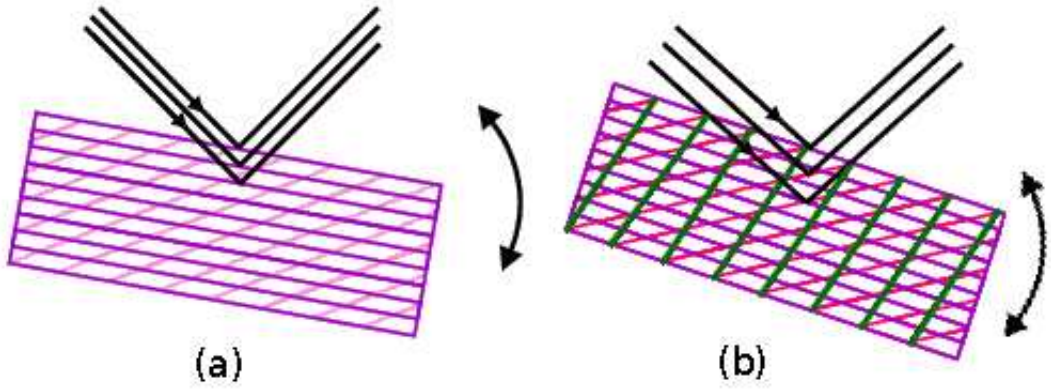

Figure 4.8: As a crystal is rotated, each crystallographic plane will eventually be orientated so that it satisfies the Bragg condition and will diffract. (http://pd.chem.ucl.ac.uk/pdnn/powintro/introind.htm)

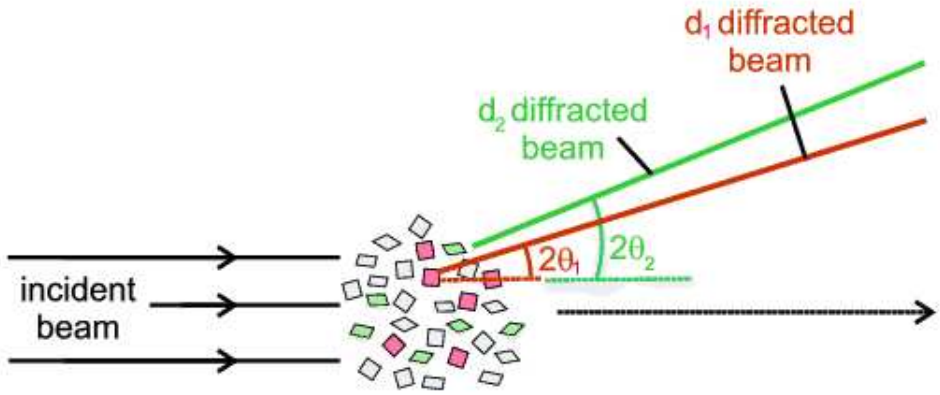

Figure 4.9: Diffraction of an X-ray beam by a powdered sample. Millions of crystallites at random orientations are presented to the beam simultaneously. (http://pd.chem.ucl.ac.uk/pdnn/powintro/introind.htm)

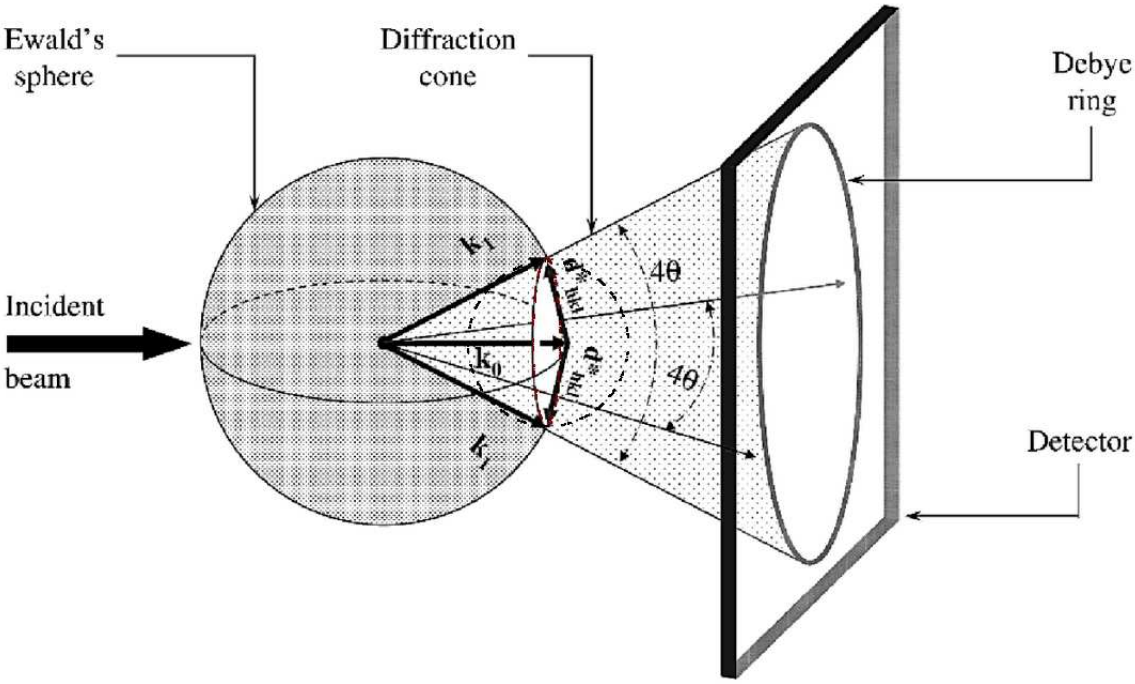

Figure 4.10: The interaction of the Ewald sphere and the reciprocal lattice spheres forming Debye-Scherrer cones in powder diffraction. This shows an example for the reflection from just one *hkl* plane. (Pecharsky & Zavalij 2009).

a Debye-Scherrer cone. Each reciprocal lattice vector has a length/magnitude related to the d-spacing of each family of planes and therefore the radius of each of the reciprocal lattice spheres is slightly different, creating a series of concentric Debye-Scherrer cones (see Figure 4.11).

When a 2D area detector is placed in line with the incident beam (as indicated in Figure. 4.10), these Debye-Scherrer cones of high scattering intensity are recorded and appear as concentric rings whose radii are proportional to the 2θ angle. A typical powder diffraction pattern obtained by a 2D area detector is shown in Figure 4.12.

It is however more common for 1D detectors to be used when performing powder diffraction experiments. One-dimensional (1D or linear detectors) do not observe the

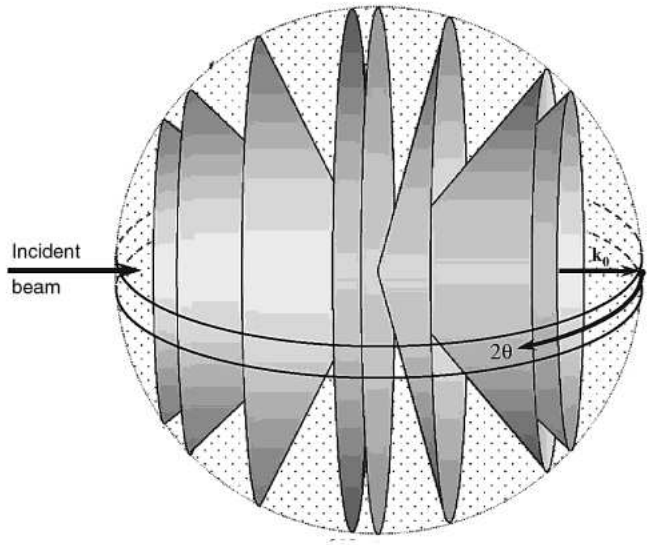

Figure 4.11: Debye-Scherrer cones produced by the diffraction of X-rays from a powdered sample. (After Pecharsky & Zavalij 2009)

full diffraction pattern, instead they are limited to only one plane, effectively observing a thin slice of the full diffraction pattern (as shown by the thin 2θ region in Figure 4.11). Data obtained using a linear detector are plotted as intensity vs 2θ angle as shown in Figure 4.13 for a Si standard.

Powder patterns collected on area detectors are very useful for determining texture or preferred orientation of samples. For example, if a sample is not randomly orientated and exhibits a preferred orientation of crystals then the Debye-Scherrer rings would not have a uniform intensity, instead the intensity distribution would vary along the rings. This can be rectified by using a cylindrical capillary as the sample mount and rotating the capillary during data collection to ensure a completely random orientation of crystal planes.

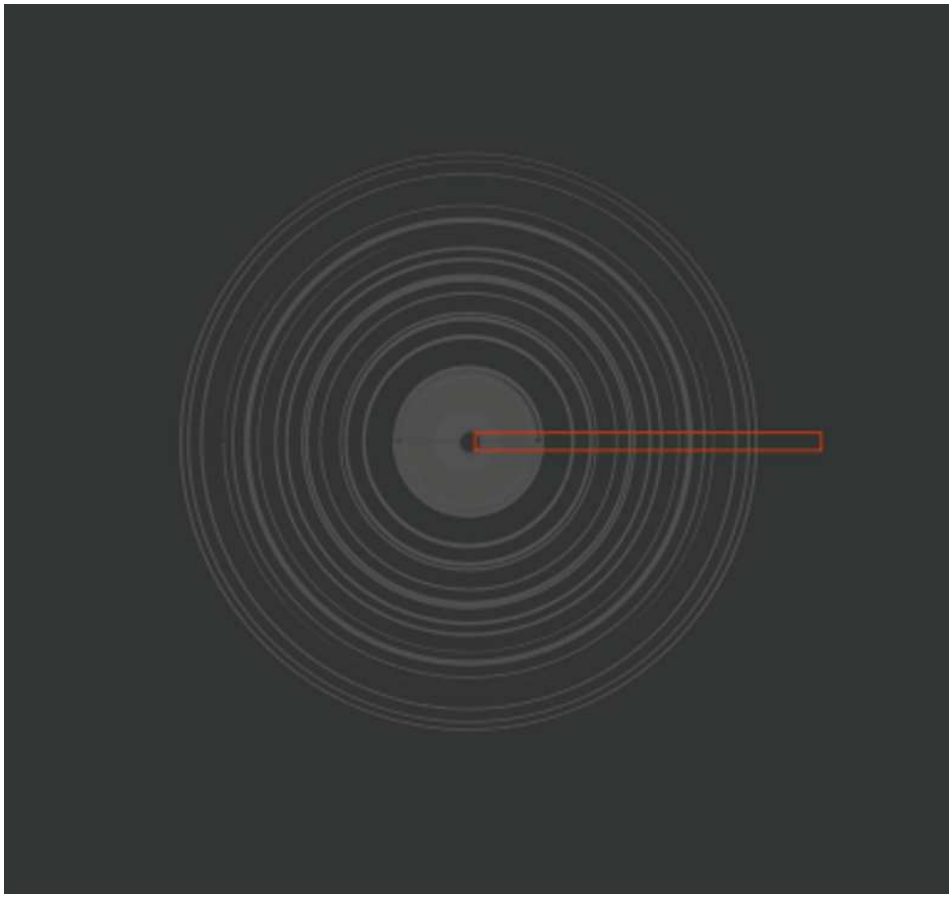

Figure 4.12: A typical diffraction image obtained using a flat-plate, 2D area detector.

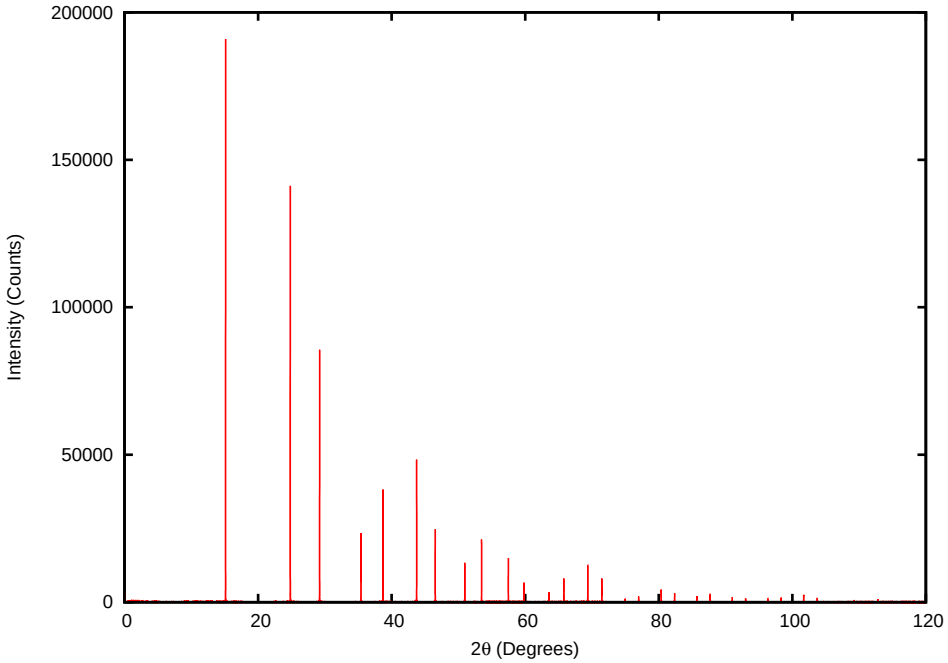

Figure 4.13: A 1D powder pattern of Si standard, obtained using a multianalysing crystal (MAC) detector on Beamline I11 at Diamond Light Source.

4.4.1 Analysis of powder diffraction data

4.4.1.1 Qualitative Analysis

The most widespread use of powder diffraction is for the identification of crystalline materials. The powder pattern produced by a material is unique, much like a fingerprint, and the position and intensity of the peaks presented on a 1D powder pattern can be used to identify the material or confirm its identity, if already known. This can be achieved through the comparison of experimental data with reference patterns obtained from the International Centre for Diffraction Data (ICDD) PDF4+ database (Fawcett et al. 2005) or the Crystallography Open Database (COD; Gražulis et al. 2009). In the case of multiple phases being present within the sample, the powder pattern is the sum of the diffraction patterns from each phase. In this case, manual identification of each of the phases would be incredibly difficult and time-consuming, therefore peak search-match programs such as Crystallographica (Siegrist 1997) or Match! (Crystal Impact 2003) are available. These programs provide simple access to multiple databases providing a search function that compares the peak positions and intensities of the experimental pattern with a large database of over forty thousand reference patterns. An example of a search-match procedure is shown in Figure 4.14 for a sample containing two calcium carbonate phases, vaterite and calcite.

It still remains very important to check the results provided by this software as many materials will have very similar diffraction patterns and the pattern suggested by the software as being the best match for your data may in fact not be. For an acceptable identification the peak positions and intensities of the reference sample and the experimental data must be a very good match. In some cases, there may be peaks within the experimental data that do not appear in the selected reference pattern, the two main reasons for this are:

1. There is another phase within the sample that requires identification.

2. The reference pattern has been obtained is of a lower quality/resolution than the experimental data.

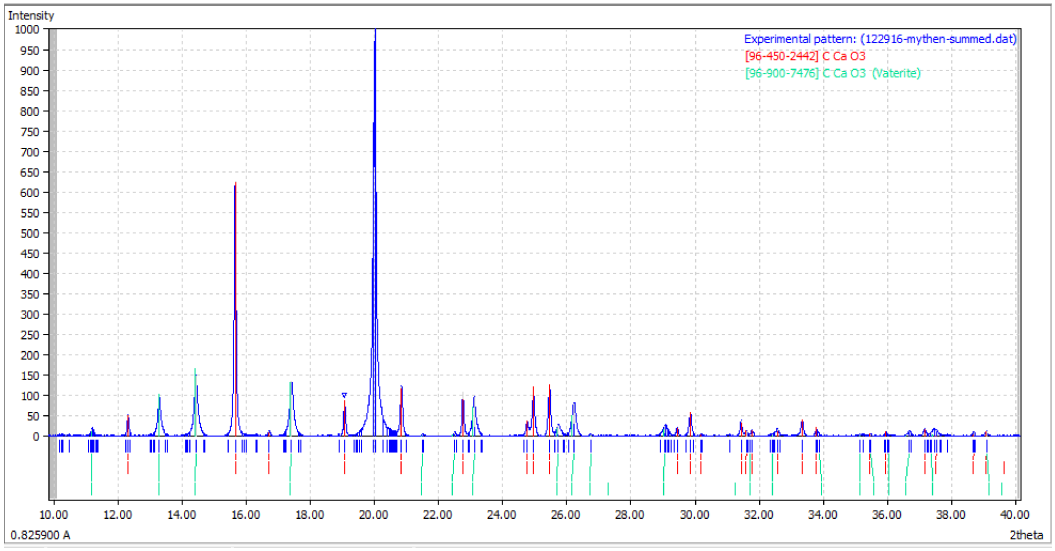

Figure 4.14: Search-match software, Match!, identifies multiple mineral phases (vaterite and calcite) that contribute to an experimental powder pattern using the Crystallography Open Database (COD; Gražulis et al. 2009).

The second item is particularly important for data obtained using a synchrotron source due to the much higher resolution, weak diffraction peaks will be observed that would be missed using standard laboratory diffractometers. An additional sign of this is that some peaks that are single in the reference data will be resolved into multiple peaks in the experimental data. If, however, there are peaks present in the reference data that are not present in the experimental data then it is very likely that the reference phase is not an accurate match to the experimental sample and further identification is required.

The use of peak search-match software, therefore, makes the identification of multiple mineral phases within a pattern much easier and once the mineral phases present in the sample have been determined a more detailed, quantitative analysis can be performed using structural models of the required phases. The sample holders used in X-ray diffraction studies are made up of amorphous materials, such as glass and

kapton, to ensure that the sample holder does not contribute additional, unnecessary features to the experimental pattern. However, these can still contribute to the diffuse scattering, sometimes leading to a higher than normal background. In order to obtain the most reliable analysis of the data it is customary to obtain at least one X-ray diffraction pattern of the empty sample capillary. This then provides a means to subtract the contribution of the sample container from the subsequent experimental data so that only diffraction features from the sample are being studied. This can be performed by most data plotting software, but for this thesis the main software packages used for plotting and manipulating X-ray powder patterns were DIPSO (part of the Starlink Project; Howarth & Murray 1991) and Gnuplot (Williams, Kelley & many others 2010). At this point it can also prove useful to simply compare the patterns visually to determine which features may appear different, or how the intensities of the peaks change, how the peak widths may change in order to determine which features require further analysis and/or fitting.

If the sample is completely unknown then indexing can be used to determine the unit-cell geometry and subsequently the space group of the material. This is performed using the CMPR program (Toby 2005), alongside DICVOL (Boultif & Louer 2004). Indexing works on the principle that each peak in the diffraction pattern relates to a specific crystallographic plane, having Miller indices hkl and a specific d-spacing. Indexing uses the peak positions to calculate the unit-cell parameters (a,b,c) which then provides information relating to the symmetry of the sample and therefore the space group. However, due to the 1D nature of the powder pattern, reflections having the same $|\mathbf{d^*_{hkl}}|$ are overlapped e.g. $(-h,-k,0)$, $(h,k,0)$, $(h,-k,0)$ and $(-h,k,0)$ in an orthorhombic system. This means that the reconstruction of the three-dimensional reciprocal lattice from a powder pattern is difficult, but special algorithms have been developed for use in indexing software to allow the determination of unit cell parameters and space groups.

Indexing of a powder pattern is based on the use of a quadratic form, obtained by squaring the reciprocal lattice vectors ($\mathbf{d^*_{hkl}} = h\mathbf{a}^* + k\mathbf{b}^* + l\mathbf{c}^*$), that relates reciprocal cell parameters to miller indices:

$$Q_{hkl} = h_i^2 Q_A + k_i^2 Q_B + l_i^2 Q_C + h_i k_i Q_D + k_i l_i Q_E + l_i h_i Q_F \tag{4.8}$$

where $Q_{hkl} = 1/d_{hkl}^2$, $Q_A = \mathbf{a}^{*2}$, $Q_B = \mathbf{b}^{*2}$, $Q_C = \mathbf{c}^{*2}$, $Q_D = 2\mathbf{a}^*.\mathbf{b}^*$, $Q_E = 2\mathbf{b}^*.\mathbf{c}^*$ and $Q_F = 2\mathbf{c}^*.\mathbf{a}^*$, d_i the interplanar spacing and h_i, k_i, l_i the miller indices of the ith reflection.

The DICVOL software package (Boultif & Louer 2004), mentioned previously, uses a successive dichotomy procedure (described in detail by Louër & Louër 1972) to solve Equation(4.8). All it requires is the input of a file containing a complete list of peak positions, generated by CMPR, from which it determines the unit cell parameters and the most likely space group for the sample based on the analysis of the whole pattern.

4.4.1.2 Quantitative analysis

When the sample is of a known composition/phase, quantitative analysis of the powder pattern can be performed. Rietveld refinement aims to produce refined values for the structural parameters of a material based on an initial structural model. The Rietveld method (Rietveld 1969) uses a least-squares procedure in order to refine a structural model with the aim of improving the agreement between the experimental pattern and that calculated from the model. Rietveld refinement of the data presented in this thesis has been performed using the TOPAS Academic (Coelho 2007) profile analysis program. For additional information a detailed discussion of the practical aspects of performing a Rietveld refinement is given by McCusker et al. (1999).

Rietveld refinement begins with the input of a structural model containing information regarding the atomic positions, unit cell parameters, occupancy and displacement parameters, as well as the space group, of a relevant material. From this structural model, a diffraction profile can be calculated using the structure factor, F_{hkl}, producing a value for the intensity of each Bragg reflection using Equation 4.9:

$$I_{obs(hkl)} = S j_{hkl} L_{hkl} P_{hkl} A_{hkl} F_{hkl}^2 \tag{4.9}$$

where S is a scale factor, L,P and A are Lorentz, polarisation and absorption corrections respectively, j is the multiplicity factor (dependent on the crystal symmetry) and F^2_{hkl} is the atomic structure factor. This method, however, lacks detail and is unable to accurately model features where two or more Bragg peaks are overlapping. Therefore, Rietveld devised a means of producing a more detailed model, calculating intensity on a point by point basis, by taking into account the peak shape function. The intensity, y_i, of any point, i, across the required 2θ range can be calculated using the equation:

$$y_{c,i} = y_{b,i} \sum_{k=k1}^{k2} G_{hkl,i} I_{obs} \tag{4.10}$$

where $y_{b,i}$ is the background intensity at any point, i, in the pattern, $k1$ and $k2$ represent the Bragg reflections contributing to point i (as multiple peaks can overlap, resulting in multiple contributions to the observed intensity at a single point) and $G_{hkl,i}$ is the peak profile function describing how the intensity of one Bragg peak ($I_{obs(hkl)}$) is distributed over a range of 2θ. The aim of a Rietveld refinement is to minimise the function $\sum_i \omega_i (y_{c,i} - y_{o,i})^2$ where $\omega_i = 1/\sigma^2[y_{o,i}]$, $y_{c,i}$ is the calculated intensity at every ith data point in the pattern, $y_{o,i}$ is the observed intensity at every ith step and $\sigma^2[y_{o,i}]$ is the square of the standard uncertainty for $y_{o,i}$. The sum is over the N measured steps that are used in the refinement and therefore the sought-after best fit is achieved when this equation is minimised for all (typically thousands) y_i points simultaneously.

This best fit is achieved through multiple refinement cycles (generally ∼100 for a typical pattern), in which a number of structural, instrumental and other parameters can be refined. Table 4.1 identifies some of the most important and commonly refined parameters used in a typical Rietveld refinement. It should be noted, however, that this is not an exhaustive list.

After each cycle in the refinement is completed an updated plot is produced containing the experimental and refined profiles, along with a difference plot (also referred to as the residual). This allows a visual comparison of the profiles to be performed in order to best guide the refinement further (dependent on how well the experimental profile is fitted) and is the best way to determine if a calculated fit is good or not. However, the quality of the fit can also be expressed numerically through

Instrumental	Notes
Lorentz polarisation factor	For synchrotron data this should be 90 (fully polarised)
Zero error	
Sample displacement	Offset of sample position from centre of diffractometer.
Profile	
Background	
Peak shape	Pseudo-Voigt profiles are used.
Scale factor	Scaling peak intensities to experimental data
Structural	
Lattice parameters	a,b,c, α, β, γ
Atomic coordinates	f_x, f_y, f_z
Site occupancy	
Atomic displacement factors	Displacement parameters

Table 4.1: A non-exhaustive list of commonly refined parameters in Rietveld refinement using TOPAS Academic

.

agreement indices, or R-factors. The weighted profile R-factor can be defined as the square root of the quantity to be minimised, scaled by the weighted intensities:

$$R_{wp} = \left[\frac{\sum_i \omega_i (y_{c,i} - y_{o,i})^2}{\sum_i \omega_i (y_{o,i})^2}\right]^{1/2} \text{x}100\% \tag{4.11}$$

An acceptable value for the R_{wp} is generally <10% but, these values are dependent on multiple factors and care must be used when comparing R-factors to data from other powder experiments. An example of this is the background contribution. If the background has been subtracted then $y_{o,i}$ is the net intensity after subtraction, but, if the background is not subtracted and is refined as part of the Rietveld procedure a significant part of the intensity of $y_{o,i}$ will be due to the background intensity and will therefore produce significantly lower R_{wp} values. The statistically expected R-factor, R_{exp}, which reflects the quality of the raw data, is defined as:

$$R_{exp} = \left[\frac{N}{\Sigma_i \omega_i (y_{o,i})^2}\right]^{1/2} \tag{4.12}$$

therefore, the final R_{wp} value should approach R_{exp}. A goodness of fit (GoF) parameter,

χ^2, is also calculated (see Equation 4.13) and this should approach 1 in the case of a good fit.

$$\chi^2 = \left(\frac{1}{N}\right) \Sigma_i \omega_i (y_{c,i} - y_{o,i})^2 \tag{4.13}$$

This can also be written in terms of the R-factors, R_{wp} and R_{exp}, as:

$$\chi^2 = \left(\frac{R_{wp}}{R_{exp}}\right)^2 \tag{4.14}$$

These values should not be used solely to determine an accurate fit to the data, it is always necessary to review the fit visually and check the refined crystallographic parameters to ensure they are realistic. Once complete, a Rietveld refinement provides the user with a refined structural model, including estimated standard deviations (e.s.d's), for the sample being studied and in the case of multi-phase samples it can calculate the relative weight percentage (wt) of each phase, based on the refined scale factors, S_n, for each phase, n:

$$\mathrm{wt}_1 = \frac{\mathrm{S}_1 \rho_1}{\Sigma_\mathrm{n} \mathrm{S}_\mathrm{n} \rho_\mathrm{n}} \tag{4.15}$$

4.4.2 Total scattering

While conventional powder diffraction is heavily dependent on Bragg scattering, the Pair Distribution Function (PDF) method, otherwise known as the Total Scattering (TS) method, also takes into account diffuse scattering from the sample. Due to only taking into account the Bragg reflections of materials, conventional powder diffraction is limited to studying crystalline materials whose lattice structures produce strong, clear Bragg reflections. In the case of the work described in this thesis, the samples are initially amorphous, only becoming crystalline once annealed at high temperature (>1073 K). These materials are therefore not efficient Bragg scatterers, instead only producing very diffuse scatter due to their short-range order. The PDF approach puts equal weighting on the Bragg and diffuse scattering, allowing further details relating to the short range ordering of materials to be observed (Egami & Billinge 2003).

Consider the example given by Proffen et al. (2003) in which they compare two simulated structures both having the same lattice and the same concentration of vacancies, but having different ordering.

The first, shown in Figure 4.15(a), has random ordering, whereas the second, shown in Figure 4.15(b), has chemical short range order. Analysis of the Bragg peaks of the two samples yields identical structures for the two samples, even though the short range order is very different. This is due to the fact that the Bragg peaks will only provide information relating to the average structure of the material, which in this case is the same. However, magnifying the background of the powder patterns by a factor of 100 allows the difference in the diffuse scattering of the samples to be observed (see inset in Figure 4.15(c)). PDF analysis puts a higher weighting on this diffuse scattering and therefore is more sensitive to the short-range order of materials. Figure 4.15(d) compares the calculated PDFs of the two samples along with a difference curve indicating that this method is effective in distinguishing the difference in the short range order of the two samples. Therefore, by taking into account the diffuse scattering of the samples, the difference in the short-range order can be resolved. For very disordered samples, such as our amorphous dust analogues, that only exhibit short range structure, the PDF method is invaluable, providing a means of observing the changes in the short range structure as the samples are annealed, prior to the appearance of well-defined Bragg peaks.

4.4.2.1 Theory

Total scattering (TS) measurements are taken in much the sample way as for conventional powder data, and the raw powder pattern can be directly compared to powder patterns obtained for conventional powder diffraction, as long as the 2θ values are scaled to the same wavelength.

In order to perform PDF analysis of such data, corrections for Compton scattering, fluorescence and scattering from the sample holder have to be made. The measured intensity, $I_m(Q)$, obtained in a total scattering experiment can be described as:

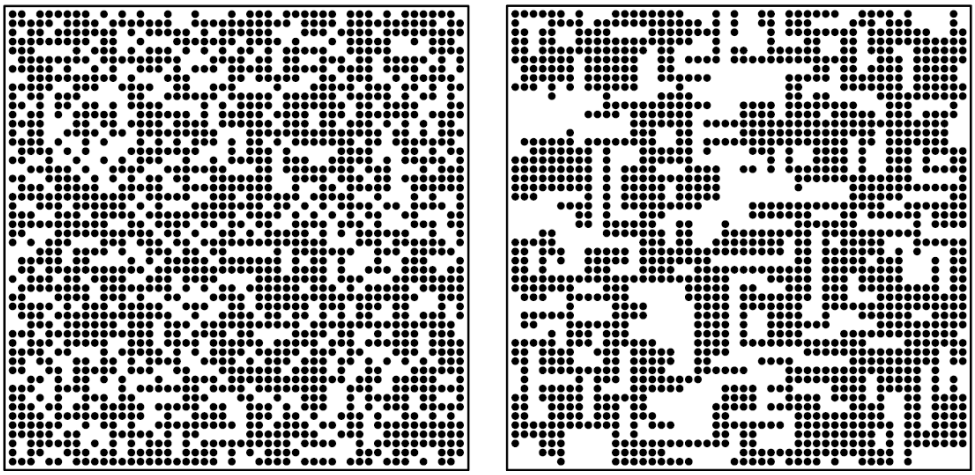

(a) Random ordering (b) Short range ordering

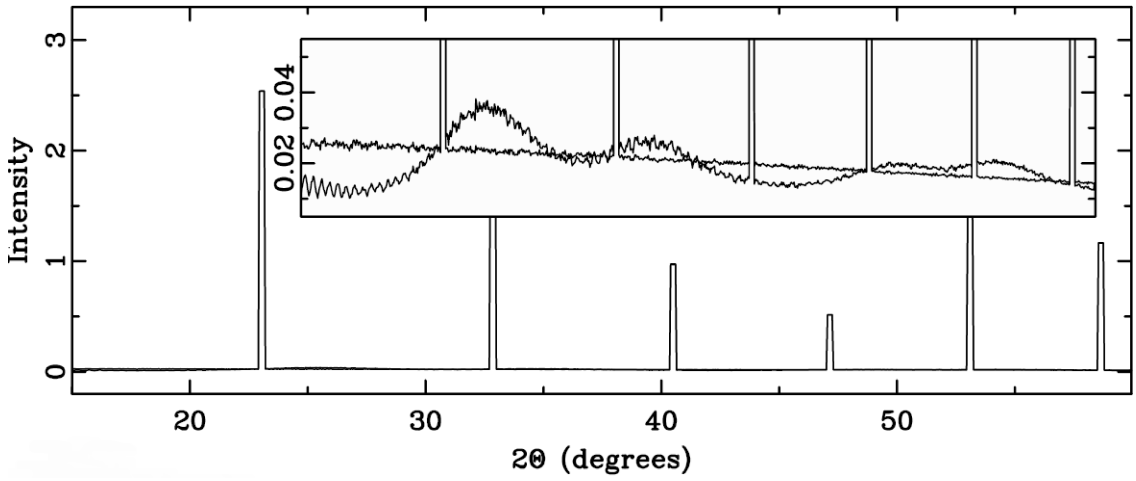

(c) Powder pattern of both samples, inset shows background magnified by a factor of 100.

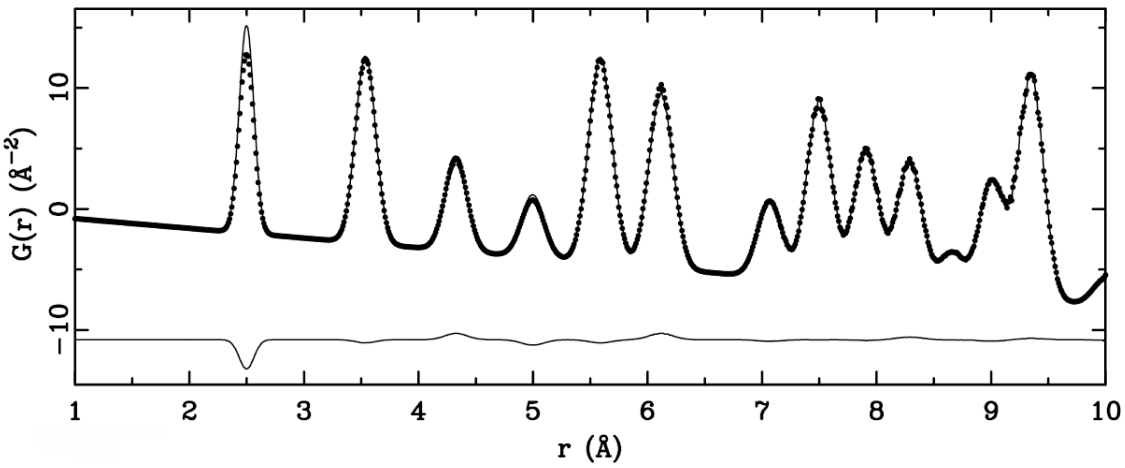

(d) Comparison of PDFs for both samples, filled circles are sample a and solid line is sample b. A difference curve is shown below.

Figure 4.15: Comparison of Bragg analysis and PDF analysis of materials exhibiting the same average structure but different ordering (Proffen et al. 2003).

$$I_m(Q) = I_{\text{coh}} + I_{\text{compt}} + I_{\text{bkg}} \tag{4.16}$$

where I_{coh} is the coherent scattering intensity, I_{compt} is the intensity due to Compton (inelastic) scattering and I_{bkg} is the intensity due to additional background scattering, such as fluorescence and scattering from the sample holder. The only term that conveys information regarding the atomic structure is the coherent scattering intensity and therefore I_m is corrected so that all additional background and Compton scattering are removed, leaving only the coherent scattering intensity, $I(Q)$, which is a continuous function of the magnitude of the scattering vector, Q. Q is defined as $Q = 4\pi\sin\theta/\lambda$, where θ is the diffraction angle and λ is the wavelength of the incident radiation. It is important to obtain the highest possible value of Q, Q_{max} in order to increase the real-space resolution and to decrease termination ripples in the resultant PDF. The value of Q_{max} is dependent on the experimental setup and is limited by the statistics on the data (Billinge 2007).

$I(Q)$ is then transformed into the structure function $S(Q)$, a normalised version of the scattering intensity, through equation(4.17)

$$S(Q) = 1 + \frac{I_{\text{coh}}(Q) - \Sigma c_i |f_i(Q)|^2}{|\Sigma c_i f_i(Q)^2|} \tag{4.17}$$

where $f_i(Q)$ is the atomic form factor, c_i is the concentration of atomic species i and the sum is over all atomic species in the sample with concentrations of c_i. As the value of Q increases, the atomic form factor becomes small and therefore, by dividing the measured intensity by the square of this, an enhancement of the high-Q scattering is observed. This is the region of the data that holds the valuable information regarding the short-range atomic structure and is ignored in conventional powder diffraction.

Subsequently, the PDF is obtained via a sine Fourier transform of the structure factor, S(Q), as shown in Equation(4.18):

$$G(r) = 4\pi r[\rho(r) - \rho_o] = \frac{2}{\pi}\int_0^\infty Q[S(Q) - 1]\sin(Q(r))dQ \tag{4.18}$$

The PDF, $G(r)$, is a weighted histogram of atom-atom distances, effectively a

bond length distribution, that provides information relating to the short-range structure of a material. The $G(r)$ function is related to the probability of finding an atom at distance, r, from a reference atom. The value of r to which peaks can be observed in the PDF indicates the range of structural order exhibited by the sample, the coherent scattering domain (CSD). The analysis of the PDF can reveal a number of properties related to the material structure – the peak position provides the bond lengths between neighbouring atoms, the area below the peaks can be fitted and used to determine the co-ordination number (number of nearest atomic neighbours) and the peak width indicates the magnitude of disorder.

4.4.2.2 Data analysis

Diffraction data are collected at the beamline using a flat plate area detector, which produces 2D images of the diffraction pattern as shown in Figure 4.16. Using an area detector for TS measurements is beneficial as the averaging of the Debye-Scherrer rings over a large angle greatly improves the counting statistics, increasing the value of $Q_{\max}$ and allowing more accurate subtraction of Compton scattering.

These images are then imported into the Fit2D software (Hammersley et al. 1996; Hammersley 1997) for the integration of the 2D images into 1D 2θ scans. The program does this in four stages:

1. Characterisation and determination of detector characteristics (e.g. detector distance, distortions)
2. Determination of experimental geometry (e.g. beam centre, tilt)
3. Data reduction procedures
4. Application of corrections related to the diffraction geometry (e.g. polarisation)

The first and second stages are performed in conjunction using a diffraction image from a known standard, for example Ceria (CeO_2), for which the d-spacings are well

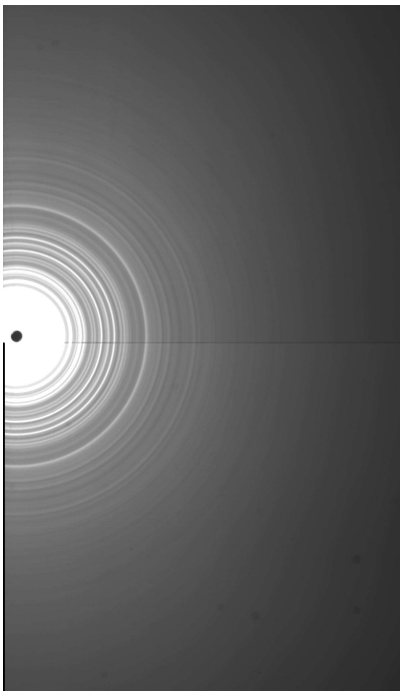

Figure 4.16: Raw image of powder diffraction pattern obtained using Pixium 4700 Flat-Panel Area Detector. The pattern is shifted to the left in order to obtain a maximum Q value of 30Å^{-1} and the dark line running horizontally across the centre of the image is due to the beamstop and is removed from the integration

known. Fitting of the powder pattern for a standard calibrant allows the detector distance, as well as the wavelength, to be refined. It also allows the beam centre and tilt to be defined with greater accuracy. Any regions of the 2D image that should not be used in the integration should at this point also be masked. This refers to a feature in the program that allows a user-defined polygon to be drawn over a particular region of the image, removing it from the integration of the rings. This is often used for the beam centre and to mask out any shadow caused by the beam stop. Once all of the required values have been calibrated using the standard, these value are set and are used for the integration of all further diffraction scans. This calibration must be performed before the analysis of any data collected using a new experimental setup. The third stage is the actual conversion of the 2D image to a 1D binned sequence. This

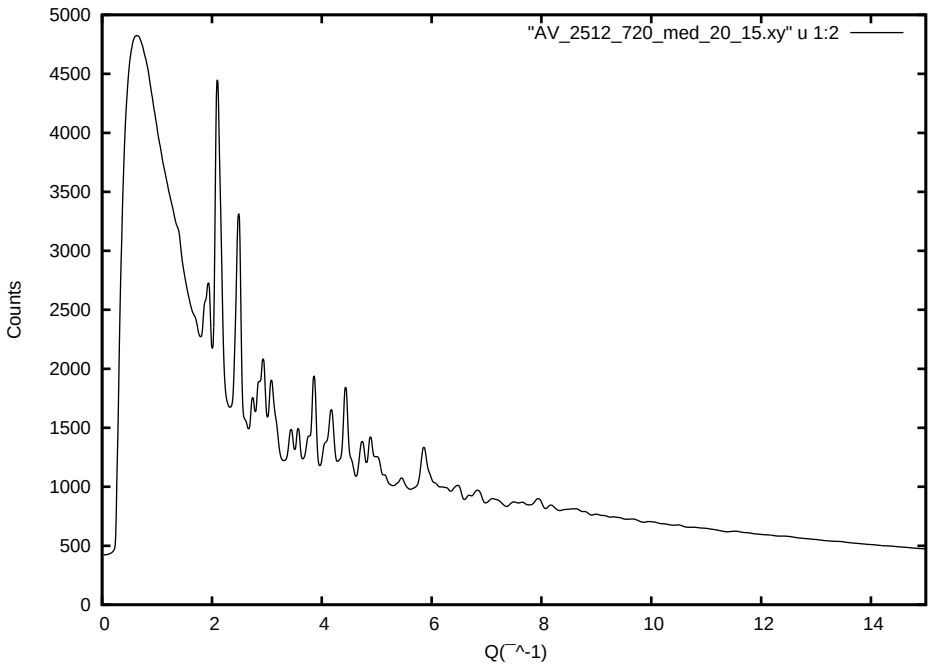

Figure 4.17: 1D powder pattern obtained after integration of the diffraction rings using FIT2D

is performed by integrating each of the Debye-Scherrer rings over the whole available range (in our case this is $\sim$180°) as a function of diffraction angle.

The fourth step accounts for any effects due to the diffraction geometry, which include polarisation, Lorentz correction and absorption corrections taking into account the sample holder and environment. This produces a 1D scan, equivalent to the raw data produced using the PSD on Beamline I11, as shown in Figure 4.17.

Once the 1D pattern has been obtained, the PDF analysis can then be performed using the PDFGETX software (Qiu, Thompson & Billinge 2004). This software performs all of the required corrections, as described in the previous section, producing $I(Q)$, $S(Q)$ and subsequently $G(r)$ plots from the initial powder pattern. Prior to performing these corrections the program requires some initial user input of experimental parameters in order to perform the corrections; this includes the wavelength of the incident radiation, the composition of the sample, and data files for background and

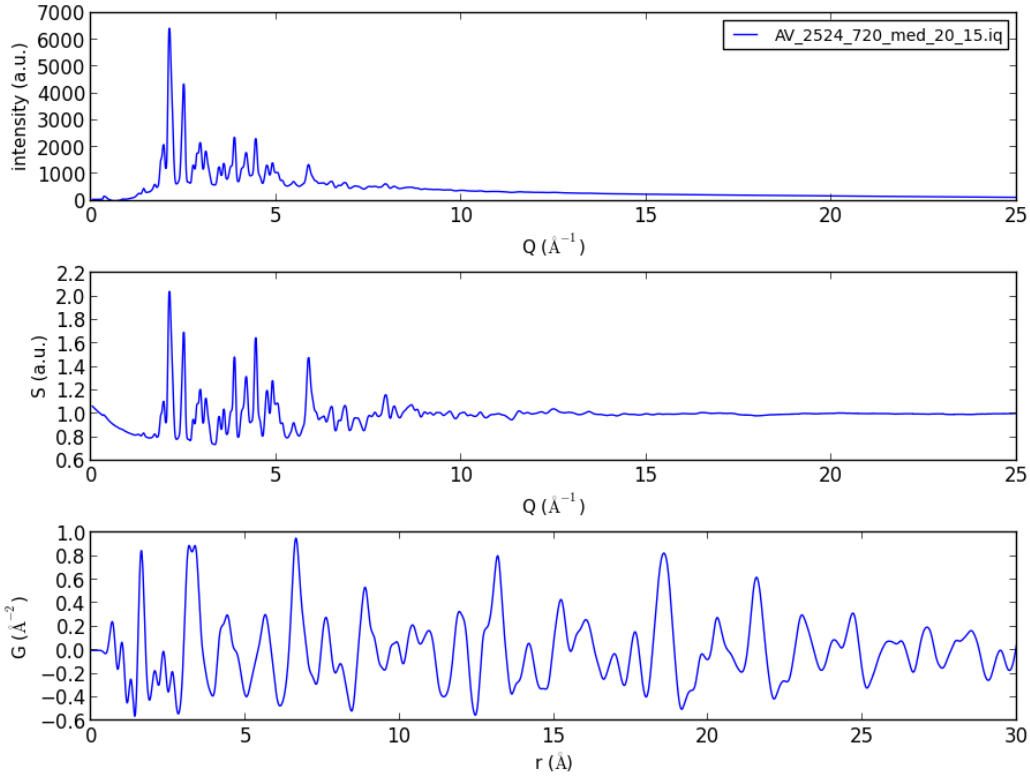

Figure 4.18: $I(Q)$, $S(Q)$ and $G(r)$ functions produced by the PDFGetX software.

sample container subtraction. Figure 4.18 shows the functions produced at each stage.

Data for samples having the same composition and collected with the same experimental setup (e.g. same sample annealed at different temperature steps) can be processed simultaneously as all the input parameters are the same. This allows for efficient data processing.

Once the PDFs have been produced the analysis of these can range from simple measurements of the peak width and position, providing information relating to the bond distances and correlated motion of the sample, to the full profile refinement of the PDF based on a given structural model. This whole-pattern fitting is performed using a program called PDFGui, which works on the PDFFit2 engine (Farrow et al.

Parameter	Symbol
Scale factor	S
Resolution factor	σ_Q
Dynamic correlation factor	δ
Lattice parameters	a,b,c, α, β, γ
Peak width ratio	ϕ
Fractional atomic coordinates	f_x, f_y, f_z
Site occupancy	Occ
Anisotropic displacement factors	u_i

Table 4.2: List of refinable parameters in the PDFFit2 program (Billinge 1998; Egami & Billinge 2003)

.

2007). Given a structural model, the software calculates a PDF $G(r)$ and uses a least-squares regression technique, as described in Billinge (1998), to find the best fit of the calculated $G(r)$ to the experimentally obtained one.

A number of parameters, listed in Table 4.2, are varied until an agreement factor, R_w, is minimised. The agreement factor in this case is defined as (Egami & Billinge 2003),

$$R_w = \sqrt{\frac{\sum_{i=1}^{N} w(r_i)[G_{\mathrm{obs}}(r_i) - G_{\mathrm{calc}}(r_i)]^2}{\sum_{i=1}^{N} w(r_i) G^2_{\mathrm{obs}}(r_i)}} \tag{4.19}$$

and is a weighted, full-profile factor equivalent to R_{wp} in Rietveld analysis. G_{obs} and G_{calc} are the calculated and observed PDFs respectively and w is the weighting factor, $\mathrm{w}(r_i) = 1/\sigma^2(r_i)$, where σ is the estimated standard deviation on the ith point at position r_i. This whole-pattern refinement provides structural information such as lattice parameters, atomic coordinates, displacement parameters and occupancies. It should be understood, however, that this yields quantitative local short-range order only, not the average structure as the Rietveld technique does. The benefit of this, for samples that are well ordered, is that short-range parameters such as the atomic

displacement (thermal) factors can be obtained with increased accuracy (due to the wider Q-range over which the data were collected).

4.5 Complementary techniques

4.5.1 Fourier Transform Infrared Spectroscopy

Fourier Transform InfraRed (FTIR) spectroscopy is a useful tool for the characterisation and analysis of materials, providing a means of identifying unknown materials and providing qualitative information relating to the amount of material present. As described in Chapter 2, IR spectroscopy is a valuable resource for studying cosmic dusts that cannot be studied by any other method. For the work presented in this thesis we have used FTIR spectroscopy to obtain IR spectra of materials synthesised in the laboratory in order to provide a direct comparison to the cosmic materials we are attempting to simulate.

IR spectroscopy results from the transition between vibrational energy states within a molecule, due to the absorption and emission of radiation whose frequency is equal to the transition energy of a particular bond within the molecule (in this case mid-IR radiation corresponds to the transition between the ground and the first excited state of most molecules). This resonant frequency at which a vibrational transition will occur is unique to each molecule, allowing the IR spectra to be used for identification of unknown molecules based on the frequency at which they absorb. However, not all molecular vibrations are IR active, there has to be a change in the dipole moment, $\mu = ql$, of the molecule for it to be promoted to the excited state.

FTIR is a method of obtaining IR spectra rapidly, without the need for long scanning times. This is achieved by measuring all IR frequencies simultaneously, through the use of a broadband light source and an interferometer (see Figure 4.19). This employs a beamsplitter which divides the incident IR beam in two, one beam is reflected off a fixed-position mirror while the other is reflected off a mirror that is moved at

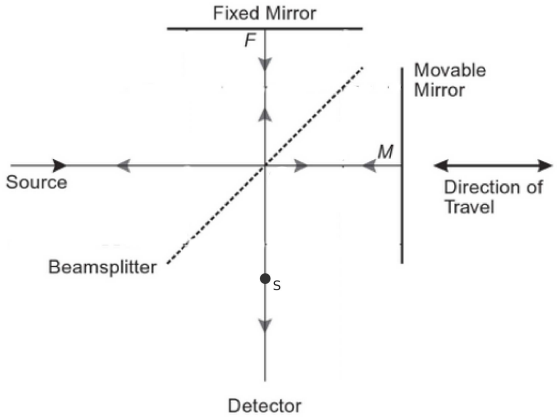

Figure 4.19: Interferometer setup used by FTIR spectrometers. The sample is placed at position S. (after Griffiths & de Haseth 2007).

a continuous velocity during data collection over a short distance (a few mm). The two beams are recombined back at the beamsplitter, however, due to the fixed path length of one beam and the changing path length of the other, the beam incident on the detector will exhibit constructive and destructive interference depending on the position of the movable mirror. The signal obtained from this process, called an 'interferogram', contains a series of data points as a function of mirror distance, where each point contains information about every infrared wavelength emitted by the source. In order to determine the absorption at individual wavelengths and obtain an absorption spectrum a Fourier transformation of the interferogram is performed. This is done automatically by the data collection software so that the user is presented with only the required absorption/transmission spectra.

IR spectroscopy can be performed on materials in any state (solid, liquid or gas) using different sample mounts/preparation techniques. For the purpose of this work we were only interested in the study of powdered, solid samples. For standard FTIR measurements, powdered samples can be mixed with a mulling agent (Nujol) and spread onto salt plates that are transparent in the IR, or the powder is ground together

with salts such as potassium bromide (KBr) and then pressed into a thin pellet that is mounted in the IR beam. These measurements can be made even simpler through the use of an Attenuated Total Reflectance (ATR) accessory which allows a powdered sample to be measured directly without the need for additional preparation. The ATR technique, originally developed by Fahrenfort (1961), uses a crystal made from an IR transparent material with a high refractive index (such as diamond or germanium) on which the sample is placed. The IR beam enters the crystal at a 45° angle, relative to the crystal surface, and experiences total internal reflection at the crystal-sample boundary (see Figure 4.20).

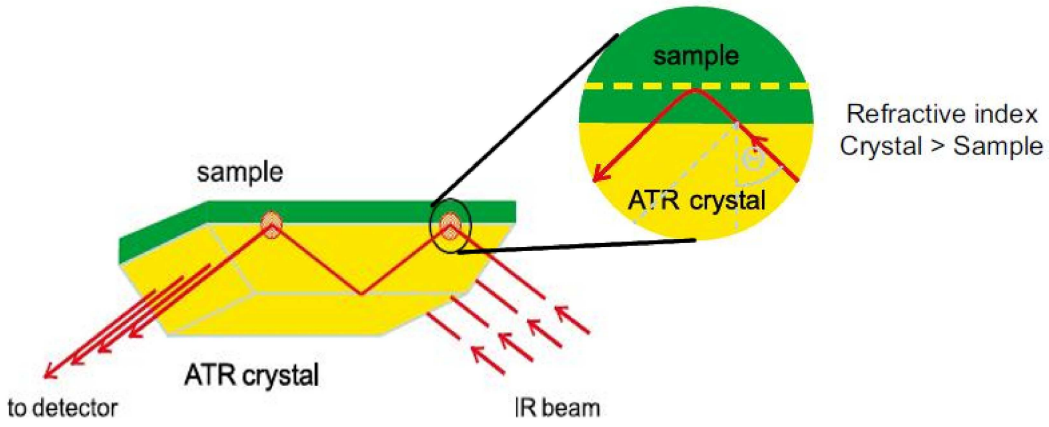

Figure 4.20: Schematic of an ATR crystal, showing the path of the beam and the interaction with the sample.

When an electromagnetic wave undergoes total internal reflection at an interface between two media of differing refractive index an evanescent wave is produced, penetrating a small distance into the second, lower refractive index medium, which in this case is the sample. An evanescent wave has an intensity that experiences exponential decay with distance from the boundary surface and therefore only penetrates a few microns into the sample layer. This phenomenon is also described by the Goos

Hänchen effect (Goos & Hänchen 1947), which explains the small lateral shift of the beam (perpendicular to the direction of propagation) when undergoing total internal reflection. This means that the beam is not reflected exactly at the boundary surface but by a virtual layer a few microns into the less optically dense sample (see inset in Figure 4.20).

4.5.2 Raman Spectroscopy

Raman spectroscopy has also been used in this work as a complementary characterisation technique to FTIR. As explained in the previous section, only certain vibrational modes are accessible with IR spectroscopy and it is found that the vibrational modes which are IR inactive are very often Raman active. Therefore obtaining information from both techniques is of great benefit. Raman spectroscopy is performed by illuminating a sample with a monochromatic beam of radiation, quite often a laser, of wavenumber, $\tilde{\nu}_0$. The photons that then interact with the sample cause the potential energy of the molecules to be raised to a virtual state, $hc\tilde{\nu}_0$, above the ground state. Most of the molecules then quickly fall back to their ground state after releasing a photon of equal energy to that of the incident photon (inelastic Rayleigh scattering), however, a few molecules fall to the first excited vibrational state. The energy of the scattered photon in this case is $hc(\tilde{\nu}_0 - \tilde{\nu}_i)$, where $\tilde{\nu}_i$ is the wavenumber of the ith vibrational mode of the molecule. This inelastic scattering of the photons is known as Stokes Raman scattering. In comparison to Rayleigh scattering, Raman scattering is very weak and therefore the Rayleigh scattering must be filtered out, allowing only the weak scattering to be observed. The Raman scattering intensity is defined by the equation (Griffiths & de Haseth 2007):

$$I_{\text{Raman}} = KI_L(\tilde{\nu}_0 - \tilde{\nu}_i)^4 \left(\frac{\mathrm{d}\alpha}{\mathrm{d}Q}\right)^2 \tag{4.20}$$

where K is a constant based on experimental parameters, I_L is the power of the incident laser, and $\mathrm{d}\alpha/\mathrm{d}Q$ is the change in polarizability, α, with respect to the normal

coordinate of vibration, Q. This indicates that a vibration will only be Raman active if a change of polarizability occurs ($\mathrm{d}\alpha/\mathrm{d}Q \neq 0$). If no change of polarizability occurs then the vibrational mode is Raman inactive.

4.6 Summary

To summarise, in this chapter I have provided an account of the theory of X-ray diffraction, focusing predominantly on synchrotron X-ray powder diffraction, and techniques used for data collection and analysis. X-ray diffraction is a very efficient technique for probing the long range order of materials, assuming that the material is of a crystalline nature and satisfies the Bragg equation. Powder diffraction measurements provide a wealth of information, reflecting the component phases that constitute a sample and allowing the chemical structure of a new or unknown material to be discovered through indexing of the powder pattern. Fitting of a powder pattern using structural models is also discussed. This allows additional quantitative information, such as refined lattice parameters and relative weight percentages of individual phases, to be obtained. The Total Scattering approach to powder diffraction has also been discussed, which can yield valuable short range structural information, such as atomic bond lengths, for disordered materials.

5 Experimental

5.1 Introduction

5.1.1 Diamond Light Source

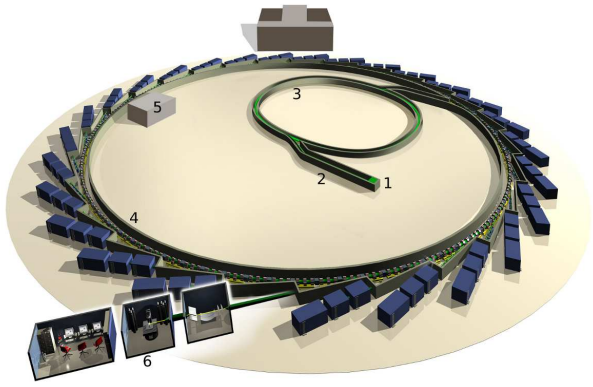

Figure 5.1: Layout of the Diamond Light Source synchrotron facility, showing the various components of the synchrotron. 1. Electron gun, 2. Linac, 3. Booster ring, 4. Storage ring, 5. RF Cavity and 6. Beamline. (http://www.diamond.ac.uk/)

Diamond Light Source is a third generation synchrotron facility located on Harwell Science and Innovation Campus in Oxfordshire. It became operational in early 2007, replacing the UK's previous synchrotron laboratory at Daresbury in Cheshire.

Electrons are produced in an electron gun, located at one end of a linear accelerator (linac), which accelerates the electrons up to 100 MeV before injecting them into the booster ring. This small particle accelerator then increases the energy of the electrons even further, up to 3 GeV, prior to their injection into the main storage ring. The storage ring, although appearing circular, is actually a 48-sided polygon made up

of 24 straight sections joined by 48 dipole (bending) magnets that are used to encourage the electrons to follow a circular path around the ring. At the location of each beamline, a bending magnet or insertion device is placed within the storage ring, using strong, alternating magnetic fields to alter the path of the electrons. The consequence of this is the production of a highly focused beam of synchrotron radiation, directed into the beamline. The storage ring is maintained under high vacuum (7.9×10^{-10} mbar) in order to minimise the amount of scattering due to electrons colliding with air molecules. The stored beam is topped-up with new electron bundles approximately every 600 seconds, ensuring that the beam maintains a constant current.

5.1.2 Beamline I11

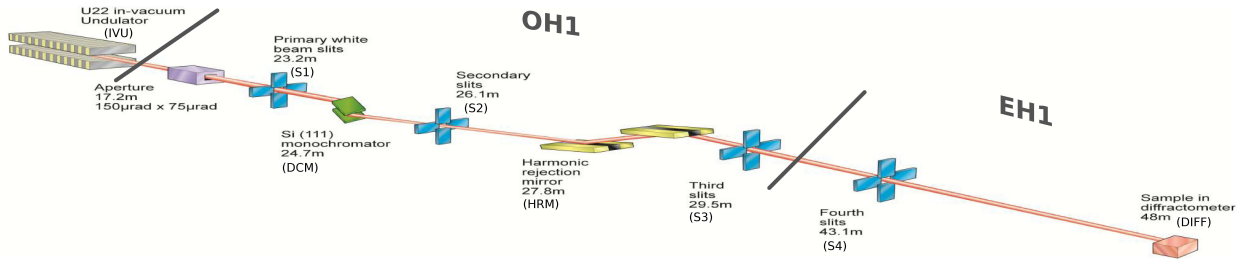

Figure 5.2: Layout of the I11 Beamline (http://www.diamond.ac.uk) prior to the Long Duration Experiment upgrade. X-ray beam travelling from left to right.

Beamline I11, at Diamond Light Source, is a high resolution powder diffraction beamline, using a high brightness, low bandpass X-ray beam to perform detailed structural analysis of powdered materials. Being a third generation synchrotron facility, insertion devices (IDs) are used on the beamlines to produce very high brightness beams. In the case of I11 the insertion device used is a 22-pole in-vacuum undulator source, made up of a 90-magnet array (Thompson et al. 2009). The energy range accessible on I11 is currently 5 to 30keV, although the highest incident flux is obtained

between 11 - 20keV and therefore the beamline is primarily set at its optimal energy of 15keV. This results in an incident wavelength of ∼0.826Å that can be calibrated, to an accuracy of 6 decimal places, using a certified silicon reference powder, NIST SRM640c. This calibration is performed at the start of each new experiment.

The technical layout of the beamline, identifying the main optical components, is shown in Figure 5.2. The majority of these components are located in the optics hutch (OH1), with the exception of the fourth slits (S4) and the diffractometer which are located in the experimental hutch (EH1). From the source (IVU), the beam is passed through a variety of components designed to trim and filter the beam, allowing specific wavelengths of radiation to be selected. Four sets of slits (S1-4) are positioned at specific locations along the beamline to trim the beam and define the size, while a large, liquid nitrogen-cooled double-crystal monochromator (DCM) with a fixed height geometry is used to select the energy range of the X-ray beam. Double-bounce harmonic rejection mirrors (HRM) are positioned after the DCM to remove contamination of the monochromatic beam by higher energy photons that may have also passed through the monochromator. To account for the full energy range used on I11 these mirrors have a three-stripe surface of (1) polished Si (<10keV), (2) high purity Rh (10 <E <22keV) and (3) high purity Pt (>22keV). The beam then exits the beam pipe at the centre of a heavy-duty three-circle diffractometer (DIFF), located in the experimental hutch. The sample sits at the centre of the diffractometer, shown in Figure 5.3, which is made up of three high-precision rotary stages (θ-, 2θ- and δ-circle) on which two detectors are mounted.

The first, a multianalysing crystal (MAC) detector, is a point detector in which 5 arms, each containing 9 Si(III) crystals, are utilised simultaneously in order to decrease data collection time whilst also providing extremely high resolution. The MAC detector is located above the sample on the 2θ-circle. Additionally a 90° arc position sensitive detector (PSD), specially designed for time-resolved measurements, is mounted on the δ-circle below the sample. This consists of 18 pixellated Si strip modules tilted to give a curved detection surface (Thompson et al. 2011). Samples are mounted onto the

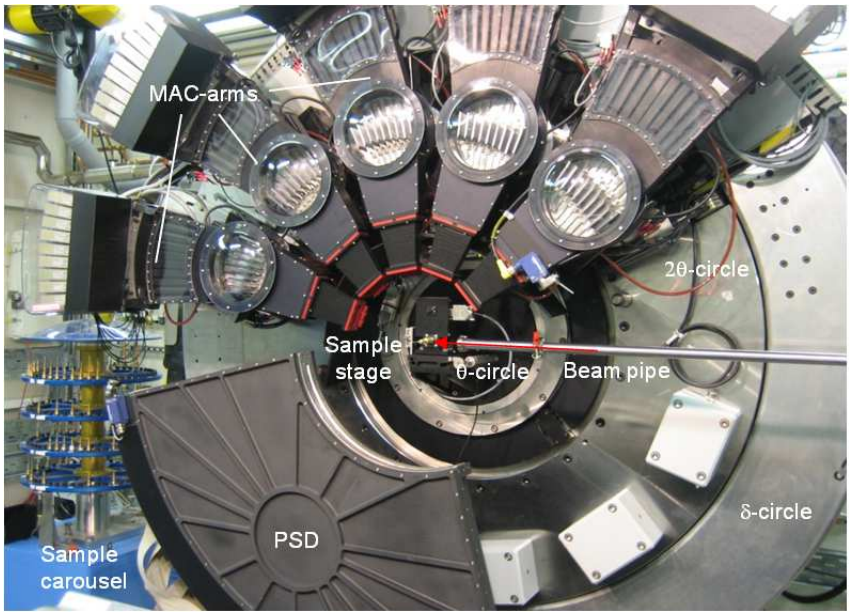

Figure 5.3: The I11 diffractometer with all major components labelled.

central θ-circle.

I11 is well equipped to simulate a number of environments using equipment such as N_2 Cryostream, hot gas blowers, liquid helium and furnaces to produce a range of temperature conditions from 4K up to 1700K – perfect for astrophysical applications.

5.1.3 Beamline I12

Beamline I12 is a high-energy beamline operating at energies between 50 – 150keV. The large energy range and ability to have monochromatic or white beam mean that I12 is a multi-purpose beamline capable of a number of techniques, including X-ray imaging and tomography, small angle x-ray scattering, small molecule diffraction and total scattering powder diffraction. Figure 5.4 shows the layout of the optical components of the beamline, which includes a 4.2T multipole wiggler (far left), a number of filters to attenuate the beam and filter out lower energies, as well as an adjustable silicon

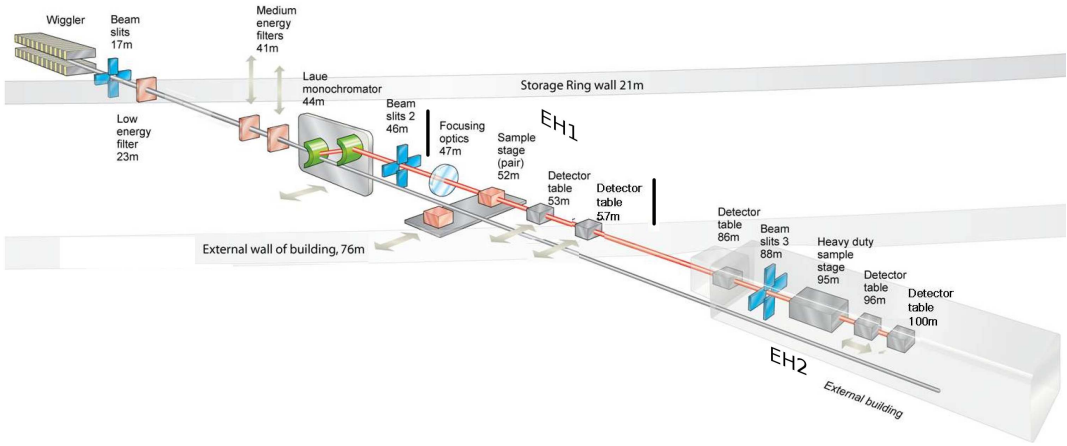

Figure 5.4: Schematic layout of the I12 Beamline (http://www.diamond.ac.uk)

crystal laue monochromator. As can be seen in Figure 5.4, I12 is comprised of two experimental hutches. The first hutch (EH1) is positioned 51m from the beam source and is used for standard samples. The second hutch (EH2) is 101m from the beam source and is specially designed for the study of large engineering components. Only the details of EH1 will be discussed here as EH2 was not used and is therefore not relevant to this work.

EH1 is equipped with a large pixellated 2D area Pixium detector (CsI scintillator on amorphous Si substrate; Daniels & Drakopoulos 2009) with an area of 2880 x 2881 pixels and individual pixel size of 148 x 148μm. A cerium oxide (CeO_2) standard is used for calibration of the wavelength for individual experiments.

5.2 Sample preparation

5.2.1 Magnesium and calcium silicates

Amorphous magnesium and calcium silicates are prepared in the laboratory using a sol-gel method adapted from Day (1976). In total, seven unique compositions were manufactured; pure-Mg silicate ($MgSiO_3$), pure-Ca silicate ($CaSiO_3$) and intermediate compositions $Mg_xCa_{1-x}(SiO_3)_2$, where $x = 0.2, 0.4, 0.5, 0.6, 0.8$. These solutions were produced by combining the following metal salts:

- Na_2SiO_3 (sodium metasilicate)
- $MgCl_2$ (anhydrous magnesium chloride)
- $CaCl_2.2H_2O$ (calcium chloride dihydrate)

all of which were in powder form. The final compositions were produced through the reactions:

$$MgCl_2 + Na_2SiO_3 \longrightarrow MgSiO_3 + 2NaCl \tag{5.1}$$

$$MgCl_2 + CaCl_2.2H_2O + 2Na_2SiO_3 \longrightarrow MgCaSiO_3 + 2NaCl + 2H_2O + Cl2[g] \tag{5.2}$$

$$CaCl_2.2H_2O + Na_2SiO_3 \longrightarrow CaSiO_3 + 2NaCl + 2H_2O \tag{5.3}$$

The preliminary materials were weighed using digital scales, with weights calculated for each substance to produce a 0.1 molar solution. The weights used for each value of x are shown in Table 5.1.

These values could then be used as a basis for producing more or less gel, as required. The specified amounts of each of the powders are then dissolved separately in 500ml of de-ionised water at room temperature. In most cases just agitating the

x	$MgCl_2$	$CaCl_2$	Na_2SiO_3
0	0	6.456g	6.104g
0.2	0.942g	5.165g	6.104g
0.4	1.884g	3.874g	6.104g
0.5	2.355g	3.228g	6.104g
0.6	2.826g	2.582g	6.104g
0.8	3.768g	1.291g	6.104g
1	4.710g	0	6.104g

Table 5.1: Weights of each powder used to produce all compositions of sol-gel silicates.

beaker by hand causes the majority of the solution to dissolve but, in some cases, stirring with a magnetic stir bar is required. The two solutions are then combined whilst being continually stirred. This has been proven to lead to the formation of amorphous end products over crystalline ones (Day 1976). Once combined the mixture produces a cloudy, fairly opaque solution. After a few (2-3) minutes, stirring is stopped and the solution is left to stand in a fume cupboard overnight to allow settling out of the gel. The solution is then left to stand for 16 hours or more to allow enough time for the gel to separate from the aqueous solution, forming a layer of gel at the base of the beaker with the excess salt solution on top. In order to remove as much of the excess liquid as possible from the gel, and to ensure that as much salt byproduct (NaCl) as possible is removed, the excess liquid is decanted and the gel separated into a number of 50ml tubes and that are then placed into a centrifuge. The gel is centrifuged at 3300rpm for 10 minutes per cycle, with a ramp up/ramp-down time of 9 seconds. After centrifuging, the excess liquid is once again decanted and the gel is washed through with more de-ionised water. This cycle is repeated 3 times to ensure that most of the salt is removed. The final, washed gels are stored in sealed tubes under a small amount of de-ionised water until required, at which point small amounts of the gel are removed and dried in a vacuum furnace.

For comparison, the gels were initially dried both in air, using a standard Carbolite furnace, and under vacuum, using a Carbolite HVT vacuum furnace purged with nitrogen. The difference between the final samples produced by the two methods was immediately obvious. Drying the gels in air produced solid, opaque grains ranging in size from a few cm down to a few mm (see Figure 5.5(a)), while drying the gel under vacuum produced a very fine-grained powder with individual grains $< 10\mu$m in size (see Figure 5.5(b)). The samples were then stored in sealed vials under argon to limit atmospheric interaction.

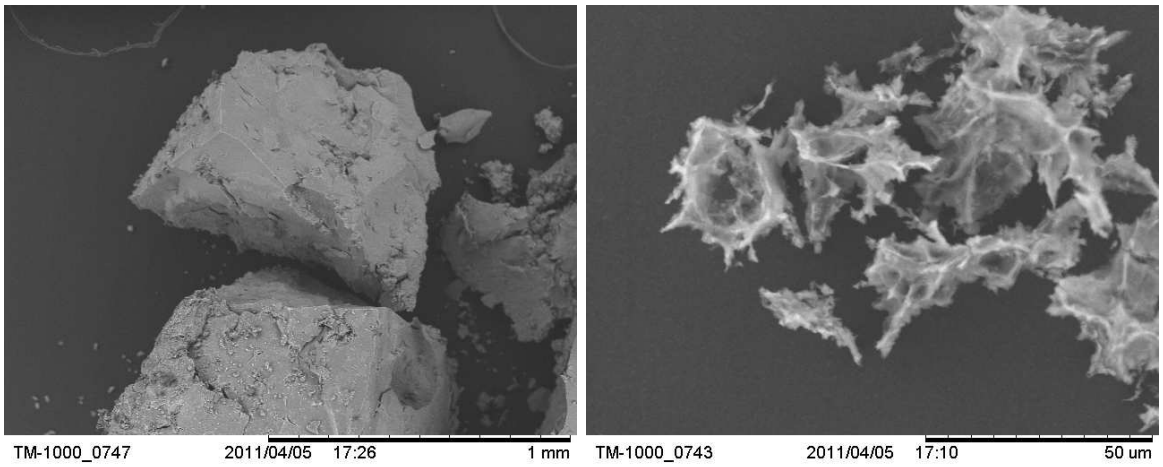

(a) Dried in air (b) Dried under vacuum

Figure 5.5: SEM images of $Mg_{0.5}Ca_{0.5}SiO_3$, comparison between air-dried and vacuum-dried end products.

5.2.2 Fe/Mg silicates

Amorphous iron and magnesium-rich silicates were also produced using a sol-gel method, as described in the previous section, by combining 0.1 molar solutions of the following metal salts:

- Na_2SiO_3 (sodium metasilicate)
- $MgCl_2$ (anhydrous magnesium chloride)
- $(NH_4)_2Fe(SO_4)_2.6H_2O$ ammonium iron(II) sulphate)

Combining solutions of these salts in varying quantities produced amorphous Fe/Mg silicates of composition $Fe_xMg_{1-x}Si_2O_6$ via the reaction:

$$(NH_4)_2Fe(SO_4)_2.6H_2O + MgCl_2 + Na_2SiO_3 \longrightarrow FeMgSiO_3 + 2NH_4Cl + 2Na_2SO_4 + 6H_2O \tag{5.4}$$

When combined, the solutions formed a blue/green gel that exhibited a gradual colour change with composition. It was found that the higher the concentration of Fe, the darker the gel appeared. This was also true for the final powdered samples after drying. Samples were made with compositions of $x = 0.2$ to $x = 0.8$ in steps of 0.1.

5.3 Characterisation

Characterisation of the as-prepared samples is performed using laboratory-based spectroscopic techniques, including Raman and Fourier Transform Infrared Spectroscopy. This section provides the technical details of the equipment used and also presents the initial characterisation data collected from the as-prepared materials.

5.3.1 Raman spectroscopy

Raman spectra of the samples were obtained using a Horiba Scientific LabRAM HR system with green laser ($\lambda = 532$ nm), using a 600-line grating and 50x objective. Calibration is performed using a silica wafer. Raman spectra are used in this work to complement SXPD data by allowing additional characterisation of the synthesised

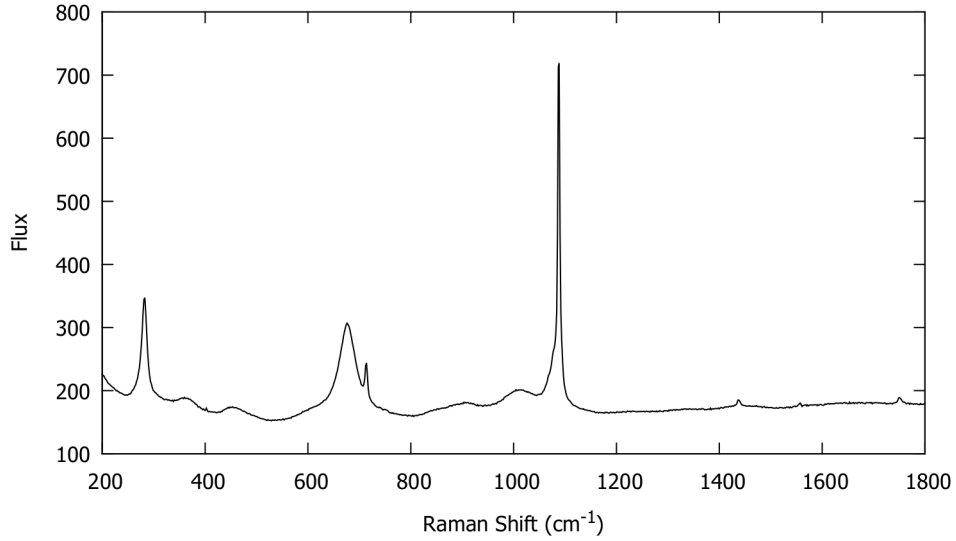

(a) Dried in air

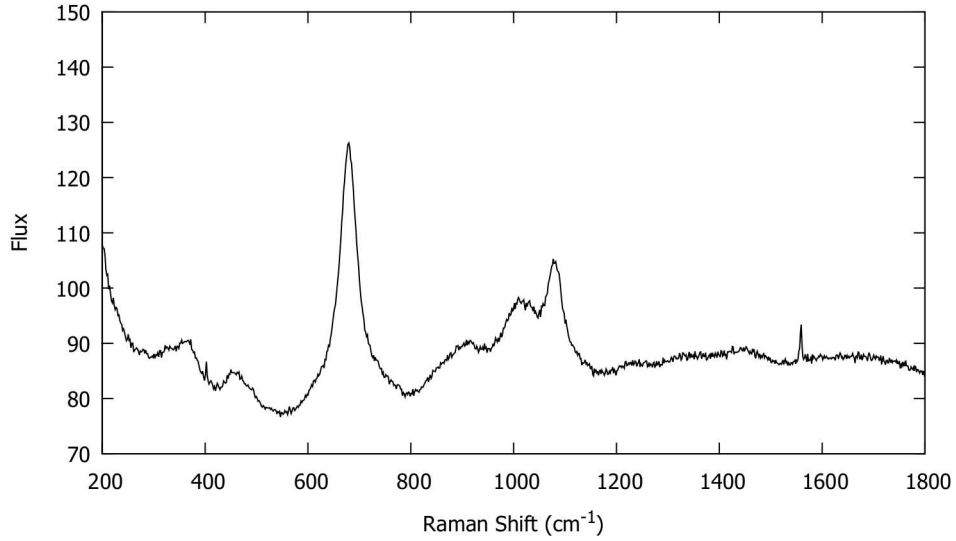

(b) Dried in vacuum

Figure 5.6: Comparison of raman spectra of $MgCaSi_3$ grains, dried in air and in vacuum

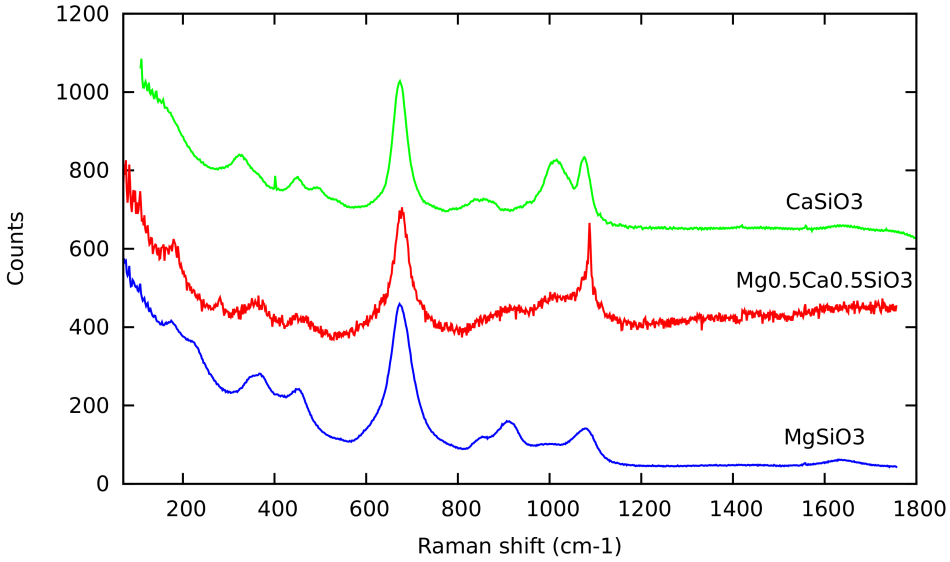

Figure 5.7: Raman spectra for Mg-Ca sample compositions $x = 0$, 0.5 and 1, as labelled. Spectra are offset along the vertical axis for clarity.

samples and to provide information relating to the hydration state of the studied samples. Figure 5.6 shows comparison spectra of the air-dried and vacuum-dried samples of composition $x = (Mg_{0.5}Ca_{0.5})SiO_3$. This indicates that both are amorphous silicates, as indicated by the broad features between 350 and 480 cm^{-1} and at 680 cm^{-1}, however, the sample dried in air exhibits sharp, crystalline features at $\tilde{2}80$ cm^{-1}, 700 cm^{-1} and 1098 cm^{-1} associated with the calcium carbonate phase calcite ($CaCO_3$). This is believed to be due to the reaction with atmospheric CO_2 during the drying process. As the intention of this study is to observe the solid-gas interaction between solid amorphous silicate grains and gaseous CO_2 it was therefore deemed necessary to use the vacuum furnace for the production of all samples so as to avoid prior contamination.

Raman spectra for three of the as-prepared, vacuum-dried sample compositions, $x = 0$, 0.5 and 1, are presented in Figure 5.7. The Raman spectra show that all three compositions have a dominant feature at 673 cm^{-1} due to the inter-tetrahedral Si-O-Si stretch, indicative of medium-range order. The position of this peak does not differ

with composition. The dominant features between 800 - 1200 cm^{-1} are associated with Si-O stretching modes of non-bridging oxygen atoms in the silicon tetrahedra (Hugh-Jones, Chopelas & Angel 1997; Serghiou, Boehler & Chopelas 2000), while the prominent features at lower wavenumbers (172, 361 and 447 cm^{-1}) are associated with internal Si-O stretching modes, as well as countercation stretching (e.g. Mg-O, Ca-O bonds; Richet, Mysen & Ingrin 1998; Serghiou, Boehler & Chopelas 2000; Huang et al. 2000).

Figure 5.8 presents three Raman spectra for vacuum-dried Fe-silicates of x_{Fe} = 0.1, x_{Fe} = 0.5 and x_{Fe} = 1. The predominant features in the three spectra are observed at 560, 685, 906 and 1100 cm^{-1}, not dissimilar to the Mg-Ca silicates described previously. These features are also very broad, confirming that the Fe-based sol-gel method is equally as suitable for producing amorphous Fe-rich silicates. It should be noted that, while all of the main features present in the $x = 0.1$ and $x = 1$ are also present in the intermediate $x = 0.5$ sample, their relative intensities are slightly different. This is believed to be due to an orientational effect, which can mean that a slightly higher concentration of one phase is being measured compared the other, leading to an increase in intensity of the vibrational modes relating to that phase.

5.3.2 Fourier Transform Infrared spectroscopy

Infrared spectra were obtained using a Bruker Vertex 70 spectrometer with a Harrick diamond attenuated total reflectance (ATR) accessory. Absorption spectra of five of the $Mg_{(x)}Ca_{(1-x)}SiO_3$ compositions, $x = 1$, 0.2, 0.5, 0.8 and 0 are shown in Figure 5.9. The IR spectra support the Raman data, showing that the samples are undoubtedly of amorphous silicate nature, showing two distinct, broad features at 10 μm and between 14-18 μm which are conclusive of amorphous silicates. A broad, weak peak can be seen at 7 μm in the $x = 0.5$ and $x = 1$ samples and can most likely be linked to a C-O stretching mode, indicating slight atmospheric contamination of these samples. There is also a pronounced shoulder at $\sim$11.5μm on the 10μm feature, becoming more prominent with increasing Mg content. This feature can be attributed to the presence

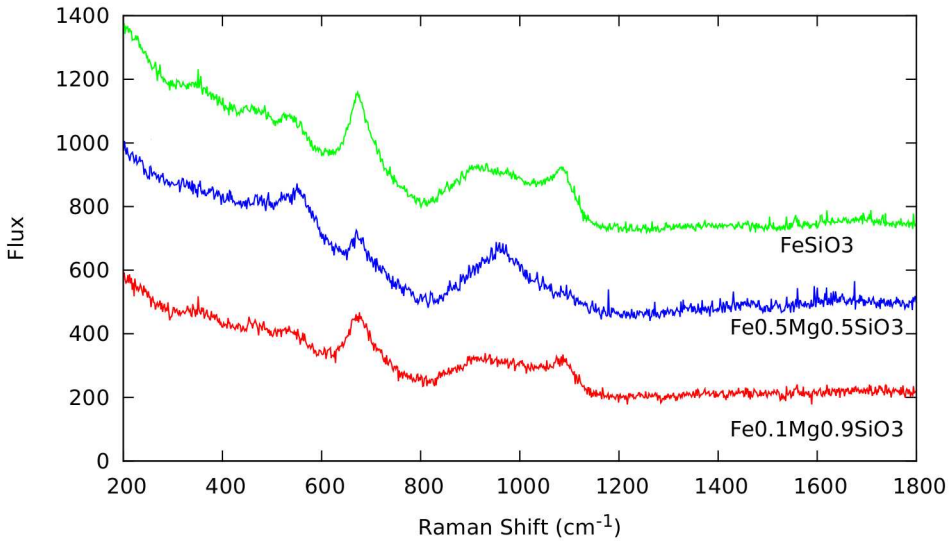

Figure 5.8: Raman spectra of 3 different compositions of $Fe_{(x)}Mg_{(1-x)}SiO_3$

of an additional silicate tetrahedral species, in this case SiO_4 (Thompson, Parker & Tang 2012), and is likely the amorphous equivalent of the 11.2μm peak of forsterite ($MgSiO_4$).

Figure 5.10 presents IR spectra for samples of $MgSiO_3$ and $CaSiO_3$ at RT, 573 K, 873 K and 1173 K. The spectra of the samples heated to $\leq$ 573 K show very little change in both of the samples, however, at a temperature of 873 K the spectra appear to lose some structure. This is more prominent in the Mg-rich sample where the two features at 10 and 11.5μm blend into one and cannot be distinguished from each other. This is also the case for the weak feature at $\sim$16μm where the feature becomes blended into the broad region between 15-20μm. In the spectra of the Ca-rich sample, the features are still visible in the 873 K spectra, but the intensities of all peaks are much weaker. When the temperature is increased to 1173 K, the spectra then change dramatically. This is due to the crystallisation of the sample, producing long range order and giving rise to many more observable vibrational modes.

Infrared spectra of the $Fe_{(x)}Mg_{(1-x)}SiO_3$ samples agree with the previously ob-

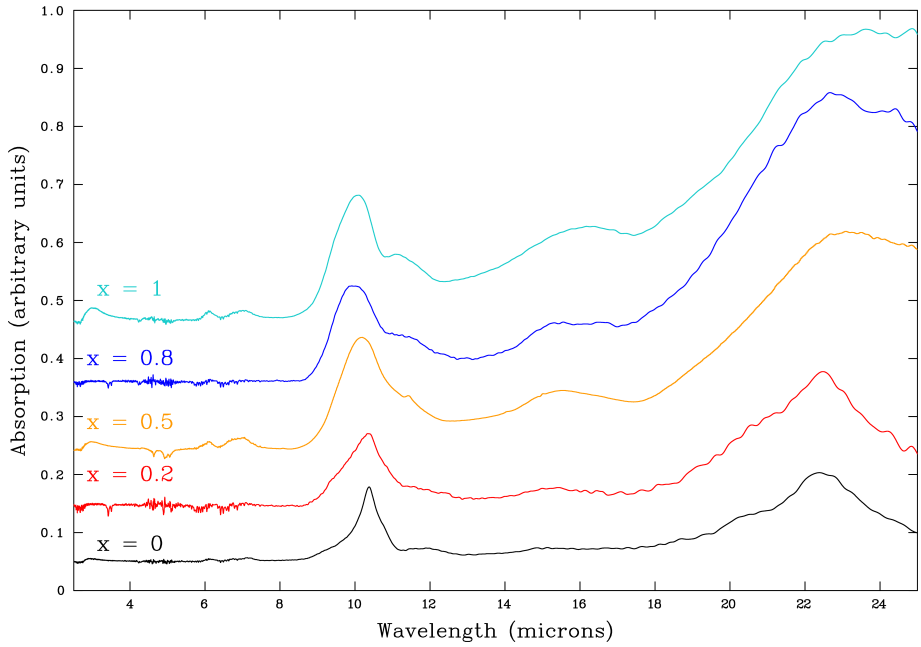

Figure 5.9: Fourier Transform Infrared Spectra of $Mg_xCa_{1-x}SiO_3$ of varying compositions between $x = 0$ and $x = 1$. Spectra are offset for clarity.

tained Raman data, confirming the amorphous silicate nature of the samples (see Figure 5.11). It can be observed that the shoulder at 11.5μm, as seen in the $MgCaSiO_3$ samples, seems to grow with increasing Fe content, eventually merging completely with the 10μm feature, producing a much broader peak. While this is only a very small effect, this could prove valuable in the differentiation of Mg-rich and Fe-rich silicates in astronomical spectra and would benefit from further study.

5.4 Powder diffraction

Due to the nature of powder diffraction, samples need to be mounted in a suitable container that is effectively transparent to X-rays. This means that the container does not satisfy the conditions for Bragg diffraction and therefore does not provide

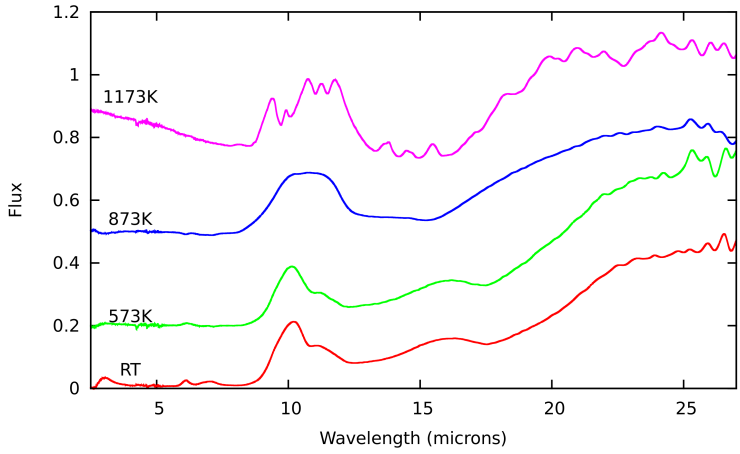

(a) $MgSiO_3$

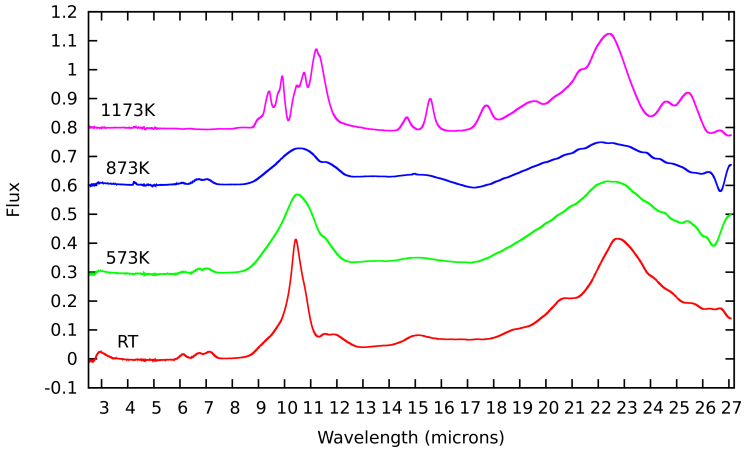

(b) $CaSiO_3$

Figure 5.10: The effect of thermal annealing on samples of a) $MgSiO_3$ and b) $CaSiO_3$

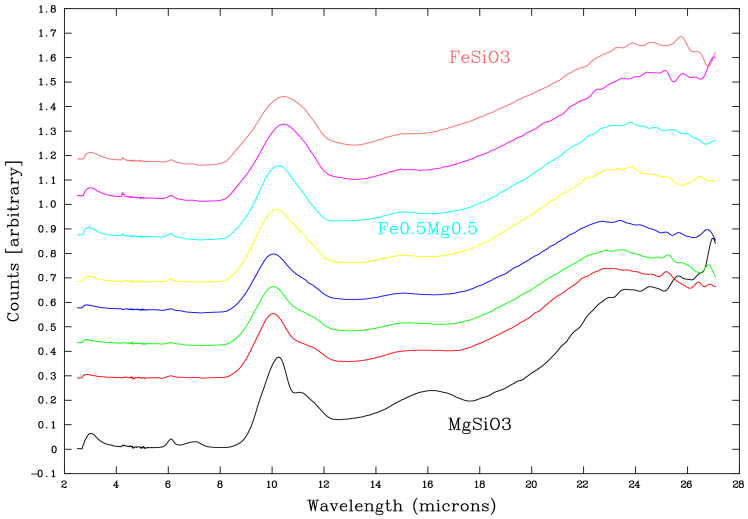

Figure 5.11: Fourier Transform Infrared Spectra of $Fe_{(x)}Mg_{(1-x)}SiO_3$ between $x = 0$ and $x = 1$.

a significant contribution to the final diffraction pattern. There are two methods for mounting samples used predominantly on I11, these are; flat-plate samples holders, in which a thin layer of the sample is spread over a flat disc and the beam is incident at a specific angle to the surface, or thin capillaries into which the powdered sample is loaded. For this work we opted for the use of capillaries as our powdered samples can easily be loaded into these and they provide good powder averaging (achieved by spinning the capillary during data collection).

5.4.1 Loading capillaries

5.4.1.1 Standard capillaries

Standard capillaries are available as borosilicate or quartz with an internal diameter ranging from 0.3mm to 1mm. The type of capillary used is dependent on the temperature and pressure conditions that it will be exposed to. Borosilicate is only stable at lower temperature and should not be used above 973 K, while quartz capillaries can be used safely up to 1873 K. Sapphire tubes are used in the case of pressures

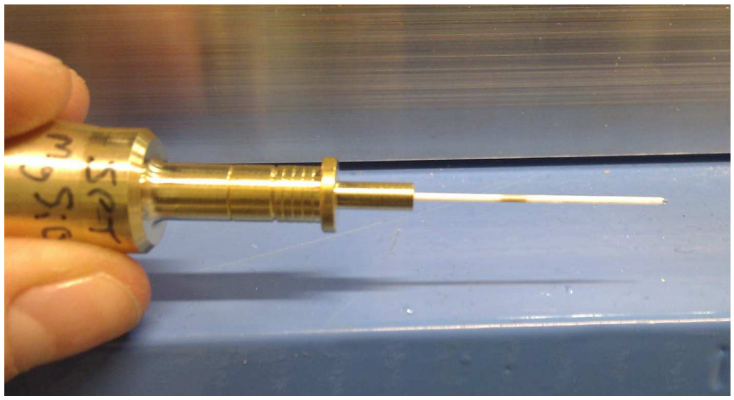

Figure 5.12: Standard capillary in holder on a brass base.

exceeding 50 bar. The brass holders used to mount the capillary onto the diffractometer are also made in different sizes to accommodate a variety of capillaries. The holder chosen should generally be at least 0.1 - 0.2mm larger than the diameter of the capillary, allowing approximately 3/4 of the capillary to protrude from the top of the holder without the fitting being too tight and fracturing the capillary. Powdering of the sample is achieved using a a pestle and mortar, although, due to the hardness of the grains, particularly those with high Mg content, it was found that a lot of the sample would escape from the mortar during the process. To avoid this the sample was mixed with acetone in the mortar which held the grains in place whilst the sample is being ground. This technique, known as trituration, also prevents unwanted localised heating of the sample during grinding. Due to the nature of acetone it does not react with the silicate sample and quickly evaporates after crushing leaving behind the powdered product. The powder was crushed until all large, visible grains were removed and the powder was as uniform in size as possible in order to provide the best particle averaging. The powder is then scooped into the open end of the capillary, vibrating the tip of the capillary regularly to ensure a even filling with as few gaps in the powder as possible. Once the capillary is filled to approximately 3/4 of its length, it is fed

into the holder and the open end of the capillary is cut and sealed using a blowtorch. Superglue then ensures the capillary stays secure before screwing the holder into the brass base.

5.4.1.2 Gas Cell capillaries

Loading a capillary for use in a gas cell, as shown in Figure 5.13, follows a similar method as for the standard capillary up until the capillary is to be placed into the holder and sealed. For a gas cell the open end of the capillary does not need to be sealed; instead once the powder is in place, quartz wool is placed into the capillary, sitting just above the powder. This acts as a filter to ensure the sample stays in place within the capillary, even when it is put under vacuum. The glass wool gets inserted into the capillary carefully, wearing gloves to protect from splinters and using a very fine needle to move it into place. A small rubber ferrule is then slid onto the capillary, along with the cap of the gas cell, this produces an airtight seal at the join of the capillary and the gas cell. The excess end of the capillary is then just cut off using sharp, thin-nose pliers and the capillary is then screwed onto the top of the gas cell. As can be seen in Figure 5.13, the gas cell does not attach magnetically, as with the standard capillary, and therefore needs to be manually aligned to the beam when fitted onto the diffractometer. The goniometers at the base allow for movement in two directions to precisely align the capillary.

A high pressure gas cell has also been developed that can withstand pressures up to 100 bar (See Figure 5.14). The high pressure gas cell can also be used in flow mode, requiring the use of open-ended sapphire capillaries, able to withstand the high pressure.

5.4.2 Data acquisition

The acquisition and plotting of data on the beamlines used for this work are both controlled by Generic Data Acquisition Software (GDA); this software provides an interface

Figure 5.13: Low Pressure Gas Cell

that allows full control of all aspects of the data collection, including the remote movement of sample stages and tables within the experimental hutch and control of the hot air blower, Cryostream and other sample environments. A scripting language known as Jython is implemented by the software, allowing users to write complex scripts that allow the beamline to be run almost autonomously. Prior to obtaining sample data, the wavelength must be calibrated. This is achieved by performing a high resolution scan (∼30 mins), using the MAC detectors, on a silicon (111) standard, of which the crystal structure is well understood. Using Braggs law ($2d\sin\theta = n\lambda$) and knowing the d-spacings for each hkl plane, the exact wavelength of the beam can be calculated from the position of the Bragg reflections with an accuracy of 6 decimal places. As the powdered samples are mounted onto the diffractometer in glass capillaries, it is good

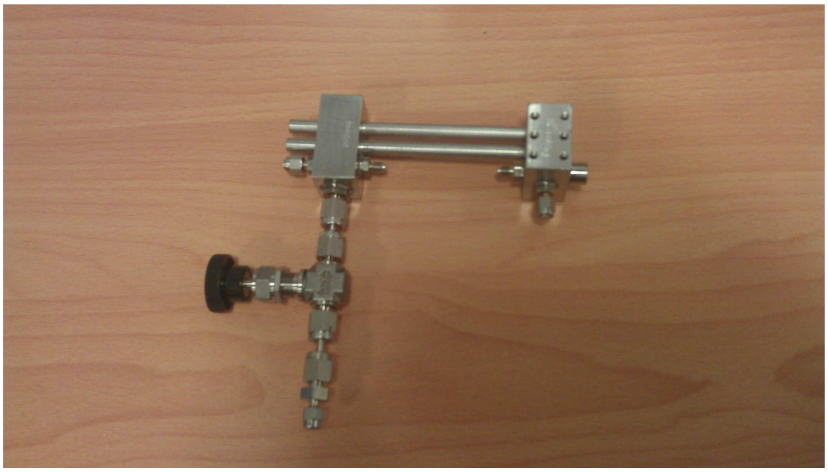

Figure 5.14: High Pressure Gas Cell

practice to obtain at least one measurement of an empty capillary. These measurements should be taken at the start of every new experiment or whenever the experimental setup or instrument parameters are significantly altered. The pattern produced by the empty capillary can then be subtracted from all subsequent sample measurements to ensure that only features of the sample are being taken into account.

6 Thermal evolution of amorphous silicates as cosmic dust analogues

In this chapter we present the results of a study focused on the thermal evolution of amorphous Mg and Ca-rich silicates synthesised as analogues of cosmic dust. This work has been published in the journal Meteoritics and Planetary Science, Day et al. (2012).

6.1 Introduction

Silicate dust was one of the most primitive, refractory dust species known to have been present within the pre-solar nebula, as evidenced by the calcic-pyroxenes (e.g. diopside; $[Ca,Mg]Si_2O_6$) and Mg-rich olivines ($MgSiO_4$) which are characteristic components of Calcium Aluminium Inclusions (CAIs; Macpherson 2005), believed to have been formed at the very beginning of the Solar System. Chondritic meteorites, containing both olivine and pyroxene minerals, also preserve evidence of crystalline silicate dust being present in the early solar nebula around the time of planet formation (Scott & Krot 2003). The chondritic matrix of such meteorites also contains more refractory forms of the silicate grains. The crystalline nature of these minerals indicates they would have been formed at temperatures greater than 1200 K (Scott 2007). The presence of diopside was identified from spectral fits to infrared data collected from the Deep Impact encounter with comet 9P/Tempel 1 (Lisse et al. 2006), while diopside and other calcium-rich clinopyroxenes have also been identified in certain portions of the STARDUST sample return encounter with comet 81P/Wild ((Zolensky et al. 2006; Keller et al. 2006), often being found in association with low-Ca pyroxene (Zolensky et al. 2006). The presence of crystalline silicates in the Wild 2 samples indicates that this comet is not simply an assemblage of preserved ISM silicates, but rather is a mixture of presolar and Solar System materials. Indeed, the comet contains an

abundance of silicate grains that are much larger than those predicted by interstellar grain models, with many grains comprising high-temperature minerals that appear to have formed in the inner regions of the solar nebula (Brownlee et al. 2006). Their presence in a comet demonstrates that the formation of the Solar System included large scale mixing of materials within the early nebula (Brownlee et al. 2006).

O-rich asymptotic giant branch (AGB) stars are the main source of interstellar medium silicates (Draine 2003). According to condensation thermodynamics, the dust condensation sequence in these O-rich circumstellar regions is expected to be (Tielens 1990):

Al_2O_3; Alumina
1760 – 1300 K
↓
$Ca_2Al_2SiO_7$; Augite
1625 – 1400 K
↓
$MgAl_2O_4$; Spinel
1513 – 1360 K
↓
$CaMgSi_2O_6$; Diopside
1450 – 1100 K
↓
$CaAl_2Si_2O_8$; Anorthite
1360 – 1000 K

Mg_2SiO_4; Forsterite
1440 –1050 K
↓
$MgSiO_3$; Enstatite
1350 – 1040 K
↓
$(Mg,Fe)_2SiO_4$; Olivine
1100 – 950 K

The sequence starts with the nucleation of alumina (Al_2O_3) at about 1760 K, with the first silicate forming by a gas-solid reaction with the alumina to produce $Ca_2Al_2SiO_7$. As the temperature drops, further gas-dust reactions occur so that magnesium substitutes for aluminum to form $CaMgSi_2O_6$. The aluminium is released and the remaining alumina converted to spinel ($MgAl_2O_4$). As further cooling occurs

$CaMgSi_2O_6$ and spinel undergo a solid-solid reaction, producing the feldspar anorthite ($CaAl_2Si_2O_8$). At even lower temperatures ($\sim$1440 K) forsterite (Mg_2SiO_4) starts to condense out. Forsterite continues to form until the temperature has dropped to $\sim$1350 K, where it reacts with gaseous SiO to produce enstatite ($MgSiO_3$). Finally, at $\sim$1100 K reactions with gaseous iron convert some enstatite into fayalite (Fe_2SiO_4) and forsterite. Kinetics, however, also play an important role in determining which silicates form in AGB outflows. Depending on the density structure of the circumstellar region the condensation sequence will halt at different points. Thus, if the density drops rapidly with distance from the central star, the only dust to form will be various high temperature (i.e. close in) oxides (e.g. Al_2O_3, $CaTiO_3$, ZrO_2). However, if the densities are a little higher further out in the circumstellar shell, gas-grain reactions can take place allowing the formation of calcium aluminium silicates. And, if the density is high enough a little further out still, magnesium silicates may form as rims on the Ca-Al silicates. For magnesium silicates to nucleate directly requires high densities to persist out to longer radial distances. SiO_2 formation likely occurs as an intermediate step in the formation of silicates. In the ISM, crystalline grains are likely to only account for between 2.2% (Kemper, Vriend & Tielens 2004) and 5% (Li & Draine 2003) of the total silicate dust mass, with the majority of grains being amorphous. The crystalline fraction of silicates is higher for certain circumstellar environments, with typical crystalline mass fractions of 5-10% when compared to amorphous silicates (Draine 2003). Although the majority of silicate grains are believed to be Mg-rich forsterite and enstatite, observations in the mid-IR using SPITZER-IRS have shown crystalline diopside to be a minor constituent of the crystalline grains in the discs surrounding T Tauri stars (Olofsson et al. 2009). Diopside exhibits features at 9.28, 10.29, 11.43, 19.5, 20.6, 25.1, 29.6, 32.1, 33.9, 40.1, 44.8 and 65.7 μm (Koike, Tsuchiyama & Suto 1999; Koike et al. 2000). The main diopside feature is at $\sim$25 μm, however, because of a blended silicate complex near 23 μm, the 25 μm feature can sometimes be combined with this, making identification difficult. The blended silicate complex can also often exhibit a shoulder which can be misinterpreted as a 25 μm feature. Another characteristic diopside feature occurs at 20.6 μm, but is weak and difficult to detect. These factors

combine to make definitive estimates of the diopside contribution difficult in these environments. Both diopside and water ice have features near 60 μm. In certain evolved objects (Molster, Waters & Tielens 2002a; Dijkstra et al. 2003), the observed 60 μm band is broader than either of the individual H_2O or diopside bands and a good fit over the 60 μm region can be obtained using a calculated emission spectrum for diopside at 70 K and crystalline water ice at 40 K (Molster, Waters & Tielens 2002a; Kemper, Jager & Waters 2002, note that adding the carbonate dolomite can improve fits even further). Unfortunately, the low abundance of diopside in combination with blending of the short wavelength diopside bands with those of forsterite and enstatite again make it hard to unambiguously identify diopside based on only the shorter wavelength bands. Unambiguous identification of this mineral may only be possible in systems which have very cool dust (T <100 K), such as OH/IR stars and planetary nebulae (Molster & Kemper 2005). However, once injected in to the ISM, any crystalline silicates formed in circumstellar regions are thought to undergo amorphization by structurally disruptive processes such as ion implantation (e.g. Demyk et al. 2001, 2004; Jager et al. 2003b; Brucato et al. 2004; Bringa et al. 2007; Davoisine et al. 2008). It is this combination of amorphous and amorphised dust that would have eventually been incorporated into the early solar nebula and similarly incorporated in meteorites as complex, processed grains and in cometary bodies.

To understand the processes that acted upon these initially disordered, amorphous grains, laboratory studies of dust grain analogues can provide both physical insights and constraints on models of the environmental conditions that existed in the early solar nebula. Since the recognition that silicates are the predominant interstellar (and therefore presolar) mineral species they have been studied in great detail in the laboratory through analogues (Jager et al. 2003a; Kimura et al. 2011; Thompson & Tang 2001), to determine their physical properties in astronomical temperature and pressure regimes, and how their structure and optical properties change though thermal annealing and/or irradiation by ultraviolet or ion bombardment (Demyk et al. 2001, 2004; Carrez et al. 2002; Jager et al. 2003b). These studies have focused mainly on Mg-rich silicates; however, as outlined above, it has become increasingly apparent in recent

years that Ca-rich silicates and Ca/Mg silicates also contribute to the crystalline silicate dust mass in a number of astrophysical environments, including protostars (Chiavassa, Ceccarelli & Tielens 2005), star-forming regions (Onaka & Okada 2003) and the atmospheres of evolved stars (Molster, Waters & Tielens 2002a). Rietmeijer et al. (2008) showed, through laboratory condensation experiments, that the formation of $CaSiO_3$ and $(Ca/Mg)Si_2O_6$ is thermodynamically favourable in such environments, proposing that $CaSiO_3$ (wollastonite) once formed could subsequently react with enstatite, via the reaction $MgSiO_3 + CaSiO_3 = CaMgSi_2O_6$, to form diopside. Thus, not only are Ca-Mg silicates important in establishing a better understanding of the environmental conditions prevalent within the early stages of Solar System and in the other astrophysical environments in which they are found, they may also be important precursors to the possible formation of carbonates in such environments. One proposed mechanism for astrophysical carbonate formation, in the absence of liquid water, is the solid-gas reaction of calcium-rich silicates, such as $CaSiO_3$ and $CaMgSi_2O_6$ with gaseous H_2O and CO_2 (Rietmeijer et al. 2008). Understanding the behaviour of Ca-bearing silicates through laboratory analogues is, therefore, a key step in better understanding the behaviour of cosmic materials embedded in the early solar nebula and other astrophysical environments. In this chapter I discuss the results of a laboratory investigation into the structural evolution, due to thermal processing, of magnesium-calcium silicates, using SXPD.

6.2 Experimental

6.2.1 Sample preparation

Amorphous magnesium-calcium silicates of composition $Mg_{(x)}Ca_{(1-x)}SiO_3$, where x = 0, 0.2, 0.5, 0.8 and 1, were produced using a sol-gel method, as described previously in Chapter 5 and in the paper by Thompson et al. (2012a). Metal salts Na_2SiO_3, $CaCl_2$, and $MgCl_2$ were dissolved separately in 18.2 MΩ deionised water, at room temperature,

to produce 0.1 molar solutions. They were then combined in stoichiometric ratios to form gels with the desired Mg/Ca compositions via the reaction:

$$Na_2SiO_3 + CaCl_2 + MgCl_2 \rightarrow MgCaSiO_3 + 2NaCl \quad (6.1)$$

The gels were dried under vacuum at 50–80°C for approximately 1 h. The resulting powder samples were then removed and immediately stored under argon in sealed glass vials. Detailed discussion of the production process and characterisation of the amorphous $CaSiO_3$ end member can be found in Thompson et al. (2012) and in Chapter 5. The samples produced using this method are highly amorphous, fine-grained white powders. Individual grains could not be resolved using an SEM (Hitatchi TM1000), suggesting that they are approximately a few micrometers in size.

6.2.2 Data collection

Synchrotron X-ray powder diffraction measurements were performed on Beamline I11 and I12 at Diamond Light Source. In situ variable temperature measurements (room temperature [RT] to 1300 K) were performed on beamline I11 and were supplemented by ex situ diffraction data obtained on beamline I12 on samples that had been annealed offline over a similar temperature range to the in situ samples, for approximately 1 h at each temperature. For the in situ measurements, a 90° arc position sensitive detector (PSD), designed for fast data collection, was used. Powdered samples, loaded into 0.7 mm quartz glass capillaries were heated by a Cyberstar hot air blower and Eurotherm temperature controller. Both the temperature of the hot air blower and operation of the detector are integrated into the beamline data acquisition and control system, allowing data to be collected in real time during the heating of the samples. The ramp rate between temperature steps was 10 K min^{-1}, with a stability at temperatures above approximately 400 K of <1 K. At each temperature step, once the controller had settled at the programmed set point temperature, the sample was allowed to equilibrate for a further 2 minutes before data collection was automatically triggered.

Diffraction data were then collected between 300 and 1300 K, with 20 s count times per temperature step using the PSD and 15 keV monochromatic X-rays ($\lambda = 0.8245590$ Å).

For the data collected on I12, samples were loaded into 2 mm Kapton capillaries and measurements were acquired using 87.4 keV monochromatic X-rays ($\lambda = 0.141834$ Å), calibrated using a CeO_2 standard) with multiple (720) 4 s exposures per sample using a large pixellated 2D area Pixium detector (Daniels & Drakopoulos 2009, CsI scintillator on amorphous Si substrate;), offset from the beam centre such that total scattering (TS) data were recorded (i.e. scattering out to high values of the X-ray scattering wavevector, Q, as described in Section 4.4.2. For the purpose of this chapter only the diffraction component of the measured TS signal is considered and has been scaled to match the 2θ angular range of the I11 data. Due to the high X-ray energy used, all the diffraction features were confined to low angle, such that no angular intensity correction was necessary to compensate for the flat detecting surface. Prior to the I12 X-ray measurements, the ex situ samples were annealed at five temperature steps between 323 and 1173 K using the Carbolite furnace. Fourier transform infrared (FTIR) spectra of the unprocessed, as-prepared samples were collected at ambient temperature using a Bruker Vertex 70 spectrometer equipped with a Harrick diamond crystal ATR accessory.

6.3 Results

6.3.1 FTIR characterisation of initially amorphous silicates

The powdered samples were initially characterised using FTIR spectroscopy in order to confirm their amorphous silicate nature. Fig. 6.1 presents a comparison of the IR absorption spectra of the five sample compositions, taken at room temperature. The main feature to observe across all compositions is the broad, featureless 10 μm bump, indicative of amorphous silicates, and observed in most astronomical absorption spectra in O-rich environments.

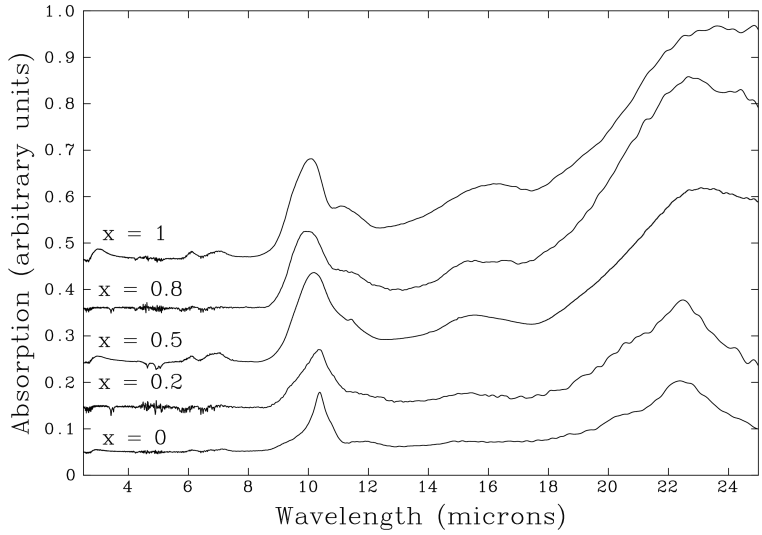

Figure 6.1: FTIR spectra of the five amorphous samples of $Mg_{(x)}Ca_{(1-x)}SiO_3$ at 323 K, where $x = 0$ is the pure Ca endmember and $x = 1$ is the pure Mg endmember.

It can be seen that, with increasing Mg content, a broad shoulder appears on the redward side of the 10 μm feature, at $\sim$11.2 μm and is attributed to the tetrahedral Si-O stretch modes of SiO_4 (e.g. forsterite), explaining why it is only seen in Mg-rich samples. There is also a broad feature, between 14 and 18 μm, only present in the spectra of compositions containing Mg ($x > 0$) which similarly strengthens with increasing Mg content.

6.3.2 Thermal processing

Fig. 6.2 shows individual sequences of SXPD powder patterns for all five of our initially amorphous samples. Scans were taken at ambient temperature for each composition prior to heating. Note the broad, weak features at $\sim$15.6° and $\sim$26° 2θ, present in all but one of the samples. Also note the shift of the 15.6° feature to lower 2θ with increasing temperature. Peak shifts to lower 2θ values during in situ annealing are indicative of thermal expansion. For the $x = 1$ composition there appears to be two distinct expansion phases, as shown in Fig. 6.3, determined by fitting the the peak

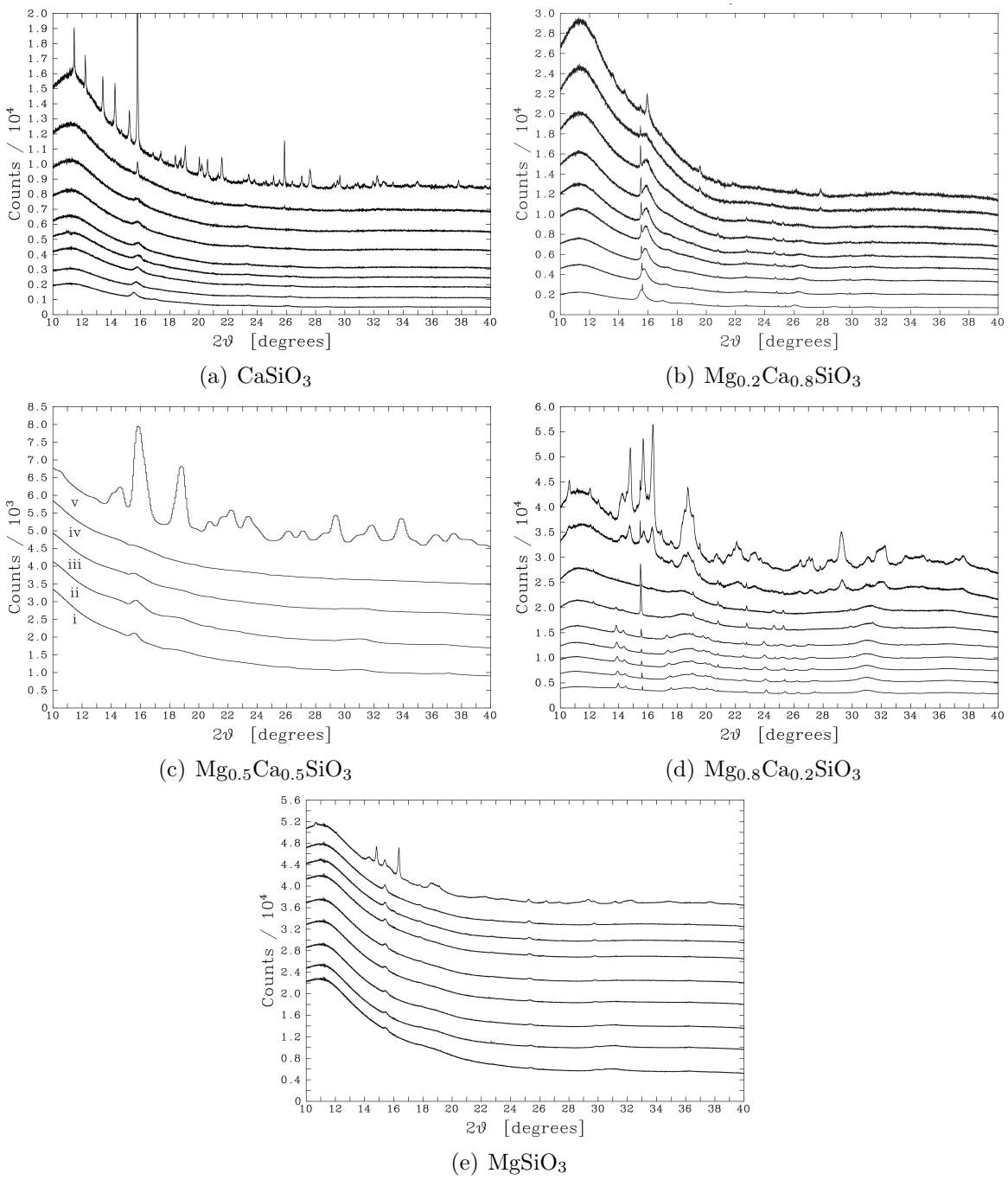

(a) $CaSiO_3$

(b) $Mg_{0.2}Ca_{0.8}SiO_3$

(c) $Mg_{0.5}Ca_{0.5}SiO_3$

(d) $Mg_{0.8}Ca_{0.2}SiO_3$

(e) $MgSiO_3$

Figure 6.2: Synchrotron X-ray powder diffraction patterns for each sample composition, showing the evolution of structure with thermal annealing. a,b,d and e scans were taken on beamline I11, with the first scan at room temperature (295 K) and subsequent scans from 473 K up to 1173 K in 100 K steps. c is data from I12, annealed offline and powder patterns taken at RT. Labelled as follows (i) 323 K, (ii) 573 K, (iii) 723 K, (iv) 873 K and (v) 1173 K. Patterns are offset vertically for clarity with temperature increasing upwards.

position of the 121 peak at each temperature step.

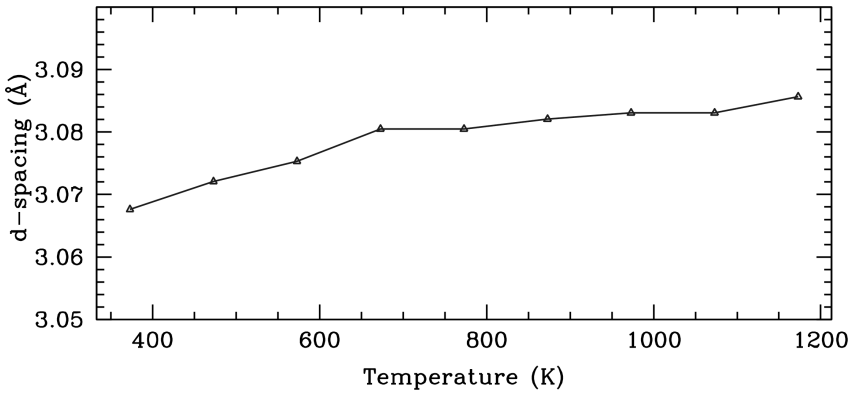

Figure 6.3: Plot of d-spacing against temperature for the 121 peak at $\sim 15.6^\circ$ 2θ in Fig. 6.2e .

The first, from 373 K to 673 K where a thermal expansion coefficient (α) of 41.9 ($\pm$ 4.1) $\times 10^{-6}$ K^{-1} is obtained, and the second (T >673 K), from which a value, α = 11.4 ($\pm$ 3.5) $\times 10^{-6}$ K^{-1} is obtained. It is possible this is due to a change in phase at 673 K as the sample begins to crystallise. The latter value of α = 11.3 ($\pm$ 3.5) $\times 10^{-6}$ K^{-1} is in agreement with the published value for the mean thermal expansion coefficient of forsterite, $\alpha = 9.9 \times 10^{-6}$ K^{-1} (Fei 1995).

The initial amorphous structure of the samples remains stable at lower temperatures (below 973 K), exhibiting little change in structure. The only exception here is for the sample of composition $x = 0.8$, as can be seen in Fig. 6.2(d), this sample shows some initial crystalline structure, represented by the sharp, but relatively weak, Bragg reflection peaks, on the initial scan at ambient temperature. Comparison of these Bragg features with the International Centre for Diffraction Data (ICDD) PDF4+ database (2011 edition) showed these to be a mixture of aragonite and calcite $CaCO_3$ phases, likely formed as minor contaminants by atmospheric contact during preparation. The remaining samples, manufactured in an identical method, do not show such features. On heating, these features gradually weaken, and are completely removed upon crystallisation of the sample; this is consistent with their identification as carbonate since

aragonite transforms to calcite at 693 K and calcite breaks down to CaO and CO_2 gas above 873 K. In particular we note that there is no evidence for CaO diffraction peaks as the carbonate peaks weaken. As the temperature approaches 973 K, the samples begin to crystallise, showing the rise of weak features prior to full crystallisation. The observed crystallisation temperatures do appear to show some variation with composition, however due to the relatively coarse temperature increment it is not possible to draw any quantitative conclusion.

6.3.3 Rietveld refinement

Rietveld refinement (Rietveld 1969) of the X-ray data for the crystalline end products for each of the five sample compositions was performed using the TOPAS-academic software package (Coelho 2007). The starting composition had a substantial effect on the mineral phases produced upon crystallisation, with the majority yielding multiple phases. Crystalline mineral phases produced include diopside ($MgCaSi_2O_6$), wollastonite ($CaSiO_3$), enstatite ($MgSiO_3$), forsterite ($MgSiO_4$) and silica (SiO_2).

Fig. 6.4 shows two of these refinements for the compositional end-members, $x = 0$ ($CaSiO_3$) and $x = 1$ ($MgSiO_3$) in situ, at a temperature of 1173 K. For the pure-Ca end member, wollastonite gave a good fit to the data (Fig. 6.4(a)), with refinement R-factor, $R_{wp} = 2.501$ % and goodness of fit (Gof) factor =1.494. A detailed discussion of nature of these parameters in the context of Rietveld refinement has been given in Section 4.4.1.2 and in McCusker et al. (1999). The refined lattice parameters are shown in Table 6.1, matching very well to published (ambient temperature) values for wollastonite given in the ICDD database.

The final end member, $MgSiO_3$ is found to contain forsterite and enstatite, as well as SiO_2, providing a good fit with refinement r-factor $R_{wp} = 0.744$ % and Gof = 1.974. Fig. 6.4(b) shows the calculated fit to the observed data. Weight percentages of each phase, derived from the refinements, are also given, showing that rather than enstatite, as would possibly be expected from the stoichiometric composition, forsterite is the dominant mineral phase in the fit, followed by enstatite and silica (SiO_2) in

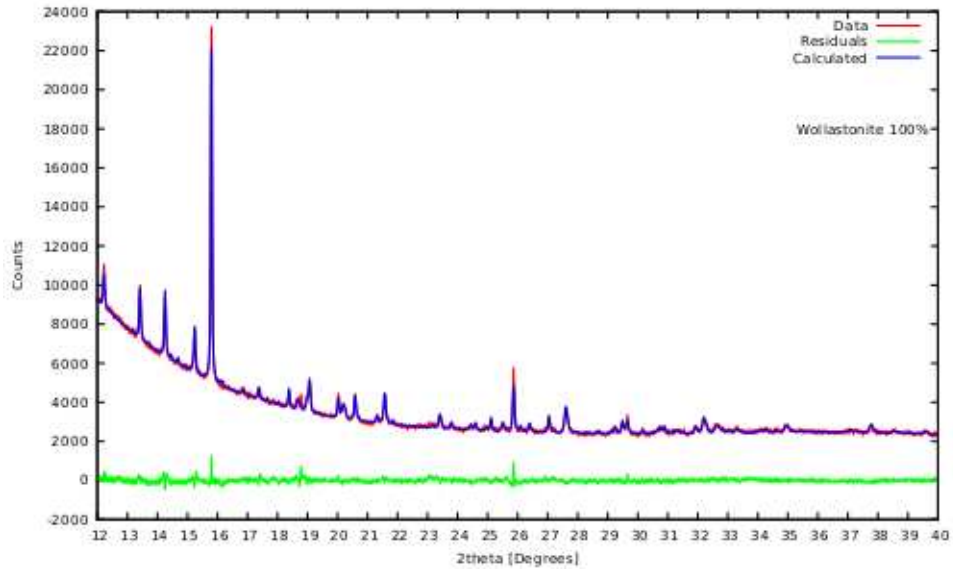

(a)

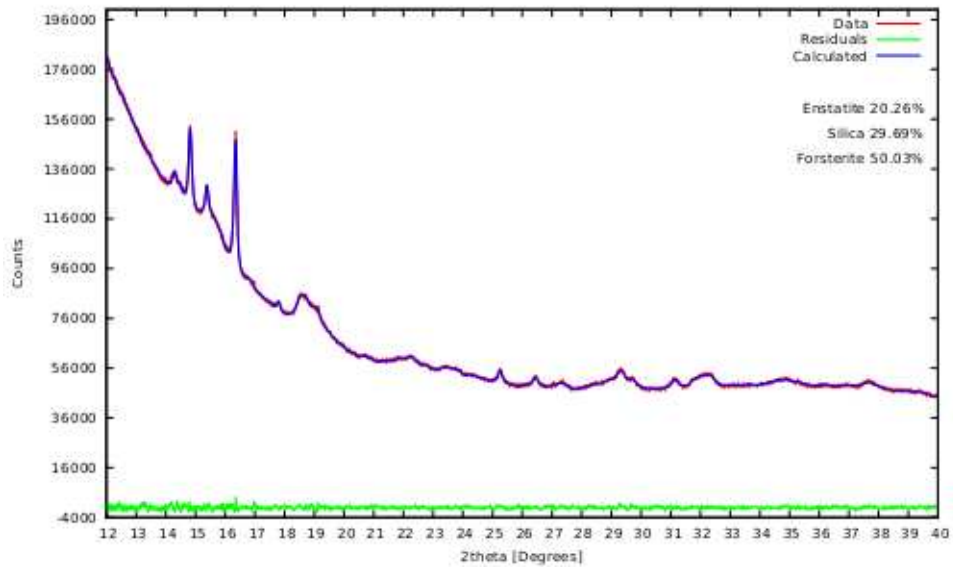

(b)

Figure 6.4: Rietveld refinements of the X-ray powder diffraction data obtained at 1173 K on Beamline I11 for $CaSiO_3$ and $MgSiO_3$ samples. a) $CaSiO_3$ fit with wollastonite ($CaSiO_3$), giving agreement R-factor of $R_{wp} = 2.54$ % and a Gof of 1.494. b) $MgSiO_3$ fit with enstatite, forsterite, and silica with percentages as shown. Agreement R-factor of $R_{wp} = 0.744$ % and Gof of 1.974 are obtained. The upper curves show the calculated fit to the data, and the residual curves are shown at the bottom.

Space Group: P-1			
Published Lattice	a/Å: 7.9258(4)	b/Å: 7.3202(4)	c/Å: 7.0653(4)
Parameters	α/°: 90.055(3)	β/°: 95.217(3)	γ/°: 103.426(3)
Refined Lattice	a/Å: 7.9918(3)	b/Å: 7.3731(1)	c/Å: 7.0849(1)
Parameters	α/°: 90.085(4)	β/°: 94.898(2)	γ/°: 103.314(6)

Table 6.1: Published and refined lattice parameters for wollastonite ($CaSiO_3$)

almost equal quantities. The formation of forsterite as the first crystallising mineral phase was previously reported by Rietmeijer, Nuth & MacKinnon (1986) during the annealing of Mg-SiO smokes and was attributed to the minimisation of surface free energy. This has more recently been reported in annealed amorphous $MgSiO_3$ grains by Thompson & Tang (2001) and Roskosz et al. (2009), while Carrez et al. (2002) also observed forsterite formation resulting from the irradiation of $MgSiO_3$ glasses with 300 keV electrons.

For the intermediate compositions the mineral phase diopside ($CaMgSi_2O_6$) is produced upon crystallisation, alongside the pure phases enstatite and wollastonite, due to the interaction of the magnesium and calcium, becoming the dominant phase as the composition approaches $x = 0.5$. Table 6.2 presents the published and refined parameters for the dominant diopside phase, taken from the refinement of the composition $x = 0.5$. A batch refinement performed on data over a temperature range of 1143 to 1223 K for the $x = 0.2$ sample also shows that, after the initial crystallisation of the sample at 1143 K, the physical structure of the sample continues to change with further increase in temperature. Fig. 6.5 shows the evolution of the two mineral components with temperature for the composition $x = 0.2$. This indicates that upon crystallisation both wollastonite and diopside are present, however with continued heating the weight percentage of each phase evolves, with wollastonite becoming more dominant.

In the $x = 0.8$ sample magnesium now dominates and therefore the magnesium-rich silicate enstatite begins to crystallise and is required alongside diopside and wollastonite to produce a good fit to the experimental data. While some wollastonite would be expected in this sample due to the remaining calcium, the weight percentage

Space Group: C 2/c			
Published Lattice	a/Å: 9.752(1)	b/Å: 8.9259(8)	c/Å: 5.254(1)
Parameters	$\alpha/°$: 90	$\beta/°$: 105.83(1)	$\gamma/°$: 90
Refined Lattice	a/Å: 9.727(6)	b/Å: 8.949(6)	c/Å: 5.235(3)
Parameters	$\alpha/°$: 90	$\beta/°$: 106.23(5)	$\gamma/°$: 90

Table 6.2: Initial and refined lattice parameters for the diopside mineral phase.

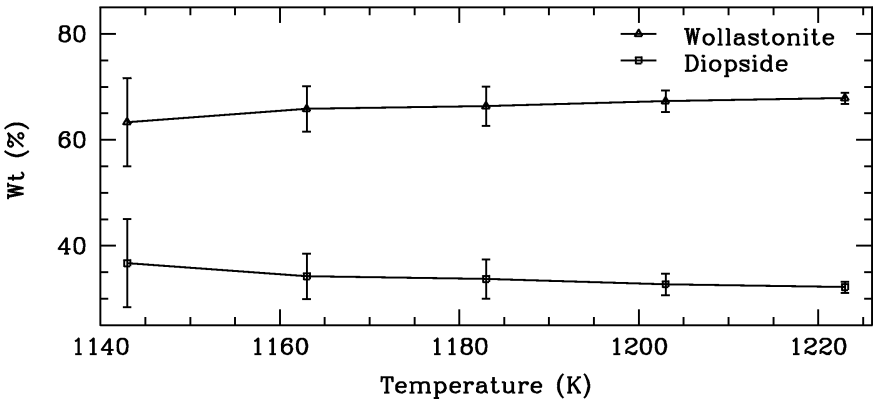

Figure 6.5: Evolution of the wollastonite and diopside relative phase fractions during crystallisation of $Mg_{0.2}Ca_{0.8}SiO_3$.

of 45% determined be the refinement is slightly higher than would be expected. It is believed that the excess wollastonite present within the $x = 0.8$ sample arises from the $CaCO_3$ contaminant discussed previously in Section 6.3.2. As this would have originally formed via the interaction of $Ca_{1-x}SiO_3$ with atmospheric CO_2 ($CaSiO_3 + CO_2 = CaCO_3 + SiO_2$), calcination during annealing could result in CaO, which could then react with silica (SiO_2) forming additional wollastonite. However, this cannot be confirmed or disproved by the present data as, while diffraction peaks due to CaO were not observed, the 100 K temperature step may not have been sufficient to capture any such intermediary reaction.

The crystallisation of forsterite in the Mg-rich end-member $x = 1$, while not consistent with the defined stoichiometry of the initial sample, is consistent with the previous FTIR data, suggesting the increasing presence of SiO_4 domains with increasing

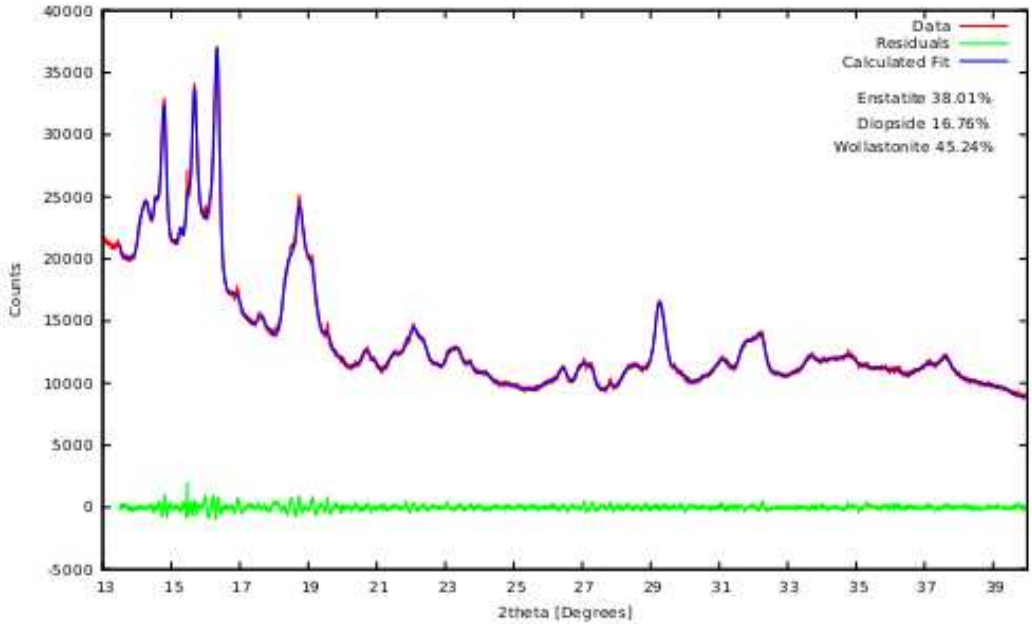

Figure 6.6: Rietveld refinement of sample composition x = 0.8, at 1173 K, fit with R-factor R_{wp} = 1.339 % and Gof = 1.682. The top curve shows the calculated fit, and the residuals of the fit are shown on the lowermost curve.

magnesium content. This also agrees with the findings reported in Thompson & Tang (2001) for sol-gel produced Mg-rich samples. It is interesting to note that forsterite is not found to be a final crystalline component in any of the other samples which contain calcium. This could suggest that the presence of calcium ions within the material leads to the preferential crystallisation of enstatite ($MgSiO_3$) over forsterite ($MgSiO_4$), or it could be the case that a significant fraction of the magnesium is initially incorporated into the diopside phase, followed by enstatite, and therefore the amount remaining to form forsterite is not significant enough to be fitted by the refinement process.

Values for crystal size obtained from the refinements, range from 1.33 μm to 9.98 μm and are comparable to the larger dust grain sizes – compared to the ISM – likely to have been present within the early Solar System (Artymowicz 1997; Shuping et al. 2006; Blum & Wurm 2008) and with the 1 – 300 μm particle sizes returned by the Stardust sample return mission to Comet 81P/ Wild 2 (Brownlee et al. 2006)

6.4 Discussion

Nuth & Johnson (2006) used the predominance of Mg-rich crystalline silicates over Fe-rich ones in cometary spectra to argue that the main route to formation of crystalline silicate minerals in the solar nebula was simple prolonged thermal annealing, rather than short lived thermal spikes due to shock events. Annealing of the samples to a maximum temperature of 1173 K was therefore performed to investigate the temperature conditions necessary to crystallise initially amorphous silicate and to produce crystalline phases similar to those found in comets, IDPs, meteorites and CAIs. It is found that for Mg-Ca silicates, temperatures exceeding 973 K are required in order to trigger structural changes noticeable with SXPD. Full crystallisation does not occur until a temperature of at least 1073 K, with certain compositions not crystallising completely until 1173 K. However, the in situ samples were only held at each temperature for ∼10 minutes which, it could be argued, may not have been long enough for the crystal phase formation and/or growth processes to complete. Colangeli et al. (2003) studied the annealing of $CaMgSi_2O_6$ smokes in the laboratory and found that their samples transformed to fully crystalline diopside within 1 hour of heating at 1050 K, which is in broad agreement with the short timescale for crystallisation that we find at 1173 K for the in situ measurements and suggests that the results obtained from the ex situ samples, annealed at temperature for only 1–2 hours, are comparable to the in situ ones. The full crystallisation of the samples at 1173 K occurred within minutes of reaching temperature; however, the initial onset of crystallisation observed at 873 K suggests that exposure at lower temperatures would also lead to crystallisation of the sample over an extended period of time. Brucato et al. (2002) similarly conducted thermal annealing experiments on initially amorphous forsterite grains, produced using the laser ablation method, at a temperature of 973 K and they found that crystallisation of the sample occurred after 72 hours at temperature. Experiments on materials of similar composition have lead other researchers to draw similar conclusions (Fabian et al. 2000; Jager et al. 2003a).

In order to match the crystalline nature of the grains observed within cometary

bodies, such as 9P/Tempel 1 (Lisse et al. 2006) and 81P/Wild2 (Zolensky et al. 2006; Keller et al. 2006), and IDPs (Zolensky 1987; Zolensky & Barratt 1994; Rietmeijer 1999; Papike 1998), Ca-Mg silicate grains of pre-solar amorphous composition would have to reside within the extreme inner regions of the solar nebula disc at R <3 AU from the central object, where temperatures would have been in excess of 1000 K (Boss 1993, 1996). The modelled temperature profiles produced by Boss (1993) are based on values inferred for typical solar-type systems, with a disc mass of $0.02M_{\odot}$ and a mass accretion rate of $\sim 10^{-6}$–$10^{-5} M_{\odot}$ yr^{-1}. This infers a temperature profile for the early solar nebula, indicating a disc midplane temperature of 1000 K within a radius of ∼2.5 AU, with temperatures quickly falling to ∼160 K at ∼4.5 AU. This is also in general agreement with the disc model proposed by Cassen (1994) and Woolum & Cassen (1999). In the solar nebula, grains would have moved inwards towards the early Sun due to gas drag on loose aggregates in Keplarian orbits, or due to the slow migration of gas and dust through the disc on its way to accretion in the protostar. In relatively quiescent conditions, such inward migrations would have taken many orbital periods and grains would have experienced a monotonic temperature increase as they moved inwards. In this scenario Ca-bearing silicate grains are likely to have spent many years at temperatures in the range 1000 – 2000 K and should have had enough time to fully crystallise. In more turbulent conditions, where residence times at higher temperatures may have been limited to one or two orbital periods and based on the results of our annealing experiments and the discussion of crystallisation timescales above, Ca-bearing silicate grains can still be expected to have fully crystallised before being transported outwards to the comet-forming zones or incorporated into other objects.

6.5 Conclusions

The structural evolution by thermal annealing of amorphous Ca-Mg silicates has been investigated by in situ SXPD. We find that rapid annealing to temperatures exceeding

1173 K successfully produces multiple crystalline silicate phases, including diopside, forsterite, enstatite, and SiO_2, all of which are known mineral components within cometary bodies, such as comets 81P/Wild 2 (Zolensky et al. 2006; Bridges et al. 2012) and Hale-Bopp (Wooden et al. 1999) and chondritic meteorites (Scott & Krot 2003). The Ca-pure endmember crystallises directly to wollastonite, while for mixed compositions of $Mg_xCa_{1-x}SiO_3$ with $0 < x < 0.5$, a two-phase end product is produced comprising crystalline diopside and wollastonite. For $x = 0.5$, wollastonite is absent from the resulting crystalline phases, which are composed of enstatite, diopside, and silica. However, for $x = 0.8$, wollastonite is once again observed, along with diopside and enstatite, although it should be noted that the wollastonite is likely the result of carbonate contamination. Finally, for the Mg-pure $x = 1$ endmember, a combination of forsterite, enstatite, and silica is found. With the exception of the Ca-pure endmember, all of the amorphous starting compositions exhibit distinct phase separation on crystallisation. While diopside is known to be present in cometary bodies, wollastonite has so far not been identified. The absence of a wollastonite phase could provide an indicator of the maximum annealing temperatures and/or Ca content on such bodies as only certain compositions were observed to crystallise wollastonite, which, based on a conservative interpretation, may suggest a value of x of approximately 0.2 or less.

Equilibrium phase formation is known to be dominated by slow reaction kinetics (Carlson 1988) which yield an array of pyroxenes with similar physical properties, as defined by the MgO-CaO-SiO equilibrium phase diagram (e.g., Boyd & Schairer 1964; Carlson 1986, 1988). While the final crystalline products formed here do not contradict what is known regarding the solid solid phases produced, we cannot rule out the possibility that different annealing rates lead to the formation of different phase combinations. It is believed that the final phases and the relative proportions of each phase produced in this work are in part due to the fast ramp rate and short dwell time at each temperature and the amorphous starting nature of the materials.

By extension of the analysis already developed by us (Thompson et al. 2012a) regarding thermally induced structural changes in the amorphous $MgSiO_3$ endmember, the formation of distinct crystalline phases may well result from the intertetrahedral

connectivity within the mixed Ca/Mg amorphous starting material being more realistically described by a domain structured model rather than the continuous random network model traditionally used for glassy silicates. In this case, the amorphous silicate comprises various distinct regions rich in one or other of the possible Si-O tetrahedral connectivities (i.e., SiO_2, Si_2O_5, SiO_3, Si_2O_7, SiO_4) that are themselves interconnected via a continuous, but more random, network of tetrahedral connections. If such models translate to cosmic silicate grains, then based on the temperature gradients of current disc models, amorphous Ca-bearing silicate grains entering the solar nebula from the giant molecular cloud that collapsed to form the Sun must have reached the inner regions of the solar nebula at a radius of R <3 AU to experience the temperatures required to induce crystallisation, but could potentially have annealed relatively quickly.

7 Carbonate formation through solid-gas interaction of amorphous silicates and gaseous CO_2 at elevated pressures.

7.1 Introduction

This chapter presents the results of in situ SXPD measurements, on Beamline I11, aiming to understand the interaction of Ca- and Mg- rich silicates with gaseous CO_2 under astrophysical conditions. Beamline I11 is capable of simulating a variety of environmental conditions, allowing data to be collected in real time as the temperature and pressure conditions are altered remotely. This provides us with an experimental means to simulate conditions in astrophysical environments in an attempt to understand the mechanism of formation of carbonate minerals, whose formation in such environments is still a matter of uncertainty.

The first suggestion that carbonate minerals were present in circumstellar dust was made by Kemper, Jager & Waters (2002), who identified a strong emission band at 92μm in the IR spectra of protoplanetary nebula (PN) NGC 6302, as being due to carbonates. This was then followed by further discoveries of this feature in other environments, including protostars (Ceccarelli & Caux 2002; Chiavassa, Ceccarelli & Tielens 2005). Kemper, Jager & Waters (2002), when attempting to determine the most likely carriers of the $\sim$90μm feature in the observed spectrum of NGC 6302, considered a selection of carbonate phases containing cosmically abundant elements. These included calcite ($CaCO_3$), magnesite ($MgCO_3$), siderite ($FeCO_3$), ankerite ($CaFe(CO_3)_2$) and dolomite ($CaMg(CO_3)_2$). They found that calcite is the only phase to have a strong feature in the 90-micron region, and this fits very well to the observed spectra, although it was also determined that dolomite contains a strong band in the IR at 62μm which is also required to produce a good fit to the spectra. They find that magnesite and siderite do not have strong Far-IR bands and therefore their presence in this case cannot be determined.

We therefore focus our experimental study on the amorphous silicate precursors that would lead to the formation of calcite and dolomite upon carbonation, in particular $CaSiO_3$, $MgCaSiO_3$ and for completeness we also look at $MgSiO_3$. A number of formation routes have been suggested in order to understand the presence of carbonates in environments such as these that are devoid of liquid water. These have been discussed in much greater detail previously in Section 2.6.2. Although these formation mechanisms are valid in theory, very little has been done so far to verify these mechanisms experimentally. Toppani et al. (2005) report the experimental formation of carbonates alongside amorphous silicates, through non-equilibrium condensation of a silicate-rich gas (of solar composition; MgO, SiO_2, Al_2O_3 and CaO) in a H_2O-CO_2 vapour and subsequent thermal annealing of the condensates which leads to the production of Ca-rich carbonate nanocrystals. However, Rietmeijer et al. (2008) believe that this two-step process is unlikely to be very efficient. They have shown, through the condensation of silica-saturated vapour (Ca-SiO-H_2-O_2), that amorphous solids of stoichiometric composition, namely $CaSiO_3$, can be formed directly and therefore support the proposed formation mechanism of carbonate grains whereby solid-gas carbonation of amorphous silicate grains can occur through the reaction:

$$CaSiO_3(\text{solid}) + CO_2(\text{gas}) \longrightarrow CaCO_3(\text{solid}) + SiO_2(\text{solid}) \tag{7.1}$$

It is this formation mechanism that we focus on within this study. Recently, Garenne et al. (2013) published a study of the gas-solid carbonation of an amorphous Ca-silicate hydrate, using IR spectra and a specially designed IR Cryocell, to determine additional formation routes of carbonates on the Martian surface. This experiment was performed at a pressure of 1 bar at 25°C to simulate Martian conditions and it was found that significant carbonation of the sample was observed after 8 hours. They suggest that the rapid reaction time indicates that the chemical stability of a material has a large influence on the efficiency of carbonation. However, we believe that we are the first to study this reaction in amorphous silicate grains that have been specially synthesised as cosmic dust analogues and the first to perform these experiments using SXPD.

7.2 Experimental

In situ carbonation of amorphous Ca-rich silicates was performed on Beamline I11 using a low pressure capillary gas cell (see Section 5.4.1.2) to expose the amorphous, powdered silicate samples to gaseous CO_2. The synthetic cosmic dust samples were produced using a sol-gel method based on the process of Day (1976) using $MgCl_2$ and $CaCl_2$ as the sources of magnesium and calcium, along with $NaSiO_3$ as the silicate base to form samples having a composition of $Mg_{(x)}Ca_{(1-x)}SiO_3$ where $0 \leq x \leq 1$. The method has been described in detail in Section 5.2 and Thompson et al. (2012a). The experimental setup of the experimental hutch (EH1) is shown in Figure 7.1, with the major components labelled. A Cyberstar hot air blower (ramp rate = 10 K/min) was used to heat the samples to a maximum temperature of 1273 K, in order to simulate temperatures and thermal cycling experienced by dust grains in circumstellar environments. Additional information regarding the temperature steps covered and the frequency of data collection is given individually for each sample in the Results section (7.3). The temperature reading provided by the hot air blower has an error of ±0.1 K, however this is measured at the tip of the hot air blower and not at the sample, therefore the actual temperature at the sample position is believed to be within a few degrees of the stated temperature. The samples were loaded into 0.5mm quartz capillaries under an Argon atmosphere inside a glove bag and mounted onto the sample stage of the diffractometer. An empty Quartz capillary was scanned prior to obtaining sample data to allow for background subtraction. SXPD data were primarily obtained using the PSD (20s scan time), to allow for time-sensitive measurements. Diffraction patterns were acquired with the PSD in two positions, 0.25° 2θ apart, in order to compensate for gaps between detecting modules, and the two data sets were then automatically merged by the data acquisition software.

Ideally, to ensure the best particle averaging the capillary would be spinning during data collection, however this is not possible with the gas cell setup and therefore to minimise effects from preferred orientation the gas cell is oscillated on the θ circle by ± 10°. PSD data were collected at regular intervals as the sample was put under

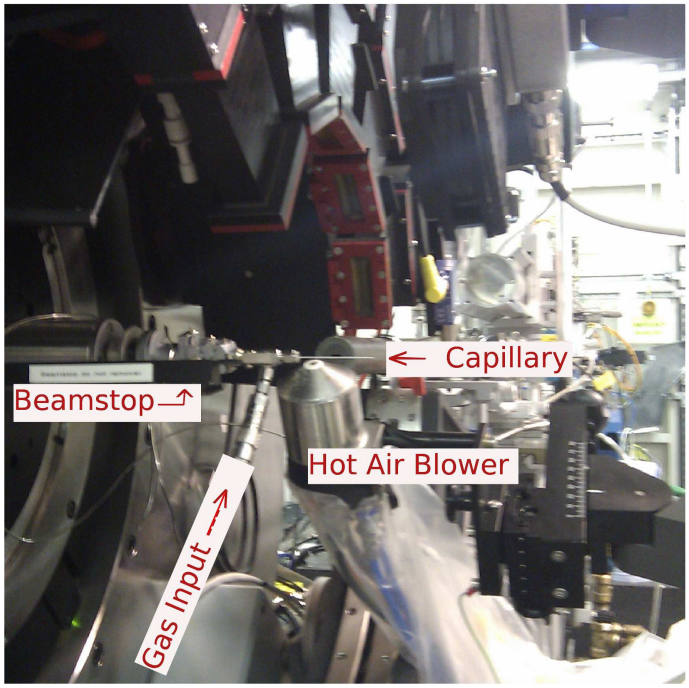

Figure 7.1: Experimental setup on the Beamline I11, with the main components labelled, including the location of the capillary, the hot air blower and the gas input.

Figure 7.2: Gas control system on I11. Controls the pressure of gas incident on the sample. Allows a vacuum of 3.1×10^{-2} bar and maximum pressure of 100 bar (Parker et al. 2012).

vacuum and then exposed to CO_2, effectively providing real-time information on the effect of the changing conditions. As the temperature of the sample was increased, scans were taken at set temperature steps throughout the process. The samples were exposed to CO_2 up to a maximum pressure of 1 bar, using a manually-operated gas control system (Figure 7.2; Parker et al. 2012). The wavelength, calibrated using NIST SRM640c standard Si powder, was 0.82559Å.

7.3 Results and Analysis

7.3.1 $CaSiO_3$

SXPD data were collected as a function of temperature for a sample of composition $x = 0$ ($CaSiO_3$), starting from room temperature (RT; 295K) up to 1273 K in steps of 100 K with a CO_2 gas pressure of 0.7bar. The temperature was held for 10 minutes at each step and four, 20s scans were taken during this time. This gave the sample a total CO_2 exposure time of 4 hours. Figure 7.3 presents the SXPD PSD data obtained across this temperature range, where the lowermost pattern was obtained at RT prior to exposing the sample to CO_2, the second pattern was obtained at RT after the injection of CO_2 and each pattern thereafter was obtained during the exposure of the sample to CO_2, with the temperature increasing in steps of 100 K from 373 K. Two SXPD patterns are shown per temperature (one at the start and end of each 10 minute hold) and the uppermost scan is the final measurement of the sample at 1273 K. The high background of the scans is due to the quartz glass capillary, and the change in the background intensity between 773 K and 873 K is due to a slight adjustment in the experimental parameters between scans, not due to the sample.

At ambient temperature and pressure the SXPD pattern is typical of an amorphous material, exhibiting no sharp Bragg reflections. There are two very broad, weak features at $15.554 \pm 4.0\times10^{-3}$ 2θ and $26.186 \pm 3.7\times10^{-2}$, whose positions are close to those of the strongest Bragg peaks in the calcium carbonate phase, calcite. The two

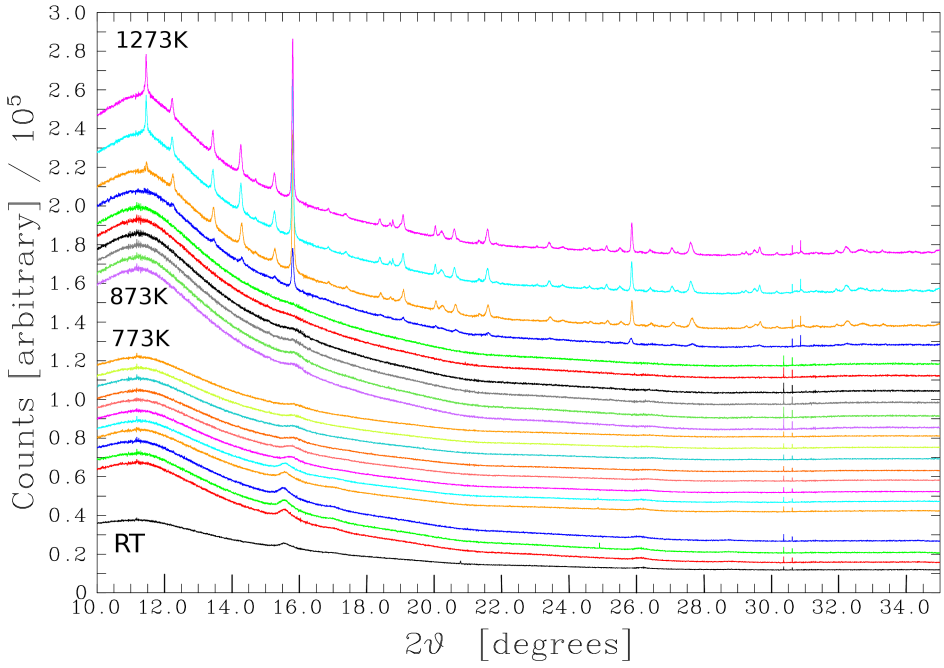

Figure 7.3: Selected in situ SXPD PSD patterns for $CaSiO_3$ exposed to CO_2 at increasing temperature. Temperature is increasing upwards with the lowermost scan representing the sample at RT and the uppermost scan representing 1273 K, and two scans per temperature throughout.

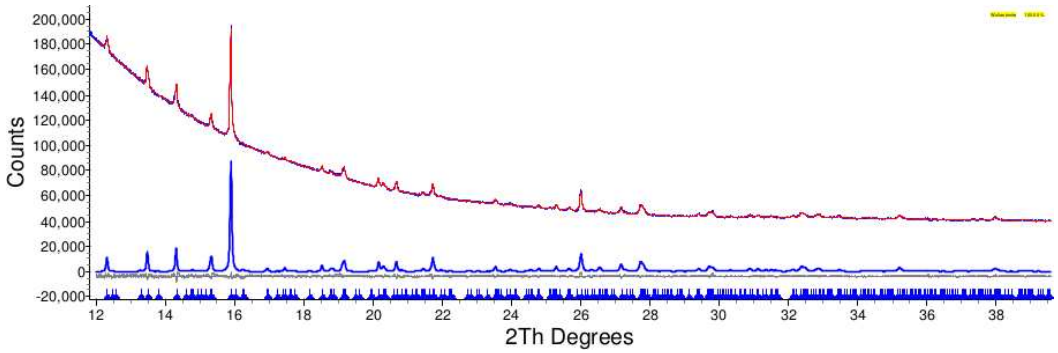

Figure 7.4: Rietveld refinement of crystalline $CaSiO_3$ at 1273 K. The experimental data is in blue, while the fit is in red and the difference is shown in grey. An agreement factor of $R_{wp} = 0.768$ % was obtained.

sharp features at $\sim 30^\circ$ 2θ are due to a detector error. It is apparent from the figure that very little changes between RT and 973 K, no additional features arise that would suggest that a reaction was occurring and the already weak carbonate features only get weaker with increasing temperature. In the two PSD patterns measured at a temperature of 973 K the carbonate feature is no longer visible, having become unstable at high temperature. The onset of crystallisation occurs suddenly as the temperature reaches 1173 K and crystallisation continues, with Bragg peaks growing in intensity, as the sample is held at temperature. A final increase in temperature to 1273 K does not appear to have any further effect on the sample, as the intensity and position of the Bragg peaks remain consistent with the final pattern obtained after 10 minutes at 1173 K. A Rietveld refinement of the final crystalline phase was performed using the software package TOPAS Academic (Coelho 2007), using a structural model for Wollastonite ($CaSiO_3$) obtained from the ICDD database. The resultant fit is shown in Figure 7.4 with initial and refined lattice parameters presented in Table 7.1. This is comparable to the final annealed phase seen previously for un-dosed $CaSiO_3$ in Chapter 6, suggesting that the presence of CO_2 does not have an effect on the final crystalline material produced when annealing at temperatures > 1273 K.

After annealing, the sample was cooled to 923 K and left on the beam overnight

Space Group: P-1			
Published Lattice	a/Å: 7.925(4)	b/Å: 7.320(4)	c/Å: 7.065(4)
Parameters	α/°: 90.055(3)	β/°: 95.217(3)	γ/°: 103.426(3)
Refined Lattice	a/Å: 7.9391(3)	b/Å: 7.3380(1)	c/Å: 7.0595(2)
Parameters	α/°: 89.928(6)	β/°: 95.054(3)	γ/°: 103.359(6)

Table 7.1: Published and refined lattice parameters for wollastonite ($CaSiO_3$)

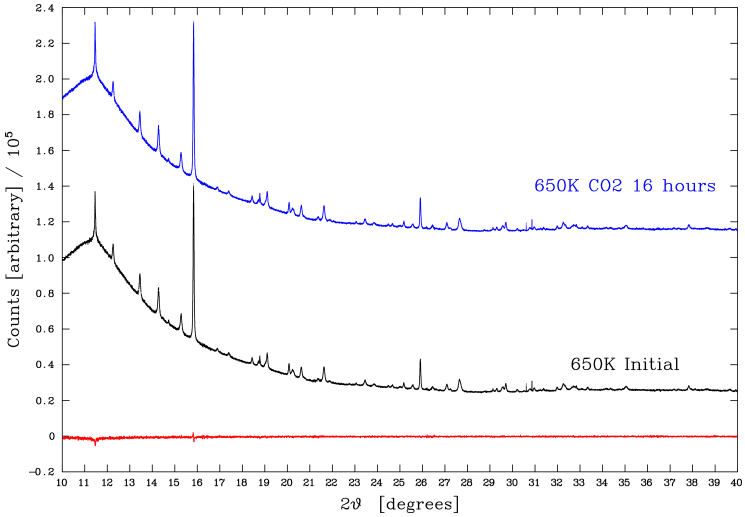

Figure 7.5: Comparison of SXPD PSD patterns for a sample of $x = 0$, exposed to CO_2 overnight. The black curve is the initial scan at 650 K and the blue curve is the final scan after 16 hours. The red curve shows the difference between the two patterns.

(a total of 16 hours) under a CO_2 pressure of 0.7bar, with 20s PSD scans being taken every 15 minutes. Figure 7.5 presents the result of this. The black curve is the initial crystalline sample at 650 K while the blue curve is the sample after being exposed to CO_2 for 16 hours. The two patterns are identical, as confirmed by the residual curve (red), suggesting that no reaction with the CO_2 occurred during this time.

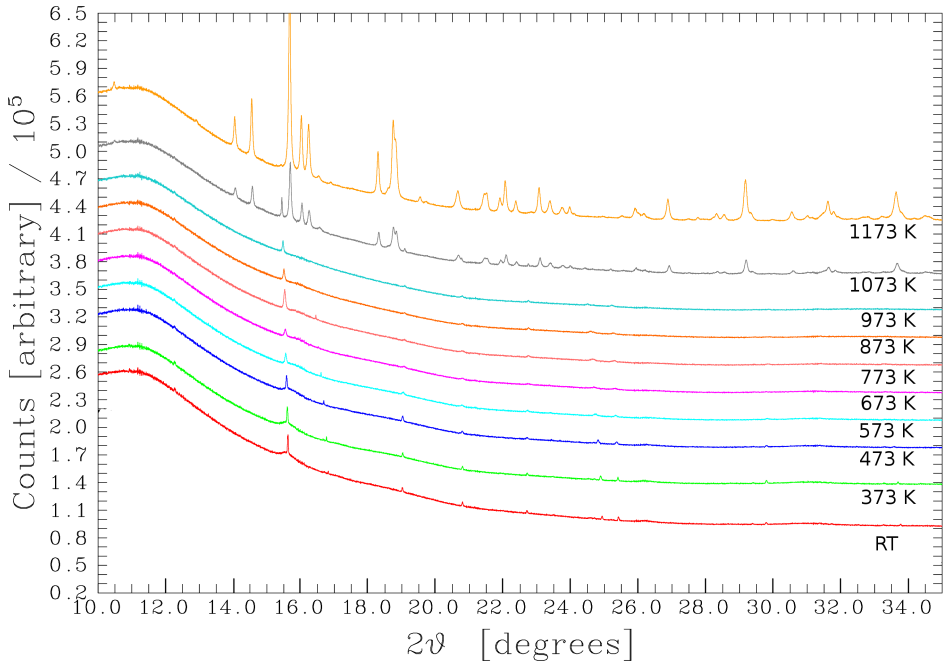

Figure 7.6: Sequence of $Mg_{0.5}Ca_{0.5}SiO_3$ SXPD patterns plotted at 100 K intervals between RT and 1173 K.

7.3.2 $Mg_{0.5}Ca_{0.5}SiO_3$

SXPD data were obtained over a similar temperature range (RT – 1173 K) for a sample of composition $x = 0.5$. Figure 7.6 presents a sequence of SXPD scans at 100 K intervals for a sample of $x = 0.5$ exposed to CO_2 at 1 bar. Unlike the previous sample, the temperature for this run was not held at 100 K intervals, instead the temperature was set to ramp up to 1173 K and data were collected every 100 degrees. The sample measured at RT, prior to the injection of CO_2, exhibits a number of weak but well defined Bragg peaks, all of which can be attributed to calcite. A closer look at the pattern reveals that the strongest calcite peak at $\sim 15.62°$ 2θ has not replaced the broad features, previously associated with calcite, but is superimposed onto it. A simple Gaussian fit within this region, as shown in Figure 7.7, reveals that two Gaussian peaks are required to fit these features, suggesting that the broad feature is not due to

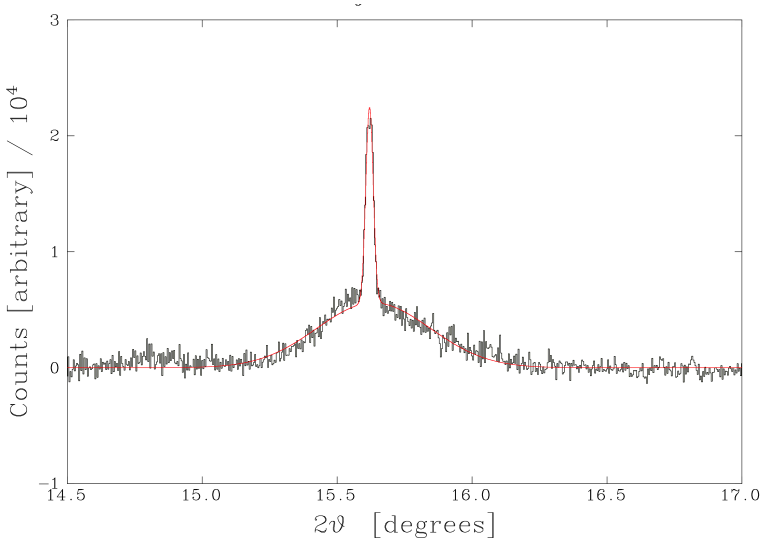

Figure 7.7: Fit of the calcite/unknown peak at ∼15.6 2θ using two Gaussian peaks, suggests that two unique phases are present.

calcite as was previously believed but is actually a separate phase. Peak search match software reveals that these features could be due to an SiO_2 phase, which is indeed very likely as SiO_2 is a by-product of the reaction (shown in Equation 7.1) describing the formation of calcite.

As the sample is heated and dosed with CO_2, the calcite features weaken, as seen previously, however they do not disappear completely. The 15.62° 2θ peak remains past 1073 K, still being present as the sample begins to crystallise, although it is no longer present in the final SXPD pattern taken after the sample has been at 1173 K for a few minutes.

Rietveld refinement of the final crystalline product for $x = 0.5$ indicates that the mineral phase produced is predominantly Diopside (87%), although very small amounts of enstatite (6%) and wollastonite (7%) are required to fit all observed features. A reliable fit to the experimental data is obtained, as shown in Figure 7.8 and the refined lattice parameters do not differ greatly from the initial model values. Table 7.2 presents the initial and refined values for the dominant diopside phase.

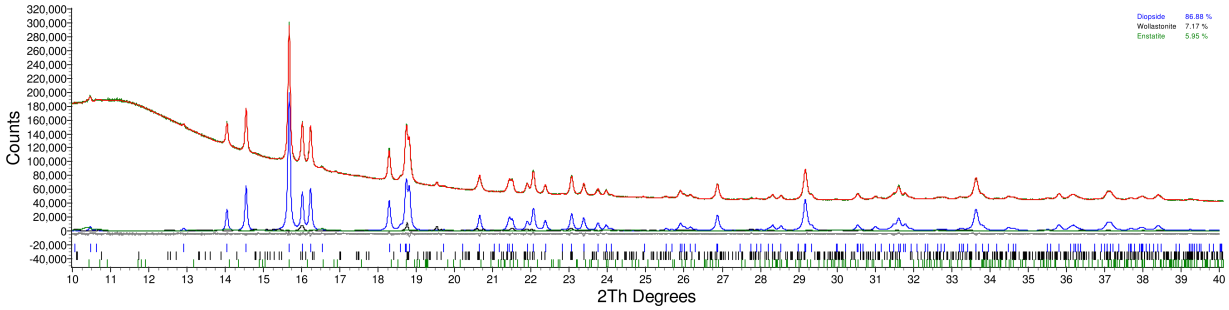

Figure 7.8: Rietveld refinement of the crystalline powder pattern for sample $x = 0.5$ identifies a good fit (Rwp = 0.805%) with structural models of diopside, enstatite and wollastonite. The experimental data are shown in blue, calculated in red and residuals in grey, while the individual phase curves of diopside, enstatite and wollastonite are blue, green and black respectively.

Space Group: C 1 2/c 1			
Published Lattice	a/Å: 9.806(1)	b/Å: 9.05(1)	c/Å: 5.28(1)
Parameters	α/°: 90	β/°: 106.00(1)	γ/°: 90
Refined Lattice	a/Å: 9.8112(1)	b/Å: 9.0439(1)	c/Å: 5.29074(7)
Parameters	α/°: 90	β/°: 106.541(7)	γ/°: 90

Table 7.2: Published and refined lattice parameters for Diopside ($MgCaSiO_3$) after refinement to the experimental data of sample $x = 0.5$

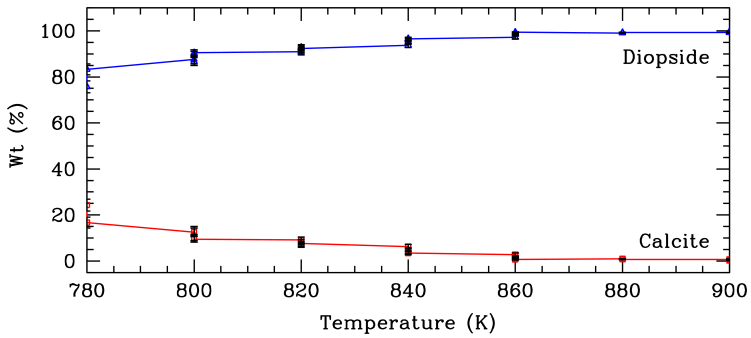

Figure 7.9: Relative weight percentages of diopside and calcite phases, as identified by Rietveld refinement, against temperature for a sample of composition $x = 0.5$.

Upon initial crystallisation of the amorphous sample at 1073 K, a Rietveld refinement suggests that a small amount of calcite is still present, providing weight percentages for the relative phases of 78.04% diopside and 21.96% calcite. As the temperature increased and the sample undergoes further crystallisation the calcite phase diminishes. The weight percentages of calcite and diopside have been plotted against temperature in Figure 7.9, up to a maximum temperature of 1173 K, at which point crystallisation is complete and calcite is no longer present.

7.3.3 $MgSiO_3$

The exposure of a pure-Mg silicate, $x = 1$, to CO_2 was also studied. CO_2 was injected at a pressure of 1.4bar. As for $x = 0$, the temperature was increased in 100 K steps and 4 scans were taken per temperature step. Figure 7.10 presents the SXPD powder patterns for this thermal evolution, with RT patterns at the bottom and temperature increasing upwards. Again, two broad, weak features are present within the amorphous sample at RT and prior to CO_2 exposure. As these features have previously been associated with calcite, their presence in a sample with no calcium was unexpected. This strengthens the hypothesis that these features are actually due to a different phase, but it has not been possible to identify the carrier.

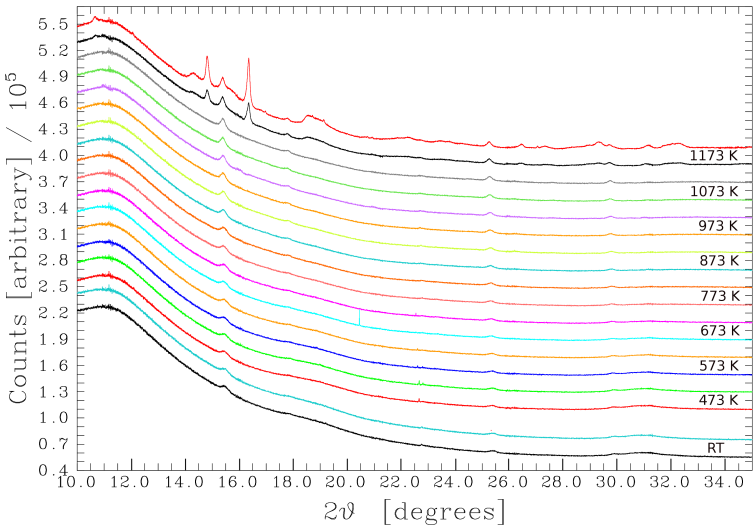

Figure 7.10: Sequence of $MgSiO_3$ SXPD patterns from RT to 1173 K in 100 K steps. Two scans per temperature are shown, one at the beginning and one at the end of the hold.

It should also be noted that, unlike the previous compositions in which the initial phase has been removed by heating to > 973 K, the features here persist throughout the annealing of the sample and grow in intensity as the sample crystallises at 1173 K. This would suggest that rather than carbonate, this feature is due to a silicate phase. As for the previous sample compositions, there is no growth of additional features and no significant change to the features already present that would indicate that a reaction is occurring due to the incorporation of CO_2 into the sample structure.

Refinement of the final crystalline phase in this case identifies multiple phases within the sample. A good fit ($R_{wp} = 0.751$) was obtained from forsterite, enstatite and SiO_2, the fit is shown in Figure 7.11. This concurs with the results from our previous thermal annealing experiment (described in Chapter 6) identifying forsterite as the dominant mineral phase (50.49%) along with minor phases of enstatite (20.11%) and SiO_2 (29.40%).

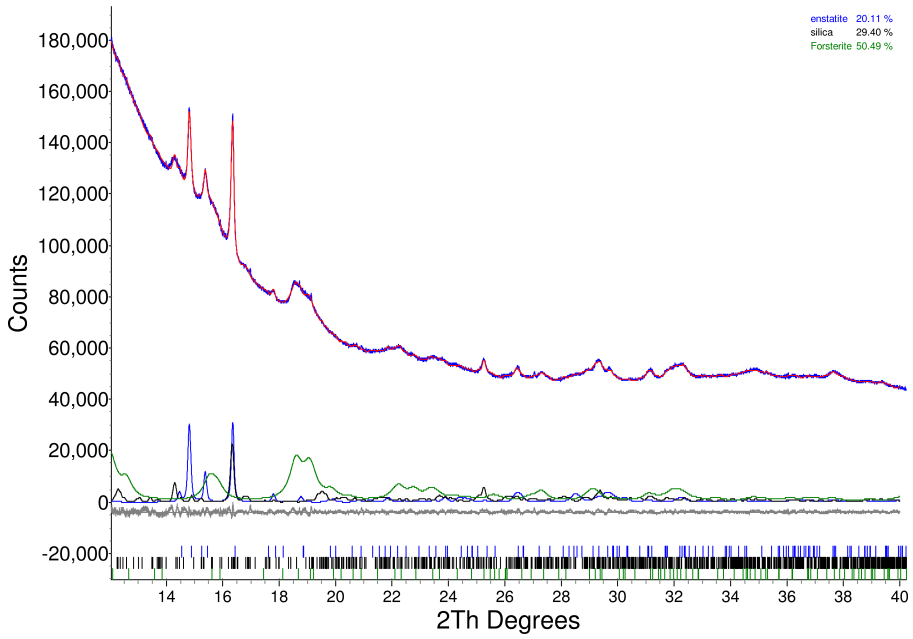

Figure 7.11: Rietveld refinement of $x = 1$ showing a good fit ($R_{wp} = 0.751$) to the experimental data produced by a combination of enstatite, forsterite and silica. The calculated profile is shown in red, the residuals in grey and the experimental data in blue, while individual phase curves for forsterite, enstatite and silica are in green, blue and black respectively.

7.4 Discussion

The origin of this carbonate phase within an amorphous silicate samples is not certain. Great care was taken to ensure minimal interaction between the sample and air (atmospheric CO_2), although there are points in the sample preparation process where brief contact with air cannot be avoided (e.g. removing samples from the furnace), even if just for a matter of seconds. In a previous paper, discussing the formation and characterisation of the $CaSiO_3$ samples used in this work, Thompson et al. (2012a) states that the weathering of silicates with atmospheric CO_2 is very slow under ambient conditions (Lim et al. 2010) and therefore, the carbonation is unlikely to have occurred after removal from the vacuum furnace. It was determined that the carbonate phase most likely originates in the gel stage of formation. In any case, the broad nature of the features and their weak relative intensity indicate that the phase responsible is likely of a disordered nature, exhibiting order over only a short range or is present as very small crystallites ($< 1\mu$m). The nature of synchrotron radiation, particularly the high X-ray intensity and good particle averaging, makes SXPD measurements highly sensitive to the presence of very dilute phases that would perhaps not be detected on standard XRD equipment. Regardless of the origin of this carbonate phase, the weak intensity of the features also suggests that only a very small amount of the calcite phase is present, relative to the total volume of the sample, and therefore it was not deemed necessary to remove it prior to conducting the experiment.

Unfortunately, during this experiment we did not observe the in situ carbonation in any of the three compositions studied, however, this is not to say that solid-gas carbonation of amorphous silicates is not a valid formation route for cosmic carbonates. To provide a comparison to the in situ measurements, a sample of $x = 0.5$ was also placed into an evacuated desiccator vessel with ammonium carbonate ($(NH_4)_2CO_3$) as a source of CO_2. This was left overnight ($\sim$16 hours) and upon removal was loaded directly into a sealed capillary. A PSD SXPD scan was performed at ambient temperature for the exposed sample and compared to an equivalent scan of the undosed sample, as shown in Figure 7.12. While both show calcite features at room tempera-

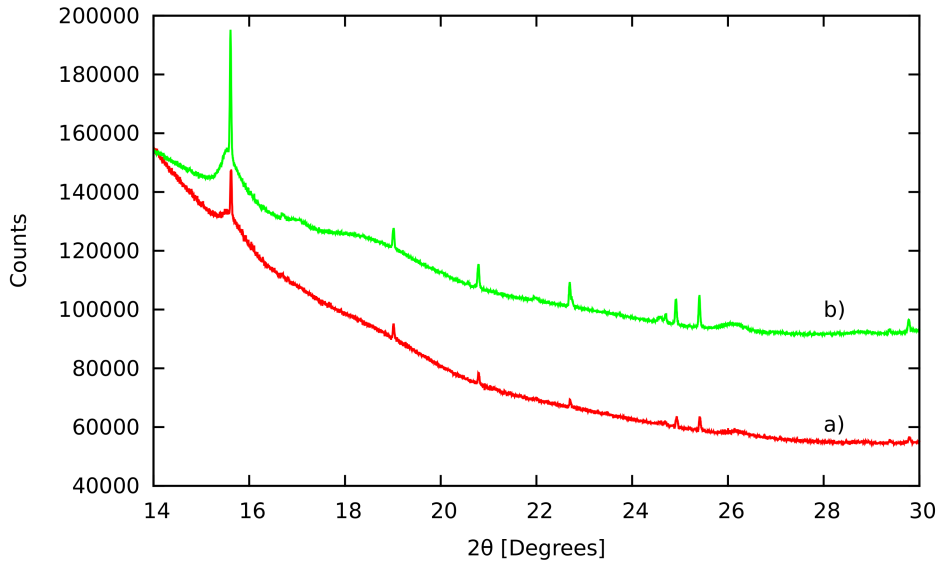

Figure 7.12: Comparison of SXPD patterns (a) at RT for $x = 0.5$ under vacuum, and (b) after a 16 hour exposure to CO_2 in a desiccator.

ture, the features present in the exposed sample show, on average, a 40% increase in peak intensity. This indicates that at pressures of $\sim$ 1 bar a reaction between solid, amorphous silicate and CO_2 does occur, leading to the conversion of amorphous silicate to calcium carbonate, although in very small amounts. It is understood that CO_2 uptake by minerals is an essential part of the global carbon cycle and is referred to as 'natural carbonation'. Natural carbonation reactions are kinetically very slow and only become significant over long periods of time (Costa et al. 2007).

Figure 7.13 displays a sequence of SXPD patterns showing the evolution of structure of the exposed $x = 0.5$ sample during heating from RT to 1173 K. As seen previously, the calcite phase diminishes with increasing temperature, however, in this case the calcite phase breaks down much earlier, no longer being present in the pattern obtained at 973 K, but having been replaced by another phase represented by three weak features at 16.94°, 19.53° and 27.79° 2θ. These features are observed in all further patterns up to 1173 K and are present, although weakly, alongside the main crys-

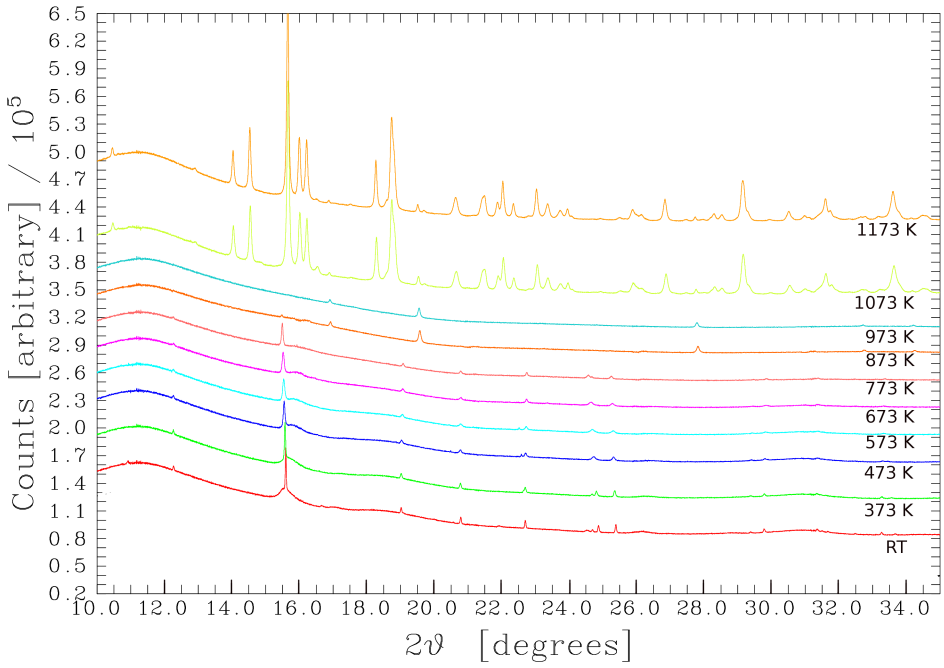

Figure 7.13: Sequence of SXPD patterns for a sample of $Mg_{0.5}Ca_{0.5}SiO_3$ ($x = 0.5$) exposed to CO_2 in a sealed desiccator vessel overnight at atmospheric pressure. The temperature was then raised from RT to 1173 K. Select patterns are plotted here at 100 K intervals.

talline phase. These additional features can be reliably linked to lime (CaO), which is produced as calcite breaks down through the reaction: $CaCO_3 \longrightarrow CaO + CO_2$.

7.5 Conclusions

While no carbonate formation was directly observed in this study using the capillary gas cell, we have shown through the ex situ carbonation of a mixed Ca/Mg sample that an interaction between CO_2 and the cosmic dust analogues does indeed occur, leading to the formation of a fairly well-formed calcite phase. We believe that the reason a reaction was not observed during the in situ carbonation of the samples is not due to the materials themselves but due to the nature of the experimental arrangement. Due to the very small beam size (2.5×0.8 mm) used in SXPD the capillaries are required to be very small, having a diameter of only 0.5mm, therefore the packing density of the sample within the capillary is high and sufficient diffusion of the gas through the sample may not have been achieved. It is possible to test this by retrieving the sample from the capillary and testing the small amount of sample directly exposed to the gas at the capillary opening in order to determine if a reaction did occur, but only in a very limited portion of the sample. This would indicate that the gas pressure is not high enough to allow for full penetration of the gas through the length of the capillary and therefore the small section of sample that was exposed to the beam for measurement had not come into contact with the CO_2. This could be solved by attempting to reduce the amount of sample loaded into the capillary, allowing CO_2 to flow throughout the capillary, although this may have a negative impact on the quality of data measured using the SXPD technique as a significant amount of sample is required for good particle averaging. An alternative method would be to increase the pressure of the incident gas on the sample, which would also improve the flow of gas throughout the capillary. The latter method was implemented in a separate experiment with great success, the results of this are presented in Chapter 9 of this thesis.

8 PDF analysis of synthetic cosmic silicates as precursors for cosmic carbonates

8.1 Introduction

As described in detail in Chapter 2, cosmic carbonates are thought to form through the solid-gas reaction of calcium-rich silicates and hot CO_2 gas in circumstellar environments via the reaction:

$$CaSiO_3 + CO_2 \longrightarrow CaCO_3 + SiO_2 \tag{8.1}$$

In the previous chapter, we used conventional high-resolution X-ray powder diffraction to study the thermal evolution and conversion of silicate dust analogues when exposed to CO_2 gas at elevated temperatures and pressures. However, this method relies on the sample having significant long-range order to produce Bragg peaks and is most effective for crystalline samples. It is widely accepted that astronomical silicates are predominantly amorphous, with crystalline silicates thought to make up <12% (Sargent et al. 2009) of the silicate dust mass observed in circumstellar environments. Therefore, the samples used in this work are initially amorphous, only crystallising at temperatures > 900 K. Using the total scattering (TS) approach to, and Pair Distribution Function (PDF) analysis of, high-energy X-ray powder diffraction data (described previously in Section 4.4.2), it is possible to study the structural changes occurring within the short range structure of the samples, prior to annealing, in much greater detail than would be possible with conventional powder diffraction. The TS method puts equal weighting on both the Bragg and diffuse scattering arising from the interaction of X-rays with the sample being studied, allowing the short-range structure of materials to be observed, including materials that are not efficient Bragg scatterers, such as amorphous materials. In order to obtain information relating to the short-range atomic distances, through Fourier inversion of the TS data, it is essential to

measure to much higher values of the X-ray scattering vector, Q, than for conventional powder diffraction. The magnitude of the scattering vector, Q, is defined by:

$$Q = 4\pi\lambda^{-1}\sin\theta, \tag{8.2}$$

where λ is the wavelength of the incident radiation and θ is the angle of the incident radiation. To reach high values of Q it is usually necessary to utilise high X-ray energies as the maximum accessible value for Q is $Q_{\max} = 4\ \pi E/hc$, where E is the X-ray energy. This technique provides information about the bond lengths within the samples and will allow us to determine the effect of increasing temperature on the short range structure of such materials in order to understand more about the annealing process and how the presence of gaseous CO_2 affects the composition and chemical structure.

8.2 Experimental

8.3 Sample preparation

Samples of composition $Mg_{(x)}Ca_{(1-x)}SiO_3$were manufactured using a sol-gel method as described previously by Thompson et al. (2012a) and in Chapter 5. These amorphous cosmic dust analogues were dried under vacuum, in a carbolite HVT vacuum furnace purged with nitrogen, at 323 K. The samples were then annealed offline, prior to the beamtime, at temperatures of 573 K, 873 K and 1173 K, under vacuum. The powders were then stored in sealed glass vials under argon. Dosing of the samples with gaseous CO_2 was achieved by placing a small amount of each sample into individual petri dishes and enclosing these in a desiccator vessel, with ammonium bicarbonate (NH_4HCO_3) as the source of CO_2. This was then left overnight for $\sim$ 16-18 hours before the samples were removed and loaded directly into capillaries ready for data collection. Diffraction data were collected at ambient temperature.

8.4 Data collection

Data were collected on Beamline I12 at DLS, using a Pixium area detector (CsI scintillator on amorphous Si substrate; Daniels & Drakopoulos 2009) and 87.4 keV monochromatic X-rays with a wavelength of 0.141328Å (calibrated using a CeO standard). Samples were loaded into 2mm Kapton capillaries and multiple (720) 4s scans were taken per sample and averaged to produce the final diffraction image. The detector was offset from the beam centre to provide a maximum value of the X-ray scattering wavevector ($Q_{\max}$) of 31Å^{-1}. To provide background correction, data were obtained in the same way for air scatter and empty capillary measurements. The experimental setup used for the data collection is shown in Figure 8.1, with the positions of the main components clearly labelled. The data were converted from 2D diffraction images into 1D powder patterns using the FIT2D software (Hammersley et al. 1996; Hammersley 1997) and subsequently converted from 1D powder data into probability distribution functions ($G(r)$) via Fourier transformation using PDFGetX3 (Juhas et al. 2013).

8.5 Results and Analysis

8.5.1 Total Scattering

Measured TS data for sample composition $x = 0$ are shown in Figure 8.2. The problem of using conventional powder diffraction when studying amorphous samples is easy to see in these scans. The low temperature samples, annealed at ≤ 873 K, exhibit diffraction patterns that are characteristic of the lack of scattering intensity from disordered materials, having a high background and showing very few features. On the other hand, the sample annealed at 1173 K exhibits strong, well defined Bragg peaks, characteristic of crystalline samples exhibiting long-range structural order. These TS functions appear different to standard powder diffraction patterns as seen in previous chapters, this is due to the Q range for which the data have been obtained. Standard powder

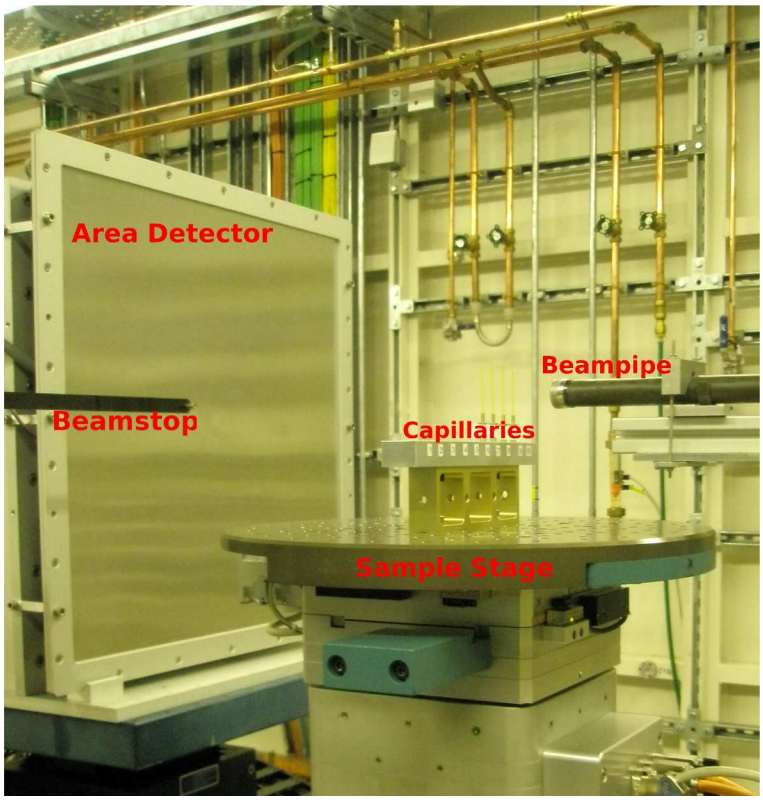

Figure 8.1: The experimental setup on Beamline I12 at Diamond Light Source. Important components, including the detector, sample holder and beampipe are labelled.

diffraction patterns generally only observe a Q-range of ≤ 6 Å^{-1}, whereas total scattering data observe out to $Q = \sim 30$ Å^{-1}. Although the visible scattering features do not extend past $Q = 10$Å^{-1} it is the weak high-Q scattering that contains the valuable short-range information, required for this study, that would otherwise be ignored in conventional XPD.

While the main focus of this study is to use PDF analysis to study the short-range structure of these materials, it is also important to investigate these fundamental data as they can often provide additional information about the structure and composition of the crystalline end-members. Figure 8.3 shows the TS data for each of the

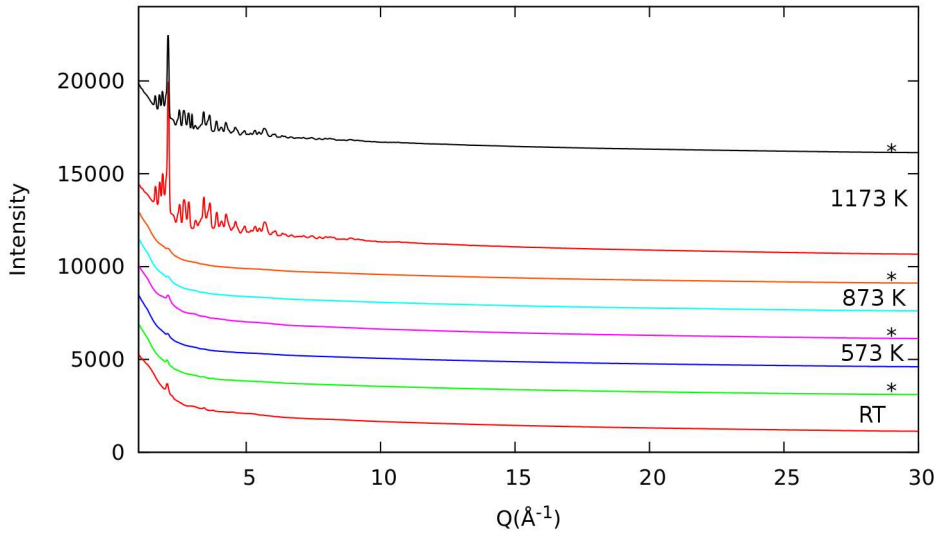

Figure 8.2: Measured X-ray total scattering diffraction patterns for samples of composition $x = 0$ at four different temperatures (as labelled). Scans labelled with the asterisk, *, have been exposed to CO_2. Patterns have been offset for clarity.

compositional end-members, annealed at 1173 K. Although the basic composition of the samples is known, we cannot be certain of the exact mineral phase, or phases, that have formed due to the high temperature annealing of the samples. Modelling of the data would confirm the precise nature of the samples; however, without knowing exactly which structural models are required this would take some time. Therefore, peak search-match software is used in order to match the experimental data to comparison data stored in a database; this provides an indication of the phases present within each sample by comparing the positions of the Bragg peaks with those of known mineral phases. Structural models of the required phases can then be obtained and structural refinements, such as Rietveld refinement (Rietveld 1969) can be performed to determine atomic positions and accurate lattice parameters. A LeBail (LeBail, Duroy & Fourquet 1988; LeBail 2005) refinement can also be performed without the use of a

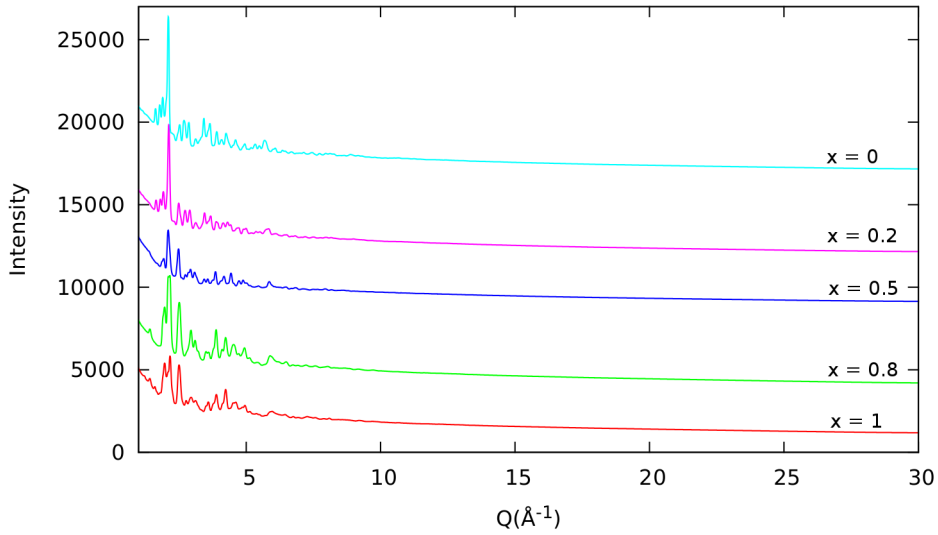

Figure 8.3: Measured total scattering patterns for all compositions at 1173 K. The lowermost scan is $x = 1$ and the uppermost scan is $x = 0$.

structural model, but the space group of the sample must be known.

8.5.2 PDF Analysis

A pair distribution function (PDF) is a weighted histogram of atom-atom distances and is based on the calculated probability of finding an atom at a specific distance from the reference atom. Each of the peaks present in the PDF pattern represents an atomic bond length within the sample; for example, in the molecular model shown in Figure 8.4 of a unit cell of diopside ($MgCaSi_2O_6$) each of the bond lengths labelled will produce a peak, and the integrated intensity of the peaks will depend on the number of atoms present at this bond distance (the co-ordination number). The distance, r, at which the oscillations in the PDF reduce to zero represents the coherent scattering domain (CSD) and is a measure of the distance over which the atoms exhibit structural

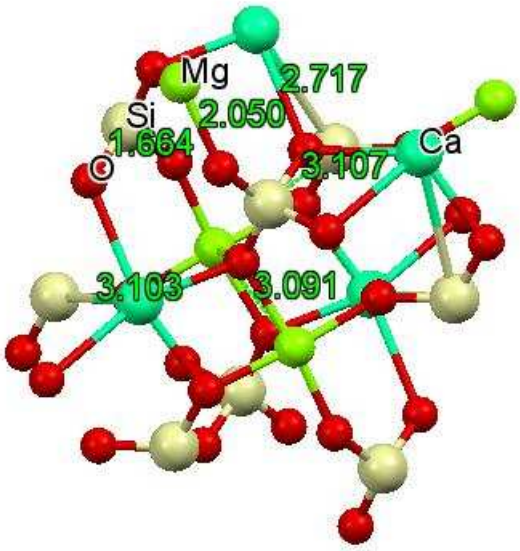

Figure 8.4: A molecular model of a typical $MgCaSiO_3$ unit cell (diopside). Atoms are colour coded where yellow = Si, light green = Mg, red = O and dark green = calcium.

correlation. Further detail regarding the theory and analysis of Total Scattering data has been discussed in Section 4.4.2. Fitting of a structural model to the experimental PDF is performed using the software package PDFGui (Farrow et al. 2007, discussed in detail in 4.4.2.2), via a least-squares regression technique (Billinge 1998). The effect of changing composition on the structure of the $G(r)$ function is evident in the calculated

$G(r)$ functions, as shown in Figure 8.5, for the as-prepared samples. The first peak at 1.6Å represents the Si-O bonds of the silicate tetrahedra of the first co-ordination shell. This bond is consistent throughout the scans, indicating that the inter-tetrahedral bonds are not affected by the change in composition. The next strong peak at 2.046Å in the $x = 1$ composition represents the Mg-O bond distance, and the intensity of this peak decreases in accordance with the decreasing amount of Mg, as the Ca content increases. A shortening of the Mg-O bond length is also observed with the introduction of Ca into the samples and this is compressed further with increasing Ca content. The initial Mg-O bond length in the $x = 1$ sample is 2.04596Å $\pm$ 0.00157, whereas, the bond length in the $x = 0.2$ sample is 1.9967Å $\pm$ 0.000152. The peak representing the Ca-O bond is present at 2.36Å in all of the Ca-bearing samples, increasing in intensity with increasing Ca content.

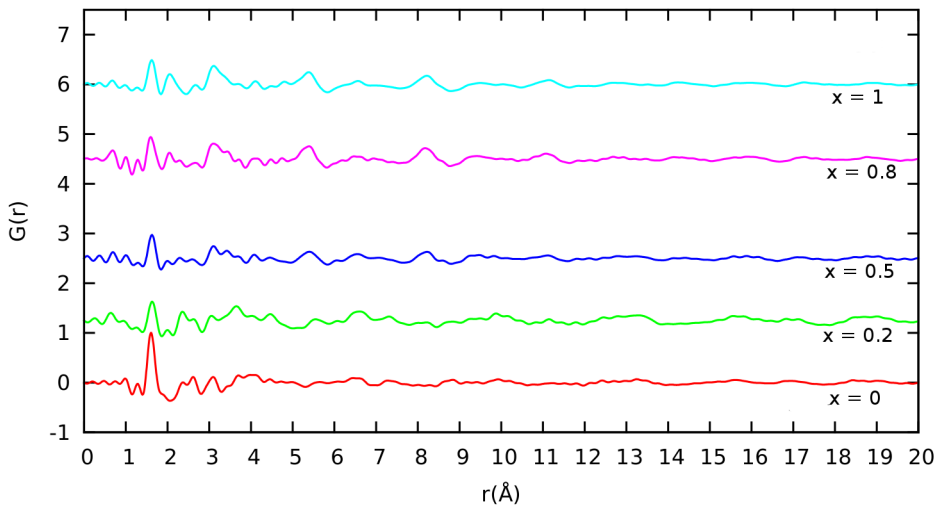

Figure 8.5: A sequence of PDF $G(r)$ plots showing the effect of composition on structure for un-annealed samples of $Mg_xCa_{1-x}SiO_3$, dried at 50°C. The lower scan is $x = 0$ and the uppermost scan is $x = 1$.

8.5.3 $MgSiO_3$

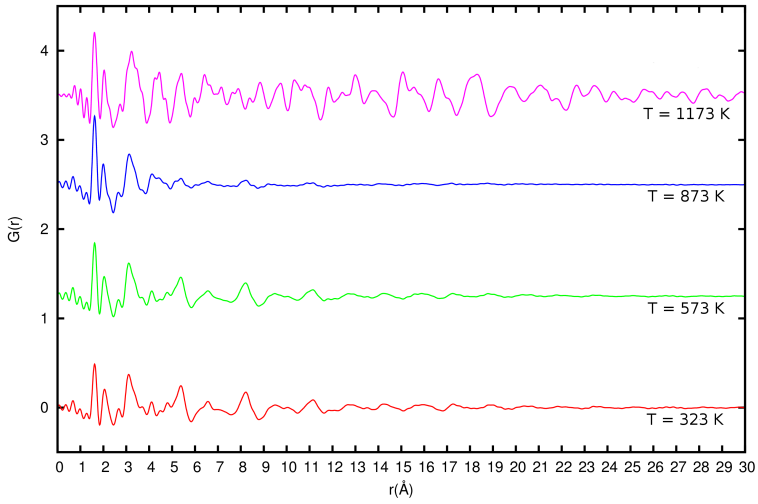

Figure 8.6: Evolution of structure for $MgSiO_3$ ($x = 1$) sample at 323 K, 573 K, 873 K and 1173 K, increasing upwards.

A comparison of the PDF, $G(r)$, functions for $MgSiO_3$ samples annealed at 323, 573, 873 and 1173 K for $\sim$ 12 hours is shown in Figure 8.6. The CSD for the still-amorphous samples show significantly damped oscillations, representing their disordered nature. The 323 and 573 K samples exhibit structural features out to a CSD of 20Å whereas the CSD of the 873 K sample shows a significant loss of longer-range structure, with a CSD of <10Å . It is believed that this is due to structural changes occurring during the very early onset of crystallisation, however this will be discussed in detail later. The 1173 K sample has crystallised, as would be expected, exhibiting features out to at least 30Å. The final crystalline phases produced have been determined to be predominantly enstatite with a small forsterite component. This agrees with our previous findings for the crystalline end-member $x = 1$ with conventional SXPD (Chapter 6 and Day et al. (2013)).

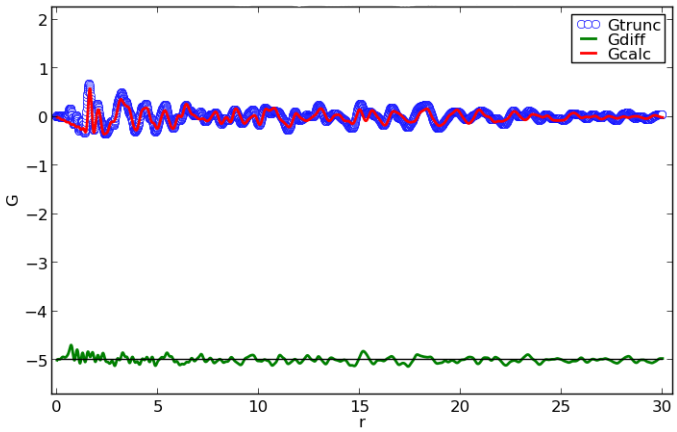

Figure 8.7: Shows the fit of a structural model of the mineral phase ensatite to the $x = 1$ sample annealed at 1173 K, producing an R_{wp} value of 4.7 %. The blue curve shows the experimental data, the red curve is the calculated fit and the green curve shows the residuals.

A structural model of enstatite ($MgSiO_3$) was fit to the experimental data, producing a good fit of the enstatite phase (See Figure. 8.7), refined lattice parameters are given in Table 8.1. A molecular model of the refined crystal structure is shown in Figure 8.8, the single-chain structure distinctive of pyroxene minerals can clearly be seen here, with Mg^{2+} ions bridging the individual chains. Fitting of the residual function (solid green line in Figure. 8.7) confirms a weak secondary phase that is matched well by forsterite (Mg_2SiO_4).

As we are focusing on the origin of Ca-rich carbonates the $x = 1$ samples were not exposed to CO_2 as it is, for the moment, beyond the scope of this study.

8.5.4 $Mg_{(0.8)}Ca_{(0.2)}SiO_3$

As for the $x = 1$ samples, the PDF, $G(r)$, functions of samples with composition $x = 0.8$ show the same evolution of structure, presented in Figure. 8.9, with CSDs of ~ 20Å

Enstatite – Space Group: Pbca			
Published	a (Å)	b (Å)	c (Å)
	18.23	8.82	5.18
Refined	a (Å)	b (Å)	c (Å)
$R_{wp} = 4.7$ %	18.15(1)	8.82(6)	5.21(4)

Table 8.1: Original and refined lattice parameters for enstatite mineral phase.

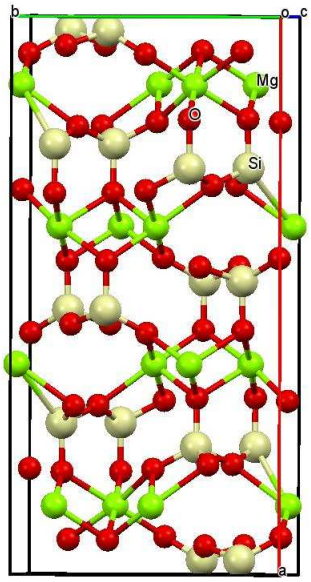

Figure 8.8: Shows the refined molecular model for the $x = 1$ sample annealed at 1173 K. Viewed down the crystallographic c-axis. Yellow atoms are Si, green are Mg and red are O.

at temperatures of 323 and 573 K and a considerable reduction to $\sim$ 7Å at 873 K. The 1173 K sample exhibits structural order out to >30Å.

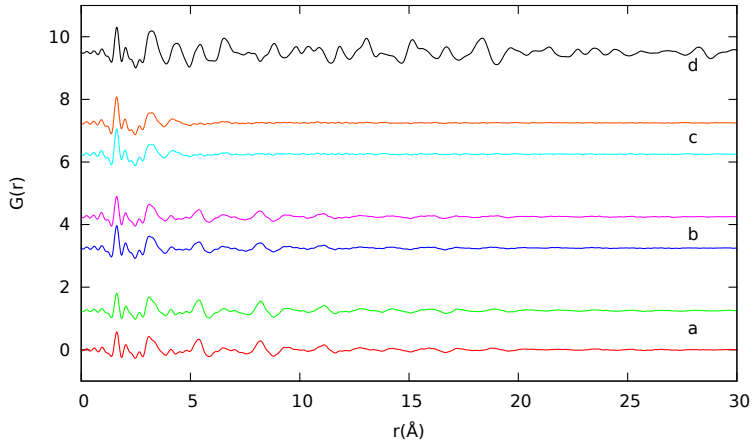

Figure 8.9: Calculated PDF, $G(r)$, functions of all samples with the composition $x = 0.8$ at 4 different temperature steps a) 323 K b) 573 K c) 873 K and d) 1173 K. With the exception of d), two PDFs are shown for each temperature step, the bottom scans are vacuum dried samples stored under Ar while the upper scan for each temperature is a sample that has been exposed to CO_2 overnight.

Figure 8.9 also presents PDF, $G(r)$, functions of samples dosed with CO_2 (uppermost scan in each pair). When comparing these functions to those of the un-dosed samples, there is very little difference in structure. There is no shifting of peak positions and no additional features observed in the CO_2 dosed samples. This would indicate that there has been no reaction between the samples and the gaseous CO_2, at least not to the extent that the short-range atomic structure has been affected. The samples of this composition can be associated with the mineral phase pigeonite ($CaMgSiO_3$), which produces a good fit to the crystalline end-member.

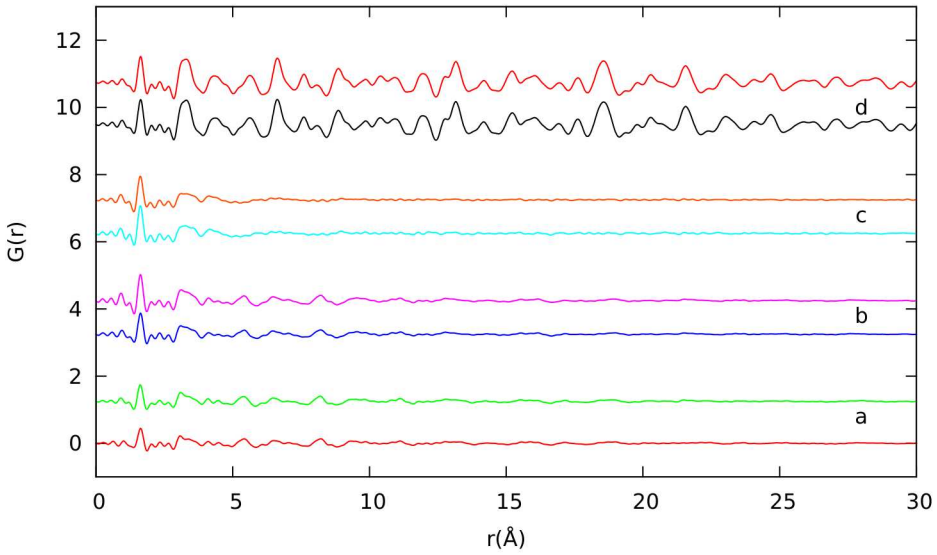

Figure 8.10: PDF, G(r), at different temperature steps for samples with the composition $x = 0.5$. a) 323 K, standard (lower) and dosed with CO_2 (upper). b) 573 K c) 873 K d) 1173 K

8.5.5 $Mg_{(0.5)}Ca_{(0.5)}SiO_3$

Figure 8.10 presents PDF $G(r)$ functions for sample composition $x = 0.5$ at each temperature step, dosed and un-dosed. Samples having composition of $x = 0.5$ are representative of the mineral phase diopside ($CaMgSi_2O_4$) and the crystalline end-members, annealed at 1173 K, are fit well using this as a structural model (see Figure 8.11). The refined lattice parameters show little variation from those of the initial model, as shown in Table 8.2. A molecular model of the refined unit cell for the crystalline sample is shown in Figure 8.12.

This is the case for both the as-prepared sample and the CO_2-dosed sample, again strengthening the notion that crystalline samples do not react with CO_2 to form an additional carbonate phase. The low temperature samples at this composition also do not show any evidence of undergoing a reaction with CO_2 as the peak positions and

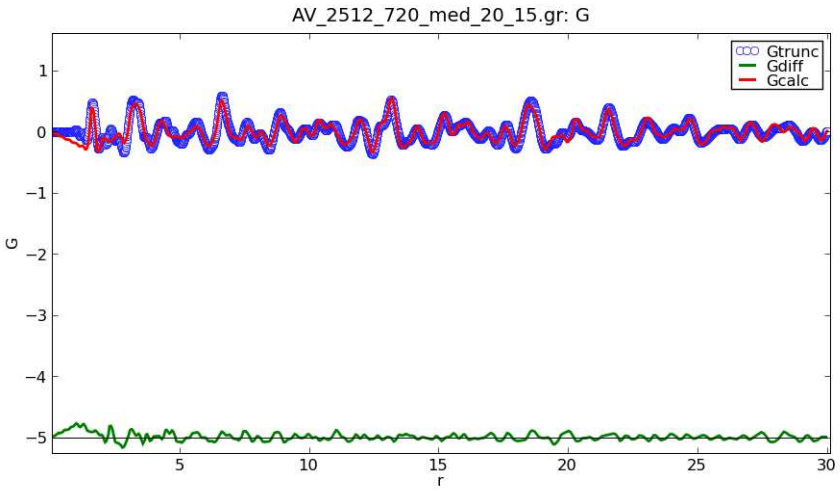

Figure 8.11: Shows the fit of a structural model of the mineral phase diopside to the $x = 0.5$ sample annealed at 1173 K, producing an R_{wp} value of 3.4 %. Experimental data are shown in blue, the calculated fit in red and the residuals are in green.

Diopside – Space Group:2/m			
	a (Å)	b (Å)	c (Å)
Published	9.78	8.98	5.27
	α	β	γ
	90	105.94	90
	a (Å)	b (Å)	c (Å)
Refined	9.74(3)	8.93(3)	5.26(2)
$R_{wp} = 3.4$ %	α	β	γ
	90	105.94	90

Table 8.2: Initial and refined lattice parameters of the Diopside mineral phase.

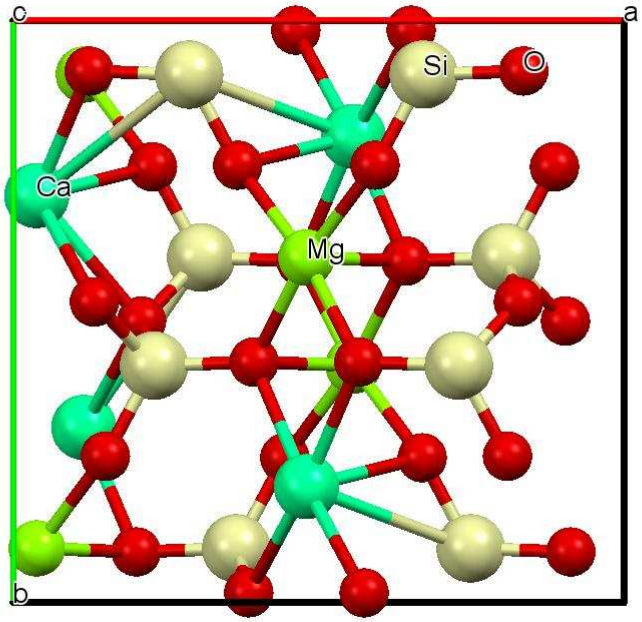

Figure 8.12: Shows the refined molecular model of the $x = 0.5$ sample annealed at 1173 K. Viewed along the crystallographic c-axis.

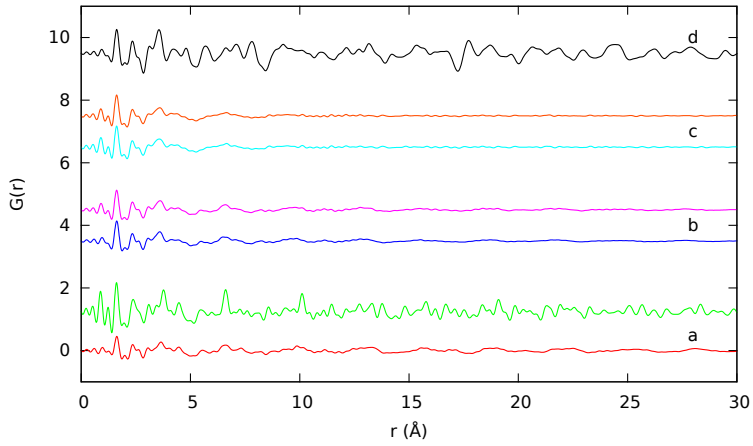

Figure 8.13: PDF, $G(r)$, plots of $x = 0.2$ samples at four temperature steps a) 323 K b) 573 K c) 873 K and d) 1173 K. The upper scan at each temperature step is the sample exposed to CO_2.

intensities are constant across all of the measured PDFs. The 873 K samples once again show a significant loss of structural correlation at r > 5Å.

8.5.6 $Mg_{(0.2)}Ca_{(0.8)}SiO_3$

Samples of composition $x = 0.2$ show a similar trend to those seen previously, exhibiting only short-range structure up to a temperature of 873 K, only crystallising at 1173 K. In this case, the crystalline phase formed at 1173 K is in fact a mixture of two phases, enstatite and wollastonite (Figure 8.13). Unlike the other combined samples ($x = 0.8$ and 0.5), that crystallised to the mineral phases pigeonite and diopside, this composition has preferentially separated into two distinct mineral phases of pure-Mg enstatite and pure-Ca wollastonite. Another difference between this compositions and those described previously is the PDF, $G(r)$, of the 323 K dosed with CO_2. For the compositions having $x \geq 0.2$ samples dosed with CO_2 overnight did not show any significant change when compared to their non-dosed equivalents; however, in this case

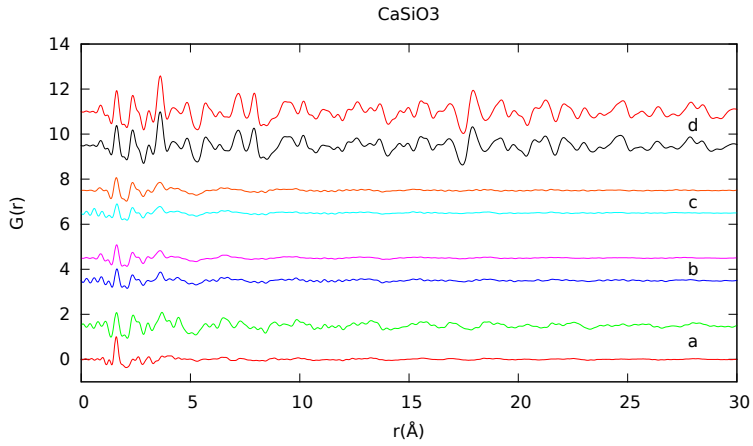

Figure 8.14: Pair distribution functions, $G(r)$, for samples of composition $x = 0$. a) as prepared (dried at 323 K) without CO_2 (bottom scan) and exposed to CO_2 (top scan). b) 573 K c) 873 K d) 1173 K

the PDF, $G(r)$, for the un-annealed sample dosed with CO_2 shows a significant increase in the structural coherence of the sample. The standard sample that had not been exposed to CO_2 has a CSD of ≤ 15Å while the equivalent sample after exposure to CO_2 exhibits a CSD of at ≥ 30Å .

8.5.7 $CaSiO_3$

Data obtained for the final group of samples, having the composition $x = 0$, are shown in Figure. 8.14. It is apparent here that the CSDs of the pure-Ca samples are smaller in comparison to that of the compositions containing Mg, only exhibiting significant structure out to ~ 10Å. This also means that the measured data for the 873 K samples does not present a loss of structure in comparison to the lower temperature data. This could suggest that the process responsible for the loss of structure, seen previously, is dominated by the magnesium component of the sample. As with the un-annealed sample of the previous composition ($x = 0.2$), exposed to CO_2, the CO_2-dosed sample at 323 K here also exhibits a significantly extended CSD and increased peak intensity when

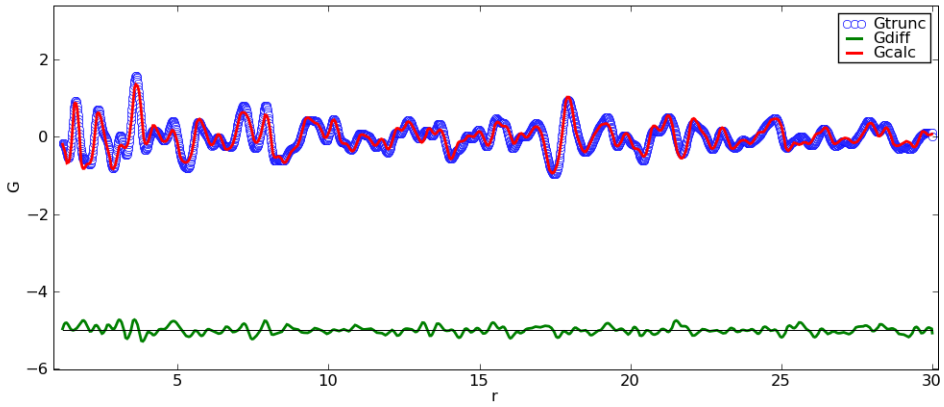

Figure 8.15: Shows the fit of a structural model of the mineral phase wollastonite to the $x = 0$ sample annealed at 1173 K. This yields an R_{wp} value of 2.8%.

Wollastonite-2M – Space Group: P 2_1			
	a (Å)	b (Å)	c (Å)
Published	15.48	7.33	7.08
	α	β	γ
	90	95.4	90
	a (Å)	b (Å)	c (Å)
Refined	15.46(3)	7.34(1)	7.07(1)
$R_{wp} = 2.8$ %	α	β	γ
	90	105.94	90

Table 8.3: Refined and initial values for the mineral phase wollastonite.

compared to its un-dosed equivalent, indicating that a reaction has occurred. The phase produced upon annealing of the sample at 1173 K has been identified as wollastonite ($CaSiO_3$) which produces a very good fit to the PDF, as shown in Figure 8.15. Results of this refinement are displayed in Table 8.3, along with a molecular model produced using the refined lattice parameters and atomic positions in Figure 8.16.

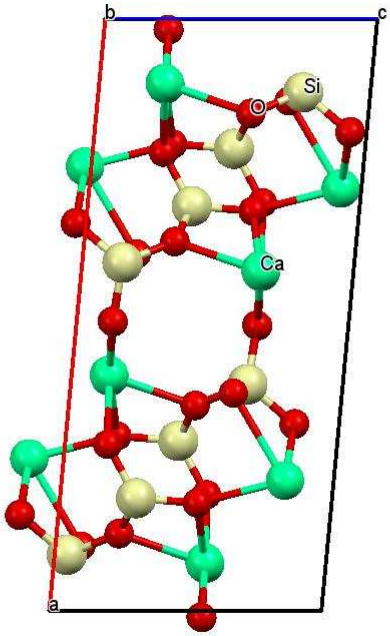

Figure 8.16: Shows the refined molecular model for the $x = 0$ sample annealed at 1173 K, viewed along the crystallographic b-axis.

The refined values obtained for the synthesised sample do not differ greatly from the supplied model parameters.

The inter-tetrahedral bonds (<5Å) are unaffected with respect to the position of the peaks, remaining consistent with the atomic-distances of wollastonite, but the intensity of the peaks is increased and the peaks appear more defined. The intensity of the peak, in general, relates to the co-ordination number of the material which is the value attributed to the number of atoms in each co-ordination shell from a reference atom. The change in co-ordination number can be explained by a re-arrangement of the atomic structure in response to a reaction with CO_2.

The difference in the appearance of the PDF begins at >4Å where the peak

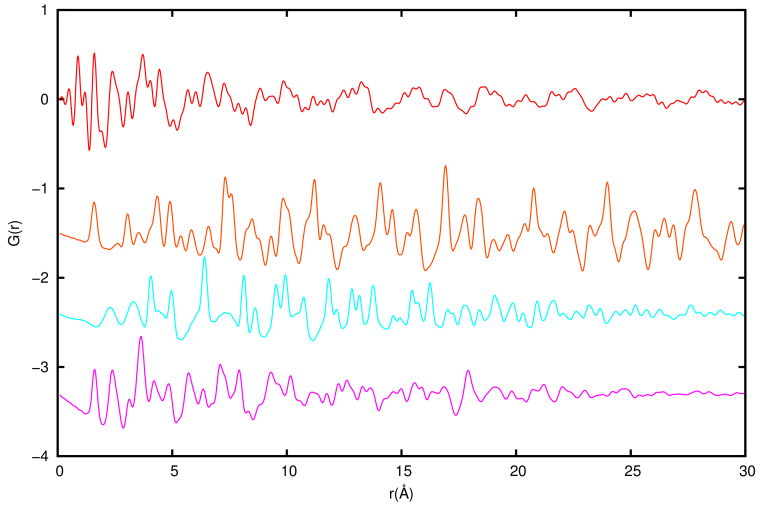

Figure 8.17: Comparison of experimental PDF of as-prepared sample $x = 0$ (top), exposed to CO_2, with calculated PDFs of wollastonite (pink), calcite (orange) and α-quartz (SiO_2; blue) suggesting that the experimental pattern contains a combination of the three phases.

positions can no longer be fitted to wollastonite. Comparison of calculated PDFs for wollastonite, calcite and α-quartz (the most common form of SiO_2) with the experimental data suggests that the additional features can be attributed to small amounts of Calcite ($CaCO_3$) and SiO_2 (see Figure 8.17). While a reliable fit of these phases could not be obtained, due in part to the disordered nature of the materials and lack of amorphous structural models, this provides good evidence that a carbonation reaction has occurred, converting $CaSiO_3$ into $CaCO_3$ and SiO_2. It is, however, undeniable that the wollastonite structure remains dominant in the observed sample and therefore after $\sim$16 hours at ambient temperature and pressure a complete conversion has not been achieved.

8.6 Discussion

8.6.1 Structural processes

Crystallised samples, annealed to 1173 K, produce the expected mineral compositions as predicted by the pyroxene quadrilateral diagram shown in Fig 8.18.

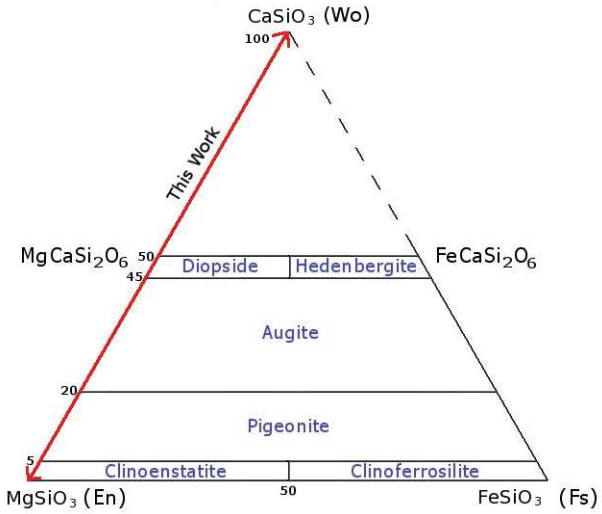

Figure 8.18: Pyroxene quadrilateral diagram showing the composition ranges for the Mg-Fe-Ca system. The dashed lines extending from the top of the diopside region up to the apex at $CaSiO_3$ indicate that there is no complete solid solution in this region. Wollastonite (Wo) is shown as it has the equivalent composition of a pure-Ca pyroxene mineral, but structural differences mean that it is not a true pyroxene. The numbers along the left hand side of the diagram represent the amount of wollastonite at each point and are referred to in the text as Wo_{50}, Wo_{100} etc.

As can be seen from the diagram there are no stable mineral phases between Wo_{50} and Wo_{100}. X-ray powder diffraction and infrared absorption data described by Shinno (1974), for structures synthesised across the range $CaSiO_3$–$CaMgSiO_3$, reveal that stable structures within the range of Wo_{100} and Wo_{85} can be synthesised, but compositions with $<Wo_{85}$ are metastable at all temperatures (Deer, Howie & Zussman

1978). This is due to the fact that the pure-Ca end-member, wollastonite, is not a true pyroxene. While wollastonite is a single-chain silicate and has a ratio of Si:O = 1:3, equivalent to the other pyroxene minerals (Deer, Howie & Zussman 1978), Warren & Biscoe (1931) determined that the unit cell of wollastonite differed from that of true pyroxenes, having a different type of infinite-chain silicate structure. True pyroxenes have a repeat distance, within their chain structure, equal to two silicate tetrahedra; however, wollastonite has a longer repeat distance, such that the unit cell is composed of three silicate tetrahedra. This is visualised in Figure 8.19.

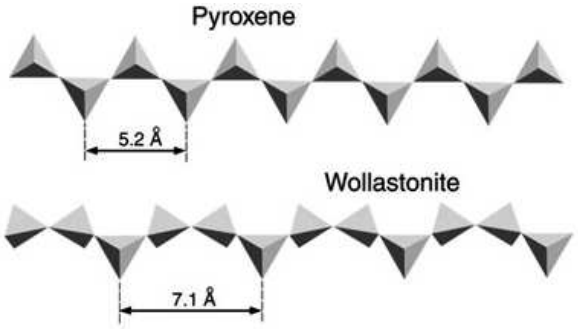

Figure 8.19: The silicate tetrahedra in the Pyroxene group of silicates link together to form long chains, sharing an oxygen atom. This figure illustrates the difference in structure between the pyroxene group and the pyroxenoids (James H. Wittke; http://www4.nau.edu/meteorite/Meteorite/Book-GlossaryP.html).

Wollastonite is therefore grouped into a separate class known as the pyroxenoids (Morimoto 1989). This creates the gap within the pyroxene quadrilateral where minerals containing $>Wo_{50}$ cannot form due to the incompatibility of the structures. This would therefore explain the crystallisation of two distinct phases, enstatite and wollastonite, observed for the $x = 0.2$ sample whose composition falls within this region (50% <Ca <100%). Additionally, the crystalline phases identified for the remaining compositions in this study all agree with the predicted mineral phases as given by Figure 8.18.

During the analysis of these data it was found that, for every composition containing magnesium ($x = 1...0.2$), there was a significant decrease of the CSD for samples annealed at a temperature of 873 K, falling from $\sim$ 20Å to $<$ 8Å. This indicates that, as a direct result of the thermal annealing, the structural coherence of the samples is reduced even further. In other words, the samples appear to have become more amorphous. In previous experiments using conventional powder diffraction (e.g. Chapter 6), the first signs of crystallisation in samples equivalent to those studied here have been observed exclusively at temperatures >1073 K. This is based on the long-range ordering of the samples, but these measurements would suggest that the local, short-range structure of the silicates is affected at a lower temperature of $\sim$873 K by the breaking of inter-tetrahedral bonds. In the amorphous state silicate tetrahedra are arranged randomly, only giving rise to very short-range structural order. There are two proposed models for the structural nature of amorphous silicates. The first is the microcrystal model (Lebiediev 1921; Randall, Rooksby & Cooper 1930a,b; Valenkow & Porai-Koshitz 1936) which suggests the formation of a domain structured material through a continuously random network that provides links between ultrafine microcrystalline regions, while the second is the Zachariasen-Warren model (Zachariasen 1932; Warren 1933, 1934) in which a continuous random network is formed with no long-range periodicity through the linking of the Si-O tetrahedra in a statistically disordered way. The amorphous samples studied here are believed to be representative of the domain structured model due to the close similarities of the structure formed for each of the amorphous samples in the region $<$ 10Å. The Si-O tetrahedra define these domains as, even with heating, the intra-tetrahedral bonds remain consistent. The features that are lost when the Mg-rich samples are heated to 873 K are representative of inter-tetrahedral distances, such as the distance between two Si atoms in neighbouring tetrahedra or the distances between successive Mg atoms within the structure. In the early stages of crystallisation, the bonds formed to produced this random structural network in the amorphous sample must be broken in order to allow the Si-O tetrahedra to re-assemble, forming the long single-chains that defined the crystalline pyroxene structure.

8.6.2 Astrophysical implications

In addition to determining the viability of a solid-gas reaction as a means of forming carbonate minerals under astrophysical conditions, it is also necessary to identify the limitations associated with this process. This experiment no only indicates that amorphous silicates do interact with gaseous CO_2 to form carbonate phases but it also places constraints on the degree of thermal annealing and on the composition of the initial silicate materials.

Based on the results presented in this chapter, we have been able to ascertain that the magnesium content of the amorphous dust analogues has a direct bearing on the success of the carbonation reaction. We find that only samples containing <50% Mg exhibit a significant structural change when exposed to gaseous CO_2 at atmospheric pressure, leading to the formation of a carbonate phase(s). This suggests that calcium more readily reacts with CO_2, leading to the formation of $CaCO_3$, while magnesium seems to actively block the reaction, also inhibiting the reaction between the CO_2 and the additional calcium within the crystal structure. This reluctance of magnesium to interact with CO_2 has also been observed by Agrinier et al. (2001) during a study to explore the reactions between CO_2 and Ca-Mg oxides (e.g. MgO, CaO and (MgCa)O). The results show that CaO exhibits a reaction with CO_2 in a very short time period < 200s, while both MgO and (Mg,Ca)O do not show any evidence of a reaction, even after >700s. They associate this with the known stability of MgO in nature where it exists in a cubic form known as periclase - a major component in marbles and ultramafic igneous rocks.

This compositional dependence would therefore suggest that, if carbonates in circumstellar environments are indeed formed through this process, they would preferentially form Ca-rich carbonates such as calcite, aragonite or vaterite over other species such as magnesite ($MgCO_3$) or dolomite ($CaMgCO_3$). The currently accepted detections of carbonates in circumstellar environments have, so far, only been able to reliably identify calcite as the main carrier of the $\sim 90\mu$m feature (Kemper, Jager & Waters 2002; Ceccarelli & Caux 2002; Chiavassa, Ceccarelli & Tielens 2005). Kemper,

Jager & Waters (2002) also attempted to associate a weak feature at $\sim$62μm in the spectrum of NGC 6302 with the magnesium-rich carbonate dolomite ($CaMgCO_3$), but this band is heavily blended with a water-ice band at 62 – 63μm and a diopside band at $\sim$65μm and is therefore ambiguous. Further analysis of these features by Posch et al. (2007) subsequently rules out dolomite as the carrier of the 60–65μm band. A compositional bias such as this could therefore provide the means to verify that the solid-gas interaction of amorphous silicates and CO_2 is the dominant process responsible for the formation of carbonates in circumstellar environments, if there is a relative abundance of Ca-rich carbonates in relation to Mg-rich carbonate species.

Additionally, we have observed that thermal annealing of the initial silicate dust analogues has a large influence on the formation process. It is found that, while the as-processed samples of $x = 0.2$ and 0 exhibit distinct structural modification after $\sim$ 16 hours of CO_2 exposure, the same samples annealed at temperatures of 573 K, 873 K and 1173 K do not exhibit any change of structure, indicating that they are resistant to the carbonation process. Due to the coarse temperature increments used for this study we can only reliably say that thermal annealing hinders the process of carbonation within the range 323 K $<T <$573 K. Finer temperature steps are required to reliably determine the temperature limit for solid-gas carbonation of amorphous silicates. This therefore places an additional constraint on the astrophysical environments in which this process can occur, limiting the temperature to a maximum of 573 K. The environments in which carbonates have been identified up to now all concur with this result, where the dust temperatures have been determined to be within the temperature range of 20 – 100 K.

8.7 Conclusions

It was found that only samples containing $< 50\%$ Mg reacted with the gaseous CO_2, leading to the formation of small amounts of the carbonate phase calcite and SiO_2. This reaction was only observed in samples of $x = 0$, 0.2 dried at 323 K and indicates that the presence of magnesium in quantities $> 50\%$ inhibits the carbonation process.

This compositional dependence would, therefore, lead to an increased abundance of Ca-rich carbonates relative to Mg-rich carbonate species and could potentially be used to verify the solid-gas interaction of CO_2 and amorphous silicates as the mechanism for carbonate formation in circumstellar environments.

These results also suggest that the temperature to which the samples have been annealed has an effect on the ability of the samples to react with CO_2. This is due to the fact that the samples at 573, 873 and 1173 K show no alteration after being exposed to CO_2 under exactly the same conditions as the lower temperature samples that exhibit a clear change in their PDFs with CO_2 exposure. This observation therefore indicates that amorphous silicates react more effectively with CO_2 than their crystalline counterparts and places an upper temperature limit on the environments in which this process could occur. This also has relevance to the sequestration of CO_2 in which the use of amorphous silicate precursors over crystalline silicates could improve the efficiency of CO_2 sequestration.

9 Non-aqueous formation of the calcium carbonate polymorph vaterite

The work presented in this chapter has been published by Day et al. (2013) in the Journal of Astronomy and Astrophysics.

9.1 Introduction

In this chapter we report on the formation of the calcium carbonate polymorph, vaterite, through a solid-gas reaction of amorphous calcium silicate powders ($CaSiO_3$) and gaseous CO_2 at elevated pressure (6–40 bar) and temperature (273 – 1223 K), with the intention of demonstrating how carbonate phases might form in non-aqueous astrophysical environments. The problems associated with the formation of carbonates in environments devoid of liquid water and the reasons behind these experiments have already been discussed in detail in Section 2.6.2 and again briefly in Section 7.1, so we will refrain from discussing this again here, instead focusing on the the significance of the vaterite phase that was formed in this experiment. We begin by giving a detailed overview of what is currently known about vaterite from the literature, especially in regard to the crystallographic structure and stability relative to the other calcium carbonate polymorphs. Obtaining the crystal structure of vaterite has been of great interest over the past few decades, but due to its inherent instability and reluctance to form large single crystals, there still remains a number of uncertainties with regard to its crystallographic structure. We then go on to discuss the experimental set-up that allowed us to obtain in situ, real time SXPD data and the pressure and temperature conditions used throughout the experiment. We then present the results and analysis of the SXPD data, followed by a discussion of the relevance of these results to the conditions pertinent to astrophysical environments.

9.1.1 The 92μm feature

Features associated with carbonate minerals have been detected in a number of circumstellar environments, exhibiting a broad peak around 92μm. The 92μm feature has been associated with calcium carbonate minerals, of which calcite, the most stable polymorph of $CaCO_3$, is predominantly suggested (Kemper, Jager & Waters 2002; Ceccarelli & Caux 2002). The feature has also been attributed to a hydrous silicate mineral montmorillonite (Malfait et al. 1999), which exhibits a broad feature at $\sim$100μm, and curved shells of graphite (known as carbon onions; Onaka & Okada 2003). Chiavassa, Ceccarelli & Tielens (2005) later identified the 92μm feature in seventeen low to intermediate mass protostars, finding that the peak of the feature shifts from source to source. For Herbig Ae/Be stars the peak lies at about 93μm, whereas for Class 0 sources the peak shifts to longer wavelengths ($\sim$105μm); Chiavassa, Ceccarelli & Tielens (2005) suggest that this is potentially due to processing of the calcite minerals or impurities within them, although it is emphasised that the composition of the material must be dominated by calcium in order to fit the observed feature.

9.1.2 Vaterite

The three predominant anhydrous calcium carbonate mineral phases are calcite, aragonite and vaterite. Of these, calcite is the most stable, with aragonite and vaterite being metastable phases, existing only under a narrow range of temperature and pressure conditions. Calcite is therefore the most abundant and as such, it is generally calcite that is attributed to carbonate features found within astrophysical environments. However, vaterite has been found in a selection of enstatite achondrite meteorites, including the Pesyanoe meteorite (DuFresne & Anders 1962) and the Norton County meteorite (Okada, Keil & Taylor 1981). The Martian meteorite ALH884001 was found to contain spherical carbonate structures that, due to their well defined shape, were initially proposed as evidence for past life on Mars (McKay et al. 1996). However, an alternative interpretation proposed by Vecht & Ireland (2000) was that

the spherical features were indicative of vaterite (metastable $CaCO_3$) known to grow in a distinctive spherical habitat, and although no longer of vateritic composition, they were likely formed inorganically by more stable carbonate phases pseudo-morphing an earlier vaterite assemblage.

Naturally forming vaterite is rarely found on Earth, predominantly occurring in association with organic tissue (Sutor & Wooley 1969) and bacteriological biomineralisation products (e.g. Rodriguez-Navarro et al. 2003; Sachez-Moral et al. 2003; Falini et al. 2005; Cacchio et al. 2004; De Muynck et al. 2008; Chen et al. 2009; Zamarreño, Inkpen & May 2009), and freshwater mollusc shells and pearls (e.g. Wehrmeister et al. 2007; Jacob et al. 2008; Soldati et al. 2008). Naturally occurring vaterite has been discovered in small amounts within zones of contact metamorphism (McConnell 1960; Kolodny & Gross 1974), drilling mud (Friedman et al. 1993) and in stagnant, natural waters, forming as a result of spontaneous precipitation (e.g. Rowlands & Webster 1971; Grasby 2003)).

Vaterite can be inorganically synthesised in the laboratory through a number of processes, including precipitation of a calcium carbonate gel from concentrated calcium and carbonate solutions (Andreassen 2005), through the decomposition of the hydrated carbonate phase ikaite ($CaCO_3.6H_2O$; Tang et al. 2009) or stabilised via biomimetic-based precipitation in the presence of organic additives (e.g. Thompson et al. 2011a,b), although these processes are often involved and, though reproducible, are often sensitive to variations in the preparation conditions. Once formed, vaterite is metastable and very soluble, more so than the calcite and aragonite polymorphs, converting into calcite in less than 25 hours at room temperature (Silk 1970) when in contact with water. In the absence of water it has been found to transform into calcite at temperatures between 730 K and 840 K (Subba Rao 1973; Peric et al. 1996).

The crystal structure of vaterite has been studied in detail over the last few decades; however, the rarity of vaterite in nature and its reluctance to form large single crystals has lead to a number of uncertainties regarding its crystallographic structure (see Table 9.1 for a summary). The main reports of the vaterite crystal structure come from Kamhi (1963) and Meyer (1960, 1969). Meyer (1960, 1969) suggests both a hexag-

onal and orthorhombic unit cell, whereas Kamhi (1963) reports a hexagonal unit cell with a prominent hexagonal pseudo-cell. These cells can be linked, and the orthorhombic cell of Meyer can be related to the hexagonal Kahmi cell via a transformation of lattice parameters (see discussion by Tang et al. 2009). More recently, LeBail, Ouhenia & Chateigner (2011), in an attempt to fit single-crystal data of vaterite, propose an $Ama2$ space group using a model based on crystal microtwinning (3 orthorhombic domains rotated by 120° to produce pseudohexagonal symmetry). Additionally, Mugnaioli et al. (2012) have used electron diffraction techniques, allowing the collection of diffraction data from single nanocrystals, to propose a monoclinic structure, with a $C2/c$ space group. Kabalah-Amitai et al. (2013) have recently used high-resolution transmission electron microscopy (TEM) to determine that vaterite is composed of at least two different crystallographic structures that coexist within a single crystal. They have identified a major structure, having hexagonal symmetry, and a minor structure believed to exist as nanodomains within the matrix of the major structure. However, carbonate anions in vaterite exhibit disorder such that their locations are still a matter of debate (Medeiros et al. 2007; Gebauer et al. 2009; Jacob et al. 2009; Wehrmeister et al. 2010). Density Functional Theory (DFT) calculations by Demichelis et al. (2012) suggest the previous $Pbnm$ and $P6_522$ structures could in fact represent unstable transition states leading towards a more stable structure with $P3_221$ symmetry. The DFT calculations suggest there are at least three distinct minima whose energies and activation barriers for interconversion are all within the accessible range of thermal energy at room temperature. Wang & Becker (2009b), however, suggest the $P6_522$ space group for a stable, fully ordered vaterite structure, obtained using first-principles calculations and molecular dynamic simulations. Therefore, the uncertainty surrounding the structure of vaterite observed in different experiments could be due to differing combinations of structures involving different symmetries.

Reference	Unit Cell Parameters (Å)			Space Grp.
Demichelis (2012)	$a = 7.12$		$c = 25.32$	$P3_221$
Mugnaioli (2012)	$a = 12.17$	$b = 7.12$	$c = 9.47$	$C2/c$
Wang & Becker (2009)	$a = 7.29$	$b = 7.29$	$c = 25.30$	$P6_522$
Le Bail (2009)	$a = 8.47$	$b = 7.16$	$c = 4.12$	$Ama2$
Kahmi (1963)	$a = 7.16$		$c = 16.98$	$P6_3/mmc$
Kamhi (1963)	$a' = 4.13$		$c' = 8.49$	$P6_3/mmc$
Meyer (1960)	$a = 4.13$	$b = 7.15$	$c = 8.48$	$Pbnm$

Table 9.1: Comparison of proposed crystal structures for vaterite from the literature.

9.2 Experimental

An amorphous calcium-rich silicate was produced via a sol-gel method, described in detail in Chapter 5, in which the metal salts $CaCl_2$, $MgCl_2$ and Na_2SiO_3 were combined in 0.1M solutions to form samples having the stoichiometric composition $CaSiO_3$ and $Mg_{0.5}Ca_{0.5}SiO_3$. Once formed, the powdered samples were stored in sealed glass vials under argon, prior to being loaded into the experimental cell. In situ SXPD measurements were taken on Beamline I11 using a position sensitive detector (PSD).

The high pressure gas cell (Thompson et al. 2012b, see Figure 9.1;) was used in order to expose the sample to high purity (99.98%) CO_2 at varying pressures (1–40 bar), and heating of the sample was performed using a Cyberstar hot air blower (Ramp rate: 10 K/min up to 1273 K) located beneath the sample capillary. Powder samples were loaded into 0.7mm diameter quartz capillaries (maximum pressure 50 bar) or 0.79mm sapphire tubes (maximum pressure 100 bar) and held in place with a quartz wool plug. It should be noted that, while the sapphire tubes are straight and have a constant diameter along their length, the quartz capillaries are tapered towards the (closed) end of the capillary; consequently they are usually smaller than their nominal diameter. It was therefore found necessary to apply greater pressure to the powder to fill the quartz capillaries, resulting in tighter packing; as discussed below this has

implications for the gas pressure required to initiate the reaction. The samples were mounted into the high pressure cell, aligned on the diffractometer and connected to the gas control system (Parker et al. 2012). Prior to connecting the sample to the system the gas supply line was pumped down to vacuum to remove air from the system and CO_2 was then injected to 1 bar.

Once the sample was mounted the CO_2 pressure was increased to 6 bar, to ensure adequate gas penetration through the length of the sample to position of the X-ray beam. However, due to the slightly smaller diameter of the quartz capillary and the tighter packing of the sample within the capillary, it was determined that an initial pressure of 20 bar was required in order to obtain adequate gas penetration through the sample and observe a reaction at the beam position.

Due to the tighter packing of the sample in the quartz capillaries, the gas is prevented from penetrating through the complete length of the capillary, instead reacting only with the material at the entrance to the capillary, outside of the section covered by the beam. In this case, the additional pressure required to observe a reaction when using the quartz capillary is not believed to be due to any difference in the sample but merely represents the additional pressure required to allow the gas to diffuse through the full length of the capillary. Thompson et al. (2012a) reported the carbonation of the same amorphous samples in a vacuum dessicator using ammonium carbonate as the source of CO_2, supporting the fact that the need for higher pressure in this study is solely due to the experimental setup, and is not necessary for such a reaction to occur.

The sample was heated steadily from room temperature (RT; 298 K) to 1223 K and data were collected at 5 K intervals. To provide sufficient powder averaging during data collection the sample capillary was rocked $\pm 15^{\circ}$ about its length. Every scan with the PSD took 10 seconds. For subsequent samples the pressure was increased at ambient temperature, in steps of 10 bar, up to a maximum pressure of 40 bar.

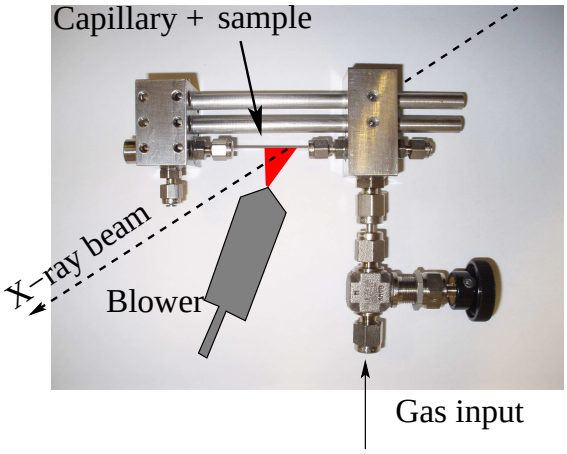

Figure 9.1: High pressure gas cell with sapphire tube. X-ray beam is at a right angles to the capillary.

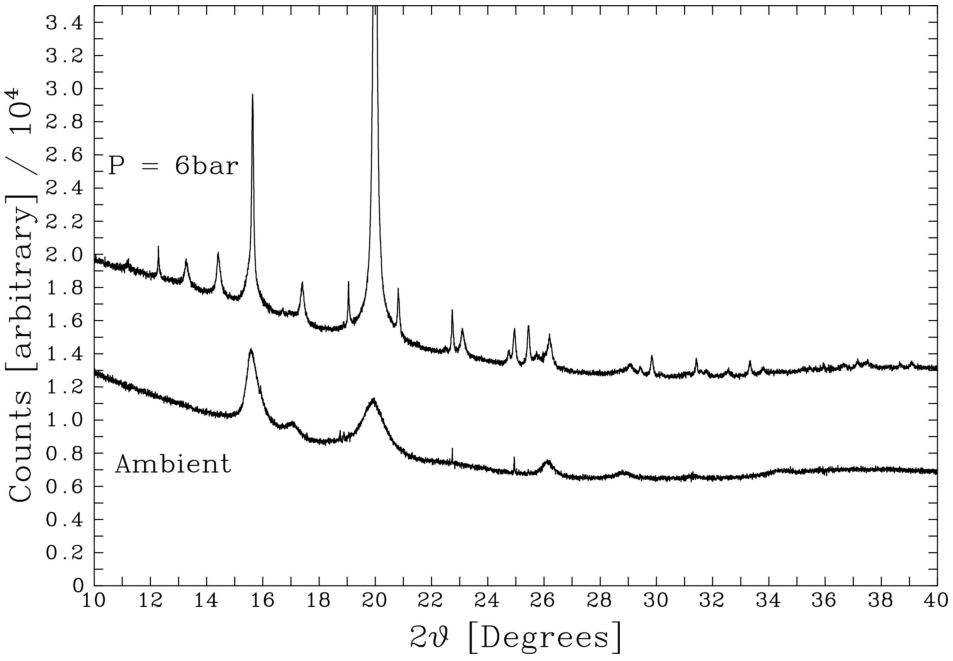

Figure 9.2: A comparison of the diffraction patterns for the powdered sample of $CaSiO_3$ before (lower curve) and after (upper curve) the injection of CO_2. The strong feature at 19.97° 2θ is due to the sapphire tube. Patterns are offset in the y-axis.

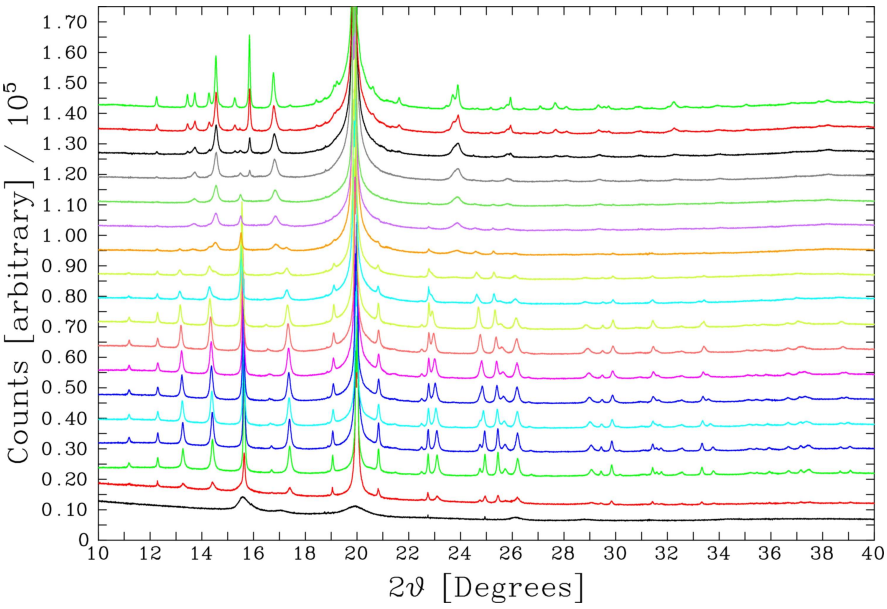

Figure 9.3: Thermal evolution of $CaSiO_3$ exposed to CO_2 at 6 bar. The lowermost pattern was taken at room temperature, with subsequent patterns increasing in temperature from 373 K to 1173 K in 50° steps. Patterns have been offset on the y-axis for clarity and temperature is increasing upwards
. The strong feature at 19.97 2θ is due to the sapphire tube.

9.3 Results

Upon initial injection of CO_2, at a pressure of 6 bar, into the larger diameter sapphire tube, the formation of a crystalline carbonate phase was observed almost instantaneously. Figure 9.2 shows a comparison of the initial SXPD pattern of the $CaSiO_3$ sample under vacuum at ambient temperature and the first SXPD scan taken as the CO_2 was opened to the sample. Injection of CO_2 triggered the formation of a crystalline phase.

Once crystallised the sample exhibits multiple strong, well-resolved features, suggesting a well ordered crystalline structure. The distinctive groups of features at 10° – 14.5° , 22° – 24° and 25° – 27° 2θ are attributed to vaterite, while the remaining

features at 12.2°, 15.8°, 19.1° and 20.9° 2θ are due to calcite. Peak search-match software Match![1] suggested that the pattern could be fitted by a mixture of the calcium carbonate phases vaterite and calcite.

The pressure was held at 6 bar at RT for approximately 30 minutes. During this time the structure continued to evolve, with the peaks steadily growing in intensity; this was accompanied by a slow but steady decrease in the CO_2 pressure at the sample. We should note however, that we cannot rule out the presence of an amorphous silicate component remaining in the sample; evidence suggests that the amorphous silicate component anneals at higher temperatures, or after prolonged exposure (∼5 hours) at T >1220 K (Fabian et al. 2000, and Chapter 6).

9.3.1 Thermal evolution

Heating of the sample was initiated after 30 minutes at a pressure of 6 bar. During this time the CO_2 pressure dropped steadily, an indication of the reaction still occurring, and was topped up to 6 bar when the pressure dropped below 4 bar (after approximately 2.5 hours). The experiment was then left to run overnight, with scans being taken at 5 K intervals (approximately every 3 mins) between RT and 1223 K, during which the pressure had dropped and settled at 2.6 bar. The results of this are plotted in Figure 9.3, presenting a selection of patterns at roughly 50 K increments. These show that, following the initial formation of the carbonate phases, they remain relatively stable during heating until the temperature exceeds 753 K, at which point the carbonate phases start to break down and the sample begins to anneal, finally crystallising, at $T>$ 1083 K, to wollastonite ($CaSiO_3$). This is discussed in greater detail in Section 9.3.3.

[1]Crystal Impact http://www.crystalimpact.com/match/

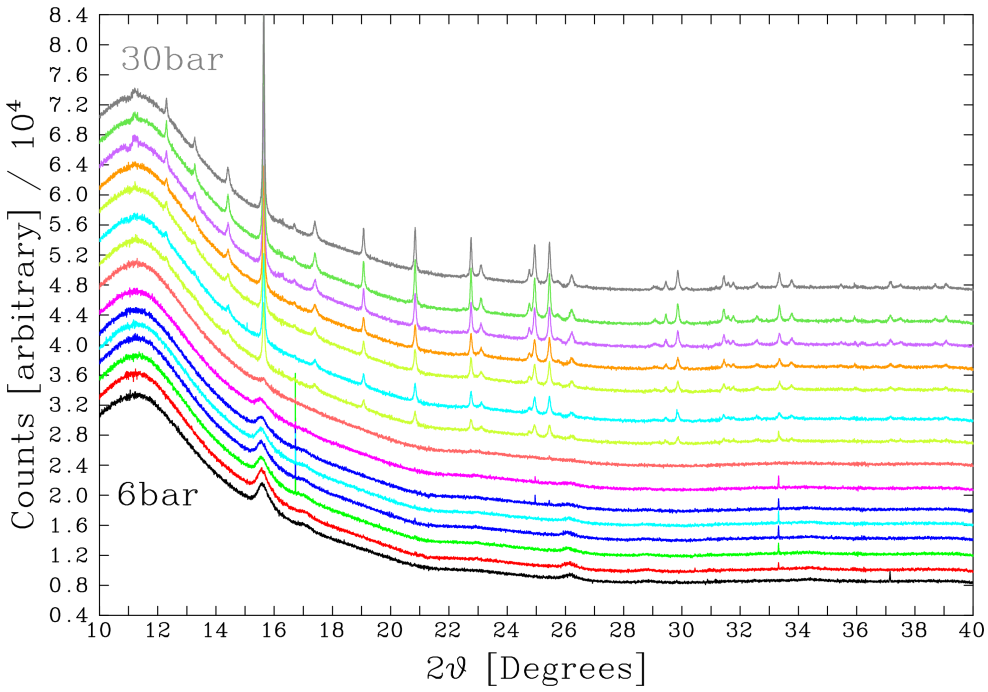

Figure 9.4: Evolution of $CaSiO_3$ in quartz capillary with increasing pressure of CO_2. Patterns have been offset on the y-axis for clarity and high backround is due to the quartz capillary. Pressure increases upwards from 6 bar to a maximum of 30 bar.

9.3.2 Pressure dependence

Due to the strong features in the diffraction patterns caused by the use of a sapphire tube it was decided to perform further experiments using quartz-glass capillaries. As before, the sample of amorphous $CaSiO_3$ was initially exposed to a CO_2 pressure of 6 bar; however, scans indicated that no major structural changes occurred upon exposure to the gas. The pressure was held at 6 bar for 10 minutes, during this time two very sharp, intense peaks appeared at 16.72 and 33.32° 2θ . These correspond to Bragg reflections of calcite, but the intensities are much higher than expected, indicating insufficient powder averaging and therefore likely result from the localised carbonation of a small number of isolated particles, some of which happen to lie in the Bragg

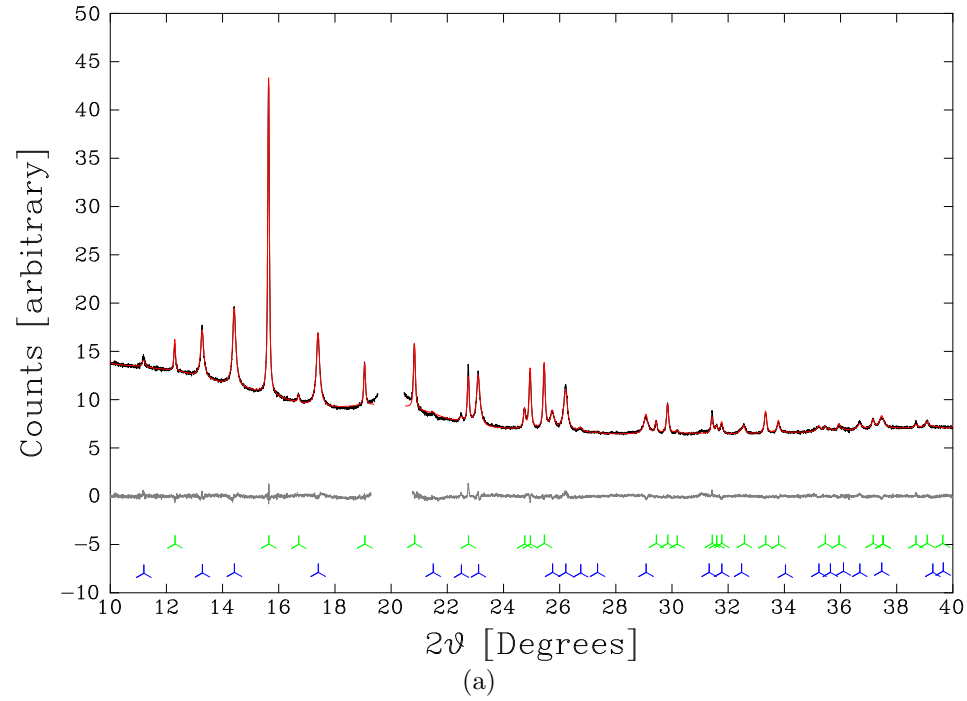

(a)

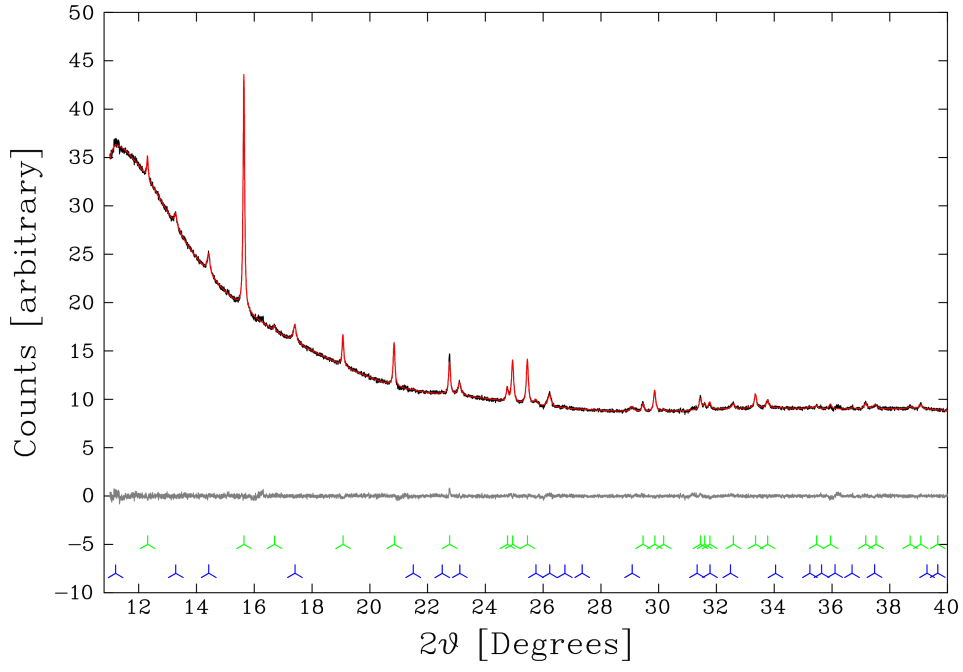

(b)

Figure 9.5: Sample rietveld refinements of powder patterns exhibiting vaterite and calcite peaks. The red curves show the fit, the grey curves show the difference curve and the markers indicate the positions of the individual vaterite (blue) and calcite (green) peaks. a) Initial sample exhibiting vaterite features in sapphire capillary. The sapphire capillary exhibits a strong peak at 19.97° 2θ which has been removed from the plot. b) Powder pattern exhibiting vaterite peaks at a CO_2 pressure of 30 bar in quartz capillary.

condition. As further crystallisation occurs, these particles are taken out of the Bragg condition and full crystallisation occurs at higher pressures.

The pressure was then increased to 10 bar and held for 15 minutes, during which the features at 16.72° and 33.32° 2θ were observed to diminish with time. Before they disappeared completely, the pressure was increased to 20 bar. Initially, there was no observable effect on the structure; however, after approximately 15 minutes at this pressure the steady growth of multiple crystalline features, due to calcite and vaterite phases, was observed. A further increase in pressure up to 30 bar appeared to accelerate the rate of carbonation, increasing the peak intensities, but did not produce any further changes to the phase structure. Figure 9.4 shows a selection of SXPD patterns as a function of increasing pressure, showing the evolution of the sample.

9.3.3 Thermal evolution of $CaSiO_3$

Figure 9.5(a) shows the result of a Rietveld structure refinement using the TOPAS-Academic software package (Coelho 2007) and published lattice parameters for vaterite and calcite as starting values. The published lattice parameters used in the refinement were obtained from the ICSD reference database[2] and are shown in Table 9.2. The vaterite phase was fit with the hexagonal pseudo-cell of Kamhi (1963), with unit cell parameters of $a' = 4.13$ Å and $c' = 8.49$ Å and space group $P6_3/mmc$. The reduced hexagonal cell structure was chosen over the larger hexagonal structure of Kamhi (1963) (see Table 9.1) as it provided the best fit to our data. The modelled fit is shown in Figure 9.5(a) along with the difference pattern between the overall fit and the measured data. The strong peak at 19.97° 2θ is due to the sapphire capillary and has therefore been excluded from the fit. The two phase fit produced agreement factors of $R_{wp} = 1.78$ % and $R_{exp} = 1.05$ with a goodness of fit (GoF) of 1.69; the very low R-factors relate to the high background present in the data.

[2]FIZ Karlsruhe http://cds.dl.ac.uk/cds/datasets/crys/icsd/llicsd.html

The refined lattice parameters and the calculated weight percentage of each phase are shown alongside the published values in Table 9.2. The refined parameters do not differ significantly from the reference values.

Vaterite – Space Group: $P6_3/mmc$				
Capillary		a' (Å)	c' (Å)	Wt %
	Published	4.13	8.49	
Sapphire	Refined	4.1226 (1)	8.4653 (3)	65.5(4)
Quartz	Refined	4.1227 (4)	8.462 (1)	50.2(4)

Calcite – Space Group: R-3c				
Capillary		a (Å)	c (Å)	Wt %
	Published	5.05	17.32	
Sapphire	Refined	4.9869 (1)	17.0492 (4)	34.4(4)
Quartz	Refined	4.9844 (4)	17.058 (1)	49.7(4)

Table 9.2: Published and refined lattice parameters for vaterite and calcite phases. Published values obtained from the ICSD database. Values given are from samples at room temperature and initial formation pressure; 6 bar for sapphire, 20 bar for quartz.

Figure 9.6 is a plot of weight percentage against temperature for the vaterite, calcite and wollastonite phases, with values taken from a batch refinement of selected data sets at approximately 20 K temperature intervals. This provides a more detailed view of what is happening, with regards to composition of the sample at higher temperatures (>800 K). From this we can clearly see that, at lower temperatures, the vaterite and calcite phases remain fairly stable, with the relative weight percentage of vaterite increasing by just 3% over a period of approximately 5 hours. However, once the temperature reaches 723 K the percentage of vaterite begins to fall, being replaced by an increasing amount of calcite. The weight percentage of vaterite continues to fall gradually until calcite supersedes it at a temperature of 770 K. At a temperature

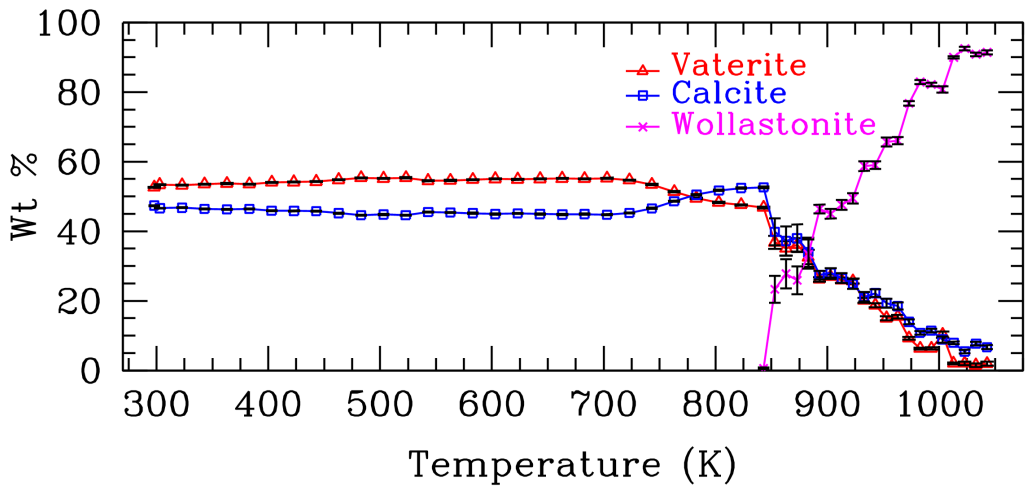

Figure 9.6: Weight percentage against temperature for calcite and vaterite phases of initial $CaSiO_3$ sample in a sapphire capillary, at a pressure of 6 bar. Where error bars are not visible they are smaller than the plotted data points.

of 840 K, wollastonite begins to crystallise and can be included in the fit; this phase then quickly dominates the sample as it continues to crystallise at higher temperatures. Figure 9.3 indicates that at a temperature of 973 K, the carbonate peaks have almost disappeared, appearing as weak, broad features, indicating that the carbonate phases are not stable at such temperatures and have broken down, this is also evidenced in Figure 9.6 as the amount of vaterite and calcite within the sample at this stage are less than 10 %. This leads to the sample fully annealing at a temperature of 1103 K to fully crystalline $CaSiO_3$(wollastonite). Alternatively, plotting lattice parameter a against temperature for the vaterite phase indicates a slight thermal expansion between RT and 943 K, this provides a thermal expansion coefficient of $\sim 5 \times 10^{-5}$ K^{-1} (see Figure 9.7).

9.3.4 $CaSiO_3$ in quartz capillary

The crystalline phase formed at a pressure of 20 bar on the second run was identified as also being a combination of calcite and vaterite. Refinement of the data using initial crystallographic parameters obtained from the ICSD database, confirmed this. A typical fit is shown in Figure 9.5(b) with the initial and refined parameters and calculated weight percentages listed in Table 9.2.

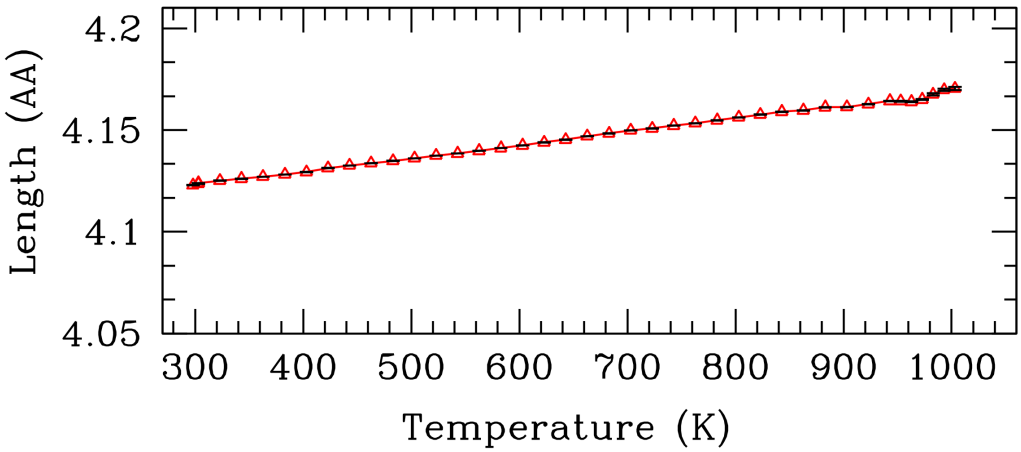

Figure 9.7: The effect of temperature on lattice parameter a for the vaterite phase. Sample in a sapphire capillary at a pressure of 6 bar.

The refined values are in good agreement with published values and the refined values for the sapphire capillary sample. Figure 9.8 shows the weight percentages of the two phases plotted against pressure and it can be concluded that once the two phases have been formed, they remain relatively stable. An increase in pressure does not appear to have a significant effect on the composition of the two phases.

9.3.5 $Mg_{0.5}Ca_{0.5}SiO_3$ in quartz capillary

The same method was used for a sample of $Mg_{0.5}Ca_{0.5}SiO_3$, loaded into a quartz capillary, with no discernible change in structure with pressure. A maximum pressure of 40

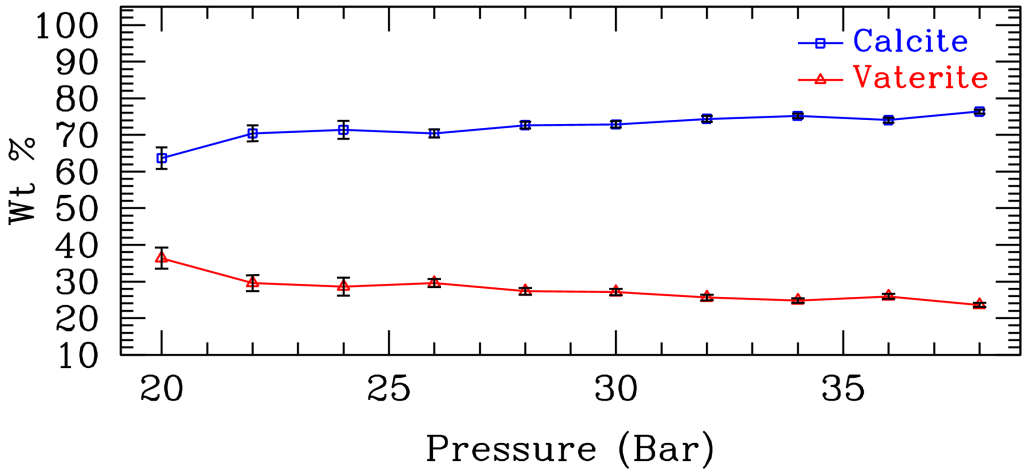

Figure 9.8: Weight percentage against pressure for calcite and vaterite phases at room temperature. Initial sample of $CaSiO_3$ in quartz glass capillary. Where error bars are not evident, they are smaller than the plotted data points.

bar was attained and the sample was held at this pressure for 30 minutes; however, the scans suggest that the structure of the sample was not affected by the presence of CO_2 at high pressures. This reinforces our findings in the previous chapter (Chapter 8), in which Mg-rich samples exposed to CO_2 at atmospheric pressure did not undergo carbonation, and indicates that the presence of Mg ions in the silicate structure are very effective in blocking this process, even under high pressures. However, the initial scan of this sample under ambient conditions showed evidence of carbonation occurring prior to the sample being mounted on the beam; it is likely that this carbonation occurred early on during the sample formation process in which atmospheric CO_2 could have reacted with the Ca in solution, prior to its incorporation into the silicate structure.

9.4 Discussion

9.4.1 Formation of vaterite

As discussed in the introduction vaterite is, with respect to aragonite and calcite, the least stable of the anhydrous calcium carbonate phases. Its formation in the present study is therefore interesting, either as a possible component of dust grains, or as a possible metastable precursor phase for the calcite grain component currently attributed to the 92μm feature (Kemper, Jager & Waters 2002). We have shown that the calcium carbonate phase vaterite can be formed through the solid-gas interaction of amorphous calcium-rich silicates and gaseous CO_2 at an elevated pressure of 6 bar. While the kinetics of the transformation into calcium carbonate are dependent on the initial packing density of the powdered $CaSiO_3$ sample, as discussed in Section 9.2, the selection of vaterite over the more thermodynamically stable calcite is likely to be due to material-dependent factors. In the following paragraphs we draw on the results of experiments regarding vaterite formation in other fields to show that the preferential stabilisation of vaterite in the present case likely arises from the presence of SiO_2 anions.

Due to its industrial and commercial potential, there is a large body of literature that shows vaterite can be stabilised (often temporarily) in the presence of various different ions or organic and inorganic additives under widely differing experimental conditions, most of which are concerned with in vitro formation (e.g. Wray & Daniels 1957; Nassrallah-Aboukais et al. 1998; Nothig-Laslo & Brečvić 1999; Han et al. 2006; Nebel & Epple 2008; Wang et al. 2009; Fernandez-Daz 2010; Gomez-Morales et al. 2010), or as a post-formation coating (Vogel et al. 2009). The origin of these stabilisation effects likely lies in the fact that vaterite, aragonite and calcite all have very similar values for their free energy (0.5–3 kJ/mol differences; Plummer & Busenberg 1982; Wolf et al. 1996, 2000; Baitalow, Wolf & Schmidt 1998). Relatively small changes in either the surface area (i.e. small particle size), or in the concentration of impurities, can change their stabilisation properties such that the order of their thermo-

dynamic stabilities becomes inverted (Navrotsky 2003, 2004). Similar thermodynamic crossovers are observed for several metal oxide systems, including the TiO_2 polymorphs (rutile, brookite and anatase; Ranade et al. 2002) and the iron oxide phases (Navrotsky, Mazeina & Majzlan 2008) and can mean that the least stable phases, in the present case vaterite, are often preferentially formed. However, many experimenters (see papers cited above) have reported that, although outcomes are highly reproducible, the actual outcome is also highly dependent on changes in conditions in a non-systematic way (e.g. Pai, Jansson & Hedin 2009; Ren et al. 2009), suggesting that kinetic factors may also be important. It is also relevant to note Ostwald's Law of Phases, which states that, due to the lower energy barrier of more disordered states, the pathways to final crystallisation of the most stable phase will pass through all less stable phases in order of increasing stability.

Calcium carbonate formation in the presence of various silicates and oxides was also investigated by Lin et al. (2009), who identified a correlation between the surface charge provided by the silicate/oxide and the choice of phase stabilised. Negative surface charge favoured the metastable vaterite and aragonite phases, while positive charges produced calcite. In crystalline silicates, the possible charge sites are limited by the crystal structure: planar regions which have a negative structural charge and edge regions whose charge arises from the protonation/deprotonation of surface hydroxyls at the side of stacking structures (sheets, chains etc.). Lin et al. (2009) found amorphous SiO_2 did not follow the surface charge rule and always stabilised calcite. However, they attributed this to the gel phase that forms when SiO_2 is exposed to water, suggesting that the hydrated porous nature of the gel is not compatible with epitaxial growth and therefore no templating effect is exerted on carbonate nucleation, allowing calcite to form rather than vaterite or aragonite.

Assuming all the Ca atoms eventually participate in $CaCO_3$, for carbonate formation to proceed via the gas-solid reaction in $CaSiO_3$ necessitates the formation of SiO_2, providing a free ionic species, while the absence of liquid water will negate the formation of a gel phase, allowing SiO_2 tetrahedra to either be partially incorporated into the the carbonate structure, as suggested by Gal, Weiner & Addadi (2010) and

Lakshminarayanan & Valiyaveettil (2003); or, to exert a templating surface charge effect on the forming carbonate as suggested by Lin et al. (2009). Since carbonation will occur at the Ca sites within the silicate structure, the initial small size of the carbonate could also contribute to the carbonate free energy to produce a Navrotsky stability inversion and similarly favour the stabilisation of vaterite. The fact that some calcite is also initially formed which, in the second experiment, was observed to be unstable possibly points to contributions such as particle size and remaining silicate "impurities" also influencing phase stabilisation priorities. We also acknowledge that kinetic factors may play a role in determining vaterite stabilisation and subsequent growth, particularly as our initial gas injections were performed at room temperature and relatively high gas pressures to overcome sample packing density. However, these effects are also likely to favour the formation of disordered structures, i.e. vaterite rather than aragonite or calcite.

The vaterite formed in both cases appears to be of the same structure, both refine well using the hexagonal pseudo-cell values of Kamhi (1963). Table 9.2 lists the refined lattice parameters for vaterite at room temperature from both sources. The values are in good agreement with each other, suggesting that, although formed independently, the structure of the vaterite is reproducible.

9.4.2 Relevance for cosmic dust

A band near 90μm was first discovered by Kemper, Jager & Waters (2002) in the spectrum of the PNe NGC 6302, followed by detections in the Class 0 proto-star IRAS 16293 and two HII regions (Ceccarelli & Caux 2002; Takashi & Yoko 2003); a subsequent survey of low mass proto-stars showed the feature to be common in such regions (Chiavassa, Ceccarelli & Tielens 2005). The circumstellar feature at $\sim$92μm was attributed by Ceccarelli & Caux (2002) to calcite, who ruled out the metastable aragonite phase on the basis that its 92μm feature is too weak and that its formation nominally requires high pressures and temperatures. Whether vaterite exhibits an observable FIR feature, or indeed could be a possible candidate for the carrier of the 92μm feature, is

difficult to assess. There are, to our knowledge, no published FIR spectra for vaterite (e.g. review of carbonate spectroscopy by Brusentsova et al. 2010), likely made difficult due to a combination of its low thermal stability in respect of producing polyethelene pellets and the difficulty of producing or obtaining a pure specimen. However, the lattice mode vibrational region is accessible by Raman spectroscopy, exhibiting a feature at $\sim$105cm^{-1} ($\sim$91μm) in the Raman spectra of 5 different vaterite samples (see Figure 9.9). While lattice modes that are Raman active will not necessarily also be IR active, due to selection rules, structural disorder within the material, identified by broading of Raman feature widths in the lattice mode region, imparts a symmetry reducing effect which can in principle lead to the relaxation of the Raman and IR activity selection rules, allowing certain bands to become both Raman and IR active (e.g. White 2005; Hernández et al. 1997; Duley, Lazarev & Scott 2005; Hopkinson, Rutt & Cressey 2008; Abe & Shigenari 2011). This therefore supports the likelihood that vaterite would indeed possess a feature at $\sim$91μm in the FIR and identifies that measurements of vaterite in the FIR should be made a matter of priority. This is discussed in greater detail in Section 5.3 of Day et al. (2012).

Although the operational pressures required for this experiment arise from the need to provide adequate diffusion of CO_2 along the length of the sample capillary, we believe similar interactions involving silicates in circumstellar outflows could occur at much lower pressures. However, even if this is not the case the formation of carbonate via this route may still be directly relevant to proto-stellar and proto-planetary envionments, where carbonates formed at higher pressure on, or in, planetesimal objects could be released as dust grains via disruptive collisional events.

9.5 Conclusions

In this chapter we have discussed the formation of the rare calcium carbonate polymorph vaterite through the solid-gas interaction of amorphous silicates, produced as cosmic dust analogues, and gaseous CO_2 at pressures >6 bar. In situ synchrotron

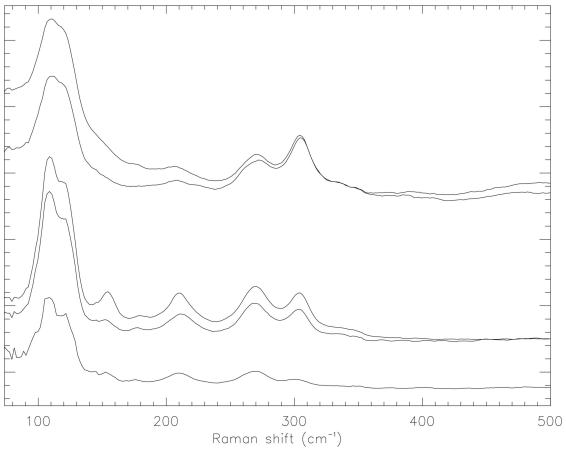

Figure 9.9: Raman spectra for samples of $CaCO_3$ vaterite produced by biomimetic synthesis, showing a strong lattice mode feature at $\sim$ 100 cm^{-1}. Spectra offset in y-axis direction for clarity and y-axis scale is arbitrary.

X-ray powder diffraction was used to observe the structural evolution of the material during its formation and subsequent heating to a temperature of 1173 K. We determined a range of stability between 6 – 30 bar and 298 K – 923 K, a much wider range than previously seen for vaterite. This has relevance to the surface compositions of Venus and ancient Mars (van Berk, Yunjiao & Ilger 2012), where the CO_2 pressure at the surface is sufficiently high for this kind of reaction to occur. Vaterite has been regarded as important due to the fact that it is rarely formed naturally and therefore its presence is usually taken as being indicative of biogenic processes. Our alternative, inorganic method provides evidence that vaterite found in Martian meteorites and on the surface of Venus and Mars are not necessarily proof of bioactivity but could have formed naturally through a processes similar to those that we describe here.

10 Formation and stability of clathrate hydrates

10.1 Introduction

10.1.1 Clathrate structure

A clathrate is a specific form of inclusion compound in which molecules of one substance (the guest) are completely trapped within 'cages' formed by the crystal lattice of another (the host), as illustrated in Figure 10.1. Clathrate compounds are typically composed of organic substances, such as polymers, but they can also be formed by water-ice and some microporous minerals, such as zeolite. Clathrates in which the host species is water, such as those being studied in this chapter, are more commonly referred to as clathrate hydrates.

Clathrate hydrates are known to form different structures depending on the nature and size of the guest molecules being trapped. Clathrates are known to naturally

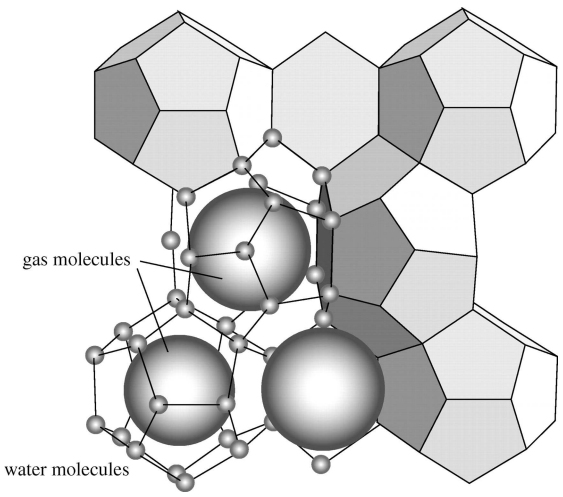

Figure 10.1: Illustration of a clathrate structure, trapping gas molecules within lattice cages formed by water molecules Maslin et al. (2010).

form three independent structures, designated sI, sII and sH (Sloan 2003; Sloan & Koh 2008), although other structures have been reported that are much more rare (Jeffrey 1984). The three structures are determined by the size, shape and arrangement of the cages formed, as summarised in Figure 10.2.

The basic unit for all three of the clathrate structures is the 5^{12} cage (i.e. 12 pentagonal faces joined to form a pentagonal dodecahedron), which also forms the basis for the model of pure water by Pauling (1959) and later confirmed by Geiger, Stillinger & Rahman (1979) and Plummer & Chen (1983, 1987), in which the guest molecule is also water. It is, however, not possible to form a stable structure with just 5^{12} cages, so to avoid breakages and strain of the hydrogen bonds, interstices between 5^{12} cages are filled with other cages (Sloan 2003). Structure I (sI) clathrates are composed of two cage types, the 5^{12} cage and a larger $5^{12}6^2$ cage (i.e. 12 pentagons, 2 hexagons) with a ratio of two small cages to every six large cages, and commonly host larger guest molecules such as CH_4 and CO_2. Structure II (sII) clathrates also consist of two cage types, 5^{12} and $5^{12}6^4$, at a ratio of sixteen small cages to eight large. As the sII structure contains twice as many small cages as large it is therefore much more suited to the trapping of smaller molecules such as O_2 and N_2. Structure H (sH) clathrates are less common and are composed of three cage types, namely 5^{12}, $4^3 5^6 6^3$ and $5^{12}6^8$, where the size of the $4^3 5^6 6^3$ cage falls in between that of the small and the large cages. The ratio of the cages making up the unit cell of the sH hydrate is three small cages to two medium cages to one large cage, and require at least two species of guest, filling all cages, in order to remain stable (Ripmeester et al. 1987; Ripmeester & Ratclife 1990).

The stability of clathrate hydrates is heavily dependent on the structure of the clathrate formed, however the necessary conditions for the formation of clathrate hydrates are very specific. They form only under low temperature (< 300 K) and high pressure (> 0.6MPa) regimes and are typically at their most stable under these conditions, however they have been found to coexist with ice and/or liquid water over a much larger range of temperatures and pressures (Sum, Koh & Sloan 2009). The stability of the clathrate structure arises from a delicate balance of hydrophobic and

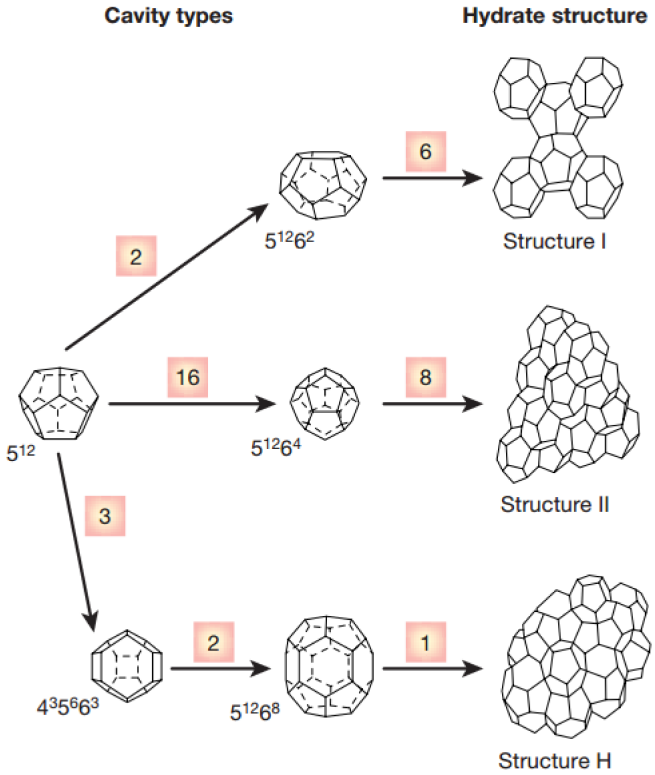

Figure 10.2: The three most common crystal structures of clathrate hydrates. After Sloan (2003)

hydrophylic interactions between the guest molecules and the water-ice lattice (Sum, Koh & Sloan 2009), therefore clathrates are very sensitive to changes in temperature and pressure.

10.1.2 Astrophysical importance

Over recent years, clathrate hydrates have been increasingly believed to be present on a number of bodies within the Solar System as a means of explaining a number of different phenomena observed by exploratory spacecraft.

Lunine & Stevenson (1985) used statistical thermodynamic calculations to produce stability curves for clathrate hydrates at temperature and pressure conditions of interest to Solar System studies. They obtained calculated stability curves for for a number of guest species, including CO, He, H_2, CO_2, Xe, Kr and O_2, over a pressure range of 10^{-12} – 10^3 bar, spanning the conditions present in gaseous nebulae, the surfaces of planetary bodies and even at the interiors of small icy bodies. They concluded that clathrate hydrates would have been formed in the turbulent, early solar nebula and would therefore have become incorporated into icy grains that subsequently went on to form early planetesimal objects. The formation of clathrates during this period in the formation of the Solar System could therefore explain the depletion of certain gases, relative to the the solar abundance, on a number of planetary bodies.

Iro et al. (2003) propose the presence of clathrates on cometary bodies as the source of N_2 depletion observed in some cometary bodies (including comets Halley and Hale-Bopp). They suggest that the depletion of N_2 relative to CO is due to the formation of clathrates within the solar nebula that then became incorporated into comets. Based on the previous calculations of Lunine & Stevenson (1985), predicting that CO is trapped in clathrates much more efficiently than N_2, they determine that where the amount of water-ice in the solar nebula was limited, not all CO and N_2 would be trapped, instead CO would preferentially be incorporated into clathrates that then went on to form cometary bodies - leading to a depletion of N_2 relative to the abundance calculated for the solar nebula. Similarly, Marboeuf et al. (2010)

show that the conditions in the interior of Halley-type comets allow for the existence of stable clathrate hydrates and propose that the disassociation and reformation of a significant volume of such clathrates would explain the compositional diversity of the volatiles being released from such comets.

The Huygens probe (Lebreton & Matson 2002), on its descent to the surface of Titan, detected a significant depletion of the noble gases Xe and Ar in its atmosphere (Niemann et al. 2005) and the incorporation of these gases into clathrate hydrates either at the surface of Titan or in sub-surface reservoirs are postulated as the source of their deficiency (Osegovic & Max 2005; Mousis et al. 2009). Theoretical investigations (Thomas et al. 2008) at temperatures relevant to Titan's surface (95 K at P = 1.47 bar) show that the trapping efficiency of clathrate hydrates on the surface of Titan is sufficient to reduce the atmospheric levels of noble gases to those measured by Huygens, forming a thin (e.g. $\sim$ few m) clathrate crust across the surface. These investigations have so far focused on the depletion of noble gases occurring within Saturn's sub-nebula during the formation of Titan. However, Mousis et al. (2011) have more recently suggested that the noble gas depletion could have occurred much later, on the surface of Titan due to surface- atmosphere interactions. It is proposed that the water-ice required for the formation of clathrates on the surface of the satellite could be produced by periodic episodes of cryovolcanism, leading to the formation of clathrates in the porous lavas, progressively removing the gases over the course of Titan's history. Niemann et al. (2005) also identifies the potential for methane storage in a large clathrate reservoir below the surface of Titan which would provide the means for the periodic replenishment of methane. High-pressure experiments conducted by Choukroun et al. (2010) to determine the stability of methane clathrates under these conditions find that the outgassing of methane clathrates in Titan's icy crust could only occur in the presence of large amounts of ammonia. They suggest that a large cryovolcanic event would be sufficient to sustain methane in Titan's atmosphere for $> 10^4$ years.

Titan's neighbouring satellite, Enceladus, could also harbour a clathrate reservoir just below its thick icy crust (Kieffer et al. 2006; Porco et al. 2006), the periodic

dissociation of which would lead to the powerful plumes observed emanating from the surface of Enceladus by the Cassini spacecraft (Formisano et al. 2004). The plumes contain water (as vapour and ice), as well as volatiles such as CO_2, CH_4 and N_2, and organics (Waite et al. 2009). Water-ice and complexed CO_2 are surface components of Enceladus, while the other gases detected within the plumes are known to have very poor solubility in liquid water. It is, therefore, very unlikely that these components would be present in an aqueous phase, and so their presence is inferred due to the trapping of the gases in the form of clathrate hydrates. Indeed, understanding the surface environment of Enceladus is currently of major interest as it bears directly on whether there are sub-surface 'oceans' capable of harbouring life. The crust is believed to consist of a 3.5km thick ice cap, overlying the clathrate reservoir.

In addition, the observed release of methane into the Martian atmosphere (Prieto-Ballesteros et al. 2006; Mumma et al. 2009) has similarly been attributed to the destabilisation of clathrates buried in the Martian subsurface (Englezos 1993).

The majority of these reports are theoretical and while much experimental work has been done to study the nature and stability of clathrate hydrates in the past these have predominantly been limited to temperature and pressure conditions relevant to terrestrial environments. The models describing clathrate behaviour in astrophysical environments, while based on sound theoretical principles, have yet to be tested experimentally, due in no small part to the (historic) difficulties (high pressures, long timescales and difficult formation environments unsuited to in situ studies (Collett & Kuuskraa 1998)) associated in both producing and monitoring the dynamic behaviour of gas hydrates.

10.1.3 Terrestrial importance

Clathrate hydrates are also of significant commercial importance. The most abundant reserve of hydrocarbons on Earth is in the form of methane gas trapped within clathrate structures (Kvenvolden 1995), buried in deep marine sediments and within Arctic permafrost. Exploiting this potential energy reserve in a way that is both

safely and economically viable is incredibly challenging due to the unstable, volatile nature of clathrates and to a lack of experimental data on the dynamic behaviour of clathrates under a range of conditions. Methane clathrates have also been associated with the largest mass extinction event in Earth's history, the Permian-Triassic extinction at 251Ma, in which it is possible that the destabilisation of clathrates injected large amounts of methane into the atmosphere (Ryskin 2003; Kiehl & Shields 2005). The potential of clathrate hydrates in the sequestration of CO_2 has also been noted by Chatti et al. (2005), along with their use in gas storage and transportation. Additionally, H_2 clathrates are also receiving much interest as potential hydrogen storage materials (Lee et al. 2005).

In this chapter we present preliminary work focusing on the study of clathrate hydrate compounds under conditions relevant to astrophysical environments. We perform in situ SXPD, along with in situ Raman spectroscopy in order to study the formation and stability of clathrate hydrates with a selection of astrophysically relevant gases (CO_2, CH_4, Xe and Kr).

10.2 Experimental

A simple gas cell system was used to study the formation and subsequent evolution of a selection of clathrate hydrate compounds. The guest species used for this experiment were CO_2, CH_4, Xe and Kr, although the main focus at this stage is the formation of CO_2 hydrates. Deionised water, with a resistivity of 18.2MΩ, was used as the host. Approximately 19.2mm^3 of deionised water was loaded into a 0.7mm diameter quartz capillary which was then placed into the gas cell and mounted onto the theta circle of the diffractometer. SXPD measurements were once again taken using the PSD, with two 10s scans taken at 0.25° apart and summed together to account for gaps between the detector units. Temperature control was provided by a LN2 Cryostream (Oxford Cryostreams), with a temperature range of 80 K – 300 K, and the gas pressure was controlled using an in-house gas delivery system (as described in Parker et al. 2012,

and Chapter 7) providing a pressure range from 30 mbar up to a maximum of 40 bar (limited by the capillary). The gas pressure can be measured to an accuracy of ± 0.01 bar, while the temperature reading provided by the Cryostream has a stability of 0.1 K, measured at the tip. The temperature values stated in this chapter are taken directly from the Cryostream, not at the sample position, therefore it likely that the actual value at the sample is in the region of ± 10 K of the given values. The experimental setup is shown in Figure 10.3(a), along with a close-up view of the gas cell used in this experiment (Figure 10.3(b)). High purity (> 99%) gases were used and the gas system was thoroughly flushed out between gases to avoid contamination.

In addition, we complemented the SXPD data with Raman spectra, obtained using the in situ, Raman spectrometer (with 532nm laser) providing parallel spectroscopic information regarding the molecular state and host-guest structural interactions during formation and processing of the clathrate structure. The Raman was calibrated to operate at no more than 40% of the maximum power (500mW) and scan times were limited to between 10-15 seconds, as to not affect the structure of the sample.

Clathrate formation is a two step nucleation and growth process and the time limiting factors in the experiment include (a) slow gas diffusion following initial nucleation, particularly at low injection pressures; and (b) a maximum temperature ramp rate available from the Cryostream of 10 K/min. The conversion of ice to clathrate is understood to be a temperature-dependent process, and based on neutron diffraction measurements by Henning et al. (2000), complete conversion is achieved by keeping the sample at pressure and increasing the temperature past that of the melting point of ice. We therefore used this information as a basis to observe clathrate formation, however, it should be noted that the gas pressures used in this study are far lower than those of Henning (60 bar).

Initially, the water was cooled to 100 K (simulating the temperature at Titan's surface); however, the formation of clathrate at this temperature is extremely slow and would likely require days to observe significant conversion; subsequent samples were frozen at 200 K. The gases were then introduced to the sample at various pressures (10 – 30bar), at which point the temperature was slowly increased to initiate the formation

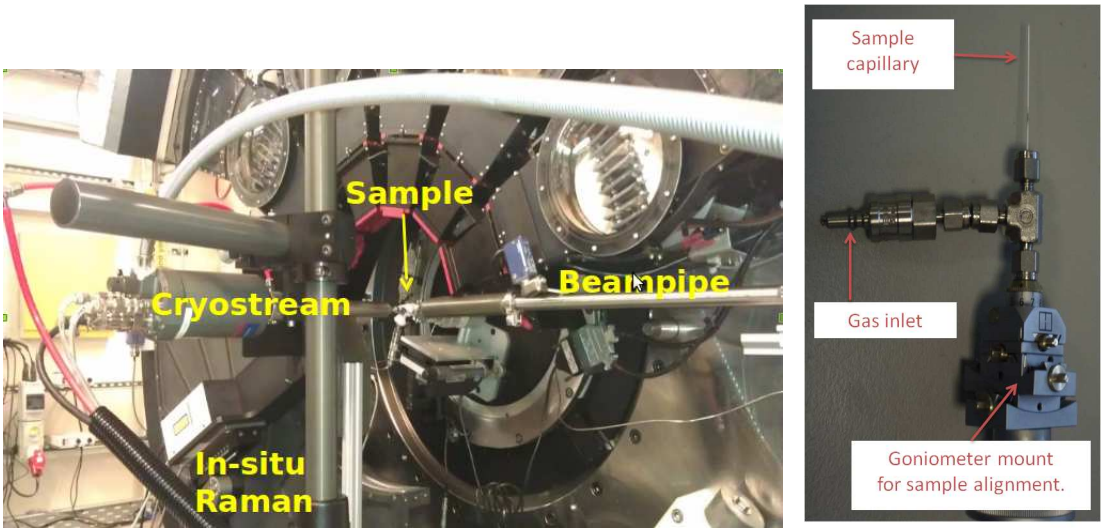

(a) (b)

Figure 10.3: a) Experimental setup in EH1 of Beamline I11, showing the relative positions of the sample, cryostream, gas input and in situ Raman spectrometer. b) Gas cell used for this experiment with 0.7mm capillary.

of a clathrate phase. Once formed, the temperature was cycled between 200 – 280K to determine the effect that repetitive cycling (such as day/night cycles or seasonal variations on a planetary body) would have on the clathrate structure. Finally, the pressure dependence of the clathrates was tested by holding the temperature at 270 K and steadily decreasing the gas pressure on the sample.

10.3 Results and Analysis

10.3.1 CO_2 Hydrates

10.3.1.1 SXPD

The initial SXPD pattern obtained was that of pure ice at 100 K. Solid H_2O ice is known to exhibit multiple crystalline phases under different temperature and pressure conditions, as identified in Figure 10.4. The temperature and pressure range covered

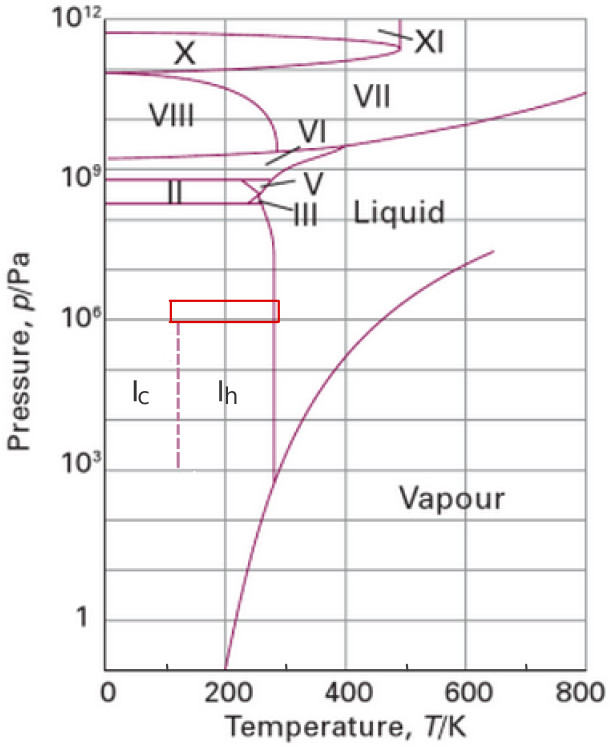

Figure 10.4: Phase diagram for water identifying the stable temperature and pressure regions. The red box indicates the temperature and pressure region covered by this work. After Atkins & de Paula (2010)

in this study is identified in the figure and, while we are mostly working in the stability region of hexagonal ice (I_h), at the lowest temperature we do encroach upon the region in which the formation of cubic ice (I_c; a metastable low-T polymorph) may occur.

Figure 10.5 shows the result of a phase identification using the peak search-match software program Match! (Crystal Impact 2003), identifying our sample as hexagonal ice (Ih). The best match to the experimental pattern, having an 85% figure of merit (FoM), is hexagonal ice of space group $P6_3/mmc$ and lattice parameters of $a = 4.4975$Å and $c = 7.3224$ Å.

Gaseous CO_2 was then injected into the ice at a pressure of 10 bar and temperature of 100 K. As stated previously, the speed of clathration at this temperature would

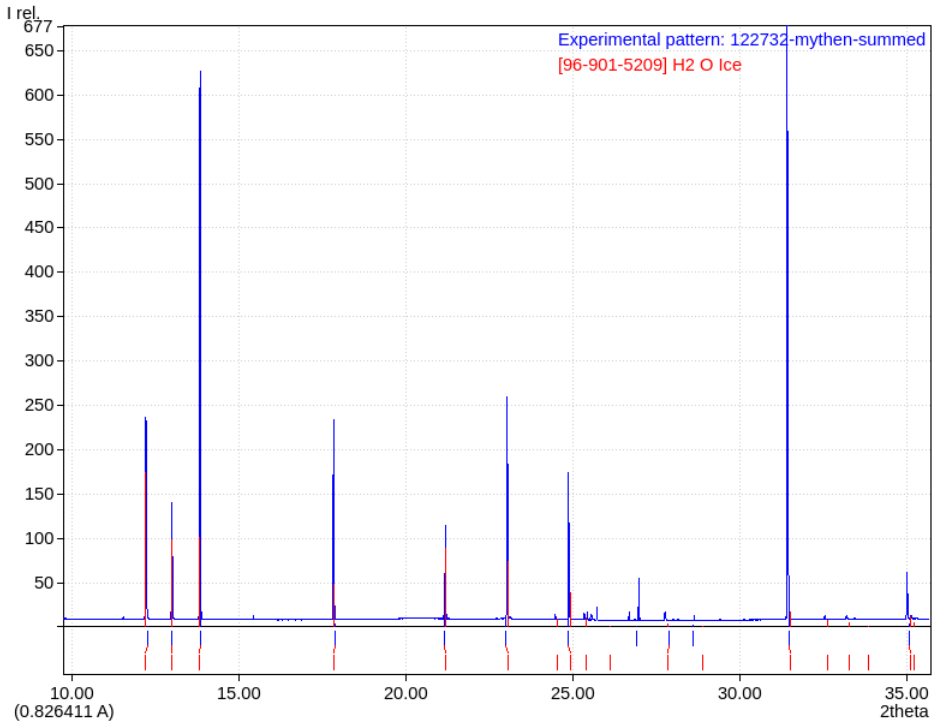

Figure 10.5: Comparison of the experimental data for ice at 100 K with that of hexagonal ice (Ih), confirming that the ice phase produced in this study is Ih.

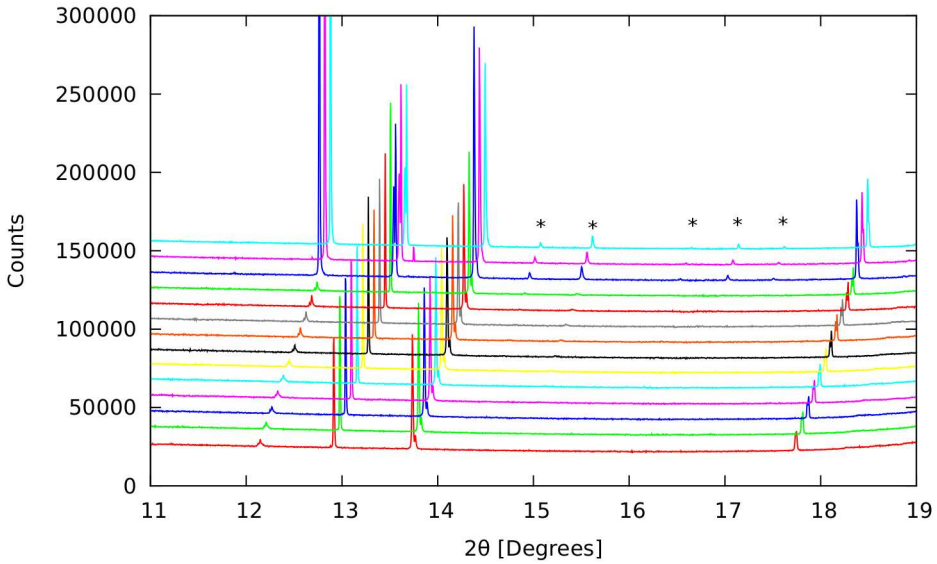

Figure 10.6: Sequence of SXPD patterns with temperature increasing upwards in approximately 11° intervals, over the range 100 - 250 K. The formation of a weak clathrate hydrate phase is first observed at 190 K, and becomes readily apparent at 225 K. Features due to the clathrate phase are marked with an asterisk.

be extremely slow and therefore the heating of the sample, up to 255 K, was initiated. Figure 10.6 shows a sequence of powder patterns taken at roughly 15° steps as the temperature was increased. The formation of clathrates, as indicated by the growth of additional Bragg peaks between 14° – 17° 2θ (identified in the Figure), was initially observed at a temperature of 190 K,however these are very weak and only become more prominent when the temperature reaches 225 K.

The clathrate features here are very weak, indicating that only a very small volume of clathrate has been formed, with the sample predominantly remaining as ice. However, this is not surprising as the total time of exposure to CO_2 at this point was slightly less than 90 mins. At least a few hours would be required for significant clathration at this temperature (Henning et al. 2000). A Pawley refinement (Pawley 1981) performed on these data produces a good fit of the peak positions, using lattice parameters of hexagonal ice and a cubic sI clathrate, as shown in Figure 10.7. The peak

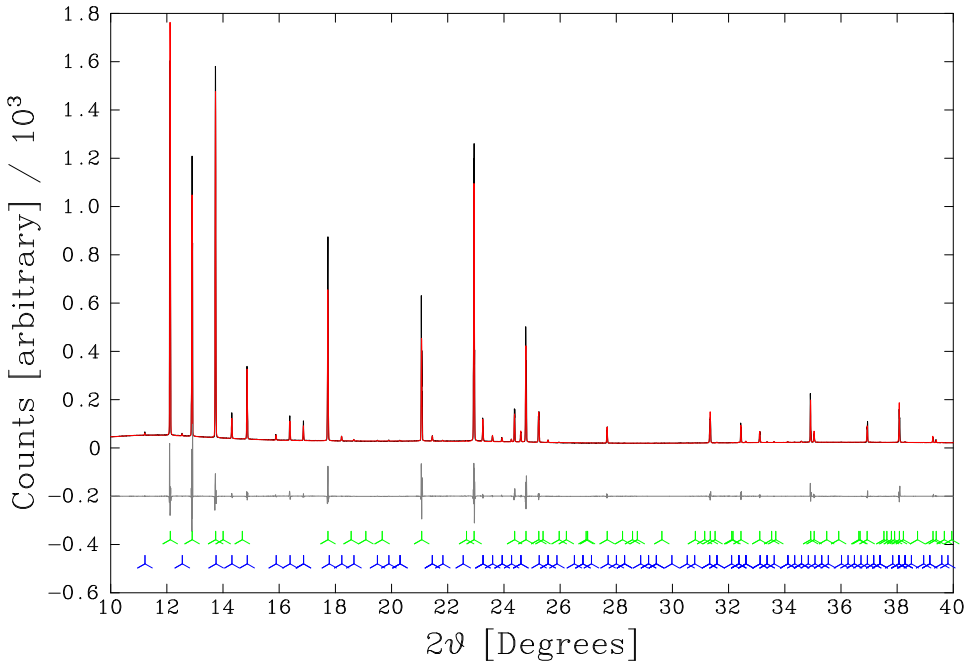

Figure 10.7: A multi-phase Pawley refinement of Ice (I_hh) and sI clathrate to an SXPD pattern obtained at a $T = 240$ K and $P = 10$bar, with agreement factor $R_{wp} = 12.45$ %

intensities are not well fitted, and this is likely due to insufficient particle averaging. A disscusion of this is provided in Section 10.4.

Upon heating the sample further, in an attempt to achieve full conversion to clathrate, all Bragg peaks were lost after just a few minutes at a temperature of 250 K. This is the point at which the ice melted, however, rather than observing independent clathrate, it appears that the clathrate phase present at this point also became unstable and broke down along with the ice. A fresh sample was mounted and cooled to a temperature of 200 K. The sample was then held at this temperature, and exposed to CO_2 at 10 bar overnight (14 hours), but no clathrate formation was observed in this time. Thermal cycling of the sample was performed at this point within the temperature range 200 K – 250 K and four cycles were completed. The results of this

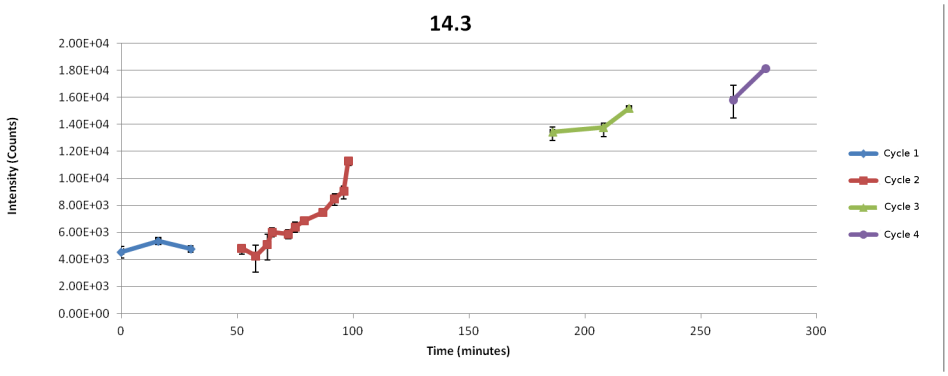

Figure 10.8: Thermal cycling of clathrate hydrates, covering their formation and dissociation, and simulating seasonal or day/night cycling.

cycling are shown in Figure 10.8 where the peak intensity of the (320) peak, at $\sim 14.3°$ 2θ in the SXPD patterns, is taken as a proxy for the relative volume of clathrate. The time on the x-axis refers to the time since first cooling to 200 K. This is discussed in greater detail in Section 10.4.

The initial process was then repeated with CO_2 being injected at a pressure of 20 bar. As the temperature was increased from 200 K to 250 K, we observed the formation of a clathrate hydrate phase exhibiting much more intense features. As the ice began to melt at a temperature of ∼240 K, the intensity of the clathrate features continued to increase, until at 255 K the ice had completely melted, leaving behind pure CO_2 clathrate. Figure 10.9 presents a comparison of three SXPD patterns at different temperature steps with a CO_2 pressure of 20 bar incident on the sample. The lowermost pattern is of pure H_2O ice (I_h), the middle scan is a mixture of ice and clathrate and the top pattern is CO_2 clathrate.

A good fit to the experimental SXPD pattern for the pure CO_2 clathrate (top pattern in Figure 10.9) is obtained using a cubic structure of space group $Pm3n$ and lattice parameter of 11.965 Å, which consistent with previously published values (Ikeda et al. 1999; Udachin, Ratcliffe & Ripmeester 2001; Takeya et al. 2010). Figure 10.10 presents the results of the fit, which converges with agreement factors of $R_{wp} = 2.882$

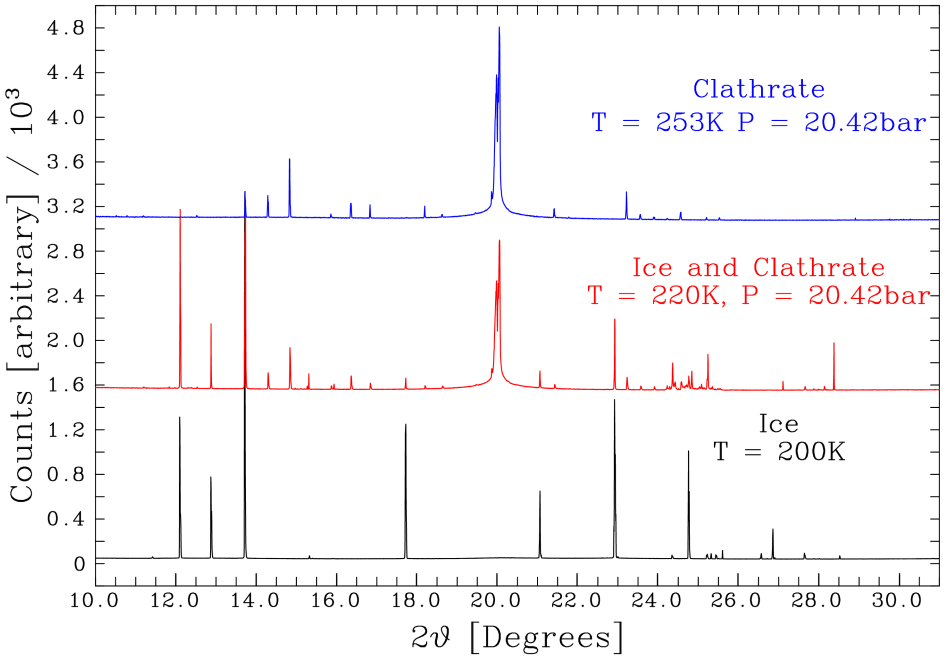

Figure 10.9: Comparison of SXPD patterns for pure H_2O cubic ice, ice and clathrate and pure clathrate hydrate at 20 bar of CO_2 pressure.

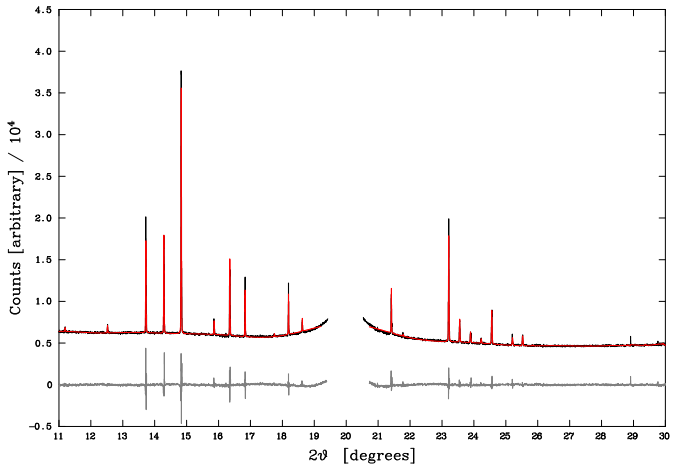

Figure 10.10: Pawley fit to the experimental SXPD pattern of pure CO_2 clathrate. This produces a good fit with agreement factors of $R_wp = 2.886$ % and gof = 2.246.

% and gof = 2.246. The high gof is a result of poor fitting of the peak intensities, which is discussed in detail in Section 10.4. However, this demonstrates that the structure of the clathrate phase produced is consistent with the standard sI clathrate structure.

10.3.1.2 Raman Spectroscopy

In situ Raman spectra were obtained up to 5000 cm^{-1} with a collection time of ~15 sec, alongside the SXPD data. Figure 10.11 identifies the main features present in the spectra of CO_2 clathrates, obtained at 260 K and 20 bar CO_2 pressure. The main features indicative of CO_2 clathrates are observed at ~200, ~1280, ~1390 and ~3200 cm^{-1}. The two sharp features at ~1753 and ~2341 cm^{-1} have not yet been identified.

The dominant feature at ~ 3200 cm^{-1} is due to a well-known O-H stretching mode, and its shape is heavily dependent on the structure of the clathrate. For example, the ratio of hexagons to pentagons in the the structure of the sI clathrate is much larger than that of the sII clathrate due to the predominance of larger cages in sI and this leads to the orientation of the water molecules and their associated vibrational

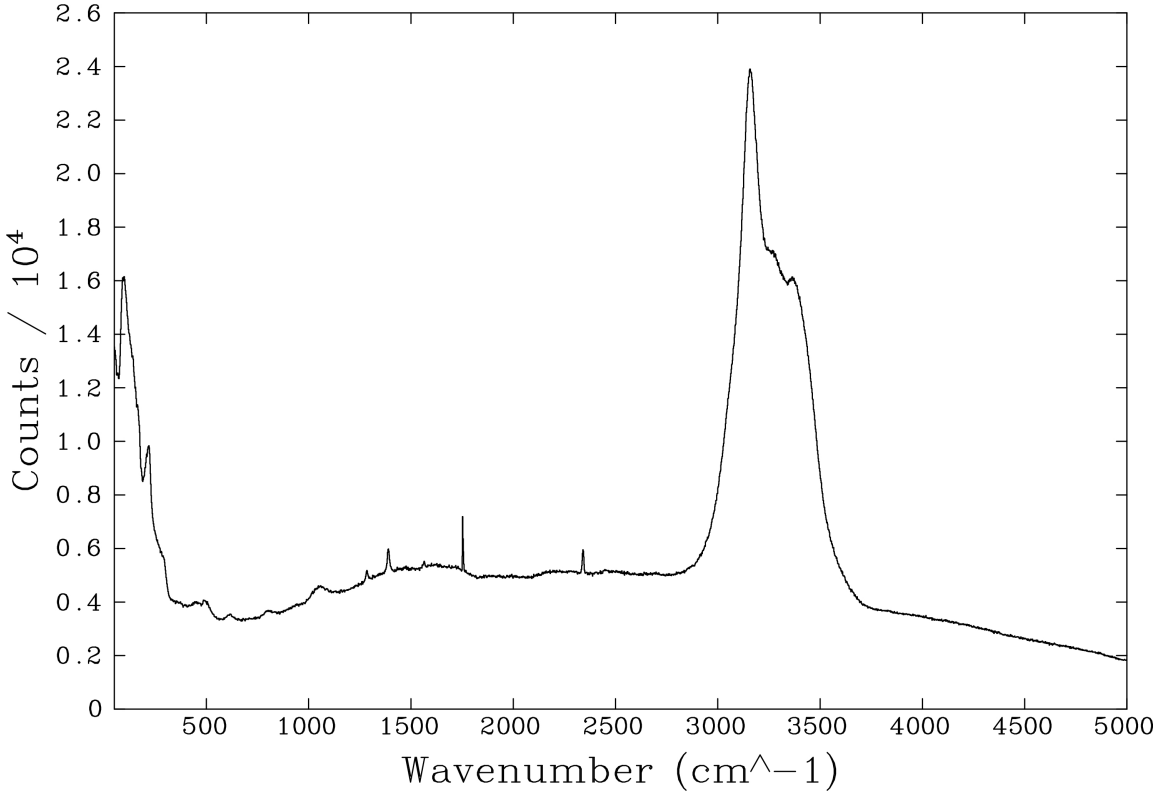

Figure 10.11: Raman spectra of CO_2 clathrate hydrate.

behaviour becoming similar to that of water molecules hydrogen-bonded in ice. Conversely, the arrangement of the molecules in the sII clathrate, due to a much higher abundance of small cages, leads to a band profile which is more similar to that of liquid water. This feature has a profile very similar to that of hexagonal ice, and therefore provides additional confirmation that the clathrate structure produced here is that of sI clathrate.

The distinctive feature at $\sim$200 cm^{-1} (see Figure 10.12(a)) is associated with the inter-molecular O-O vibration of the water molecules forming the clathrate cage structure (Nakano, Moritoki & Ohgaki 1998) and, as with the O-H stretching feature at $\sim$3200 cm^{-1}, it can be used to identify the structure of the clathrate. While it is well defined here, for sII clathrates and in liquid water a much broader feature is observed

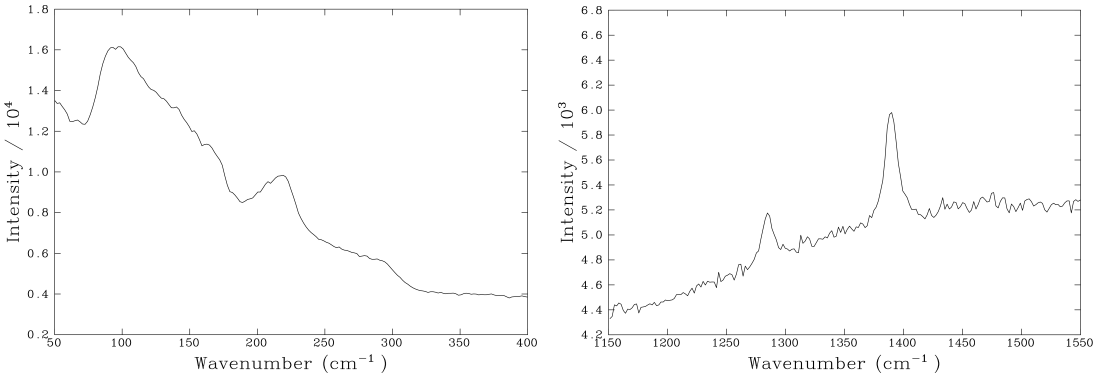

(a) O-O Intra-molecular bond stretch showing a peak $\sim$ 200cm^{-1}

(b) Fermi diad bands of the due to the trapped CO_2 molecules.

Figure 10.12: Two regions of interest in the Raman spectra of CO_2 clathrates.

in this region.

The two features at $\sim$1280 cm^{-1} and $\sim$1390 cm^{-1} (see Figure 10.12(b)) are the CO_2 Fermi diad resonance, which result from the coupling of fundamental stretching and bending modes (ν_1 and $2\nu_2$ respectively) of the CO_2 guest molecule (Windisch et al. 2012).

10.3.2 Other clathrate hydrates

Subsequent attempts at producing different clathrate species were attempted for this study, including Kr, Ar and CH_4. Unfortunately, these were not successful and no additional clathrate hydrates were formed. It is believed that there just was not enough time during this experiment to allow for significant penetration of these gases into the ice structure at the low temperatures studied (80 – 200 K).

10.4 Discussion

The results shown here are believed to be the first in situ, real-time measurements combining SXPD and Raman spectroscopy to study the formation of clathrate hydrates. We found that the formation of clathrates can occur at a fairly low pressure of 10 bar CO_2, within a period of 90 minutes, but the data suggest that the stability of the clathrate hydrate structure in this case is dependent on a water-ice phase also being present. This could indicate that the clathrate phase is poorly formed, perhaps due to the short timescale over which this study was conducted. It could be the case that the clathrate cages had formed, however, not enough time was given to allow the necessary diffusion of CO_2 throughout the sample and therefore the occupancy of the clathrate cages was not adequate to stabilise the structure.

At a pressure of 20 bar and after a period of 8 hours the formation clathrate phase was also observed and upon melting of the residual ice the clathrate phase remained stable. This implies that; 1) the formation of a stable clathrate phase can occur with an incident CO_2 pressure of 10 bar as long as enough time is provided for the CO_2 to diffuse throughout the structure, or 2) that a pressure of 10 bar is not significant enough to form an independently stable clathrate phase at this temperature, providing us with a lower limit on the pressure required to sustain the clathrate structure.

In order to investigate the pressure dependence of the clathrate phase formed in this study, and to understand the effect of decreasing pressure on a stable clathrate hydrate phase we fixed the temperature of the clathrate at 253 K and steadily decreased the pressure from 20 bar to 10 bar. Figure 10.13 shows SXPD patterns measured at 5 bar intervals as the pressure was being decreased. We found that the reduction of pressure to 10 bar resulted in rapid ($\leq$ 20 mins) dissociation of the clathrate structure. The dissociation of clathrates through a sudden decrease in pressure could have relevance to the origin of the plumes on Saturn's moon Enceladus, the driving mechanism of which is still not understood.

Clathrates are believed to be present below the icy surface of the moon, within a hypothesised sub-surface 'ocean' (Kieffer et al. 2006; Porco et al. 2006). The icy crust

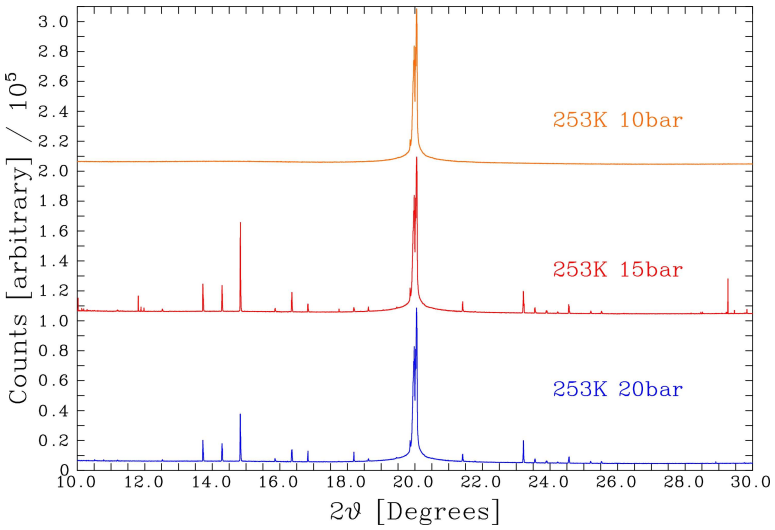

Figure 10.13: Three SXPD patterns at 5 bar intervals, showing the effect of decreasing pressure on the structure of CO_2 clathrate hydrates.

forming the surface of Enceladus is estimated to be a few km in thickness, however, due to the proximity of its host planet Enceladus experiences extreme tidal forces throughout its orbit. These tidal forces are the main source of heat that allows a sub-surface ocean to exist but they also lead to major stressing of the thick icy crust. This eventually leads to deep fractures within the crust that cause a sudden release of pressure. If clathrates are indeed present below the surface, a sudden decrease in pressure would no doubt lead to a sudden dissociation of the clathrate structure, as seen in our experiment. If a large enough volume of clathrates were to all dissociate at once, releasing large amounts of volatiles in a short periods of time, this could provide a driving force for the observed plumes emanating from the surface of Enceladus. Further experiments to determine the energy released by the rapid dissociation of clathrates would be required to properly quantify this.

These spectra can tell us a great deal about the nature of the guest molecule itself but they can also provide valuable information regarding the nature of the host lattice. The main features in the Raman spectra of CO_2 clathrates that are due to the trapped guest molecule are the Fermi diad features which are present throughout our

data at 1284.8 ± 0.3 cm^{-1} and 1389 ± 0.2 cm^{-1}. The positions of these two peaks show very little variation throughout our data at various temperatures and pressures, this would suggest that these features are insensitive to changes in temperature and pressure, at least over the range studied here. Nakano, Moritoki & Ohgaki (1998) previously noted that no pressure dependance was observed for these features up to a pressure of 5000 bar. While not sensitive to temperature and pressure variations, these features have been known to exhibit sensitivity to isotopic composition of the CO_2 molecule in the fluid state (Windisch et al. 2012), although no information is currently available for CO_2 vapour. The Fermi diad bands are also good indicators for the molecular state of the CO_2 and can be used to differentiate between CO_2 vapour and CO_2 trapped within a clathrate structure. Raman spectra of CO_2 vapours have two additional bands, known as hot bands, that are coupled to the Fermi diad bands by the Fermi resonance. When the CO_2 molecule becomes enclathrated, the major diad features persist, however the hot bands convolve into them, causing a noticeable broadening of the peaks (Sum, Burruss & Sloan 1997). Splitting of the diad peaks is believed to signify that CO_2 molecules are present in both large and small cages of the clathrate structure (Ratcliffe & Ripmeester 1986). We do not observe any splitting of the Fermi diad bands in our data, therefore indicating that the CO_2 molecules occupy only the small cages of our clathrate phase. Anisotropy of the peak intensities in this region can provide information about the influence of the cage geometry on the motion of the guest molecule, and can indeed identify which cage of the sI structure the CO_2 molecule is residing in (Ikeda, Mae & Uchida 1998). The $5^{12}6^2$ cage of the sI structure has a distortion along one axis, that contorts its shape into that of an oblate spheroid. This has the implication that when a CO_2 molecule occupies these cages the interaction between the CO_2 molecules and the water molecules forming the cage is different along the major and minor axis which causes the anisotropic rotation of the CO_2 molecule. On the other hand, the smaller 5^{12} cages of the structure are very close to spherical and therefore the CO_2 molecules can rotate isotropically (McMullen & Jeffrey 1965).

As described previously (see Section 10.3.1.2), the O-H stretching band at $\sim 3200\ cm^{-1}$ can be used to differentiate between the different clathrate structures, however, the

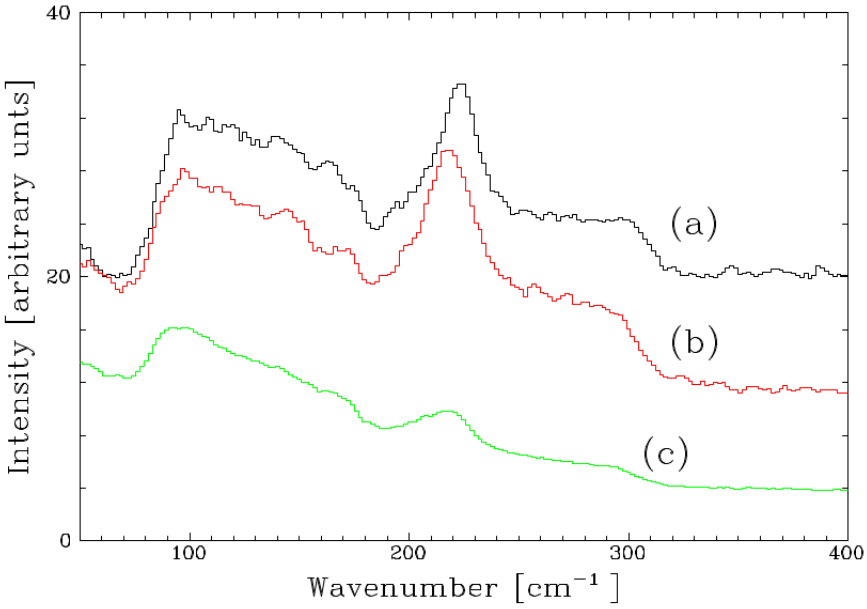

Figure 10.14: Raman spectra in the O-O inter-molecular bond vibration region for (a) ice and clathrate under 10 bar pressure at 225 K, (b) ice and clathrate under 10 bar pressure at 265 K and (c) pure clathrate hydrate at 20 bar and 260 K.

much weaker feature at ~ 200 cm^{-1} can also provide a great deal of information relating to the structure of the host lattice; however this very often gets overlooked. The broadness of this peak can be used to differentiate between clathrate, ice and water, as well as sI and sII clathrate structures. In Figure 10.14 we show a selection of Raman spectra in the region of 20 – 400 cm^{-1} at 225K, 260 K and 265 K, it is clear that, unlike the O-H stretch, the inter-molecular O-O vibration is very sensitive to changes in temperature and pressure. This has previously been reported by Nakano, Moritoki & Ohgaki (1998) who determined that over a pressure range of 100 – 5000 bar the Raman shift varies from 205 cm^{-1} to 224 cm^{-1}. We determine the peak values our Raman data for ice and clathrate at 10 bar and 225 K, ice and clathrate at 10 bar, 263 K and pure clathrate at 20 bar, 260 K to be 223.1 ± 0.5 cm^{-1}, 218.8 ± 0.3 cm^{-1} and 216.2 ± 0.3 cm^{-1} respectively.

10.4.1 Thermal cycling

All bodies within the Solar System undergo some from of thermal cycling, whether it is on a short diurnal cycles or over longer seasonal cycles. Thermal cycling can also occur on bodies such as Titan and Enceladus through tidal stress caused by their host planets, this can vary throughout their orbital period leading to cycles of increasing and decreasing stress (Hurford et al. 2007; Halevy & Stewart 2008). We performed thermal cycling of the clathrates in an attempt to simulate such temperature variations conducting a total of four cycles covering the temperature range 200 – 253K, as shown previously in Figure 10.8. A clear hysteresis effect becomes apparent with a systematic increase in the peak intensity with each successive cycle. As this experiment is being conducted using a closed system, the volume of water present within the capillary is unchanged and therefore an increase in the intensity of the Bragg features associated with the clathrate phase would ultimately suggest that with each cycle, more CO_2 is being incorporated into the clathrate structure leading to an increased proportion of clathrate relative to ice with each cycle. We only performed this cycling over a relatively small temperature range and over a significantly contracted period of time, however this result would suggest that in environments where the temperatures are very low and the standard formation of clathrates is very slow, thermal cycling could provide a means by which clathrates are formed at an increased rate, or could play a factor in the build up of large volumes of clathrates over very long timescales.

10.5 Conclusions

We have shown that the use of in situ SXPD and Raman spectroscopy has great potential for studying the formation and stability of clathrate hydrates in astrophysical, particularly Solar System, environments. This work has relevance to the presence of clathrates on Enceladus where it is believed the plumes could be due to removal of surface pressure, causing the sudden dissociation of clathrates. The weak Raman features

at $\sim$200cm^{-1} are indicative of clathrates and are sensitive to changes in environmental conditions; these features could potentially be used as identifiers of clathrate hydrates or to determine environmental conditions using future remote sensing missions. This would also benefit from the study of clathrates with other guest species such as N_2, CH_4, Kr, Xe and Ar. The formation of clathrates at temperatures <200K was found to be extremely slow and within the time frame of the beamtime allocation could not be observed; however, this would be a perfect experiment for the Long Duration Experiment (LDE) Beamline, currently available on I11.

11 Conclusions and Future Work

In this thesis I have presented the results of work undertaken during a joint PhD project between Keele University and Diamond Light Source. We used in situ synchrotron X-ray powder diffraction, alongside spectroscopic techniques such as Raman and IR spectroscopy, to study cosmic dust analogues with the aim of understanding the formation and structural evolution of cosmic dust grains under a range of temperature and pressure conditions relevant to astrophysical environments. Due to the limited supply of genuine cosmic dust particles available for study, this work was accomplished using laboratory synthesised materials manufactured exclusively as analogues of amorphous cosmic dust grains. The key feature of this work is the in situ, real time data collection we are performing, taking advantage of the fast scanning times of synchrotron radiation, allowing us to observe structural changes as they occur.

11.1 Effect of thermal annealing

In the thermal annealing experiments the effect of increasing temperature on amorphous Mg/Ca silicates ($Mg_xCa_{1-x}SiO_3$) of five compositions ($x = 0$, 0.2, 0.5, 0.8, 1), in the temperature range 293 K – 1273 K was studied (Chapter 6). The results of these experiments reveal the formation of multiple crystalline silicate phases, including diopside, forsterite, enstatite, and silica, all of which are known mineral components within cometary bodies, such as comet 81P/Wild 2 (Zolensky et al. 2006; Bridges et al. 2012) and Hale-Bopp (Wooden et al. 1999), and chondritic meteorites (Scott & Krot 2003). The formation of the wollastonite is also observed in the final crystalline products produced in these experiments; however, wollastonite has, so far, not been identified in cometary bodies. It was determined that wollastonite only formed in the samples containing $0.8 \leq x \leq 1$. This result was reproduced in the total scattering measurements of the same sample compositions, annealed offline, as described in Chapter 8. In these

experiments, the formation of wollastonite is also limited to the samples containing >80% Ca (relative to Mg).

We therefore suggest that the absence of wollastonite on cometary bodies could provide an indication of the maximum Ca content on such bodies. We identify a minimum temperature of 873 K for amorphous cosmic dust grains to crystallise, although a prolonged period of time is required at this temperature to achieve complete crystallisation. Almost instant crystallisation of the samples can be achieved at temperatures exceeding 1173 K. This temperature range allows us to determine that amorphous silicate grains in the solar nebula would have to have reached the inner regions of the nebula at <3AU from the Sun (based on the model temperature profiles by Boss (1993) in order to reach temperatures that would induce crystallisation.

11.2 Carbonation of amorphous silicates

The detection of carbonate minerals as a component of cosmic dust in a number of circumstellar and planetary environments has led to many theories being proposed to explain their formation in environments devoid of liquid water, but there is currently a lack of experimental evidence to support these. We therefore provide an experimental approach to the understanding of the origin of carbonate materials in astrophysical environments in which liquid water is not present. The results presented here improve our knowledge of the structural and compositional evolution of dust grains upon annealing at temperatures in excess of 1100 K and we present the results of a proof-of-concept experiment demonstrating that a crystalline carbonate phase can be formed through the solid-gas interaction of amorphous Mg-Ca silicates and gaseous CO_2 in the absence of water.

The carbonation of amorphous Mg/Ca silicates through the interaction with gaseous CO_2 was studied in situ by SXPD (Chapters 7 and 9) using a capillary gas cell. We successfully observed the formation of a carbonate phase upon exposure of the amorphous silicate analogues to CO_2 in the absence of water and present a new

formation route of the rare, metastable calcium carbonate polymorph vaterite. We determine that vaterite could be a mineral component of circumstellar dust; however, no published FIR spectra are available for vaterite that would allow us to confirm this. We highlight that these measurements should be made as a matter of priority.

A pressure of at least 6 bar was required to observe the formation of the carbonate phases in the experimental setup used for this work, which is significantly higher than the pressures that would be found in circumstellar outflows; this is a known limitation of the experimental setup. However, due to the results presented in Chapter 8 which indicate that the formation of a carbonate phase occurs when the amorphous silicates are dosed with CO_2 in a dessicator vessel at $\sim$ 1 bar, we are confident that the high pressures required during the in situ work are required only in order to allow the gas to adequately penetrate the capillary and are not indicative of the minimum pressure required for such a reaction to occur in other circumstances. It should be noted however that the pressures studied here for the formation of carbonates, particularly vaterite, could have direct relevance to proto-stellar and protoplanetary environments in which similar solid-gas reactions could occur at higher pressures in newly forming planetesimal objects. This can also be extended to the surfaces of planetary bodies in our Solar System such as Mars and Venus where the CO_2 pressure at the surface is, or once was, on the order of a few bars. This result has relevance to the formation of carbonate complexes on the surface of Mars (Bandfield, Gloch & Christensen 2003; Ehlmann et al. 2008), identifying an alternative formation route for vaterite on the Martian surface and within Martian meteorites that does not require liquid water or living organisms. From this research we have also been able to identify a compositional dependence of carbonate formation. Results from both ex situ and in situ carbonation (Chapters 7 and 8) of the amorphous silicate samples of composition $x = 0$, 0.2, 0.5, 0.8 and 1 would suggest that samples having $\geq 50\%$ Mg content do not exhibit a reaction when exposed to CO_2 at the pressures studied here. It is determined that the Mg ions present within the silicate structure act as inhibitors for the carbonation process. If this is indeed the mechanism responsible for carbonate formation in circumstellar environments then this dependence on composition would lead to the preferential formation of Ca-rich

carbonates over Mg-rich ones. Therefore, observing an abundance of Ca-carbonates relative to Mg-carbonates in such environments would support this process as the dominant formation mechanism of cosmic carbonates.

11.3 Formation of clathrate hydrates

We observed the formation of CO_2 clathrate hydrate compounds in samples of deionsised water using in situ SXPD and Raman spectroscopy (Chapter 10). We have shown that these techniques, when used in conjunction, have great potential for studying the formation and stability of clathrate hydrates in astrophysical environments, particularly Solar System bodies. Obtaining experimental data relating to the stability and formation of clathrates under conditions relevant to such environments could provide compelling evidence that clathrate hydrates are indeed present in the sub-surface oceans on Enceladus, the dissociation of which has been associated with the violent plumes seen emanating from the surface (Kieffer et al. 2006). We observe a weak feature in the Raman spectra of CO_2 clathrates at $\sim$220 cm^{-1}. This feature is known to be sensitive to changes in environmental conditions (Nakano, Moritoki & Ohgaki 1998) and is indicative of the presence of clathrate hydrates. We suggest that, with further study of laboratory analogues to constrain the temperature dependence, the feature at 200 cm^{-1} could be used in future remote sensing missions containing Raman spectrometers (e.g., ExoMars; Rull et al. 2013) to identify the presence of clathrate hydrates on planetary surfaces and also to determine environmental conditions.

11.4 Future Work

In this work we have attempted to simulate temperatures and pressures that would be found in a number of astrophysical environments, but due to experimental limitations, the gas pressures used in this work are significantly higher than that would be expected

in circumstellar environments. Therefore, a modified gas cell is required that would allow the adequate penetration of CO_2 throughout the extent of the sample, even at low pressures. This modified gas cell would also be greatly beneficial to the study of clathrate hydrates in low pressure environments (e.g., cometary bodies Iro et al. 2003).

Our work on clathrate hydrates could be expanded to include a range of gases that have astrophysical relevance. The depletion of the noble gases Kr and Xe from the atmosphere of Saturn's largest moon Titan has been attributed to the presence of clathrate hydrates on its surface (Chapter 10 and Mousis et al. 2009, 2011), these hypotheses are predominantly based on thermodynamical calculations of clathrate stability and therefore suffer from a lack of experimental backing. While experimental work has been performed for methane hydrates (Loveday et al. 2001; Choukroun et al. 2010), in relation to their stability on Titan and Mars, very little experimental work has been performed using noble gases under the conditions found on Titan's surface. A depletion of N_2 in cometary bodies has also been associated with the presence of clathrate hydrates in the early solar nebula. We therefore propose future experiments using SXPD and in situ Raman spectroscopy that would observe the formation and stability of clathrate hydrates formed with CH_4, Xe, Kr, N_2 and H_2, and provide laboratory Raman spectra that can be used as a reference for future remote sensing missions. In the experiments discussed in this thesis, deionised water was used as the host species, but if our experiments are to accurately simulate natural environments the effect of impurity ions within the host lattice need to be taken into account. This could be achieved through the use of realistic salt solutions of varying composition (e.g. NaCl, $MgSO_4$, sea water) and concentration (5-10g salt/kg H_2O) as the host species, along with gaseous CO_2 to study the effect this has on the stability of the clathrate structure. This is extremely relevant to the icy moons Enceladus and Europa.

Also of great benefit to future studies in this field is the Long Duration Experiment (LDE) now available on Beamline I11. This facility provides the means to study the evolution of samples over periods ranging from a few months to two years. Considering the long timescales over which dust grains in astronomical environments evolve, this will provide the perfect means to more closely replicate the conditions in

astrophysical environments. In particular, it is understood that at low pressures and temperatures, the kinetics of carbonate formation can be very slow. Therefore, due to time constraints, laboratory simulations often require the used of increased temperatures and pressures to ensure a reaction. The LDE provides the means necessary to study such reactions at low temperatures and pressures over extended periods of time, and it is the only facility of its kind currently available for synchrotron powder diffraction. This facility therefore provide an excellent opportunity for the further study of silicate carbonation at low pressures and also provides us with the opportunity to study the thermal cycling of clathrate hydrates over more realistic timescales, such as a few days or even a few months, which has relevance to seasonal cycles on Solar System bodies.

Bibliography

Abe K., Shigenari T., 2011, J. Chem. Phys., 134, 104506

Agrinier P., Deutsch A., Schärer U., Martinez I., 2001, Geochimica et Cosmochimica Acta, 65, 2615

A'Hearn M. F. et al., 2005, Science, 310, 258

Andreassen J. P., 2005, J. Cryst. Growth, 274, 256

Artymowicz P., 1997, Annual Review of Earth and Planetary Sciences, 25, 175

Atkins P., de Paula J., 2010, Atkins' Physical Chemistry, 9th edn. Oxford University Press, Oxford

Baitalow F., Wolf G., Schmidt H.-G., 1998, J. Therm. Analysis, 52, 5

Bandfield J. L., Gloch T., Christensen P., 2003, Science, 301, 1084

Bansal N. P., 1988, J. American Ceramic Society, 71, 666

Barnes P., Jaques S., Vickers M., 2006, Advanced certificate of powder diffraction on the web. `pd.chem.ucl.ac.uk/pdnn/pdindex.htm#diff1`

Billinge S. J. L., 1998, Local Structure from Diffraction, Billinge S. J. L., Thorpe M. F., eds. Kluwer Academic Publishers, pp. 17–26

Billinge S. J. L., 2007, Z. Kristallogr. Suppl., 26, 17

Blum J., Wurm G., 2008, Annu. Rev. of Astro. and Astrophys., 46, 21

Boss A., 1993, ApJ, 417, 351

Boss A., 1996, ApJ, 469, 906

Boultif A., Louer D., 2004, J. Appl. Cryst., 37, 724

Boyd F. R., Schairer J. F., 1964, Journal of Petrology, 5, 275

Bradley J. et al., 2005, Science, 307, 244

Bradley J. P., 1994, Science, 265, 925

Bridges J. C., Changela H. G., Nayakshin S., Starkey N. A., Franchi I. A., 2012, Earth and Planetary Science Letters, 341, 186

Bringa E. M. et al., 2007, ApJ, 662, 372

Brownlee D. et al., 2006, Science, 314, 1711

Brucato J., Colangeli L., Mennella, V.and Palumbo P., Bussoletti E., 1999, A&A, 348, 1012

Brucato J., Mennella V., Colangeli L., Rotundi A., Palumbo P., 2002, Planetary and Space Science, 50, 829

Brucato J., Strazzulla G., Baratta G., Colangeli L., 2004, A&A, 413, 395

Brusentsova T. N., Peale R. E., Maukonen D., Harlow G. E., Boesenberg J. S., Ebel D., 2010, Am. Mineral., 95, 1515

Cacchio P., Contento R., Ercole C., Cappuccio G., Martinez M. P., Ledepi A., 2004, Geomicrobiology, 21, 497

Carlson W. D., 1986, Contributions to Mineralogy and Petrology, 92, 218

Carlson W. D., 1988, American Mineralogist, 73, 232

Carrez P., Demyk K., Cordier P., Gengembre L., Grimblot J., D'Hendecourt L., Jones A., 2002, MAPS, 37, 1599

Cassen P., 1994, Icarus, 112, 405

Ceccarelli C., Caux E., 2002, A&A, 395, L29

Chatti I., Delahaye A., Fournaison L., Petitet J.-P., 2005, Energy Conservation and Management, 46, 1333

Chen J., Li M., Li A., Wang Y., 2008, in Organic Matter in Space, Kwok S., Sandford S., eds., Vol. 251, IAU Symposium

Chen L., Shen Y., Xie A., Huang B., Jia R., Guo R., Tang W., 2009, Cryst. Growth Des., 9, 743

Chiavassa A., Ceccarelli C., Tielens A., 2005, A&A, 432, 547

Chihara H., Koike C., Tsuchiyama A., 2001, PASJ, 53, 243

Choukroun M., Grasset O., Tobie G., Sotin C., 2010, Icarus, 205, 581

Coelho A., 2007, Topas-academic. `http://www.topas-academic.net/`, version 4.1 (Computer Software)

Colangeli L. et al., 2003, A&A Review, 11, 97

Collett T., Kuuskraa V., 1998, Oil and Gas Journal, 96, 90

Compiegne M., 2011, ASP Conference Series, 438, 55

Costa G., Baciocchi R., Polettini A., Pomi R., Hills C. D., Carey P. J., 2007, Environ. Monit. Assess., 135, 55

Crystal Impact, 2003, Match! phase identification from powder diffraction [computer software]. Version 1.11

Daniels J., Drakopoulos M., 2009, J. Synchrotron Radiation, 16, 463

Davoisine C. et al., 2008, A&A, 482, 541

Day K., 1976, Icarus, 27, 561

Day K., 1977, MNRAS, 178, 49P

Day K., 1979, Astroph. and Space Sci., 65, 173

Day S., Thompson S., Evans A., Parker J. E., Connor L. D., Tang C. C., 2013, MAPS, 48, 1459

Day S., Thompson S., Parker J., Evans A., 2012, A&A, 553, A68

De Muynck W., Debrouwer D., De Belie N., Verstaete W., 2008, Cement Concrete Res., 38, 1005

Deer W., Howie R., Zussman J., 1992, An Introduction to the rock forming minerals., 2nd edn. Longman Group, London

Deer W., Howie R. A., Zussman J., 1978, Rock Forming Minerals: Single-chain silicates., 2nd edn. Longman Group

Demichelis R., Raiteri P., Gale J., Roberto D., 2012, Cryst. Eng. Comm, 14, 44

Demyk K. et al., 2001, A&A, 368, L38

Demyk K., d'Hendecourt L., Leroux H., Jones A. P., Borg J., 2004, A&A, 420, 233

Dijkstra C., Speck A., Reid R., Abraham P., 2005, ApJ, 633, L133

Dijkstra C., Waters L., Kemper F., Min M., Matsuura M., Zijlstra A., de Koter A., Dominik C., 2003, A&A, 399, 1037

Dinnebier R. E., Billinge S. J. L., 2008, Powder Diffraction Theory and Practice. RSC Publishing, Cambridge

Draine B., 2003, Annu. Rev. of Astron. and Astrophys., 41, 241

DuFresne E. R., Anders A., 1962, Geochimica et Cosmochimica Acta, 26, 251

Dukes C. A., Baragiola R. A., McFadden L. A., 1999, J. Geophys. Res., 104, 1865

Duley W., Lazarev S., Scott A., 2005, ApJ, 620, L135

Ebel D. S., 2000, JGR Space Physics, 105, 10363

Egami T., Billinge S. J. L., 2003, Underneath the Bragg Peaks: Structural Analysis of Complex Materials. Pergamon Press, Elsevier, Oxford, England

Ehlmann B. L., Mustard J. F., Murchie S. L., Poulet F., Bishop J. L., Brown A. J., Calvin W. M., 2008, Science, 322, 1828

Elder F. R., Gurewitsch A. M., Langmuir R. V., Pollock H. C., 1947, Physical Review, 71, 829

Englezos P., 1993, Industrial & Engineering Chemistry Research, 32, 1251

Ewald P. P., 1913, Physik. Z., 14, 465

Fabian D., Jäger C., Henning T., Dorschner J., Mutschke H., 2000, A&A, 364, 282

Fahrenfort J., 1961, Spectrochimica Acta, 17, 698

Falini G., Fermani S., Vanzo S., Miletic M., Zaffino G., 2005, Eur. Jour. Organ. Chem., 1, 162

Farrow C. L., Juhas P., Liu J. W., Bryndin D., Bozin E. S., Bloch J., Proffen T., Billinge S. J. L., 2007, J. Phys. Condens. Matter, 19, 335219

Fawcett T. G., Faber J., Kabbekodu S., McClune F., Rafaja D., 2005

Fei Y., 1995, Mineral Physics and Crystallography: A Handbook of Physical Constants, Ahrens T. J., ed., American Geophysical Union, Washington D.C., p. 29

Fernandez-Daz L., 2010, Geochimi. Cosmochimi. Acta, 74, 6064

Ferrarotti A., Gail H.-P., 2005, A&A, 430, 959

Ferrarotti A., Gail H.-P., 2006, A&A, 447, 553

Fitzpatrick E., Massa U., 1986, ApJ, 307, 286

Fitzpatrick E., Massa U., 2007, ApJ, 663, 320

Formisano V., Atreya S., Encrenaz T., Ignatiev N., Giuranna M., 2004, Science, 306, 1758

Friedman G., Schultz D., Guo B., Sanders J., 1993, J. Sediment. Petrol., 63, 663

Gail H.-P., 2003, Astromineralogy, Henning T., ed., Vol. 609, Springer, Heidelberg, p. 55

Gail H.-P., Sedlmayr E., 1999, A&A, 347, 594

Gail H.-P., Sedlymayr E., 1998, Faraday Discussion, 109, 303

Gal A., Weiner S., Addadi L., 2010, J. Am. Chem. Soc., 132, 13208

Garenne A., Montes-Hernandez G., Beck P., Schmitt B., Brissaud O., Pommerol A., 2013, Planetary and Space Sci., 76, 28

Gebauer D., Verch A., Borner H. G., Colfen H., 2009, J. Cryst. Growth Des., 9(5), 2398

Gehrz R., 1989, in Interstellar Dust, Allamandola L., Tielens A., eds., IAU Symposium, p. 445

Geiger A., Stillinger F. H., Rahman A., 1979, J. Chem. Phys., 70, 4185

Gillot J., Roskosz M., Depecker C., Roussel P., Leroux H., 2009, in Lunar and Planetary Inst. Technical Report, Vol. 40, Lunar and Planetary Institute Science Conference Abstracts, p. 1755

Gomez-Morales J., Hernandez-Hernandez A., Sazaki G., Garcia-Ruiz J. M., 2010, Cryst. Growth Des., 10, 963

Goos F., Hänchen H., 1947, Annalen der Physisk, 436, 333

Grasby S., 2003, Geochimica et Cosmochimica Acta, 67, 1659

Gražulis S. et al., 2009, J. Appl. Cryst., 42, 726

Griffin M. J. et al., 2010, A&A, 518, L3

Griffiths P. R., de Haseth J. A., 2007, Fourier Transform Infrared Spectroscopy, 2nd edn. John Wiley and Sons, Inc., New Jersey

Hale G. E., 1899, ApJ, 9, 360

Halevy I., Stewart S. T., 2008, Geophys. Res. Lett., 35, L12203

Hallenbeck S. L., 1997, Icarus, 131, 198

Hallenbeck S. L., Nuth J., Daukantas P., 1998, Icarus, 131, 198

Hammersley A. P., 1997, ESRF Internal Report, V9, 129

Hammersley A. P., Svensson S. O., Hanfland M., Fitch A. N., Häusermann D., 1996, High Pressure Research, 14, 235

Hammond C., 2009, The Basics of Crystallography and Diffraction, third edition edn. Oxford University Press, Oxford

Han Y. S., Hadiko G., Fuli M., Takahashi M., 2006, J. Cryst. Growth, 289, 269

Hecht J. H., 1986, ApJ, 305, 817

Henning R. W., Schultz A. J., Thieu V., Halpern Y., 2000, The Journal of Physical Chemistry A, 104, 5066

Henning T., 2010, Annu. Rev. Astron. Astrophys., 48, 21

Henning T., Grun E., Jurgen S., eds., 2009, Cosmic Dust Near and Far, Henning T., Grun E., Jurgen S., eds., Vol. 414

Hernández V., Berlin A., Zotti G., Lõpez Navarrete J. T., 1997, J. Raman Spec., 28, 855

Hopkinson H., Rutt K., Cressey G., 2008, J. Geol., 116, 387

Howarth J. D., Murray J., 1991, Dipso–a friendly spectrum analysis program

Hoyle F., Wickramasinge N., 1962, M.N., 124, 417

Huang E., Chen C., Huang T., Lin E., Xu J.-A., 2000, Am. Mineralogist, 85, 473

Huggins W., 1869, Proc. Royal Soc., 17, 309

Hugh-Jones D., Chopelas A., Angel R., 1997, Phys. Chem. Minerals, 24, 301

Hurford T. A., Helfenstein G. V., Hoppa R., Greenburg R., Bills B., 2007, Nature, 447, 292

Ikeda T., Mae S., Uchida T., 1998, J. Chem. Phys., 108, 1352

Ikeda T. et al., 1999, J. Phys. Chem. Solids, 60, 1527

Iro N., Gautier D., Hersant F., Bockelée-Morvan D., Lunine J. I., 2003, Icarus, 161, 511

Jacob D. E., Soldati A. L., Wirth R., Huth J., Wehrmeister U., Hofmeister W., 2008, Geochimica et Cosmochimica Acta, 72, 5401

Jacob D. E., Wehrmeister U., Soldati A. L., Hofmeister W., 2009, Geophys. Res. Abstr., 11, 11969

Jäger C., Dorschner J., Mutschke H., Posch T., Henning T., 1998, A&A, 339, 904

Jager C., Dorschner J., Mutschke H., Posch T., Henning T., 2003a, A&A, 408, 193

Jager C., Fabien D., Schrempel F., Dorschner J., Henning, Th. and. Wesch W., 2003b, A&A, 401, 57

Jeffrey G. A., 1984, Inclusion Compounds, Atwood J., Davies J. E. D., MacNichol D. D., eds., Vol. 1, Academic Press, London, p. 135

Johnson H. L., 1962, ApJ, 135, 69

Johnson H. L., 1966, ARAA, 4, 193

Jones A., 2004, ASP Conference Series, 309, 347

Juhas P., Davis T., Farrow C. L., Billinge S. J. L., 2013, Journal of Applied Crystallography, 46, 560

Kabalah-Amitai L., Mayzel B., Kaufmann Y., Fitch A., Bloch L., 2013, Science, 340, 454

Kamhi S., 1963, Acta Cryst., 16, 770

Kamijo F., 1963, PASJ, 15, 440

Keller L. P. et al., 2006, Science, 314, 1728

Kemper F., Jager C., Waters L., 2002, Nature, 415, 295

Kemper F., Markwick A. J., Woods P. M., 2011, MNRAS, 107

Kemper F., Vriend W., Tielens A., 2004, ApJ, 609, 826

Kemper F., Vriend W., Tielens A., 2005, ApJ, 633, 534

Kemper F., Waters L., de Koter A., Tielens A., 2001, A&A, 369, 132

Kerschbaum F., Posch T., Nowotny W., 2009, Spica Workshop, 03004

Kessler M., Steinz J., Anderegg M., 1996, A&A, 315, L27

Kieffer S. W., Lu X., Bethke C. M., Spencer J. R., Marshak S., Navrotsky A., 2006, Science, 314, 1764

Kiehl J. T., Shields C. A., 2005, Geology, 33, 757

Kimura Y., Nuth J., Tsukamoto K., Kaito C., 2011, MAPS, 46, 92

Koike C., Imai H., Chihara H., Suto H., Murata K., Tsuchiyama A., Tachibana S., Ohara S., 2010, ApJ, 709, 983

Koike C., Tsuchiyama A., Shibai H., Suto H., Tanabe T., Chihara H. e. a., 2000, A&A, 363, 1115

Koike C., Tsuchiyama A., Suto H., 1999, Proceedings of the 32nd ISAS Lunar and Planetary Symposium, 32, 175

Kolodny Y., Gross S., 1974, J. Geol., 82, 489

Kraetschmer W., Huffman D. R., 1979, Astroph. and Space Sci., 61, 195

Kvenvolden K. A., 1995, Org. Geochem., 23, 997

Lakshminarayanan R., Valiyaveettil S., 2003, Cryst. Growth Des., 3(4), 611

LeBail A., 2005, Powder Diffraction, 20, 316

LeBail A., Duroy H., Fourquet J. L., 1988, Materials Research Bulletin, 23, 447

LeBail A., Ouhenia S., Chateigner D., 2011, Powder Diffraction, 26(1), 16

Lebiediev A. A., 1921, Trans. Opt. Inst. Petr., 2, 10

Lebreton J.-P., Matson D. L., 2002, Space Sci. Rev., 104, 59

Lee H. et al., 2005, Nature, 434, 743

Leroux H., 2009, EAS Publication Series, 35, 153

Li A., Draine B., 2003, ApJ, 550, L213

Lim M., Ham G., Ahn J., You K., 2010, Int. J. Environ. Res. Public Health, 7, 203

Lin Y., Hu Q., Chen J., Ji J., Teng H., 2009, Cryst. Growth Des., 9, 4634

Lisse C., VanCleve J., Adams A., A'Hearn, F. et al, 2006, Science, 313, 635

Lodders K., 2003, ApJ, 591, 1220

Louër D., Louër M., 1972, J. Appl. Cryst., 5, 271

Loveday J. S., Nelmes R. J., Guthrie M., Belmonte S. A., Allan D. R., Klug D. D., 2001, Nature, 410, 661

Low F. J., Johnson H. L., 1965, ApJ Letts, 141, L336

Lunine J. I., Stevenson D. J., 1985, ApJ Suppl., 58, 493

Macpherson G., 2005, Astronomical Society of the Pacific Conference Series, 341, 225

Malfait K., Waelkens C., Bouwman J., de Koter A., Waters L. B. F. M., 1999, A&A, 345, 181

Marboeuf U., Mousis O., Petit J.-M., Schmitt B., 2010, ApJ, 708, 812

Maslin M., Owen M., Betts R., Day S., Jones T. D., Ridgwell A., 2010, Phil. Trans. R. Soc. A., 368, 2369

Mathis J. S., 1990, Annu. Rev. Astron. Astrophys., 28, 37

Mattsson L., 2011, MNRAS, 414, 781

McConnell J., 1960, Mineral Mag., 32, 535

McCusker L., von Dreele R., Cox D., Louer D., Scardi P., 1999, J. Appl. Cryst., 32, 36

McDonald I., Sloan G. C., Zijlstra A. A., Matsunaga N., Matsuura M., Kraemer K. E., Bernard-Salas J., Markwick A. J., 2010, ApJ Letters, 717, L92

McKay D. S., Gibson E. K., Thomas-Keprta K. L., Vali H., Romanek C. S., 1996, Science, 273, 924

McMullen R. K., Jeffrey G. A., 1965, J. Chem. Phys., 42, 2725

Medeiros S. K., Albuquerque E. L., Maia F. F. J., Caetano E. W. S., Freire V. N., 2007, CHem. Phys. Lett., 435, 5964

Mennella V., Brucato J., Colangeli L., 2001, Spectrochimica Acta, 57, 787

Meyer H.-R., 1960, Fortschr. Mineral., 38, 186

Meyer H.-R., 1969, Z. Kristallogr., 128, 183

Molster F., Kemper C., 2005, Space Science Reviews, 119, 3

Molster F., Waters L., Tielens A., 2002a, A&A, 382, 222

Molster F. J. et al., 2001, A&A, 372, 165

Molster F. J., Waters L., 2003, Astromineralogy, Henning T., ed., Vol. 609, Springer, Heidelberg, pp. 121–170

Molster F. J., Waters L. B. F. M., Tielens A. G. G. M., Barlow M. J., 2002, A&A

Morimoto N., 1989, Canadian Mineralogist, 27, 143

Mousis O., Lunine J. I., Picaud S., Cordier D., Waite, Jr. J. H., Mandt K. E., 2011, ApJ Letts, 740, L9

Mousis O. et al., 2009, ApJ, 691, 1780

Mugnaioli E., Andrusenko I., Schuler T., Loges N., Dinnebier R. E., Panthofer M., Tremel W., Kolb U., 2012, Angew. Chem. Int. Ed., 51, 1

Mumma M. J., Villanueva G. L., Novak R. E., Hewagama T., Bonev B. P., DiSanti M. A., Mandell A. M., Smith M. D., 2009, Science, 323, 1041

Nakano S., Moritoki M., Ohgaki K., 1998, J. Chem. Eng. Data, 43, 807

Nassrallah-Aboukais N., Boughriet A., Gengembre L., Aboukais A., 1998, J. Chem. Soc., 94, 2399

Navrotsky A., 2003, Geochem. Trans., 4(6), 34

Navrotsky A., 2004, Proc. Natl. Acad. Sci., 101, 12096

Navrotsky A., Mazeina L., Majzlan J., 2008, Science, 319, 1635

Nebel H., Epple M., 2008, Z. Anorg. Allg. Chem., 634, 1439

Nelson R., Thiemens M., Nuth J., Donn B., 1989, Lunar Planet. Sci. Conf., 19, 559

Niemann H. B. et al., 2005, Nature, 438, 779

Niyogi S. G., Speck A. K., Onaka T., 2011, ArXiv e-prints

Nothig-Laslo V., Brečvić L., 1999, Phys. Chem. Chem. Phys., 1, 3697

Nuth J., 1996, Cosmic Dust Connection, Greenburg J., ed. Norwell, p. 205

Nuth J., Ferguson F., 1993, Ceramic Trans., 30, 23

Nuth J., Johnson N., 2006, Icarus, 180, 243

Okada A., Keil K., Taylor G. J., 1981, Meteoritics, 16, 141

Okada Y., Onaka T., Kaneda H., Sakon I., 2009, SPICA joint workshop, 03008

Olofsson J. et al., 2009, A&A, 507, 327

Onaka T., Okada Y., 2003, ApJ, 585, 872

Osegovic J. P., Max M. D., 2005, J. Geophys. Res., 110, 2156

Pai R. K., Jansson K., Hedin N., 2009, Cryst. Growth Des., 9, 4581

Papike J. J., 1998, Planetary Materials reviews in mineralogy, Vol. 36. Mineralogical Society of America

Parker J., Potter J., Thompson S., Lennie A., Tang C., 2012, Materials Science Forum, 706, 1707

Pauling L., 1959, Hydrogen Bonding, Hadzi D., ed., Pergamon Press, New York

Pawley G. S., 1981, J. Appl. Cryst., 14, 357

Pecharsky V., Zavalij P., 2009, Fundamentals of Powder Diffraction and Structural Characterization of Materials, 2nd edn. Springer

Peric J., Vucak M., Krstulovic R., Brecevic L., Kralj D., 1996, Thermochimica Acta, 277, 175

Pilbratt G. L. et al., 2010, A&A, 518, L1

Plummer L. N., Busenberg E., 1982, Geochim. Cosmochim. Acta, 46, 1011

Plummer P. L. M., Chen T. S., 1983, J. Phys. Chem, 87, 4190

Plummer P. L. M., Chen T. S., 1987, J. Chem. Phys., 86, 7149

Poglitsch A., Waelkens C., Geis N., Feuchtgruber H., Vandenbussche B., Rodriguez L., Krause O., Renotte E., 2010, A&A, 518, L2

Porco C. C. et al., 2006, Science, 311, 1393

Posch T., Baier A., Mutschke H., Henning T., 2007, ApJ, 668, 993

Prieto-Ballesteros O., Kargel J. S., Fairén A. G., Fernández-Remolar D. C., Dohm J. M., Amils R., 2006, Geology, 34, 149

Proffen T., Billinge S. J. L., Egami T., Louca D., 2003, Zeitschrift fr Kristallographie - Crystalline Materials, 218, 132

Qiu X., Thompson J. W., Billinge S. J. L., 2004, J. Appl. Cryst., 37, 6780

Ranade M. R., Navrotsky A., Zhang H. Z., Banfield J. F., Elder S. H., Zaban A., 2002, Proc. Natl. Acad. Sci., 99, 6476

Randall J. T., Rooksby H. P., Cooper B. S., 1930a, J. Soc. Glass Technol., 14, 219

Randall J. T., Rooksby H. P., Cooper B. S., 1930b, Z. Krist., 75, 196

Ranyard A. C., 1878, Astron. Regist., 16, 309

Ratcliffe C. I., Ripmeester J. A., 1986, J. Phys. Chem., 90, 1259

Ren F., Wan X., Ma Z., Su J., 2009, Mater. Chem. Phys., 114, 367

Richet P., Mysen B., Ingrin J., 1998, Phys. Chem. Minerals, 25, 401

Rieke G. H., 2009, Exp Astron., 25, 125

Rietmeijer F., 1999, American Mineralogist, 84, 1883

Rietmeijer F., Hallenbeck S. L., Nuth J. A., Karner J. M., 2002, Icarus, 195, 493

Rietmeijer F., Nuth J., MacKinnon I., 1986, Icarus, 66, 211

Rietmeijer F., Pun A., Kimura Y., Nuth J., 2008, Icarus, 195, 493

Rietmeijer F. J. M., Pun A., Kimura Y., Nuth III J., 2008, Icarus, 195, 493

Rietveld H. M., 1969, J. Appl. Cryst., 2, 65

Ripmeester J. A., Ratclife C. L., 1990, J. Phys. Chem., 94, 8773

Ripmeester J. A., Tse J. S., Ratclife C. L., Powell B. M., 1987, Nature, 325, 135

Rodriguez-Navarro C., Rodriguez-Gallego M., Chekroun K. B., Gonzalez-Munoz M. T., 2003, Appl. Environ. Microbiol., 69, 2182

Roskosz M., Gillot J., Capet F., Roussel P., Leroux H., 2009, ApJ, 707, L174

Rotundi A., Rietmeijer F. J. M., Brucato J. R., Colangeli L., Mennella V., Palumbo P., Bussoletti E., 2000, Planetary and Space Sci., 48, 371

Rowlands D., Webster R., 1971, Nat. Physical Sci., 229, 158

Rull F., Maurice S., Diaz E., Lopez G., Catala A., 2013, in Lunar and Planetary Institute Science Conference Abstracts, Vol. 44, Lunar and Planetary Institute Science Conference Abstracts, p. 3110

Ryskin G., 2003, Geology, 31, 741

Sabatier G., 1950, Acad. Sci. Paris, 230, 1962

Sachez-Moral S., Canaveras J. C., Laiz L., Saiz-Jimenez C., Bedoya J., Luque L., 2003, Geomicrobiol., 20(5), 491

Sargent B. et al., 2009, ApJ Supp. Ser.., 182, 477

Scott E., 2007, Annual review of Earth and Planetary Science, 35, 577

Scott E., Krot A., 2003, Treatise on Geochemistry, 1, 143

Serghiou G., Boehler R., Chopelas A., 2000, J. Phys.: Condensed Matter, 12, 849

Shinno I., 1974, Min. J. Jap., 7, 456

Shuping R. Y., Kassis M., Morris M., Smith N., Bally J., 2006, ApJ, 644, L71

Siegrist T., 1997, Crystallographica - a software toolkit for crystallography

Silk S. T., 1970, PhD thesis, New York University

Singh R. J., 2012, Solid State Physics, 1st edn. Dorling Kindersley

Sitko M. L., Lynch D. K., Russell R. W., Hanner M. S., 2004, ApJ, 612, 576

Sloan E. D., 2003, Nature, 426, 353

Sloan E. D., Koh C., 2008, Clathrate Hydrates of Natural Gases, 3rd edn. Taylor & Francis: Boca Raton, FL

Snow T., 2004, ASP Conference Series, 309, 93

Soldati A. L., Jacob D. E., Wehrmeister U., Hofmeister W., 2008, Mineralogical Mag., 72, 579

Speck A., Whittington A., Hofmeister A., 2011, ApJ, 740, 93

Stecher T., 1965, ApJ, 142, 1683

Subba Rao M., 1973, Bull. Chem. Soc. Japan, 46, 1414

Sum A. K., Burruss C., Sloan E. D., 1997, J. Phys. Chem., 101, 7371

Sum A. K., Koh C. A., Sloan E. D., 2009, Ind. Eng. Chem. Res., 48, 7457

Sutor D. J., Wooley S. E., 1969, Gut, 10, 681

Sylvester R. J., Kemper F., Barlow M. J., de Jong T., Waters L. B. F. M., Tielens A. G. G. M., Omont A., 1999, A&A, 352, 587

Takashi O., Yoko O., 2003, ApJ, 872, 877

Takeya S., Konstantin A. U., Moudrakovski I. L., Susilo R., Ripmeester J. A., 2010, J. Amer. Chem. Soc., 132, 524

Tang C. C., Thompson S. P., Parker J. E., Lennie A. R., Azough F., Kato K., 2009, J. Appl. Cryst., 42, 225

Thomas C., Picaud S., Mousis O., Ballenegger V., 2008, Planetary & Space Sci., 56, 1607

Thompson S., Day S., Evans A., Parker J., 2012a, J. Non-Cryst. Solids, 358, 885

Thompson S., Day S., Parker J., Evans A., Tang C., 2012b, Proceedings on the European Conference on Laboratory Astrophysics, Stehlé C., Joblin C., d'Hendecourt L., eds., Vol. 58. European Astronomical Society Publication Series

Thompson S., Evans A., Jones A., 1996, A&A, 308, 309

Thompson S., Fonti S., Verrienti C., Blanco A., Orofino V., Tang C., 2002, A&A, 395, 705

Thompson S., Parker J., Marchal J., et al., 2011a, J. Synchrotron Radiat., 18, 637

Thompson S., Parker J., Potter J., Hill T., Brit A., Cobb T., Yuan F., Tang C., 2009, Rev. Sci. Instrum., 80, 75107

Thompson S., Parker J., Street S., Tang C., 2011b, J. Phys. Conf. Ser., 286, 012030

Thompson S., Tang C., 2001, A&A, 368, 721

Thompson S., Verrienti C., Fonti S., Orofino V., Blanco A., 2007, Advances in Space Research, 39, 375

Thompson S. P., Parker J., Tang C. C., 2012, A&A, 545

Tielens A., 1990, Proceedings of the International Colloquium, 186

Tielens A., 2008, Annu. Rev. Astron. Astrophys., 46, 289

Toby B. H., 2005, J. Appl. Cryst., 38, 1040

Toppani A., Robert F., Libourel G., de Donato P., Barres O., d'Hendecourt L., Ghanbaja J., 2005, Nature Letts., 437, 1121

Trumpler R., 1930, Publications of the Astronomical Society of the Pacific, 42, 214

Udachin A. K., Ratcliffe C. I., Ripmeester J. A., 2001, J. Phys. Chem. B, 105, 4200

Valenkow N., Porai-Koshitz E., 1936, Z. Krist., 95, 195

van Berk W., Yunjiao F., Ilger J. M., 2012, J. Geophys. Res.: Planets, 117, E10008

van Breemen J. M. et al., 2011, A&A, 526, A152

van Loon J., Cioni M.-R., Zijlstra A., Loup C., 2005, A&A, 438, 273

Vecht A., Ireland T., 2000, Geochimica et Cosmochimica Acta, 64, 2719

Vogel R., Persson M., Feng C., Parkin S. J., Nieminen T. A., Wood B., He N. R., 2009, Langmuir, 25, 11672

Waite, Jr. J. H. et al., 2009, Nature, 460, 487

Wang J., Becker U., 2009b, Am. Mineral., 94, 380

Wang X. Q., Kong R., Pan X. X., Xu H., Xia D. H., Shan H. H., Lu J. R., 2009, J. Phys. Chem. B, 113, 8975

Warren B. E., 1933, Z. Krist., 86, 349

Warren B. E., 1934, J. Am. Ceram. Soc., 17, 249

Warren B. E., Biscoe J., 1931, Z. Krist., 80, 391

Waters L. B. F. M. et al., 1996, A&A, 315, L361

Wehrmeister U., Jacob D. E., Soldati A. L., Hager T., Hofmeister W., 2007, J. Gemmology, 30, 399

Wehrmeister U., Soldati A. L., Jacob D. E., Hager T., Hofmeister W., 2010, J. Raman Spec., 41, 193

Werner M. W. et al., 2004, ApJ, 154, 1

White W. B., 2005, J. Ceram. Proc. Res., 6, 1

Whittet D., 2003, Dust in the Galactic Environment, 2nd edn. Institute of Physics Publishing

Wildey R. L., Murray B. C., 1963, ApJ, 68, 300

Williams T., Kelley C., many others, 2010, Gnuplot 4.4: an interactive plotting program. http://gnuplot.sourceforge.net/

Windisch C. F., Glezakou V.-A., Martin P. F., McGrail B. P., Schaef H. T., 2012, Phys. Chem. Chem. Phys., 14, 2560

Wolf G., Konigsberger E., Schmidt H.-G., Konigsberger L.-C., Gamsjager H., 2000, J. Therm. Analysis Calorim., 60, 463

Wolf G., Lercher J., Schmidt H.-G., Gamsjager H., Konigsberger E., Schmidt P., 1996, J. Therm. Analysis, 46, 353

Wooden D., Harker D. E., Woodward C. E., Bunter H. M., Koike C., Witteborn F. C., McMurty C. W., 1999, ApJ, 517, 1034

Woodward C. E., Bockelee-Morvan D., Kelley M. S., Wooden D. H., 2009, in Bulletin of the American Astronomical Society, Vol. 41, American Astronomical Society Meeting Abstracts 213, p. 401.04

Woolf N., 1973, in Interstellar Dust and Related Topics, Greenburg J., van De Hulst, eds., IAU, p. 485

Woolum D. S., Cassen P., 1999, Meteoritics and Planetary Science, 34, 897

Wray J. L., Daniels F., 1957, J. Am. Chem. Soc., 79(9), 2031

Zachariasen W. H., 1932, J. Am. Ceram. Soc., 17, 3841

Zamarreño D. V., Inkpen R., May E., 2009, Appl. Environ. Microbiol., 75, 5981

Zolensky M., 1987, Science, 237, 1466

Zolensky M., Barratt R., 1994, Meteoritics and Planetary Science, 29, 616

Zolensky M. E. et al., 2006, Science, 314, 1735

A Publications List

A.1 Peer-reviewed Journal Papers

Day, S.J., Thompson, S.P., Evans, A. and Parker, J.E. 2013. Non-aqueous formation of the calcium carbonate polymorph vaterite: astrophysical implications. Astronomy and Astrophysics 553, A68.

Day, S.J., Thompson, S.P., Parker, J.E., Evans, A. and Connor, L. 2013. Thermal Processing and Crystallization of Amorphous Mg-Ca Silicates. Meteoritics and Planetary Science, 48, 1459 - 1471.

Thompson, S.P., **Day, S.J.**, Parker, J.E., Evans, A. and Tang, C.C. 2012. Fine-grained amorphous calcium silicate $CaSiO_3$ from vacuum dried sol-gel - Production, characterisation and thermal behaviour. J. Non-Cryst. Solids 358, 885-892.

Thompson, S. P.,Parker, J. E., **Day, S. J.**, Connor, L. D. and Evans, A. 2013. Photoluminescence in amorphous $MgSiO_3$ silicate. Monthly Notices of the Royal Astronomical Society, 434, 2582 - 2592.

A.2 Peer-reviewed Journal Papers - In Press

Day, S.J., Thompson, S.P., Evans, A. and Parker, J.E. 2014. In situ study of the formation and stability of clathrate hydrates using synchrotron radiation and Raman spectroscopy (Research Note). Astronomy and Astrophysics, *In Press.*

A.3 Refereed Conference Proceedings

Day, S.J., Thompson, S.P., Evans, A. and Parker, J. 2012. Carbonate Formation in Non-Aqueous Environments by Solid-Gas Carbonation of Silicates. EAS Publications Series 58, 283-

Thompson, S.P., Parker, J.E., **Day, S.J.**, Evans, A. and Tang, C.C. 2012. In situ measurement of gas-solid interactions in astrophysical dust and planetary analogues. EAS Publication Series 58, 225-229